# Investigation of the Effects of Image Signal-to-Noise Ratio on TSPO PET Quantification of Neuroinflammation

Christopher Constable

A thesis submitted in fulfilment of the requirements of

Doctor of Philosophy

Discipline of Medical Radiation Sciences

University of Sydney

March, 2013

## Declaration of Authorship and Originality

I, Christopher John Constable (student ID 199591180), hereby declare that this thesis is entirely my own original work and that no other person's work has been used without due acknowledgement. I further declare that this thesis has not been submitted previously, either in part or in full, for degree or diploma, at any institution of higher education.

Signed: Date: 8th August 2013

# Acknowledgements

For their support, encouragement, patience and optimism at every stage of this project, I gratefully acknowledge my primary and associate supervisors at the University of Sydney: Professor Steven Meikle and Associate Professor Roger Fulton. The opportunity to work with such accomplished medical physicists has been a privilege. Acknowledgement is also due to Professor Richard Banati, whose enthusiasm for the 18kDa Translocator Protein sparked my own interest in this topic and whose guidance has been invaluable along the way.

During my candidature, I received a post-graduate scholarship from the Australian Institute of Nuclear Science and Engineering (AINSE), which enabled access to facilities at the Australian Nuclear Science and Technology Organisation (ANSTO). I extend my thanks to Drs Mark Reinhard and Dale Prokopovich at the ANSTO Detector Laboratory, not only for allowing access to the 'PISA' high performance computer cluster, but also for their support, helpful advice and training during the early phase of this project.

I gratefully acknowledge the assistance of Dr Will Ryder at the University of Sydney's Brain and Mind Research Institute (BMRI), for his support and advice on image reconstruction and data storage issues during the latter stages of this project. For helpful advice and information on many PET-related technical issues, and practical assistance too, I thank Robbie Barnett from the Department of Nuclear Medicine, Westmead Hospital, Sydney. I also thank my faculty colleagues and fellow PhD candidates within the Discipline of Medical Radiation Sciences and the BMRI for their support over the years (in reverse alphabetical order): Catriona Wimberley, Sheruna Naidoo, Wencke Lehnert, Andre Kyme, Peter Kench and Paul Callaghan.

Finally I acknowledge with the utmost gratitude my family, who gave support in many ways, but always with great generosity, and without which this undertaking would not have been possible.

# Abstract

Neuroinflammation may be imaged using positron emission tomography (PET) and the tracer [$^{11}$C]-PK11195. Accurate and precise quantification of 18 kilodalton Translocator Protein (TSPO) binding parameters in the brain has proven difficult with this tracer, due to an unfavourable combination of low target concentration in tissue, low brain uptake of the tracer and relatively high non-specific binding, all of which leads to higher levels of relative image noise. To address these limitations, research into new radioligands for the TSPO, with higher brain uptake and lower non-specific binding relative to [$^{11}$C]-PK11195, is being conducted world-wide. However, factors other than radioligand properties are known to influence signal-to-noise ratio in quantitative PET studies, including the scanner sensitivity, image reconstruction algorithms and data analysis methodology. The aim of this thesis was to investigate and validate computational tools for predicting image noise in dynamic TSPO PET studies, and to employ those tools to investigate the factors that affect image SNR and reliability of TSPO quantification in the human brain.

The feasibility of performing multiple ($n \geq 40$) independent Monte Carlo simulations for each dynamic [$^{11}$C]-PK11195 frame- with realistic modelling of the radioactivity source, attenuation and PET tomograph geometries- was investigated. A Beowulf-type high performance computer cluster, constructed from commodity components, was found to be well suited to this task. Timing tests on a single desktop computer system indicated that a computer cluster capable of simulating an hour-long dynamic [$^{11}$C]-PK11195 PET scan, with 40 independent repeats, and with a total simulation time of less than 6 weeks, could be constructed for less than 10,000 Australian dollars. A computer cluster containing 44 computing cores was therefore assembled, and a peak simulation rate of $2.84 \times 10^5$ photon pairs per second was achieved using the GEANT4 Application for Tomographic Emission (GATE) Monte Carlo simulation software.

A simulated PET tomograph was developed in GATE that closely modelled the performance characteristics of several real-world clinical PET systems in terms of spatial resolution, sensitivity, scatter fraction and counting rate performance. The simulated PET system was validated using adaptations of the National Electrical Manufacturers Association (NEMA) quality assurance procedures within GATE.

Image noise in dynamic TSPO PET scans was estimated by performing $n$=40 independent Monte Carlo simulations of an hour-long [$^{11}$C]-PK11195 scan, and of an hour-

long dynamic scan for a hypothetical TSPO ligand with double the brain activity concentration of [$^{11}$C]-PK11195. From these data an analytical noise model was developed that allowed image noise to be predicted for any combination of brain tissue activity concentration and scan duration. The noise model was validated for the purpose of determining the precision of kinetic parameter estimates for TSPO PET.

An investigation was made into the effects of activity concentration in tissue, radionuclide half-life, injected dose and compartmental model complexity on the reproducibility of kinetic parameters. Injecting 555 MBq of carbon-11 labelled TSPO tracer produced similar binding parameter precision to 185 MBq of fluorine-18, and a moderate (20%) reduction in precision was observed for the reduced carbon-11 dose of 370 MBq. Results indicated that a factor of 2 increase in frame count level (relative to [$^{11}$C]-PK11195, and due for example to higher ligand uptake, injected dose or absolute scanner sensitivity) is required to obtain reliable binding parameter estimates for small regions of interest when fitting a two-tissue compartment, four-parameter compartmental model. However, compartmental model complexity had a similarly large effect, with the reduction of model complexity from the two-tissue compartment, four-parameter to a one-tissue compartment, two-parameter model producing a 78% reduction in coefficient of variation of the binding parameter estimates at each tissue activity level and region size studied.

In summary, this thesis describes the development and validation of Monte Carlo methods for estimating image noise in dynamic TSPO PET scans, and analytical methods for predicting relative image noise for a wide range of tissue activity concentration and acquisition durations. The findings of this research suggest that a broader consideration of the kinetic properties of novel TSPO radioligands, with a view to selection of ligands that are potentially amenable to analysis with a simple one-tissue compartment model, is at least as important as efforts directed towards reducing image noise, such as higher brain uptake, in the search for the next generation of TSPO PET tracers.

# Table of Contents

# List of Illustrations

# List of Tables

# Chapter 1

## 1.1 Motivation for the Work

Neuroinflammation is implicated in a wide range of neurological diseases, and is of considerable interest both clinically and as a focus of basic neuroscience research. Positron emission tomography (PET) has been employed successfully to image neuroinflammation via the tracer [$^{11}$C]-PK11195- a radioligand for the 18 kilodalton Translocator Protein (TSPO). However accurate and precise quantification of the PET data has proven challenging due to a combination of adverse tracer properties, and the ubiquitous yet sparse distribution of the TSPO in the normal human brain. New radiotracers for the TSPO are under development in an attempt to address some of the well documented shortcomings of [$^{11}$C]-PK11195: specifically tracers with higher levels of brain tissue uptake and lower non-specific binding are sought in order to improve image signal-to-noise ratio and allow more accurate and precise measurements of neuroinflammation.

Estimation of image noise in PET is a challenging problem, due to the practical difficulties in obtaining a large number of independent repeated measurements and the complex way in which noise propagates through the PET image formation process and subsequent analysis algorithms. It is therefore difficult to predict the relative gains in image SNR that may be expected of novel TSPO radiotracers based on brain uptake alone, other than to say that 'more uptake is better'. An accurate estimate of image SNR, for different levels of TSPO tracer uptake in the brain, would therefore allow more reliable predictions to be made concerning the changes in quantification precision associated with different tracers, and enable a more informed assessment of the relative importance of the various determinants of quantification reliability for TSPO PET.

Recent advances in computer hardware and software technology mean that present-day computer clusters built from inexpensive commodity hardware components can provide levels of computational power that, as recently as the late 1990's, were available only from multi-million dollar supercomputers. Computing clusters are well suited to Monte Carlo simulation tasks, which are typically amenable to parallel execution with minimal modification to the code. Therefore the rapid improvement in computing cost-to-performance ratio due to commodity clusters has enhanced the feasibility and accessibility of Monte Carlo

simulations of greater complexity and scale, thus providing an ideal tool to study image signal-to-noise and its effect on quantification of TSPO PET scans.

## 1.2 Overall Aims and Organisation of the Thesis

The purpose of this research was to develop and validate computational tools that allow a detailed investigation to be undertaken of factors that impact on quantification error for TSPO PET studies, and to use those tools to investigate the relative contributions of these factors to image SNR and reliability of TSPO quantification in the human brain.

This research was conducted with three broad aims:

1. To design, develop and validate a low cost, high performance computing cluster dedicated to Monte Carlo simulation of clinical PET systems. Specifically, a system was required that was: capable of simulating a realistic [$^{11}$C]-PK11195 dynamic scan of the human brain, of at least sixty minutes duration, including attenuation and scatter, with at least forty independent repeats, without the use of variance reduction and with a total simulation time of four weeks or less.
2. Using the computing resources developed in stage 1; validate a Monte Carlo code for simulating a realistic human PET system, and develop and validate a noise model for predicting image noise from tissue time-activity data for the TSPO PET scans.
3. Using the simulation tools developed in stages 1 and 2; investigate the image signal-to-noise properties of TSPO radiotracers in dynamic scanning of the human brain, and the subsequent effects of tracer properties on quantitative parameter estimation.

The remainder of this thesis is organised as follows. In Chapter 2, a survey of the literature is made with respect to the estimation of image noise in PET. Monte Carlo simulation is then discussed, and the potential use of Monte Carlo as a tool for estimating image noise is explored. High performance computing with low-cost commodity hardware is introduced, and an argument is made for the suitability of such systems to Monte Carlo simulations for the study of PET image noise. Finally, a review of the current literature on TSPO PET brain imaging is presented, with an emphasis on the limitations of [$^{11}$C]-PK11195, the development of new TSPO tracers and physiological quantification of TSPO PET images.

Chapter 2 concludes with a summary of the current state-of-the-art with respect to high performance computing and Monte Carlo software, and the state of knowledge regarding TSPO PET imaging. It is hypothesised that recent advances in high performance computer design, current Monte Carlo simulation software and methods for estimating noise in positron emission tomography (PET) might be combined to permit an analysis of image signal-to-noise ratio (SNR) within the context of neuroinflammation imaging and TSPO PET tracers.

In Chapter 3 the feasibility of constructing a high performance computer cluster from commodity components is explored, within the context of using the GEANT4 Application for Tomographic Emission (GATE) Monte Carlo software package to estimate image noise from realistic PET simulations. Pilot experiments are described from which an assessment was made of the computer hardware required and associated costs to meet the design goals articulated in the first aim above.

In 3.2 methods available for accelerating GATE simulations are tested. In particular, the 'fictitious interactions' photon tracking algorithm and gamma discard energy settings are investigated with respect to their effect on execution time and the statistical properties of the output data.

In 3.3 a design for a low cost computer cluster is presented, capable of meeting the specific goals articulated in the first aim above.

In Chapter 4 the development and validation of a detailed model of a generic PET tomograph within the GATE software package, with performance characteristics broadly similar to modern clinical PET systems, is described.

In 4.2 experiments are described in which the image SNR was estimated for a multi-frame dynamic PET simulation of the human brain for the tracer $^{11}$C-PK11195, and for a second hypothetical tracer with twice the brain uptake. A total of forty independent noise realisations for each frame were obtained, allowing the standard deviation for each image voxel, and various regions-of-interest, to be calculated. Procedures for image reconstruction using a publicly available software package are also described and validated, including realistic corrections for random and scatter coincidences, attenuation and variable geometric detector efficiencies.

In 4.3 a mathematical model is derived that relates the relative image noise to the tissue concentration of radioactivity in grey matter and scan duration, under the conditions

studied in the previous experiments. The validity of this model for estimating the reliability of kinetic parameter estimates for TSPO tracers is established.

In Chapter 5 an investigation into the impact of various factors on the reliability of kinetic parameter estimation in TSPO PET is described. In particular, the relative contribution of brain uptake, region-of-interest size, radionuclide half-life and compartmental model complexity to the reliability of parameter estimates is explored.

In Chapter 6 the main findings and conclusions of the work presented in this thesis are summarised, and potential for further investigation is discussed.

## 1.3 Conference Proceedings

Results presented in 4.2 were presented at the Australian and New Zealand Society of Nuclear Medicine Annual Scientific Meeting, 2012.

Constable, C., Meikle, S., & Fulton, R. (2012). THE EFFECT OF TRACER UPTAKE AND IMAGE RECONSTRUCTION METHOD ON IMAGE NOISE FOR TSPO PET LIGANDS. *Paper presented at the Australian and New Zealand Society of Nuclear Medicine Annual Scientific Meeting 2012, Melbourne.*

# Chapter 2 Background and Literature Review

## 2.1 Overview

Positron emission tomography (PET) is a functional medical imaging modality that may be used to study a variety of physiological processes in healthy and diseased states. Recently, PET has been used to study the process of neuroinflammation and the potential research and clinical applications of this technology are of increasing interest worldwide. Neuroinflammation is characteristic of many diseases of the central nervous system. The radiotracer [$^{11}$C]-PK11195, which binds to the 18 kilodalton (18kDa) Translocator Protein (TSPO), has been used successfully as an imaging probe for this process in subjects with a range of neurological diseases. Nonetheless, accurate and precise quantification of neuroinflammation with this TSPO PET tracer has proven challenging, due to an unfavourable combination of adverse tracer properties and the sparse yet ubiquitous distribution of TSPO in the normal brain. In an attempt to address some of the well documented shortcomings of the tracer [$^{11}$C]-PK11195, considerable research effort has been expended in developing new radioligands for the TSPO. In particular, ligands with higher levels of brain tissue uptake and lower non-specific binding are sought in order to reduce image noise and allow more accurate and precise measurements of neuroinflammation. This review will cover the causes, effects and measurement of image noise in PET, how this noise relates to the quantification challenges associated with [$^{11}$C]-PK11195 PET, and how modern developments in high performance computer technology and Monte Carlo simulation software might be exploited to investigate the factors that affect accurate and precise quantification of neuroinflammation with TSPO tracers.

## 2.2 Positron Emission Tomography

### 2.2.1 Introduction to Positron Emission Tomography

Positron emission tomography is a medical imaging modality that operates on the detection of the dual 511 keV gamma photon emissions that follow the annihilation of a positron and an electron. A positron emitting radionuclide is introduced into the biological system under investigation. An emitted positron then combines with an electron from the surrounding matter, releasing two annihilation gamma photons of exactly 511 keV energy each. PET scanners exploit the simultaneous and 180° separation of these 511 keV photons to

provide information on the location of the positron emission: a 'prompt coincident' event is recorded between two opposing detectors only if both detectors register an event within a very narrow time window, typically less than 10 nanoseconds duration. Over a period of several minutes, enough coincident events are collected to permit images of the spatial distribution of positron emitting radionuclide within the scanner's field-of-view to be reconstructed into three-dimensional tomographic (i.e. cross-sectional) images (Figure 2.1 and Figure 2.2).

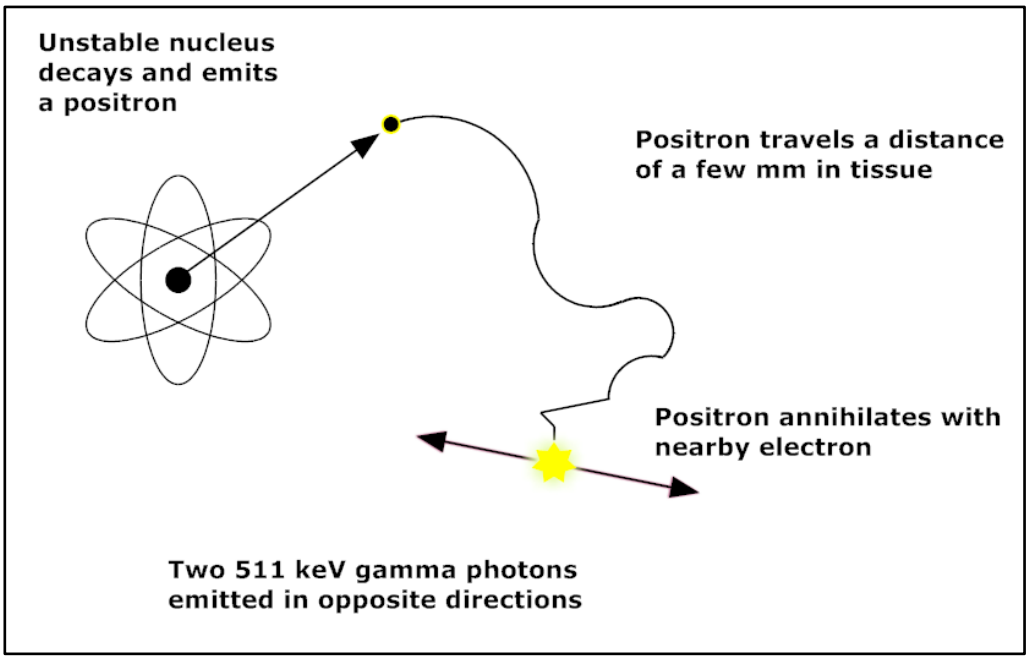


Figure 2.1. Diagram illustrating the production of two 511 keV photons following a positron decay. An unstable nucleus undergoes positron decay, emitting a positron- the antiparticle of the electron. The positron typically undergoes several scattering interactions in surrounding matter before annihilating with a nearby electron. Upon annihilation, two gamma photons of 511 keV are emitted in opposite directions. Typically the range travelled by the positron in soft tissue is a few millimetres or less, depending on its kinetic energy. The angle of separation of the two 511 keV photons is 180° ± 0.5°FWHM (Cherry, Sorenson, & Phelps, 2003).

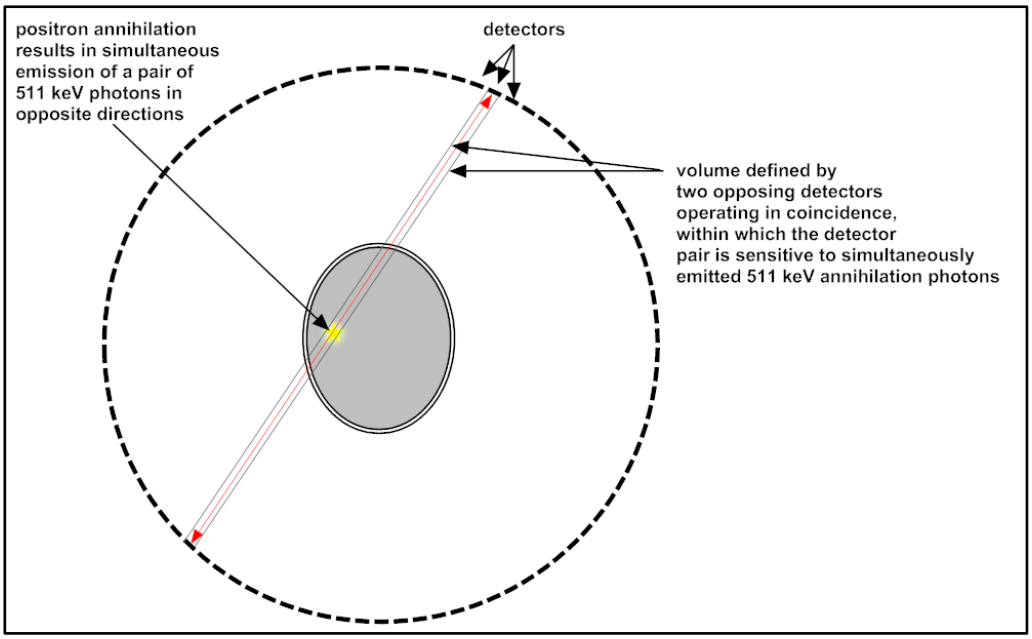


Figure 2.2. Schematic illustration of a PET scanner. Detectors are arranged in a 360° array and operated in 'coincidence' mode: two photons that are detected by opposing detectors within a narrow time window (typically 5-10 nanoseconds) are accepted as 'prompt coincident' events. These coincident events are assumed to originate from a single positron/electron annihilation lying somewhere along the 'line-of-response', which is really the volume defined by the two detectors. By collecting a large number (typically $10^7$ – $10^8$) of such events, an image may be reconstructed that represents the spatial distribution of positron emitting radionuclide within the field-of-view. Modern PET systems employ multiple rings of radiation detectors optimised for the efficient detection of 511 keV photons. A typical clinical (human) scanner has a ring diameter of around 80-100 cm and an axial field-of-view of 15-25 cm.

Inorganic scintillators such as Bismuth Germanate (BGO), Gadolinium Oxyorthosilicate (GSO) or Lutetium Oxyorthosilicate (LSO) are the dominant type of radiation detector used in modern PET scanners, due to their generally favourable combinations of low cost, high detection efficiency at 511 keV, good energy resolution and timing resolution (Phelps, 2006). Individual detectors are generally cut from larger blocks or assembled into panels, containing tens or hundreds of individual detectors separated by a small gap, and arranged in a cylindrical configuration around the central axis of the scanner. Detectors are usually square or rectangular cuboids, measuring between 4 to 6 mm in the shortest two dimensions and between 20 to 30 mm in the longest dimension for clinical (human use) systems. Detector-to-detector diameter of a modern clinical scanner is typically 80 cm to 100 cm, and the axial field-of-view is usually between 15 cm and 25 cm.

A distinction is made between two-dimensional (2D) and three-dimensional (3D) acquisition mode PET scanners. A PET system that collects data in 2D mode does so with the presence of axial septa: lead or tungsten shields which limit the angle of acceptance of

coincident events to those originating within a narrowly defined number of axial image slices. A PET system operating in 3D mode does so without such axial septa, thereby accepting coincident events over a much wider range of axial slices. Most modern PET systems are of the '3D' type, and have a much higher sensitivity than older 2D systems (Phelps, 2006).

Spatial resolution of a PET scanner is specified by the full width half maximum (FWHM) of the image profile of a very small point source of radioactivity, or the 'point response function'. Current clinical PET systems can achieve spatial resolutions of around 4-6 mm FWHM. Higher spatial resolution systems dedicated for imaging the human brain, and small animal research systems, can achieve spatial resolutions down to about 1 mm FWHM (Phelps, 2006; Zanzonico, 2011). This resolution is somewhat poorer than other medical imaging modalities like Computed Tomography (≈0.1 mm) and Magnetic Resonance Imaging (≈1 mm) (Bourne, 2010).

Sensitivity of a PET scanner is defined generally as the number of coincidence events detected per unit time per unit activity in the field-of-view. Sensitivity at the centre of the field-of-view depends on the exact geometry of the system and mode of operation, but is generally around 5% to 10% for modern '3D mode' PET scanners (Phelps, 2006).

A prompt coincident event recorded by two detectors in a PET scanner may be one of four types: a true coincident event, a random coincident event, a scattered coincident event or a multiple coincident event (Cherry et al., 2003). As their name suggests, true coincident events ('trues') result from the detection of a pair of 511 keV photons that arise from single positron-electron annihilations occurring between the two detectors. Random coincident events ('randoms') result from the detection of two unrelated photons, as do multiple coincident events. Random events are approximately evenly distributed across the field-of-view, and the rate of random event collection increases exponentially as the activity within the field-of-view increases, and linearly as the coincidence timing acceptance window is widened. Scattered coincident events ('scatters') result from the detection of a pair of photons that arise from single positron-electron annihilations, one or both of which have undergone a scattering interaction before being detected. Scattering causes a photon to lose energy and change direction, and usually results in the affected photon arriving somewhat 'off-target' with respect to the detectors. Scatter distribution across the field-of-view is partly correlated with the distribution of radioactivity and matter within the scanner's field-of-view, and unlike random events, the rate of scatter collection is not dependent on the quantity of gamma

photons striking the detectors. Figure 2.3 illustrates the four types of coincidence event in PET.

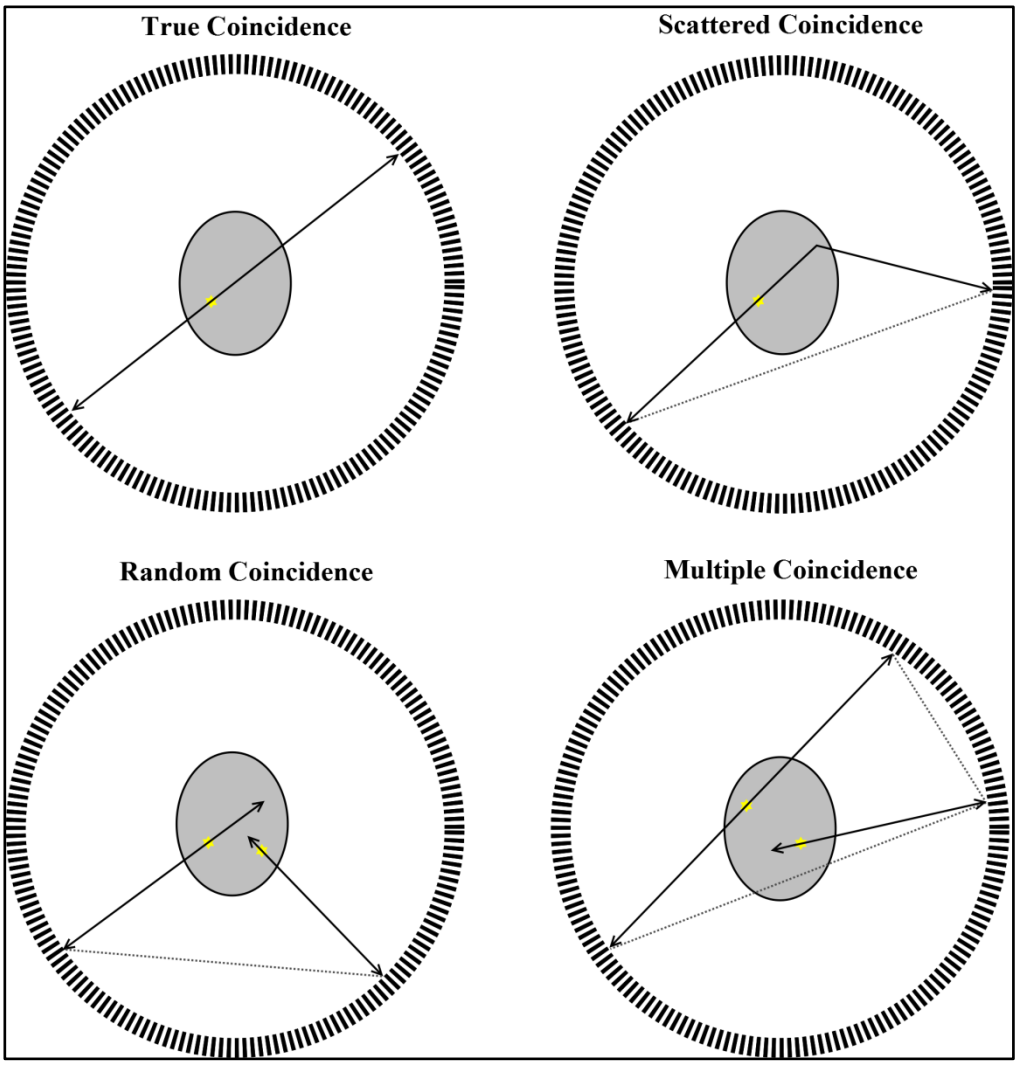


Figure 2.3. Four types of coincidence events in PET. Only true coincidences carry useful information about the location of positron-emitting radionuclide within the field-of-view.

True coincident events are the only desirable type of coincident event in PET because they alone carry useful information on the location of positron-emitting radionuclides within the scanner's field-of-view. Randoms and scatters are nuisance events that tend to add an approximately uniform background signal to the PET data. Accurate correction for random and scattered events is therefore very important to ensure that the PET images accurately reflect the distribution of positron emitting nuclide within the object being scanned. Scintillator detectors used in PET are capable of energy discrimination, and this ability is used to screen out many scattered photons which are less than 511 keV. However the energy resolution of the PET detectors is limited, and many scattered photons have an energy only

slightly less than 511 keV (Phelps, 2006), so many scattered events are still accepted and must be corrected for by other means.

Data correction methods vary, but usually involve estimation of the scatter and/or random contribution, followed by subtraction of this estimate from the original data prior to or during image reconstruction (Meikle & Badawi, 2003). The rate of random coincidence events may be estimated with a delayed coincidence circuit, or by applying a model that relates the singles count rate data to the rate of random coincidences for each detector block or panel (Brasse et al., 2005). Scatter correction methods may employ multiple energy windows (Grootoonk, Spinks, Sashin, Spyrou, & Jones, 1996), Monte Carlo simulation (Holdsworth, 2002) or analytical modelling (Ollinger, 1996; Watson, Newport, & Casey, 1996) to arrive at an estimate of the scatter in the raw PET data.

Attenuation of photons in matter is another nuisance issue that affects PET. Many gamma photons will be scattered and absorbed by the matter within the body or object being scanned before they can reach the detectors. Attenuation therefore reduces the number of detected events relative to what would be expected in the absence of attenuation. The likelihood of photon attenuation is greater for those originating deep within the object, and less for those originating near the surface. However, since two annihilation photons are required for a true coincident event to be recorded, photon attenuation along the entire line-of-response (LOR) between two detectors will affect the observed number of coincidences for that LOR. In human brain scanning, up to 30% of coincidence counts may be lost within some LORs. As is the case for scatter and random coincidences, attenuation must also be corrected for in PET. This correction usually involves measurement or estimation of the attenuation properties of the object being scanned, and application of a correction factor for each LOR during image reconstruction. Measured attenuation correction factors may be obtained from an externally located source of radioactivity or, in the case of combined PET/CT scanners, a Computed Tomography (CT) scan carried out at the same time as the PET scan (Beyer et al., 2000; Zaidi, Montandon, & Meikle, 2007).

Detector normalization, whereby inevitable variations in sensitivity between different detectors is compensated for, is another correction that must be performed on PET data. Detectors may vary in efficiency due to electronic errors, differences in crystal composition, mechanical misalignments or geometrical effects. Correction factors are usually determined via long-duration acquisitions from a uniform source phantom at pre-defined service

intervals, usually in combination with pre-determined correction factors describing the long-term stable components of non-uniformity for a particular scanner (Oakes, Sossi, & Ruth, 1998).

All methods of data correction described above have the potential to introduce random noise into the PET data, especially if the measurements used for estimating the corrections are themselves noisy. Structural errors may also be introduced by data corrections, manifesting as image artefacts. The concept of the noise equivalent counts (NEC) attempts to take the effects of randoms and scatter subtraction on image signal-to-noise ratio into account (Strother, Casey, & Hoffman, 1990), and is defined as:

$$NEC = \frac{T^2}{T^2 + S + \alpha R} \tag{1}$$

where $T$ is the total number of true coincidences, $S$ is the total scatter coincidences and $R$ is the total random coincidences, and $\alpha$ is equal to 1 or 2, depending on the method of randoms correction. The $\alpha$ factor takes a value of 2 when the randoms correction propagates noise into the data, as is the case for the delayed event subtraction algorithm. When the relative noise level of the randoms estimate is considered low, then the $\alpha$ factor takes a value of 1. As the above equation implies, maximising NEC is achieved by minimising the contribution of random and scattered coincidences, while maximising the sensitivity of the scanner to true coincidences. Noise equivalent count rate (NECR) is defined similarly, where $T$, $S$ and $R$ in equation 1 are expresses as count rates, typically counts per second (cps) or kilocounts per second (kcps).

Image reconstruction is the process of converting the coincident event projection data from the PET scanner into a three-dimensional image of the spatial distribution of positron emitting radionuclide. Prior to reconstruction, PET projection data are commonly sorted into two-dimensional digital arrays called ‘sinograms’, with each sinogram element corresponding to a particular LOR location and angle (Figure 2.4). Scanners operated in 3D mode produce large sinogram arrays, and compression of these 3D sinograms down to 2D equivalent sinograms is often done as a means of speeding up image reconstruction and saving storage space. Direct storage of individual event locations and times in a ‘list mode’ file is also possible.

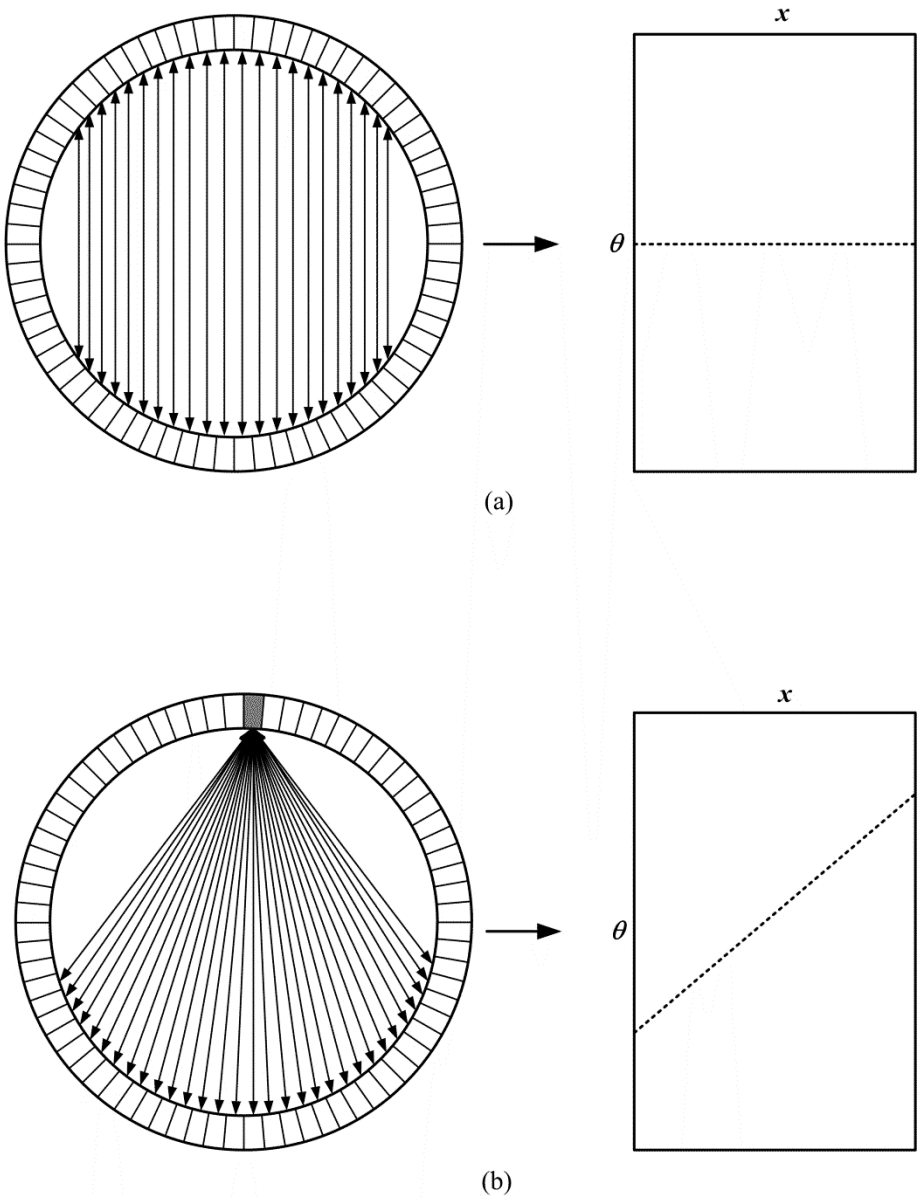


Figure 2.4. PET sinogram formation, single 2D slice example. By convention, the horizontal axis ($x$) of the sinogram represents the distance of a LOR from the transverse centre of the scanner and the vertical axis ($\theta$) represents the angular displacement of the LOR. In (a) parallel LORs form a horizontal line at $\theta$=0°. In (b) all LORs formed between the top crystal and those opposite form a diagonal line in the sinogram. (Diagram courtesy of Dr Andre Kyme, University of Sydney).

Currently there are two broad classes of reconstruction algorithm applied in PET: Analytic reconstruction methods, of which filtered back projection (FBP) is the most common and iterative reconstruction methods, of which the Maximum Likelihood Expectation Maximisation with Ordered Subsets acceleration (OS-EM) is most often used. Corrections for the above mentioned effects (scatter, randoms, attenuation and normalization) are applied to the PET sinograms prior to FBP reconstruction, while corrections may be applied prior to or during reconstruction with the OS-EM algorithm.

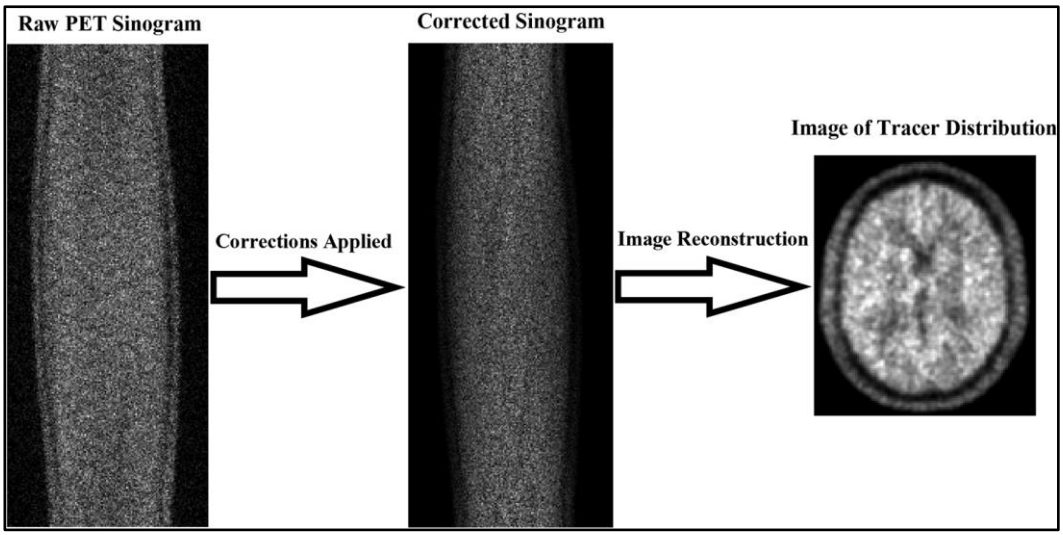


Figure 2.5. Image reconstruction in PET. In this example a representative sinogram corresponding to one transverse slice through the human brain is shown. Coincidence counts are sorted into a series of 2D arrays called 'sinograms'. Corrections for randoms, scatters, relative detector efficiency and attenuation are applied prior to image reconstruction. Iterative reconstruction algorithms may also incorporate these corrections directly into the reconstruction process. Note the effects of applying the corrections on the sinogram data: scattered and random events, which are especially evident towards the darker edges of the sinogram outside the main object, are removed. Attenuation correction boosts the sinogram values towards the middle of the object where attenuation effects are greatest. Detector normalization has also been applied, however its effects are harder to discern visually due to the presence of noise in this example. (Sinograms generated by Monte Carlo simulation using a digital model of the human head).

### 2.2.2 Radiotracers

A tracer is a substance that, when introduced into a biological or other system, allows measurements to be made of dynamic processes within that system (Hevesy, 1923). To qualify as a tracer, the mass of the substance introduced must be very small relative to the system being studied, so as not to disturb the system and influence the obtained measurements. In order to allow measurement, a tracer must also be amenable to some kind of external detection. The tracer principle is applied in PET: a positron emitting radionuclide is chemically 'labelled' to a molecule that interacts with the biological system of interest. A quantity of this labelled substance- the radiotracer- is administered into the system: for human and animal studies this is usually accomplished by intravenous injection of the tracer in liquid form. The radiotracer then localises in the subject's body according to the biochemical properties of the tracer, and the physiological or pathophysiological pathway that the tracer is designed to follow. Images are then obtained that accurately represent the spatial and temporal distribution of the radiotracer within the body.

Some examples of positron emitting radionuclides (and their half-lives) commonly used in PET include: fluorine-18 (110 minutes), carbon-11 (20 minutes), nitrogen-13 (10 minutes) oxygen-15 (2 minutes), rubidium-82 (76 seconds) and gallium-68 (68 minutes). Positron emitters include several of the elements most commonly found in biological systems, and this makes them particularly suited to the study of living systems, since biologically active molecules may be labelled for use as tracers by chemically substituting carbon-12 for carbon-11, nitrogen-14 for nitrogen-13 and so on. Although no positron emitting isotope of hydrogen exists, fluorine-18 may be substituted for $OH^-$ in large molecules with negligible change to their chemical properties (Bourne, 2010).

With the exception of the coincidence detection methodology and the energy of the emitted gamma photons, PET has much in common with other imaging modalities that utilise radionuclides and the tracer principle, such as Single Photon Emission Computed Tomography (SPECT) and planar scintigraphy. PET may therefore be characterised as a nuclear medicine modality, as well as a molecular imaging modality.

### 2.2.3 Clinical and Research Applications of PET

The majority of clinical PET scans performed on humans today are whole body metabolism studies with the radiotracer 2-[$^{18}$F]-fluorodeoxy-D-glucose (FDG). An analogue of glucose that follows a very similar metabolic pathway to glucose in the body, FDG is widely used to study the location and metabolic activity of malignant tumours. Other applications of PET include functional imaging of the human brain and heart (Herholz, Herscovitch, & Heiss, 2004). To date, brain scanning with PET has largely been focused on the detection and measurement of such aspects of neuronal function as regional cerebral glucose metabolism, using the radiotracer FDG, and regional cerebral blood flow, using $H_2{}^{15}O$. In addition to these two common applications, radiotracers that bind to specific neuro-receptors in the brain have been developed, such as [$^{18}$F]-FDOPA for assessment of dopamine synthesis (Garnett, Firnau, & Nahmias, 1983), [$^{11}$C] –raclopride for assessment of dopamine D2 receptor function (Farde et al., 1985), or [$^{11}$C]-flumazenil for assessment of Central Benzodiazepine Receptor function (Persson et al., 1985). Many other neuro-receptors have been studied with PET, along with other biological processes in the brain, such as amino acid uptake into tumours (Herholz et al., 2004).

In addition to its clinical applications, PET is used extensively as a research tool to study physiological processes non-invasively in humans and animals (Bentourkia & Zaidi, 2006).

### 2.2.4 Quantification and Kinetic Modelling in PET

Image quantification in combination with the tracer principle allows PET to measure regional physiological parameters in living tissue. These measurements are spatially discrete and specific to regions of the human body typically in the order of 10 – 20 $mm^3$ in volume (Herholz et al., 2004).

It is well recognised that the accuracy of PET quantification is dependent on the ability to accurately calibrate the scanner's sensitivity to radioactivity, and to accurately measure or estimate corrections for the various sources of error inherent in PET imaging. These errors include the loss of information due to photon attenuation and scatter, random coincidence events, system dead time counting losses, variations in detector efficiency and partial volume averaging effects (Meikle & Badawi, 2003). All the above sources of error, with the possible exception of partial volume effects, are routinely corrected for on modern PET systems either during scanning or during image reconstruction (Phelps, 2006). In addition, other potential sources of error specific to an individual PET study might include blurring due to in-voluntary patient motion, and technical errors such as an imperfect intravenous injection, radioactive contamination or scanner malfunction.

Assuming that accurate calibration and corrections have been made as outlined above, and that other sources of error have been eliminated, then each PET image voxel (three-dimensional pixel) will hold a value that accurately represents the absolute radioactivity concentrations at that location, in units such as kilobequerels per millilitre (kBq/mL). In other words, the images are quantitative spatial representations of the underlying PET tracer distribution in-vivo at the time of scanning. For absolute physiological quantification, these activity concentration measurements must now be translated into physiologically relevant measurements. This is done through the application of a mathematical model that describes the kinetic behaviour of the radiotracer in the body. Kinetic modelling requires accurate measurements of the regional tracer concentration in the body in four dimensions: three spatial dimensions and time. Therefore, a dynamic PET scan, starting at the same time as tracer injection, is usually required. Most commonly in PET, the kinetic model used is a compartmental model (Huang & Phelps, 1986).

Compartmental models incorporate known information about the tracer and its interaction with the physiological process under study, providing a framework within which to interpret the PET data (Huang & Phelps, 1986). A 'compartment' represents a physical or chemical form in which the tracer exists, which may or may not correspond to a discrete physical space. The rate at which tracer leaves one compartment is proportional to the concentration of tracer in that compartment, and is described by a first order linear equation with rate constant '*k*', in units of inverse time. A rate constant equal to 0.2/minute therefore means that twenty per cent of the tracer will exit the compartment every minute. The following diagram (Figure 2.6) presents an example of a compartmental model with three tissue compartments and an arterial plasma compartment.

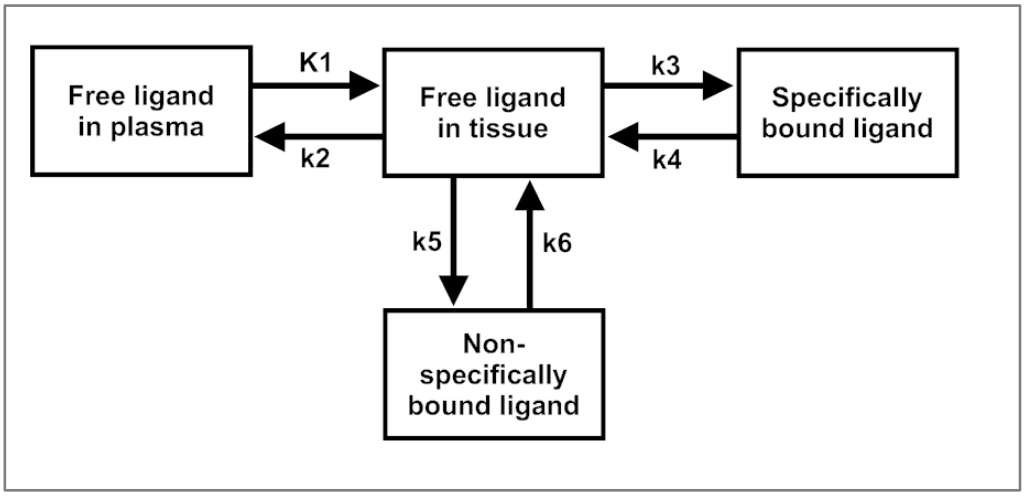


Figure 2.6. Example of a compartmental model that describes the kinetic behaviour of a neuro-receptor binding radiotracer in brain tissue. There are four compartments and six rate constants in this model. The PET image measurement will incorporate all three 'tissue compartments' on the right, as well as some of the blood plasma compartment on the left. The values of the rate constants in an individual PET study may be estimated using non-linear least squares curve fitting.

By convention in PET imaging, rate constants are numbered sequentially from left to right in a compartmental model (Huang & Phelps, 1986). It is the estimation of these rate constants describing the kinetic behaviour of the tracer in tissue that provides the physiological parameters of interest in a PET study (Bentourkia & Zaidi, 2006). In particular, for neuro-receptor studies the parameter known as binding potential (*BP*) is most often sought, and is usually defined as the ratio of $k_3/k_4$ (Laruelle, Slifstein, & Huang, 2003), although the exact definition can depend on what model is used (see 2.2.5). These parameters may be calculated for a collection of anatomically or functionally related image voxels-

known as a region-of-interest (ROI), or for each image voxel individually- resulting in a parametric image.

In the compartmental model illustrated above (Figure 2.6), the first compartment represents the time varying concentration of free (i.e. not bound to proteins) radiotracer in blood plasma that is available for transport into tissue ($C_{plasma}(t)$). The tracer is typically administered by intravenous injection as a single bolus over thirty seconds or less, so the arterial concentration of tracer in plasma usually rises to a peak early and then drops rapidly as the tracer is taken up into the tissues of the body. This plasma time-activity curve is also known as the input function to the model, and it is usually necessary to measure this separately from the PET scan using arterial blood samples taken during the PET study. This arterial sampling requirement is often considered the most invasive and technically challenging part of a quantitative PET examination, and alternative methods for obtaining the arterial input data are often sought. These methods include measurement of arterial time-activity functions from the dynamic PET images directly over a large blood pool structure like the heart or large blood vessels in the brain, or using a pre-determined population average input function, scaled to each patient using a reduced number of arterial or even venous blood samples (Bentourkia & Zaidi, 2006).

The other three tissue compartments in Figure 2.6 represent three possible binding states in which this hypothetical radioligand is expected to exist within the tissues of interest: free (i.e. in the intracellular or interstitial fluid and not bound to any site), specifically bound (to the imaging target), and non-specifically bound (to other non-target sites). A system of differential equations describing the rate of change over time ($t$) of the net tracer concentration ($C$) for each tissue compartment in Figure 2.6 is given below in equations 2, 3 and 4 (PMOD Technologies Ltd., 2010):

$$\frac{dC_{non\text{–}specific}(t)}{dt} = k_6 C_{free}(t) - k_5 C_{non\text{–}specific}(t) \qquad 2$$

$$\frac{dC_{specific}(t)}{dt} = k_3 C_{free}(t) - k_4 C_{specific}(t) \qquad 3$$

$$\frac{dC_{free}(t)}{dt} = K_1 C_{plasma}(t) - (k_2 + k_3 + k_6) C_{free}(t) + k_4 C_{specific}(t) + k_5 C_{non\text{–}specific}(t) \qquad 4$$

Each voxel or region within the PET scan image will contain a contribution from all three of the tissue compartments, as well as a contribution from the tracer that is still circulating in the blood. Fractional blood volume in the tissue of interest ($V_B$), as well as blood concentration of tracer at each time point ($t$) during the PET acquisition ($C_{blood}(t)$), are required to estimate the contribution of blood-borne tracer to the total signal from a region of interest. Therefore the activity concentration of tracer as measured by PET at time $t$ ($C_{PET}(t)$) is the sum of the tissue compartment activity concentrations at time $t$ ($C_{tissue}(t)$) plus the blood activity concentration at time $t$. Equation 5 (PMOD Technologies Ltd., 2010) expresses this concept:

$$C_{PET}(t) = (1 - V_B)C_{tissue}(t) + V_B C_{blood}(t) \qquad 5$$

A value between 2 – 5% is sometimes assumed for $V_B$ in human brain tissue, although higher values have been reported for some tracers (Kropholler et al., 2005).

Comprehensive compartmental models that describe every identifiable compartment for a given tracer are rarely applicable to PET studies, because of limitations in the signal-to-noise ratio of the PET data, limitations to the temporal sampling rates that may be achieved, and the high degree of uncertainty associated with estimating many parameters at once (non-uniqueness of parameters). For these reasons, model simplification, whereby the number of compartments is reduced, is usually required before the model can be considered practically applicable to PET (Koeppe, Holthoff, Frey, Kilbourn, & Kuhl, 1991). Two compartments may be merged into one when the rate constants describing the transport between them are much larger (i.e. faster) than the rate constants describing the transport in and out of the combined compartment (Huang & Phelps, 1986; Koeppe et al., 1991). Using the example from Figure 2.6 above, if the rate constants $k_5$ and $k_6$ are known to be relatively large compared to $K_1$, $k_2$, $k_3$ and $k_4$, then the model may be simplified from four compartments down to three compartments. In this case, the 'free' and 'non-specifically bound' ligand compartments should equilibrate rapidly relative to the other compartments and relative to the overall scan duration, and so may be combined into one compartment without significant loss of model accuracy. This yields a simpler model for which parameter estimation is likely to be more precise than was the case for the original six-parameter model. This model is hereafter referred to as a two-tissue compartmental model (2TCM) and is illustrated in Figure 2.7 below.

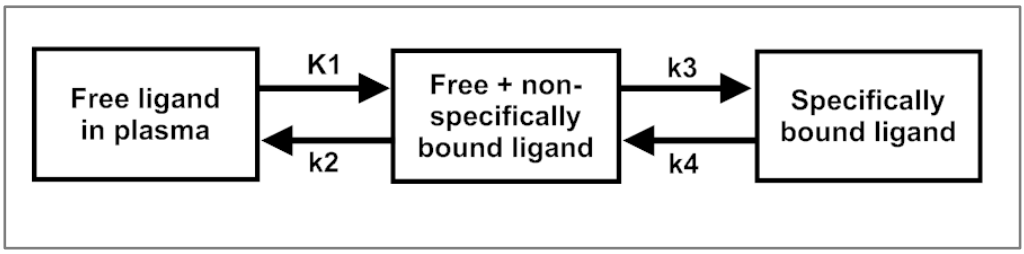


Figure 2.7. Simplified kinetic model with three compartments and four rate constants. The 'free' and 'non-specifically bound' ligand compartments from Figure 2.6 have been merged into one compartment. This is valid only if the rate constants $k_5$ and $k_6$ are much larger than the other rate constants, causing the 'non-specifically bound' compartment to equilibrate rapidly with the 'free ligand' compartment.

Differential equations describing the rate of change over time ($t$) of the net tracer concentration ($C$) for each tissue compartment in Figure 2.7 are shown below in equations 6 and 7:

$$\frac{dC_{specific}(t)}{dt} = k_3 C_{free+non\text{-}specific}(t) - k_4 C_{specific}(t) \qquad 6$$

$$\frac{dC_{free+non\text{-}specific}(t)}{dt} = K_1 C_{plasma}(t) - (k_2 + k_3) C_{free+non\text{-}specific}(t) + k_4 C_{specific}(t) \qquad 7$$

Further simplification of this model is possible. If one can assume that the $k_3$ and $k_4$ rate constants are large (i.e. rapid exchange) with respect to the $K_1$ and $k_2$ rate constants, then the last two compartments may be merged into a single tissue compartment (Figure 2.8). This level of model simplification has been shown to provide an adequate description of the kinetics of some radiotracers in PET, for example [$^{11}$C]-flumazenil in the human brain (Koeppe et al., 1991). This model is hereafter referred to as a one-tissue compartmental model (1TCM).

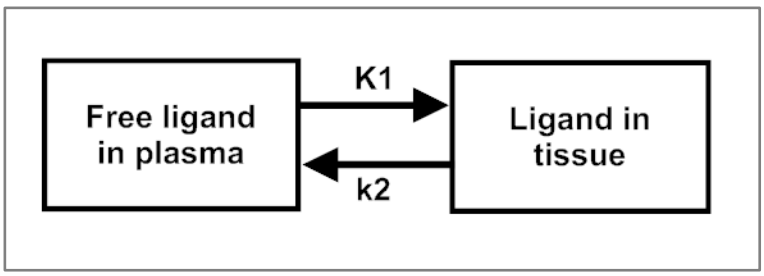


Figure 2.8. Simplified one-tissue compartmental model, with only two rate constants. The 'ligand in tissue' compartment now includes specifically bound, non-specifically bound and free ligand in tissue.

In the case of Figure 2.8, a single differential equation (equation 8) describes the rate of change over time ($t$) of the net tracer concentration in tissue ($C_{tissue}$):

$$\frac{dC_{tissue}(t)}{dt} = K_1 C_{plasma}(t) - k_2 C_{tissue}(t) \qquad 8$$

In terms of their general kinetic properties, tracers that might be adequately described by a simple model should, as far as possible, have: kinetics that are specifically related only to the process being studied; low extraction fraction from the blood into tissue- to reduce dependence on blood flow; trapping of the tracer in a 'slow turnover pool' after the tracer has gone through the main process of interest; rapid turnover rates for the non-specific compartment to allow merging of this compartment with others and rapid reduction of background signal in the kinetic data at later times; fast plasma clearance to reduce the relative blood volume signal in the PET data and to reduce the time taken to reach a steady-state; and no radiolabelled metabolites or changes in chemical form of the tracer in the blood or tissue (Huang & Phelps, 1986).

Using a-priori information to assign a fixed value to one or more rate constants is an alternative to model simplification for reducing uncertainty in the parameter estimation process. In this case, model complexity is not reduced; instead the number of parameters to be estimated is reduced. To yield accurate parameter estimates, this method requires accurate knowledge of the true value of the parameter(s) being fixed. Sometimes assumptions are made: for example that the value of $K_1$ or the ratio of $K_1/k_2$ is constant across all regions within an organ or system for a given tracer (Kropholler et al., 2005).

Reference region models are an alternative to arterial input compartmental models for neuro-receptor imaging. They are non-invasive and more suited to routine clinical application because they do not require arterial blood sampling, but instead rely on a region of reference tissue that is assumed to contain insignificant levels of specific tracer binding (Hume et al., 1992). This reference region is often defined anatomically based on the expected spatial distribution of target receptors in the brain. The simplified reference tissue model (SRTM) was developed (Lammertsma & Hume, 1996) and makes the further assumption that the exchange between the free and specifically bound compartments is rapid- which is to say that a one-tissue model adequately represents the exchange of tracer from blood to specific binding sites. The SRTM requires that only three parameters be estimated, and can provide a

reliable estimate of binding potential, which is the most often sought parameter from neuro-receptor PET studies (Figure 2.9).

Brain PET image volumes usually contain around $10^6$ voxels; therefore parametric image generation is only feasible when, in addition to being accurate and reliable, the parameter estimation procedure is computationally efficient. For example, a parameter estimation algorithm that took 0.5 seconds to fit one TAC would require approximately 6 days to fit the TACs of $10^6$ image voxels. Further evolution of the SRTM method has allowed its application to individual image voxels (Gunn, Lammertsma, Hume, & Cunningham, 1997), allowing parametric images of receptor binding potential to be generated within period of minutes or less.

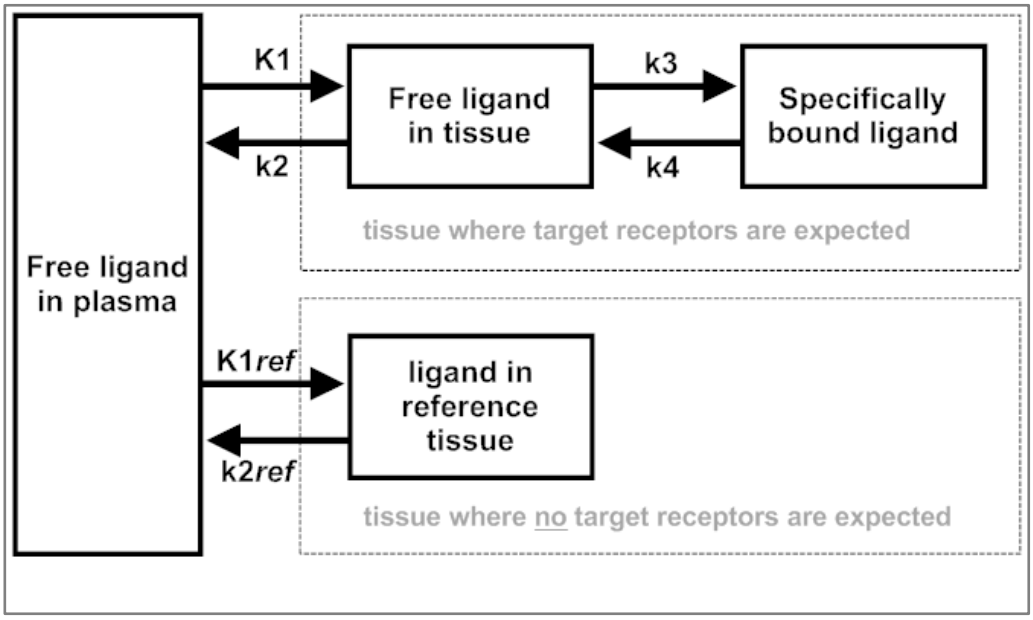


Figure 2.9. Reference tissue model. A two-tissue four parameter compartmental model is assumed for the target tissue, while a one-tissue two parameter model is assumed for the reference tissue. The reference tissue is assumed to be devoid of specific binding sites, and is often selected anatomically based on the expected location of the target receptors in the brain.

In many clinical applications of PET, a semi-quantitative index known as the Standardized Uptake Value (SUV) is used in preference to the more time consuming and slightly more invasive procedures associated with 'true' physiological modelling (Huang, 2000). The SUV is simply the concentration of radioactivity within a pixel or region at a single time point after injection, normalised to the injected dose of radioactivity and some measure of the subject's size, such as their body weight or surface area. Due to the simplicity of its application (no blood sampling and only one short scan), the SUV is usually preferred

in clinical PET applications where scanner time and patient compliance are finite (Basu et al., 2007; Carson, 2003). Indeed, the SUV is the most widely employed semi-quantitative index in clinical PET studies worldwide, particularly in relation to the uptake of FDG into malignant tumours (Basu et al., 2007).

The SUV has long been criticised due to the numerous assumptions that underpin its derivation, and the various sources of error to which it is subject (Huang, 2000; Keyes, 1995). Such semi-quantitative measurements make the implicit assumption that the observed tracer uptake in tissue at a certain time after injection represents exclusively the underlying process of interest. For many research studies and those involving novel radiotracers, full quantification using kinetic modelling is preferred because it can provide a more complete description of the tracer's behaviour in-vivo, and more relevant information about the underlying physiology of interest (receptor density, metabolic rate, perfusion etc.), without having to make this assumption.

### 2.2.5 Quantification of Neuro-receptor Function in PET

Radiotracers exist that may be used to image specific receptors in the brain with PET. Two examples are: [$^{11}$C]-raclopride for imaging dopaminergic D2 receptors, and [$^{11}$C]-AFM for imaging serotonin receptors. The fundamental goal of any neuro-receptor imaging with PET is to obtain an image that accurately quantifies the regional concentration of receptor in the brain. Compartmental modelling provides a suitable tool to achieve this.

Binding potential is the outcome measure of most interest for neuro-receptor PET studies. Binding potential is not a direct measure of receptor concentration, but rather a unitless index of receptor availability (Schiffer, 2011), and is defined as the ratio of receptor density ($B_{max}$) to the affinity ($K_D$) of the radioligand for that receptor, which is also equal to the ratio of specifically bound ($B$) to free radioligand ($F$) at tracer doses (Laruelle et al., 2003):

$$BP = \frac{B_{\max}}{K_D} = \frac{B}{F} \tag{9}$$

Affinity in this equation is represented by the dissociation constant ($K_D$), and is a measure of how tightly a ligand binds to a particular protein or receptor. Conceptually, a high affinity ligand introduced into a region of high receptor density ($B_{max}$) therefore has a high binding potential in that region. At tracer doses, occupancy of the target sites is expected to

be less than 1% (Hume, Gunn, & Jones, 1998) to avoid compromising the measurement of binding potential. If the fraction of free unmetabolised radioligand in plasma is known ($f_1$), then binding potential may be calculated from the parameters of the two-tissue model in Figure 2.7 as:

$$BP = \frac{K_1 k_3}{k_2 k_4 f_1} \tag{10}$$

Other definitions of binding potential may be used, depending on the information available for its derivation. Most often, it is defined as:

$$BP = \frac{k_3}{k_4} \tag{11}$$

The above definition of binding potential is widely used, however it is not related to receptor density alone, and is dependent also on the level of non-specific binding in the brain (Laruelle et al., 2003). Estimation of binding potential using a reference region in the brain that is devoid of the receptors of interest is usually a more robust method of estimating binding potential, but requires the selection of an appropriate region of reference, and the assumption that the reference tissue has the same non-specific binding characteristics as the target region (Laruelle, Slifstein, & Huang, 2002).

Distribution volume ($V$) of a compartment is defined as the equilibrium ratio of tracer concentration in that compartment to the concentration of free tracer in arterial blood (Laruelle et al., 2003):

$$V_i = \frac{C_i}{f_1 C_a} \tag{12}$$

Where $C$ is concentration of tracer, subscript $i$ refers to compartment $i$, subscript $a$ refers to arterial plasma and $f_1$ is the fraction of free tracer in plasma. The distribution volume known as $V_2$ is defined as the distribution volume of the second compartment (i.e. the free and non-specifically bound tracer compartment in Figure 2.7). The distribution volume known as $V_3$ is defined as the distribution volume of the third compartment (i.e. specifically bound tracer compartment in Figure 2.7). Total distribution volume ($V_T$) is the sum of $V_1$ and $V_2$. These compartments may also be referred to as the non-displaceable (second) and displaceable (third) compartments, which relates to the ability of a large quantity of 'cold'

ligand to displace the tracer from these compartments in so-called 'displacement' experiments (Laruelle et al., 2003).

## 2.3 Image Noise in PET

Accurate image quantification is dependent on the ability to accurately calibrate the scanner system, and to apply accurate corrections for the various sources of error inherent in PET imaging, such as photon attenuation, scatter, dead time counting losses and partial volume averaging effects (Meikle & Badawi, 2003). Accuracy of image quantification will also be affected by the signal-to-noise ratio (SNR) of the PET data; however the sources of noise, in particular statistical noise, are complex in PET and are not solely due to the number of counts collected, as is usually the case for single photon counting situations. The image signal-to-noise ratio is partly determined by the total number of true, scatter and random co-incidence events collected in a scan, with the SNR increasing as true events increase and decreasing as random and scatter events increase (Hoffman & Phelps, 1986). Noise may then be added or amplified by the various methods employed to correct the data for the physical effects listed above. Noise will also be greatly influenced by the choice of image reconstruction algorithm and the various parameters and filters that may be applied therein (Hutton, Nuyts, & Zaidi, 2006).

### 2.3.1 Definition of Noise and Signal-to-Noise Ratio in PET

Noise in PET imaging refers to the uncertainty associated with any measurement, such as the value of an image voxel or group of voxels. Noise can be classified as either random noise: originating from the statistical uncertainty inherent with radiation counting measurements, or structured noise: originating from more systematic errors caused by the application of imperfect PET data corrections, artefacts introduced during image reconstruction, equipment malfunctions or undesired uptake of the radiotracer in or near an area of interest (Cherry et al., 2003; Hoffman & Phelps, 1986).

Signal-to-noise ratio (SNR) may be defined in imaging as the mean or expected value of a pixel divided by the standard deviation of the mean (σ), or an estimate thereof (Cherry et al., 2003):

$$SNR = \frac{Mean}{\sigma} \tag{13}$$

The primary source of noise in PET measurements is the random noise associated with the radioactive decay and photon detection process (Haynor & Woods, 1989), and is described mathematically by the Poisson distribution (Cherry et al., 2003):

$$P(N;\lambda) = \frac{\lambda^N e^{-\lambda}}{N!} \tag{14}$$

Where $P(N;\lambda)$ is the probability of detecting $N$ counts if the expected (or 'true') value is $\lambda$. The variance of the Poisson distribution is equal to the expected value, $\lambda$. The Poisson distribution is defined only for non-negative integer values of $N$ (Stroud, 2001). When $\lambda \approx 20$ or more, the Poisson distribution becomes very similar to the Gaussian distribution (Cherry et al., 2003).

An important feature of this distribution is that larger numbers of collected photon counts are associated with smaller relative uncertainties, and hence with less relative noise. Therefore any improvement in imaging procedure that gives rise to more collected counts over the volume of interest will, in general, result in a higher image SNR. Specific methods for increasing the counts in PET include: increasing the imaging time, increasing the injected dose of radiotracer, increasing the sensitivity of the scanner to valid coincident events, and using a different radiotracer with higher levels of uptake at the site(s) of interest. A convenient feature of Poisson counting statistics is that the standard deviation ($\sigma$) associated with a mean number of collected counts ($N$) is given by:

$$\sigma \approx \sqrt{N} \tag{15}$$

Although the image SNR depends fundamentally on the total collected counts, the exact relationship between collected counts and image SNR in PET is more complicated than equation 15 implies. The application of corrections to the data, image reconstruction and filtering operations all tend to add either random or structured noise to the data. Some operations, such as filtering, are applied for the purpose of suppressing image noise (Cherry et al., 2003). The spatial distribution of radiotracer being imaged can also have an effect on regional image SNR and image reconstruction also tends to produce images in which the pixel noise is highly correlated (Hoffman & Phelps, 1986). Because of this, the final pixel values of reconstructed PET images, and subsequently derived time-activity curves (TACs), contain noise that is combined from a large number of sources and is often assumed to be

represented by the Gaussian distribution (Cherry et al., 2003; Haynor & Woods, 1989), the mean and standard deviation of which must usually be determined empirically.

### 2.3.2 Effects of Image Noise on Quantitative Modelling in PET

Noise in the images and TACs limits both the reliability of physiological parameter estimation and the complexity of the compartmental model that may be used and is therefore of prime concern when attempting to derive such parameters (Carson, 2003). Parameter estimation by non-linear least squares fitting suffers from very high levels of uncertainty, expressed as the coefficient of variation (CoV) of the parameters, when the input data are noisy. Despite this uncertainty, the method is free from bias even when the input data are quite noisy. Linear least squares fitting and graphical methods are less prone to parameter uncertainty, but suffer from bias when input data are noisy (Ikoma, Watabe, Shidahara, Naganawa, & Kimura, 2008).

Regions-of-interest (ROIs) are a collection of image voxels grouped together for the purpose of analysis. This has the effect of reducing noise substantially, since an average of all voxel values is taken. It is therefore expected that large ROIs will contain much lower levels of noise than smaller ROIs and individual voxels. For this reason, methods for generating parametric images must be robust with respect to image noise because they operate on individual voxels.

Measuring the noise levels in dynamic PET images is therefore of potential interest in the study of image quantification and modelling. Since quantitative analysis is highly dependent on the image noise, a method to accurately predict the noise levels would allow studies into the precision and accuracy of kinetic modelling, and the development of optimal quantification strategies.

### 2.3.3 Estimating Image SNR in PET

Estimation of the SNR in PET images is not a straight forward problem. The most direct way to measure noise is to perform repeated measurements (i.e. multiple PET acquisitions) of the same subject under identical conditions and then to calculate the mean and standard deviation for each pixel or ROI. Signal-to-noise ratio would then be the mean of the repeated measures- which is an estimate of the true signal for each pixel or region- divided by the standard deviation- which is a measure of the variability. Performing repeated data acquisitions is impractical for most imaging situations because a large number of

acquisitions are required to obtain a reliable estimate of the mean and standard deviation, while radioisotope decay, time, radiation exposure constraints and compliance limitations that apply when imaging living subjects make this impossible (Dahlbom, 2002). Phantoms containing long-lived positron emitting radionuclides do allow such repeated measurements to be made, however one is limited to the fixed source distribution and geometry of the phantom.

Consequently most methods for estimating noise in PET employ either an empirically derived formula to calculate the pixel variance as a function of collected counts (Budinger, Derenzo, Greenberg, Gullberg, & Huesman, 1978) or use statistical resampling methods to derive pseudo-repeat datasets from which the mean and $\sigma$ may be calculated. An example of an empirical formula for calculating image pixel SNR in PET is (Cherry et al., 2003; Phelps, Mazziota, & Schelbert, 1986):

$$SNR(pixel) \approx \sqrt{\frac{12N}{\pi^2 (D/\Delta r)^3}} \tag{16}$$

Where $N$ = the number of true coincidence counts collected, $D$ = the reconstructed image size and $\Delta r$ = the projection linear sampling interval and also the reconstructed pixel size. This formula is simplistic in that it makes a series of assumptions about the imaging situation which are rarely true in practice, including: a uniform tracer distribution, the application of filtered back projection reconstruction with a ramp filter only, image pixels that are exactly equivalent to the projection linear sampling interval, and sufficient angular sampling to avoid additional noise in the form of streaking artefacts. Nor does this formula take into account the potentially degrading effects of attenuation, random and scattered events in the PET data acquisition process. Despite these shortcomings, it does illustrate the general relationship between collected counts, image spatial sampling and SNR in PET. Specifically, this equation implies that SNR improves in proportion to the square root of the number of counts collected, and that as spatial resolution is improved (i.e. as sampling distance $\Delta r$ is decreased) the counts required to maintain image SNR are inversely proportional to the cube of $\Delta r$. In numerical terms, a factor of two improvement in the spatial resolution would require a factor of 8 increase in collected counts in order to maintain image SNR. It should be noted that noise equivalent counts (NEC) could be substituted for N in this equation to better take the effects of scatter and random coincidences into account.

Another commonly used approach to estimating image noise is to calculate the pixel mean and $\sigma$ within a large region of interest covering a volume in which the radioactivity is assumed to be uniformly distributed. Although straightforward to perform, this method is considered suboptimal due to the absence of such ideal uniform regions in most clinical imaging situations and because the noise in any given pixel is not necessarily independent of other pixels in the image (Haynor & Woods, 1989). Dahlbom (2002) also demonstrated that it provides an inadequate estimation of image noise when compared to the repeated scan and bootstrap resampling methods, even when applied to a radioactive test phantom of near perfect uniform spatial distribution.

An alternative approach to estimating noise in PET images is to use bootstrap resampling techniques (Dahlbom, 2002; Haynor & Woods, 1989). These methods use statistical resampling of one or more raw PET datasets to generate a series of pseudo-repeat PET data sets from the original PET scan. These datasets are then reconstructed and the mean and variance for each pixel are calculated directly from the pseudo-repeated measurements. Bootstrap methods have an advantage over empirical formulae such Equation 8: they do not require any assumptions to be made concerning the various sources of noise or their propagation through to the final image. The bootstrap methods have been shown to provide accurate estimates of image variance, achieving similar results to actual repeated PET scans on phantom acquisitions. Their primary drawback is that they are computationally intense, being described by one author as the “brute force” method (Dahlbom, 2002).

A recent study compared several bootstrap resampling methods for 3D PET (Lartizien, Aubin, & Buvat, 2010), including the methods of Haynor & Woods and Dahlbom, and found that at very low counts, bootstrap resampling from a single scan dataset did not produce a good estimate of the mean and variance in PET images reconstructed with 3D Filtered Back Projection and 2D Ordered Subset Expectation Maximisation (OSEM). Bootstrap resampling based on fifty independent scans performed much better. The authors hypothesised that the resampling methods would likely perform better at ‘clinical’ count levels. These findings indicate that care should be exercised when using bootstrap methods to study noise levels in PET, especially for very low count (noisy) data.

Monte Carlo simulation is another method for estimating noise in PET and is now discussed in more detail in section 2.4 .

## 2.4 Monte Carlo Simulation

### 2.4.1 Applications of Monte Carlo Simulation to PET

Monte Carlo methods are a class of computational algorithms that use random sampling to solve problems for which deterministic algorithms are unsuitable. Modern Monte Carlo algorithms rely on fast digital computers and pseudo-random number generators to provide a sufficient number of samples within an acceptable period of time. Monte Carlo methods may be used to simulate complex systems, and to study the outcomes given a set of starting variables (Upton, 2011; Zaidi, 2006).

Predicting the passage of photons through matter is a problem well suited to the Monte Carlo methodology, and several algorithms and software packages have been developed for this task, for example the Electron Gamma Shower (EGS) package (Rogers, Bielajew, Nelson, & Hirayama, 1986) and GEANT4 package (Agostinelli et al., 2003). Since the raw data in PET is essentially the result of the transport of many photons through tissue and the detectors, Monte Carlo methods may be used to simulate a PET scan. In addition to accurate modelling of the physics of photon interactions with matter, realistic and relevant simulations require that the PET acquisition itself be modelled accurately, taking into account the physical geometry and composition of the detectors in the scanner and the distribution of radioactivity and attenuating matter in the digital phantom. Subsequent data processing and image reconstruction algorithms must be similar or identical to those used in real-world systems.

The large number of computations required to accurately model a complete PET scan necessitates the use of very fast computers. The increasing availability of faster computer systems has led to a steady increase in the use of Monte Carlo simulation to study the physical properties of PET and SPECT over the last decade-and-a-half (Buvat & Lazaro, 2006). There are now several software packages dedicated to Monte Carlo simulations of PET and SPECT, for example: Simulation System for Emission Tomography (SimSET) (Harrison, 2011), PET Simulation of Realistic Tridimensional Emitting Objects (PET Sorteo) (Reilhac, 2013), PeneloPET (Espana et al., 2009) and the Geant4 Application for Tomographic Emission (GATE) (Jan et al., 2004).

### 2.4.2 Image Noise Estimation with Monte Carlo Simulation

Monte Carlo simulation allows noise to be measured by repeated data acquisitions in a way that is difficult to achieve with phantom studies, and impossible with real human or animal studies. Noise in PET data originates from the Poisson distribution of detected radiation counts and is inherently associated with the random nature of radioactive decay and the passage of radiation through matter. Monte Carlo simulation, which seeks to model these processes by random sampling, is therefore suited to estimating image noise in PET. Assuming that the statistical properties of the output data are equivalent to the real-world data, Monte Carlo simulations can provide realistic PET data with the same statistical properties as real-world PET data. By acquiring data from repeated simulations under identical conditions (but with different random number generator seeds), noise due to random fluctuations in photon counts in the raw sinograms and reconstructed images may be estimated by calculating a measure of spread across the independent noise realisations, such as the standard deviation or variance.

An alternative to Monte Carlo methods for estimating noise levels are the bootstrap resampling methods (Dahlbom, 2002; Haynor & Woods, 1989) discussed previously in 2.3.3. Although these methods have been shown to provide good estimates of the image variance, they may not perform so well for very noisy data (Lartizien et al., 2010). They also require one or more original scan datasets from a patient PET scan. Monte Carlo simulation avoids these limitations, allowing the underlying radioactivity and matter distribution to be controlled by the investigator. Some Monte Carlo codes also allow the PET scanner geometry to be likewise controlled.

Variance reduction techniques, like importance sampling and stratification, are often used as a means of accelerating Monte Carlo simulations (Haynor, Harrison, & Lewellen, 1991). However variance reduction must be used with caution as it is known to affect the statistical properties of the simulated data. Buvat et al. (2005) reported a factor of five speedup when the forced detection option was activated for a PET simulation using the SimSET package, however the variance of the sinogram data output was markedly altered (Buvat, Castiglioni, Feuardent, & Gilardi, 2005). Therefore, when attempting to study the noise properties of PET scanning scenarios, acceleration methods that alter the variance reduction techniques should be avoided.

Despite the advantages over bootstrap resampling and other techniques, long computation times associated with repeated simulations and the necessity to avoid variance reduction techniques potentially makes Monte Carlo impractical as a method for estimating image noise. Repeated simulations numbering in the hundreds or thousands are not feasible with current computer systems and software, even at low count levels. For example, an investigation into acceleration methods for the Geant4 Application for Tomographic Emission (GATE) simulator (Rehfeld, Stute, Apostolakis, Soret, & Buvat, 2009) reported a computation time of just over 90 hours to simulate ten seconds of PET data acquisition at clinically realistic activity levels and attenuation distribution on a single modern computer. With acceleration methods applied, which included discarding low energy gamma photons and using a method known as 'Woodcock tracking' (Rehfeld et al., 2009), the computation time was reduced to around 5 hours. Extrapolating these results reveals that simulation of 10 minutes of scan time with 500 repeats would take approximately 17 years on a single central processing unit (CPU) even at maximum acceleration. Without acceleration the computation time is over 300 years. It is noteworthy that the Woodcock tracking algorithm used to speed up the GATE simulations, also known as the 'fictitious interactions' algorithm, was found to preserve the statistical properties of the output data.

Combining Monte Carlo with another noise estimation method might help to overcome the problem of long simulation time. Lartizien at al. (2010) suggest such an approach in the context of bootstrap resampling methods. Their results suggest that bootstrap resampling works best when multiple original samples are used rather than a single scan. Generation of around fifty independent scans using Monte Carlo is suggested, from which five hundred or more bootstrap resamples may be made to estimate the noise. Extrapolating again from the work of Rehfeld et al. (2009) it would take around 600 days to generate fifty independent scans of ten minutes duration using GATE on a single computer. With modern computer clusters, discussed in detail in 2.5 below, this could be reduced to a more manageable 2 weeks of simulation time.

The analytical equation for image SNR (Equation 8 in previous section) has the advantage of being rapid to compute for a wide range of collected counts, while the main drawback is the need to make unrealistic assumptions about the PET scan, such as uniform source distribution and absent attenuation and scatter. Monte Carlo and bootstrap resampling methods avoid these assumptions by using an original scan, or a realistic simulation of one, to take these effects into account. It might be possible to combine Monte Carlo and the

analytical methods of noise estimation. A limited number of repeat Monte Carlo simulations at several different total count levels could be performed, allowing approximate noise levels to be calculated for each count level. Curve fitting of the Monte Carlo noise estimates as a function of collected counts could then be used to derive an analytical equation of similar form to Equation 8. Image noise could then be computed rapidly for any combination of radioactivity concentration and acquisition time, allowing noise to be predicted for a range of total count levels. The validity of the equation would be limited to the particular conditions of the original simulation: scanner geometry, source distribution, attenuating media, and data correction and reconstruction algorithms, making this technique most suitable for long-duration dynamic acquisitions over a fixed region of the body. Another drawback is that the effects of variable system response characteristics at different count rates might not be taken into account with this method, limiting its suitability to low count rate studies on systems with relatively 'fast' detectors and electronics. However, this might be a reasonable assumption for dynamic neuro-receptor PET studies performed on modern PET hardware.

## 2.5 Beowulf High Performance Computing Clusters: Application to Monte Carlo Simulations

### 2.5.1 Definition and Historical Development

A Beowulf cluster for high performance computing is a parallel multiprocessor computer system built from commodity hardware and freely available software (Gropp, 2003). Originally developed by Donald Becker and Thomas Sterling in 1995 at the National Aeronautics and Space Administration's Goddard Space Flight Centre (Becker, 1995; Warren, Becker, Goda, Salmon, & Sterling, 1997), Beowulf clusters have since become widespread due to their favourable cost-to-performance ratio, and have largely replaced the traditional supercomputer for high performance scientific applications (Gropp, 2003).

The rapid and widespread adoption of the personal computer during the 1980's and 1990's led to a marked reduction in the cost of their components due to economies of scale, and a rapid increase in the capacity to manufacture and distribute computers of increasingly higher performance at lower cost (Gropp, 2003). Meanwhile the large supercomputers, which were built by hand and in small numbers with dedicated software and operating systems, were becoming less attractive to institutions interested in high-performance scientific computing. Supercomputers were generally too expensive to replace at short intervals, and this weakness exposed them to competition from the rapidly improving commodity systems,

which could often rival the performance of a given supercomputer as it approached the end of its lifespan.

### 2.5.2 Advantages of a Beowulf Cluster

The original Beowulf project (Becker, 1995; Ridge, Becker, Merkey, & Sterling, 1997) used sixteen commodity desktop personal computer systems that were commercially available at the time: each with a 100 MHz Intel x486 central processing unit (CPU), 500 Mbyte hard disk and 256 Mbytes RAM. Communication between nodes was provided by dual Ethernet connections. The recently developed and free Linux operating system was also used. The authors reported floating point operation speeds within range of that expected from contemporary supercomputers, for applications that were well suited to parallel execution: 60 megaflops (i.e. 60 million floating point operations or MFlops) was achieved on the Beowulf for a fluid dynamics simulation task, while a Cray T3D supercomputer performed “less than 2.5 times better than Beowulf” (Becker, 1995). As was expected, applications that required more frequent inter-node communication of data performed less well on the Beowulf cluster compared to conventional supercomputers. Nonetheless, the use of only mass-produced commodity components and free software gave the Beowulf cluster a significant cost advantage over the traditional supercomputer.

Although not stated by the authors, the cost in United States Dollars ($US) of the original sixteen-node Beowulf hardware components was reported by others to be less than $US 50,000 at the time of its construction (Adams & Brom, 2008; Ridge et al., 1997). For comparison, a Cray T3D supercomputer of the same era cost between $US 2.2 million and $US 31 million depending on the exact configuration ("Cray Duly Launches Its $2.2m to $31m Parallel T3D," 1993).

### 2.5.3 Microwulf: The Personal Supercomputer

In 2007, a Beowulf cluster was built that matched the floating point performance of one of the fastest supercomputers from eleven years prior: the 1996 Cray model T3D MC256-8/464. Named ‘Microwulf’, it was designed as a very low cost and portable tool for teaching parallel programming at a tertiary college, and was referred to by its creators as the personal Beowulf cluster “for every desk” (Figure 2.10). Microwulf had a total component cost of under $US 2,500 (Adams & Brom, 2008). For comparison, the U.S. Census Bureau reported median annual household income in the United States for 2007 was $US 52,673

(Semega, 2009), and the approximate retail costs of new desktop and laptop personal computers was reported in a consumer's product review publication of the same year to range from $US 500 to $US 3,500 depending on specifications (Finnie, 2007). Microwulf was small by cluster computing standards: occupying 28 cm x 31 cm 43 cm, and could run from a single power outlet, drawing 450 watts under full load. No special cooling other than standard room air-conditioning was necessary.

Innovative design features of this cluster included a 'minimalist' approach to hardware casing, favouring an open design with the motherboards, hard disk and power supply units mounted directly on scrap polycarbonate sheets and held up with threaded rods. Space, weight and cost were reduced by choosing not to mount the components in a conventional computer case or rack. Electrical grounding- usually provided by the metallic case of a desktop computer- was accomplished by the addition of grounding wires from each component to one of the power supplies. Microwulf was open to the external environment on all sides, which allowed air to flow more freely and removed the need for powerful and potentially noisy cooling fans. Multi-core CPUs were exploited to help maximise the performance, space, cost and energy efficiency of the cluster. Space and cost were further reduced by using only a single shared hard disk for all nodes. Recycled or cast-off components were used where possible: the polycarbonate sheets, mouse and monitor were reportedly scavenged in this manner.

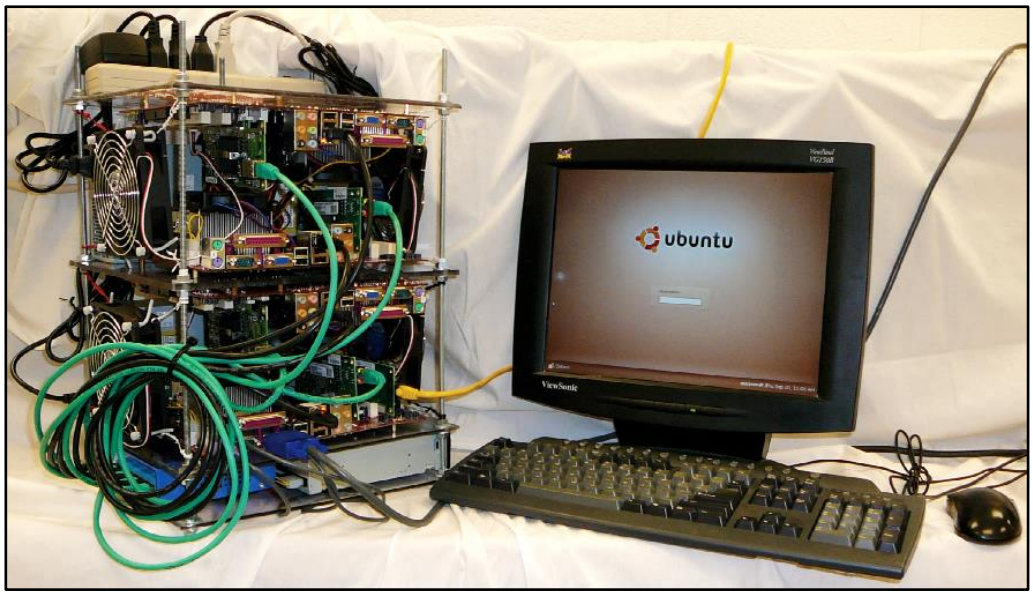


Figure 2.10. The original Microwulf cluster designed and built by Dr Joel Adams and Timothy Brom in 2007 at the Calvin College, Michigan. Microwulf was designed as a personal desktop cluster and required one standard power outlet and room air-conditioning to operate. Components cost less than $US 2,500 at January 2007 retail prices, and it could outperform a state-of-the-art Cray supercomputer from 1996. (Photo taken from Adams & Brom, 2008).

The personal desktop nature of the Microwulf cluster, which was emphasized by its creators, is an important attribute of this system. A study conducted from 1982 to 1983 (Quillard, 1983) on the introduction of personal computers into ten large commercial organisations, reported several advantages of moving from centralised time-shared computing to personal desktop computing. It was found that devolving responsibility of hardware and software selection to the end user meant that: there was a better matching of the user's requirements to the computing resources purchased; hardware and software updates could be carried out more frequently in a more targeted and user-specific manner without disruption to the entire user community; and the overall cost of errors such as hardware failure or incorrect software choice was lower, being confined to just one user. They also noted a strong user preference for moving to personal desktop systems over the previous centralised time-share systems (although company managers who had recently purchased a large scale system reported less enthusiasm!) and that the end-users were often becoming more expert in the particular software packages they used than the information technology specialists within the company. Disadvantages noted at that time by the authors included: loss of strategic control over hardware and software purchasing and use by the organisation; and loss of information on system usage rates. Another problem identified was the increased burden of knowledge on the end users, who might require different forms of computer support and training than was previously the case.

It is reasonable to suppose that the advantages and disadvantages of transitioning to personal desktop computers recorded three decades ago will apply to the use of 'personal clusters' in scientific research today. If a small foot-print, high-performance computing machine can be constructed for around the cost of a premium desktop personal computer, as exemplified by the Microwulf project, then a user preference for such personal clusters over shared resources might be expected. Projects that have a large computational component running over several months or years might derive benefit from the low cost custom approach. End-users would be given responsibility for matching their own cluster's characteristics to their particular problem and chosen software, rather than trying to fit the problem and software onto an existing shared system. Obsolescence of the hardware is still a problem, however the low initial cost of the equipment, and its dedication to a small number of projects, means that the cost and inconvenience of equipment obsolescence could be minimised, or at least confined to a small number of users. Inevitable hardware upgrades, or recycling of the components of the cluster, may be better coordinated with the project(s) for which it was built, thereby minimising inconvenient down-time on other researchers. A personal cluster might also offer more flexibility to an individual researcher for a particularly computationally intensive project by removing the administrative burden of negotiating for resources on a shared system.

The disadvantages identified at the time of desktop PC introduction three decades ago might also apply to the personal cluster. Despite the dissemination of simpler cluster building tools, individual researchers might not have the expertise or time required to build and maintain their own system. Decentralization of high performance computing resources could also result in a loss of control and oversight by the organisation, and require a new level of support and training from existing information technology support staff.

### 2.5.4 Relevance to Monte Carlo Simulations

Monte Carlo simulation of PET systems is computationally intensive, and the time needed to simulate a sufficient number of events has long motivated the use of parallel distributed computers (Zaidi, Labbe, & Morel, 1998). Clusters like the Beowulf perform very well when inter-process communication is low, because the Ethernet connection is often slow relative to the CPU and memory sizes (Becker, 1995). Tasks which require very little communication between processors during execution are said to be 'coarse-grained', while a task that requires no communication at all is categorised as 'embarrassingly parallel' (Scott,

2005). Monte Carlo simulations fit the description of an 'embarrassingly parallel' task because photon transport histories are independent of one another and so no communication between processes is required. Indeed it is well recognised that Monte Carlo simulations are suited to parallel implementation (De Beenhouwer et al., 2005; Zaidi et al., 1998) and the development of parallel systems has made Monte Carlo methods feasible for simulating complex PET and phantom geometries with high accuracy (Jan et al., 2004).

Despite the 'embarrassingly parallel' nature of Monte Carlo simulations, there is still a communications overhead to consider when running one on a cluster: the task requires some form of splitting before execution and the output data must usually be merged at the end of a simulation. For a PET simulation involving large 3D sinogram or list mode data outputs, this can also impose a considerable transfer and storage space penalty for parallel execution (De Beenhouwer et al., 2005; De Beenhouwer, Staelens, D'Asseler, & Lemahieu, 2006).

Limitations imposed by data housekeeping on parallel computing were first identified by Dr Gene M. Amdahl, and have since been formulated as 'Amdahl's Law' (Amdahl, 1967). Essentially a law of diminishing returns, it predicts that for each additional CPU recruited to a given task, the additional burdens of task splitting and data merging reduce the incremental speedup that is achieved. Fractional data merging overheads associated with parallel implementation of Monte Carlo simulations must take into account many variables associated with the simulation task at hand, including the expected length of the simulation and the format of the output data. For example, a data merge time of thirty minutes might be deemed an unacceptably high cost of parallelizing a simulation run to seventy CPUs if the total simulation time on a single CPU is only twenty minutes. On the other hand, thirty minutes of data merging might be acceptable for a simulation expected to take seven days to run.

De Beenhouwer et al. (2005) explored the implications of Amdahl's law in relation to the Monte Carlo simulation of PET and SPECT scans using Geant4 Application for Tomographic Emission (GATE). They reported data output merging overheads of less than 15% of total execution time for a seventy CPU cluster when running a SPECT simulation. This overhead increased to 70% for a high sensitivity PET simulation in which the data output rate was higher. They recommended that the fractional overheads be calculated from small scale simulation runs for the simulation task under consideration to determine the optimum number of computing cores that should be used for each job. Despite the data

merging issues reported for some simulations, they concluded that cluster computing represented the best way to accelerate GATE simulations for PET and SPECT.

### 2.5.5 High Performance Computing Options for Monte Carlo: Shared Resources versus User-Built Systems

Research projects requiring high performance computing resources have several options available, which may be broadly categorised as shared resource systems and dedicated user-built systems. Shared resources may take the form of a high-performance system dedicated for use within a laboratory or department, or a more centralised solution that is shared across an institution or wider geographic region. Cloud computing environments and grid solutions also exist that allow resources to be pooled across a wide area using local area networks and the internet, for example the European Grid Infrastructure (http://www.egi.eu).

Shared resource solutions offer potential efficiencies for scientific applications: multiple users can queue jobs which are executed as appropriate resources become available, thereby minimising computer idle time and sharing the benefits (and the costs) of the high performance hardware between multiple users. Energy efficiency, due to consolidation of resources and high utilization rates, is also cited as an advantage of large-scale cloud computing and centralised high-performance computing facilities (Yelick, 2011). Nonetheless, potential disadvantages of shared resource systems include the necessity to wait in a job queue, and the possible uncertainty in knowing when the computations will be finished. Further administrative burdens might also exist with the need to justify and negotiate for resources, either locally or to an external agency. Other drawbacks identified include security concerns with transferring sensitive data, and limitations in transferring large volumes of input and/or output data across networks (Yelick, 2011). This last point is particularly relevant for PET simulations where the data output files may be measured in gigabytes: a large size relative to many currently available network speeds.

On the other hand, personalised desktop clusters, such as the Microwulf cluster outlined in the previous section, are an emerging alternative to shared resource systems. Although energy efficiency and utilization rates are likely to be worse for personal clusters in comparison to shared resource systems- possibly leading to reduced cost-efficiency at the institutional level- they nonetheless have many potential advantages. Microwulf demonstrated that a high degree of efficiency with respect to cost, energy, space and

computational speed could be achieved with the personal desktop cluster approach. Construction of this and similar systems is well documented on the World Wide Web (for example: (Adams, 2012), http://www.calvin.edu/~adams/research/microwulf/) and requires only a moderate degree of computer assembly and software installation experience. In keeping with the principles of the Beowulf cluster, the software and operating system is free, publicly available and in widespread use, therefore documentation and user-community support is often available. Other potential advantages of the personal cluster include: greater availability and flexibility of use, the ability to match the cluster hardware and software to the task at hand, and the option to upgrade or discard components in response to the likely obsolescence of components over time, in a manner that is coordinated with the project for which it was built. Administrative burdens associated with shared resource-type computing facilities, and the data upload and security issues identified above, are also minimised with the personal cluster approach.

Taken together, these positive attributes of the Microwulf-type cluster, and the suitability of Monte Carlo simulations to parallel execution, make it feasible for small laboratories with modest resources to perform large scale PET simulations within a reasonable time frame.

## 2.6 PET Imaging of Neuroinflammation

### 2.6.1 Microglial, Neuroinflammation and the Role of PET

Microglia are one type of glial cell, and along with astrocytes, oligodendrocytes and ependymal cells are found in the brain. In general, glial cells play a supporting role in the central nervous system (CNS) and are distinguished from neurons, to which the control and cognition functions of the CNS have traditionally been attributed (Tortora & Grabowski, 1993). Microglia are distributed throughout the central nervous system and have an immune function, transforming into tissue macrophages as part of the neuroinflammatory response to brain injury. In the absence of brain injury or disease, microglia are considered to exist in a ‘resting’ state, although recent studies have shown that such non-activated microglia are not entirely static, possessing numerous ramifications that are constantly extended and retracted into their immediate surroundings, carrying out what is presumed to be an immune surveillance function (Nimmerjahn, Kirchhoff, & Helmchen, 2005). In response to injury, microglia become ‘activated’, changing shape and increasing in number in a manner that is highly localised to the region of injury (Banati, 2002). Activated microglia can therefore

serve as a marker of active brain disease, delineating such regions potentially before clinical or overt structural changes are evident (Kassiou, Meikle, & Banati, 2005).

Upon activation, microglia express a number of molecules. One such molecule is the 18kDa Translocator Protein, abbreviated to TSPO and previously known as the Peripheral Benzodiazepine Receptor or PBR (for additional notes on the historical nomenclature of this protein see appendix 7.1). Although distributed widely throughout the human body, the TSPO exists only in very low concentration in the normal brain, where it may be found on the outer mitochondrial membranes within astrocytes and microglia cells. However the abundance of the TSPO increases substantially and exclusively within activated microglia following neuronal injury (Banati, 2002). Radioligands that bind the TSPO therefore have the potential to be useful imaging tracers for delineating and quantifying regions of neuroinflammation.

It should be noted that activated microglia are, in this context, a non-specific marker of disease: their presence is not specifically associated with one or another particular pathology or syndrome (Banati, 2003). However since the late 1990's, there have been multiple reports in the literature of successful TSPO PET imaging studies that document the presence of neuroinflammation in human subjects who have clinically established neurological conditions. Many of these studies were conducted by comparing cohorts of healthy control subjects to cohorts of disease-affected subjects, and include studies involving:

- Multiple Sclerosis (Banati et al., 2000; Debruyne et al., 2002; Debruyne et al., 2003; Ratchford et al., 2012),
- Neurodegenerative dementias (Cagnin, Kassiou, Meikle, & Banati, 2006; Cagnin, Rossor, Sampson, Mackinnon, & Banati, 2004; Doorduin, de Vries, Dierckx, & Klein, 2008; Edison et al., 2008; Groom, Junck, Foster, Frey, & Kuhl, 1993, 1995; Gulyas et al., 2011; Mackenzie, 2000; Tomasi et al., 2008; Venneti, Wiley, & Kofler, 2009; Yasuno et al., 2008; Yokokura et al., 2011),
- Parkinson's Disease (Gerhard et al., 2006; Ouchi et al., 2005),
- Huntington's Disease (Pavese et al., 2006; Tai et al., 2007),
- Stroke (Gerhard, Schwarz, Myers, Wise, & Banati, 2005; Gulyas et al., 2012; Price et al., 2006; Thiel & Heiss, 2011),
- Encephalitis (Banati et al., 1999),
- Amyotrophic Lateral Sclerosis (Turner et al., 2004),
- HIV/AIDS (Hammoud et al., 2005; Wiley et al., 2006), and

- Methamphetamine abuse (Sekine et al., 2008). An age related increase in overall TSPO expression in the human brain, in the absence of disease, has also been documented with PET (Cagnin A, 2001; Gulyas et al., 2011).

Figure 2.11 shows a schematic representation of the TSPO and its relationship to other proteins in the outer mitochondrial membrane. The structure of the TSPO is believed to consist of five α-helices spanning an outer phospholipid layer of the mitochondrial membrane (Bernassau, Reversat, Ferrara, Caput, & Lefur, 1993). Cholesterol transport across the mitochondrial membrane is the best characterised function of the TSPO, which is essential for steroidogenesis, and explains the abundance of TSPO found in in steroidogenic tissues such as the gonads and adrenal gland (Chauveau et al., 2009; Papadopoulos et al., 2006).

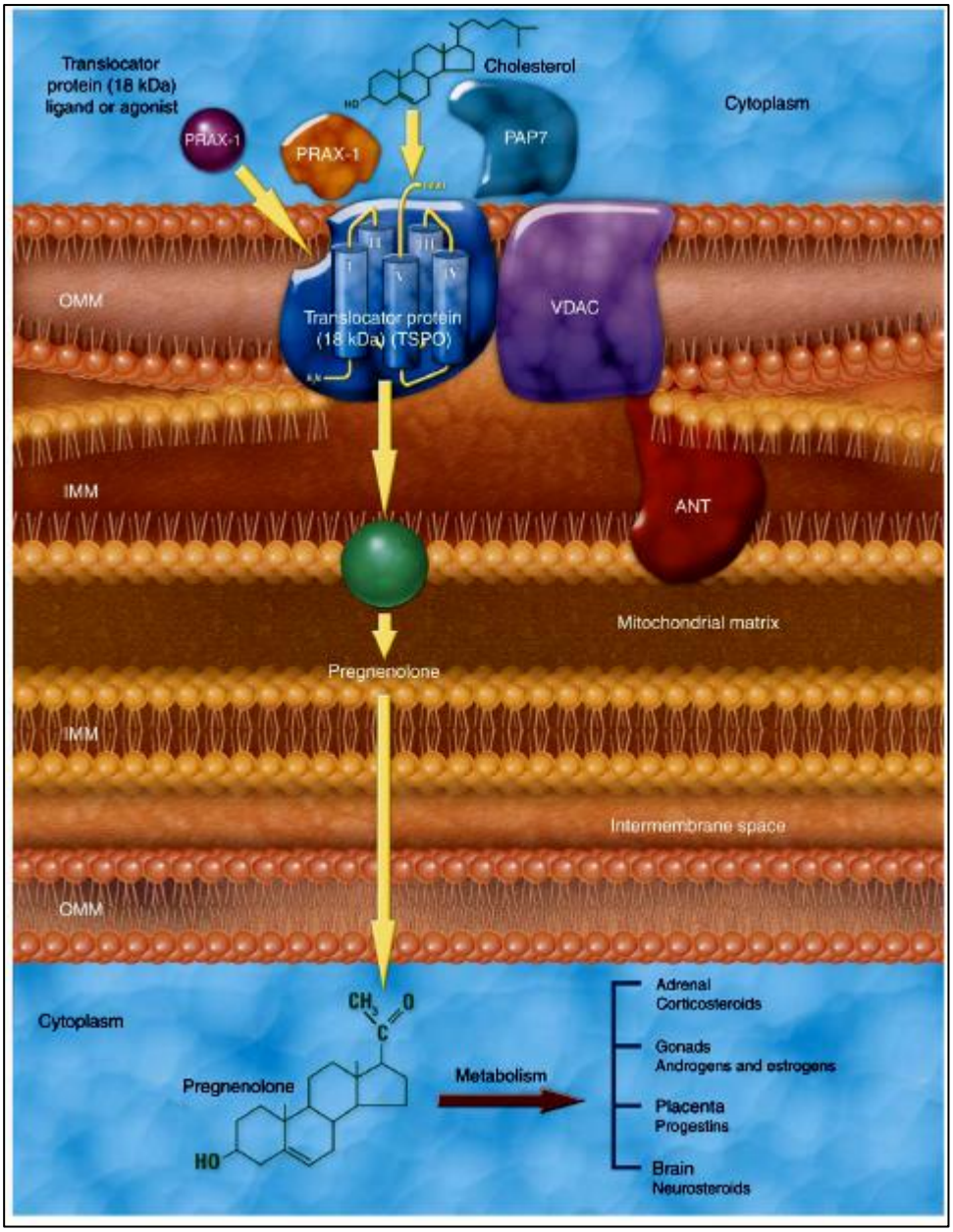


Figure 2.11. Schematic diagram of the TSPO, illustrating its place in the outer mitochondrial membrane, and some of the functions attributed to it. Diagram taken from Papadopoulos et al. (2006).

### 2.6.2 TSPO PET with [$^{11}$C]-R-PK11195: Successes

One of the earliest radioligands investigated for TSPO imaging, N-[$^{11}$C] methyl, N-(methyl-1 propyl), (chloro-2 phenyl)-1 Isoquinoleine Carboxamide-3, more widely known as [$^{11}$C]-PK11195, is also the most widely employed to date for this purpose (Camsonne et al., 1984; Chauveau et al., 2008). Due to its higher affinity for the TSPO (Shah, Hume, Pike, Ashworth, & McDermott, 1994), the R-enantiomer of this ligand, [$^{11}$C]-R-PK11195, has been used in most studies to date (Chauveau et al., 2008). In many of the earlier studies listed above, the utility of TSPO PET imaging with [$^{11}$C]-PK11195 was demonstrated by

correlating the observed radioligand binding on PET with the patient's known neurological symptoms or anatomical lesions. This is somewhat unusual in that the normal biodistribution and kinetic behaviour of novel radiotracers is typically established in healthy volunteers, before applying the techniques thus developed to study neurological diseases. The virtual absence of TSPO expression in the healthy brain renders this strategy inadequate for TSPO radiotracers, hence the early application of TSPO PET to studying a wide variety of neurological pathologies. In other studies that followed, [$^{11}$C]-PK11195 PET was used as a tool to investigate neuroinflammation in various diseases. Examples of [$^{11}$C]-PK11195 PET images are reproduced in Figure 2.12, Figure 2.13 and Figure 2.14 below.

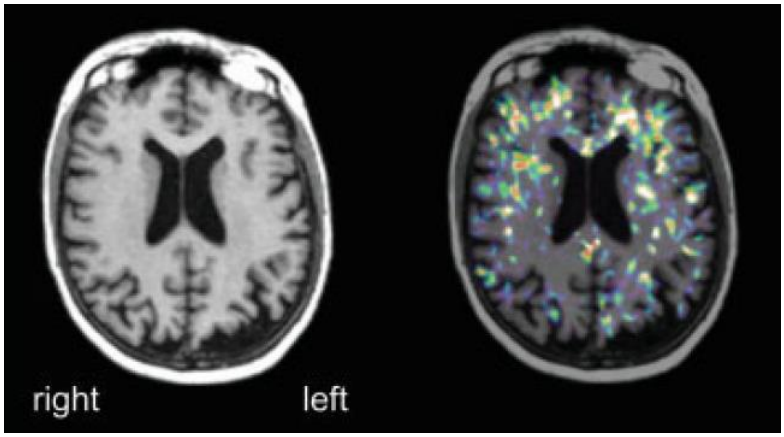


Figure 2.12. Example images from of a patient with frontotemporal lobar degeneration. Avid binding of TSPO PET radioligand [$^{11}$C]-PK11195 was seen in the frontal lobes in the image on the right (coloured pixels represent TSPO ligand Binding, overlaid with a co-registered MRI image), indicating the presence of activated microglia in a region of the brain that corresponds to the patient's clinical symptoms and regions of cortical loss (Cagnin et al., 2004).

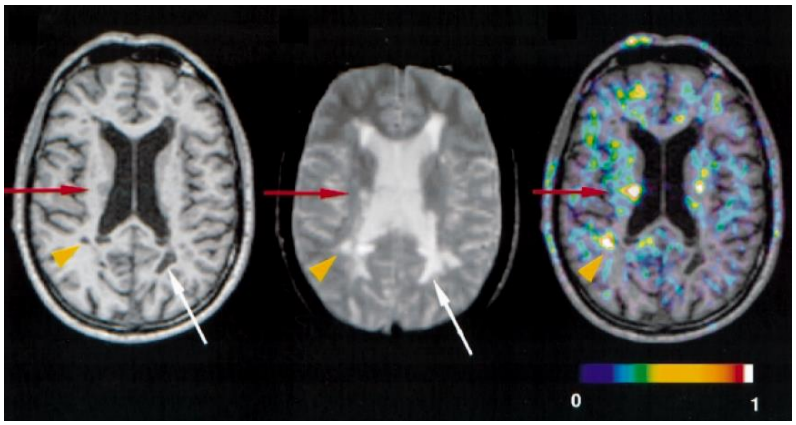


Figure 2.13. Example images from a patient with Multiple Sclerosis. Significantly increased binding of TSPO PET radioligand [$^{11}$C]-PK11195 was observed at some sites corresponding to structural lesions identified in the MRI of the brain. Colour scale represents Binding Potential of the TSPO radioligand (Banati et al., 2000).

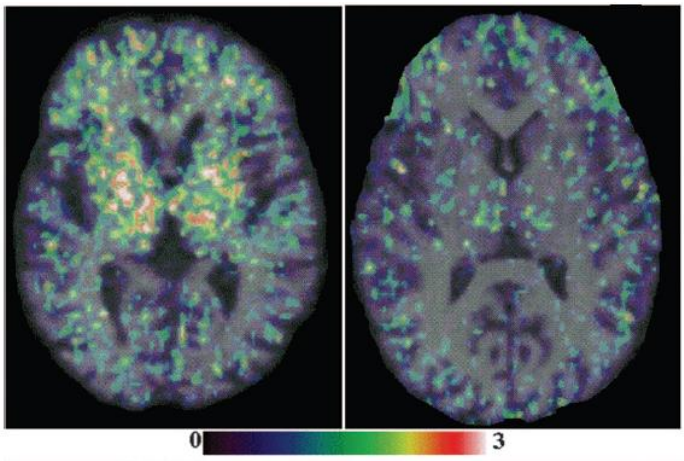


Figure 2.14. Example of [$^{11}$C]-PK11195 PET imaging of a patient with Huntington Disease (left) and a normal control subject (right). In this study, significantly increased levels of TSPO radioligand binding were reported in the striatum, fontal and parietal lobes of disease-affected patients. The extent of TSPO ligand binding was found to correlate with the clinical severity of the disease in this cohort of patients (Pavese et al., 2006).

Ligands for the TSPO labelled with tritium ($^{3}$H) have also been used in autoradiography studies of human and animal brain tissue. Pre-clinical PET imaging studies of small animals and non-human primates have also been carried out, especially in relation to the development of new radioligands for the TSPO (Luus, Hanani, Reynolds, & Kassiou, 2010).

Kropholler et al. (2005) published the first tracer kinetic compartmental model with measured plasma input function for [$^{11}$C]-R-PK11195 in the human brain (Figure 2.15). They found that a two-tissue, four rate constant model described the observed kinetics for this tracer in normal human grey matter most accurately. Values reported for the parameters of this model were: $K_1$=0.06, $k_2$=0.16, $k_3$=0.06, $k_4$=0.04. Binding potential was estimated at 1.6 and relative blood volume ($V_B$) was found to be 7%. It was further observed that for small ROIs, and therefore increasing noise in the data, fixing the ratio of $K_1/k_2$ to a value determined from a whole brain ROI provided the best compromise between accuracy and precision of the estimated parameters, due to the reduced number of parameters that required to be estimated. Reduction to a simple one-tissue, two-parameter model was also investigated but found to provide an inaccurate description of the tracer kinetics.

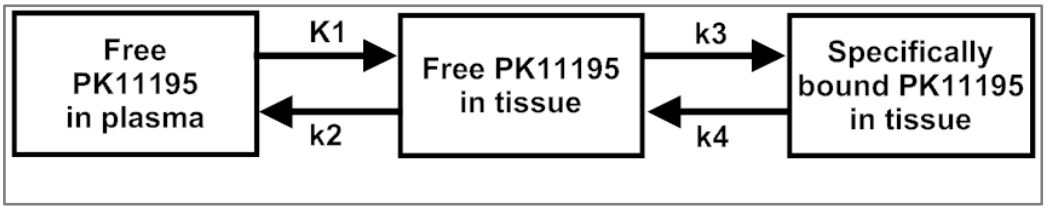


Figure 2.15. Compartmental model for [11C]-R-PK11195 in the normal human brain (Kropholler et al., 2005)

The model in Figure 2.15 was the first published for the PK11195 tracer in humans, and somewhat unusually it appeared after at least seven other studies that had used a reference region analysis method to quantify TSPO expression with the tracer. Typically in PET, reference region models are validated against compartmental models already established. Kropholler et al. (2005) reported some discrepancies between the binding potential (*BP*) values estimated from his plasma input model and those published previously, with reference region methods tending to yield lower estimates of binding than the two-tissue plasma input model. Possible sources of this discrepancy were identified as a slowly equilibrating non-specific binding which inflated the *BP* for the two-tissue model, and possible inclusion of specific binding within the reference region which would tend to decrease the *BP* estimate for those models.

These issues were further explored (Kropholler et al., 2006; Turkheimer et al., 2007). Clustering algorithms that extract the reference tissue TAC from voxels in the brain by comparing their shape to a set of pre-determined normal control TAC were employed (Gunn, Lammertsma, & Cunningham, 1998) and refined (Turkheimer et al., 2007) and were found to provide *BP* estimates that were well correlated to those determined by plasma input modelling. Turkheimer et al. (2007) reported a slowly equilibrating component, thought to originate from binding of PK11195 to the TSPO in vascular walls, using their supervised clustering analysis. The shape of this kinetic component was found to match that observed in a previous study of the canine heart (Charbonneau et al., 1986). Exclusion of these vascular voxels from the reference tissue TAC was found to improve the binding estimates in the brain.

### 2.6.3 TSPO PET with [$^{11}$C]-R-PK11195: Limitations

Despite the apparent success of TSPO PET imaging with this tracer, it has several important limitations. It has long been recognised that the level of non-specific binding in the brain is very high, probably higher than 50% in normal brain tissue (Petittaboue et al., 1991;

Shah et al., 1994). High levels of [$^{11}$C]-PK11195 binding to ά1-acid glycoprotein (AGP) in human plasma limit the availability of tracer for uptake in the brain. Plasma concentration of free tracer over time is also reported to vary between individuals (Banati et al., 2000). Because plasma levels of this protein may change during infections and inflammatory diseases, it has been identified as the primary cause of the observed variability in kinetic behaviour of [$^{11}$C]-PK11195 (Lockhart et al., 2003). This might preclude the application of a population average arterial input function, a technique sometimes employed to simplify kinetic quantitative analysis of PET data by avoiding arterial blood sampling (Takikawa et al., 1993; Takikawa et al., 1992).

Low levels of brain uptake, even in the presence of pathology, and high levels of non-specific binding in the brain are the most widely discussed limitations of [$^{11}$C]-PK11195 in the literature, and it is these limitations that new TSPO tracers are expected to overcome. Additionally, the relatively short physical half-life of carbon-11 (20 minutes) is sometimes considered a limitation for logistical reasons, since it is not feasible to distribute such short-lived tracers to remote imaging centres, thereby limiting the application of TSPO PET scanning to centres with an on-site cyclotron. The short half-life also precludes imaging at times greater than about one hour after injection, and generally means there are fewer counts available for collection (i.e. greater relative noise) when compared to fluorine-18 labelled tracers (half-life 110 minutes).

Low brain uptake and short half-life fundamentally limit the image SNR by limiting the number of gamma photons available for collection over the brain. Referring again to Figure 2.12, Figure 2.13 and Figure 2.14, the high levels of image noise can be readily appreciated in the grainy appearance of the coloured [$^{11}$C]-PK11195 binding images from each study.

High non-specific binding adversely affects image SNR by reducing the amount of signal that is related to the process of interest, in this case the density of TSPO expression in the brain. The non-specific binding that is observed throughout the brain with [$^{11}$C]-PK11195 is generally independent of pathology and represents a low spatial frequency ‘background’ upon which any useful signal must be superimposed. Low SNR reduces the ability to detect more subtle lesions and makes the quantification of TSPO density less precise and possibly less accurate (Chauveau et al., 2008; Luus et al., 2010).

### 2.6.3.1 Lesion Detection Problems with PK11195

Problems with lesion detectability were encountered during the early use of [$^{11}$C]-PK11195 in humans. Positive findings of increased tracer uptake relative to normal grey matter in malignant brain tumours were reported as early as 1989 (Junck et al., 1989). However the same group reported no apparent increase in [$^{11}$C]-PK11195 uptake in eight patients with a clinical diagnosis of mild to moderate Alzheimer's Disease, despite observing regional brain metabolism changes on FDG PET in same patients (Groom et al., 1995). The report also discussed similar negative findings when attempting to image mesial temporal sclerosis in patients with medically refractory temporal lobe epilepsy using [$^{11}$C]-PK11195, although these data were not published. The authors hypothesised that the levels of microglial activation in Alzheimer's disease and mesial temporal sclerosis were insufficient to be detected using their methods. Using previously published autoradiographic data, they estimated that only a 2-fold increase in PK11195 binding was occurring in these lesions and "*that an ~5-fold increase in PBBS density can be readily imaged with [11C] PK11195 and PET*"… "*but not (a 2-fold increase) in vivo, where the unbound and nonspecifically bound ligand are greater*". From this it may be inferred that the SNR was insufficient to allow detection of the expected brain pathology, due to an unfavourable combination of low inherent lesion contrast, small lesion size and high image noise levels.

In contrast to these findings, a study published six years later showed "*significantly increased regional [11C](R)-PK11195 binding in the entorhinal, temporoparietal, and cingulate cortex*" of eight patients with mild to moderate Alzheimer's disease (Cagnin et al., 2001). The authors were aware of the previous study's discordant findings and attributed their own success to the use of a more sensitive PET scanner operated in 3D mode, and their use of the higher affinity R-enantiomer (mirror-image stereoisomer) of [$^{11}$C]-R- PK11195. Analysis of published performance data reveals the PET scanner that was used in the latter study, a Siemens ECAT953B, was approximately five times more sensitive at 13.8 cps/Bq/mL than the older scanner used in the original study, a Siemens ECAT931 operated in 2D mode, at 2.5 cps/Bq/mL (Spinks et al., 1992; Spinks, Jones, Gilardi, & Heather, 1988). This means that the newer scanner was able to collect about five times as many counts over the same time period than the older system, thereby improving the image SNR. The exact improvement in image SNR is difficult to quantify, since the newer 3D scanner also had a much higher scatter fraction and random coincidence rate, and likely used different data correction and reconstruction methods than was used on the earlier system. Also the increase in brain uptake

due to the higher affinity R-enantiomer of PK11195 is difficult to predict: published data suggest an increased tissue uptake of around 20%, in a photochemically induced ischaemic lesion in rat brain, when using the R-enantiomer compared to the racemic ligand.

#### 2.6.3.2 Image Quantification Problems with PK11195

High levels of non-specific binding and high levels of image noise is an unfortunate combination with respect to deriving accurate kinetic parameters from the [$^{11}$C]-PK11195 PET data. Noise in the images and TACs limits the accuracy and precision of physiological parameter estimation and the complexity of the compartmental model that may be used, and is therefore of prime concern when attempting to derive such parameters (Carson, 2003). In the case of TSPO imaging, noise has been shown to increase bias in physiological parameter estimation for [$^{11}$C]-PK11195 (Yaqub, Boellaard, Kropholler, Lubberink, & Lammertsma, 2004). The authors conclude that reducing bias in the estimation of parameters such as Binding Potential would best be achieved by reducing noise in the TAC. Kropholler et al. (2005) demonstrated that bias and variance in the estimation of parameters for [$^{11}$C]-PK11195 increased with increasing noise when using a reversible two-tissue compartmental model of tracer kinetics (Kropholler et al., 2005). However the high noise levels make application of the (more complex) four parameter model feasible for large regions of interest only, where averaging of image voxels reduces the relative noise substantially.

Application of reference tissue models, which are typically less sensitive to noise and may be applied at the image voxel level, are affected by another unique challenge associated with [$^{11}$C]-PK11195: the very low level of ubiquitous TSPO expression in the normal brain (Rao & Butterworth, 1997). The *specific* uptake found in small and medium sized artery walls, as well as blood-borne cells and even in the normal brain tissues contributes a significant amount to the low level background signal in PET, independent of anatomical region (Turkheimer et al., 2007). Indeed, the slowly equilibrating vascular component identified by Turkheimer et al. (2007) was found to be responsible for approximately three-quarters of the total grey matter radioactivity by one hour post injection.

Calculation of quantitative parameters using reference tissue models requires a region of reference, which by definition must be devoid of specific tracer binding (Gunn, Lammertsma, Hume, & Cunningham, 1997). Since such a region is difficult to define anatomically in the brain with respect to the TSPO, application of the simplified reference tissue model is less straightforward than for other PET tracers. Some investigators have used

the cerebellum as reference region, acknowledging the potential error this might involve. Others have applied a sophisticated cluster analysis method to extract a reference TAC from voxels that are identified as having a similar kinetic profile to those of grey matter TACs in healthy control subjects. Considerable success has been reported with this method for analysing [$^{11}$C]-PK11195 PET studies in humans (Turkheimer et al., 2007) and is preferred for clinical application over other methods that require arterial blood sampling due to its non-invasiveness, and good correlation with TSPO binding parameters derived from the plasma input method (Ratchford et al., 2012; Turkheimer et al., 2007).

### 2.6.4 Evaluation of New PET Ligands for the TSPO

The limitations of the TSPO PET tracer [$^{11}$C]-PK11195 have motivated some researchers to investigate new TSPO ligands with better pharmacokinetic properties than PK11195. Examples of such 'second generation' TSPO PET tracers that have been developed and tested recently include: [$^{18}$F]-PBR111, [$^{18}$F]-PBR06, [$^{11}$C]-PBR28, [$^{11}$C]-DPA713, [$^{18}$F]-DPA-714, [$^{11}$C]-DAA1106, [$^{18}$F]-FEDAA1106 and [$^{11}$C]-CLINME. Between 1984 to 2008, one reviewer estimated that over forty ligands for the TSPO had been labelled for SPECT and PET imaging with iodine-123, carbon-11 or fluorine-18 (Chauveau et al., 2008). Of these ligands, twelve have been investigated in rodents, primates and human subjects as potential alternatives to [$^{11}$C]-PK11195 for TSPO PET imaging, between 1999 and 2009 (Luus et al., 2010).

Since the primary objective is to find a replacement for [$^{11}$C]-PK11195, potential new ligands for TSPO PET are often studied by comparing their performance against PK11195, and under the assumption that new ligands bind to exactly the same site as PK11195. It has been pointed out by at least one reviewer that this strategy is inadequate, particularly at the early screening stage of ligand development, due to the presence of binding sites on TSPO other than that to which PK11195 binds (Luus et al., 2010). Evidence for more than one binding site on the TSPO for different ligands, and the possibility of additional TSPO binding sites found only in activated microglia, suggests that increased uptake in normal brain tissue alone is not necessarily indicative of a better ligand for measuring TSPO expression in disease. The same authors also point out that, unlike many other PET tracers, evaluation of novel TSPO radioligands in the healthy primate or human brain is of limited use, since specific uptake is extremely low in the disease-free state.

Analysis of radiotracer uptake in rodent models of brain injury is often used as a means of comparing novel tracers to [$^{11}$C]-PK11195, where an improvement in lesion to non-lesion ratio of uptake is usually interpreted as a promising improvement in tracer performance. Increases in lesion to non-lesion ratio of uptake of a factor of 1.5 to 2 in a rat model of acute neuroinflammation were reported for the second generation TSPO radiotracers [$^{11}$C]-DPA-713 and [$^{18}$F]-DPA-714 in comparison to [$^{11}$C]-PK11195 (Chauveau et al., 2009). A similar improvement in lesion uptake, using similar rat model methodology, was observed for the tracer [$^{11}$C]-CLINME (Boutin et al., 2007).

Evaluation of [$^{18}$F]-FEDAA1106 uptake in the occipital cortex of one healthy monkey showed a six-fold increase in comparison to [$^{11}$C]-PK11195 (Zhang et al., 2004). Although this finding relates to a single disease-free primate, it demonstrates one potential advantage of this particular tracer over PK11195- a significant increase in brain uptake and therefore a potential increase in image signal-to-noise ratio. Similar findings were reported for [$^{11}$C]-DAA1097 with a 3.5 to 4-fold increase in uptake in the occipital cortex of a rhesus monkey over [$^{11}$C]-PK11195 (Zhang et al., 2006). Evaluation of [$^{11}$C]- PBR01 and [$^{18}$F ]- PBR06 in the brains of 3 healthy rhesus monkeys demonstrated an approximately 10:1 ratio of specific to non-specific binding to the TSPO (Imaizumi et al., 2007). This group also reported more reliable kinetic analysis results with the fluorine-18 labelled PBR06 compound when compared to the otherwise similar carbon-11 labelled PBR01, attributing this improvement to the longer half-life of fluorine-18 over carbon-11, allowing longer dynamic imaging to be performed with less noise at later time points.

The second generation TSPO radioligand [$^{11}$C]-DPA713 was evaluated in five healthy humans and compared to [$^{11}$C]-PK11195 in 2 additional healthy subjects (Endres et al., 2009). The new tracer was shown to have a factor of 3 higher brain uptake compared to PK11195, a finding that was attributed to greater affinity and lower plasma binding of the new tracer.

### 2.6.5 Population Variation of TSPO Affinity for Second Generation Ligands

Fujita et al. evaluated the TSPO tracer [$^{11}$C]-PBR28 in twelve healthy human subjects (Fujita et al., 2008) and found indirect evidence of approximately 25% non-specific binding. Quantification using a two-tissue compartmental model was found to best fit the kinetic data, despite a simpler one-tissue model having been found to suffice for the same tracer in

monkeys (Imaizumi et al., 2007). This finding was attributed to species differences, with humans having higher levels of non-specific binding compared to the primates studied. However a particularly remarkable finding of this study was the existence of so-called "non-binders": two subjects from their cohort of twelve who appeared not to show any specific binding of [$^{11}$C]-PBR28 in the brain or TSPO rich organs in the periphery. A similar finding had been reported previously for the same radioligand (Brown et al., 2007), with one out of a cohort of seven normal subjects showing an apparent absence of specific [$^{11}$C]-PBR28 binding in the whole body dosimetry study. This phenomenon had not previously been reported for other TSPO tracers.

These studies were followed up with a detailed investigation into the existence of "non-binders" (Kreisl et al., 2010), which reported that the absence of specific TSPO binding observed in approximately 10% of the scanned subjects was due to very low affinity of [$^{11}$C]-PBR28 for the TSPO in these "non-binders". This sub-class or individuals, now referred to as the "low affinity binders", was not evident with [$^{11}$C]-PK11195 (see Figure 2.16).

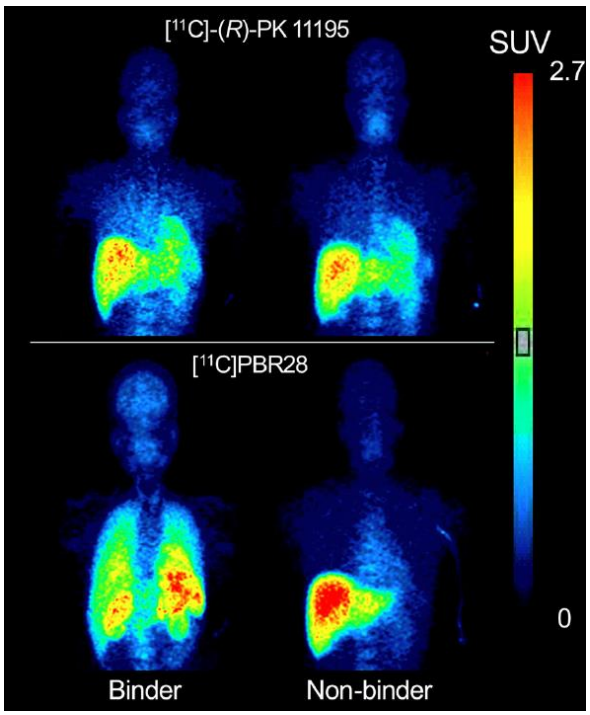


Figure 2.16. PET projection images from skull vertex to lower abdomen taken at 10minutes after injection. The subject identified as a "binder" and the subject identified as a "non-binder" show a similar distribution of [$^{11}$C]-PK11195 but very different distribution of [$^{11}$C]-PBR28. Uptake of PBR28 in organs known to have a high TSPO density (lungs, heart and kidneys) is absent in the non-binder subject, and brain uptake is apparently reduced. [$^{11}$C]-PBR28 was found to have a very low affinity for the TSPO in approximately 10% of human subjects studied. Images taken from Kreisl et al. (2010).

Further investigations (Owen, Howell, et al., 2010; Owen, Rabiner, Gunn, Matthews, & Parker, 2010; Owen et al., 2011) revealed that this phenomenon was not restricted to [$^{11}$C]- PBR28, but was also evident in the same subjects to some extent for all other second generation TSPO tracers in clinical use: [$^{18}$F]-PBR111, [$^{18}$F]-PBR06, [$^{11}$C]-DPA713, and [$^{11}$C]-DAA1106. In addition to the existence of "high affinity binders" and "low affinity binders", a third class of "mixed affinity binders" was identified. Two TSPO binding sites have been postulated to exist in humans, referred to as the "low affinity binding site" and the "high affinity binding site". Individuals who are "low affinity binders" express only the low affinity sites; while those designated "high affinity binders" express only the high affinity sites. Individuals who are mixed affinity binders express the high affinity and low affinity binding sites in approximately equal number. A single nucleotide polymorphism in the gene encoding the TSPO has since been postulated as the likely cause of this phenomenon, and its presence is known to vary across different ethnic groups (Owen, 2012). The implications for TSPO PET imaging are that changes in measured TSPO binding in-vivo cannot directly be attributed to changes in receptor density without knowledge of each subject's binding class and the ligand's relative affinities for each site. In a simulation study (Guo, 2012) it was predicted that the second generation TSPO tracers listed above are still likely to give more precise quantitative parameter estimates than [$^{11}$C]-PK11195, but only if the subject's binding class is known a-priori. This information is obtainable from a blood assay or a genetic test (Guo, 2012).

### 2.6.6 Relationship Between TSPO Tracer Properties, Image Noise and Quantification Error

It may safely be assumed that higher brain uptake and lower non-specific binding will reduce relative image noise and improve image quantification for TSPO PET. However given the difficulties in measuring image noise, this expected improvement in quantification is also difficult to measure. In 2.4.2 it was argued that it might be feasible to use Monte Carlo simulations to derive a simple analytical model of image noise that is valid over the range of count rates and simulation parameters studied. It was further argued that a model so derived would be most useful for the study of dynamic brain scans where the body region remains constant and where the count rates are low with respect to the maximum count rate performance of the PET system.

A typical time-activity curve for [$^{11}$C]-PK11195 in the brain is reproduced below (Figure 2.17), as is the count rate response curve for a current generation PET system. It can be seen that the range of activity concentrations in the brain for this tracer is well within the linear portion of the count rate curve, indicating that tracers such as [$^{11}$C]-PK11195 are potentially suitable for analysis with a noise model that ignores the non-linear response of the PET system at higher count rates. It might also be possible to incorporate the non-linear count rate response of the system into the model, but this would require the Monte Carlo code to accurately imitate this aspect of scanner performance, and might also necessitate additional simulation runs.

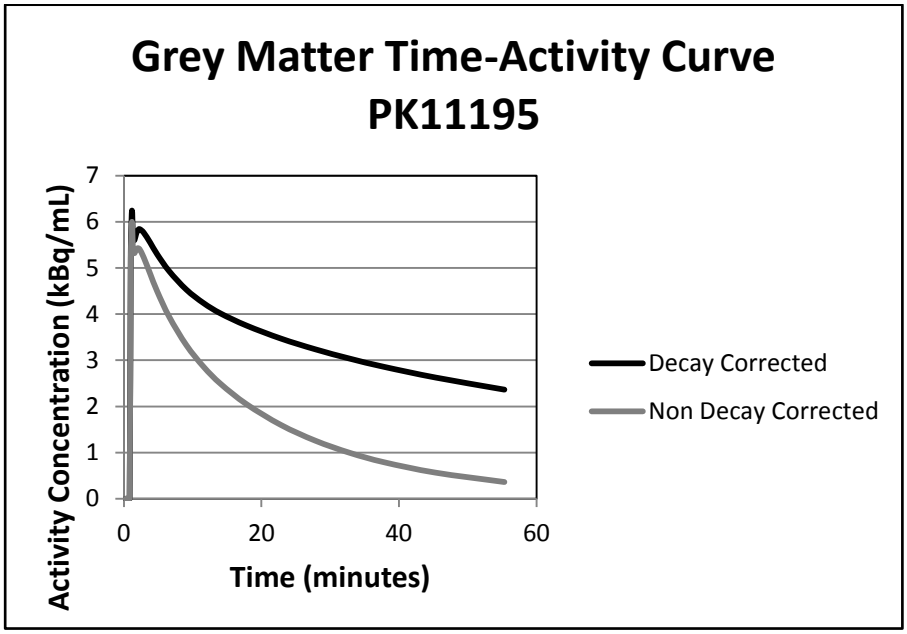


Figure 2.17. Time-activity curve for [$^{11}$C]-R-PK11195 from Kropholler at al. (2005). The non-decay corrected curve (grey line) is relevant to image noise calculations because it is the collected counts at the time of scanning that determines the image SNR.

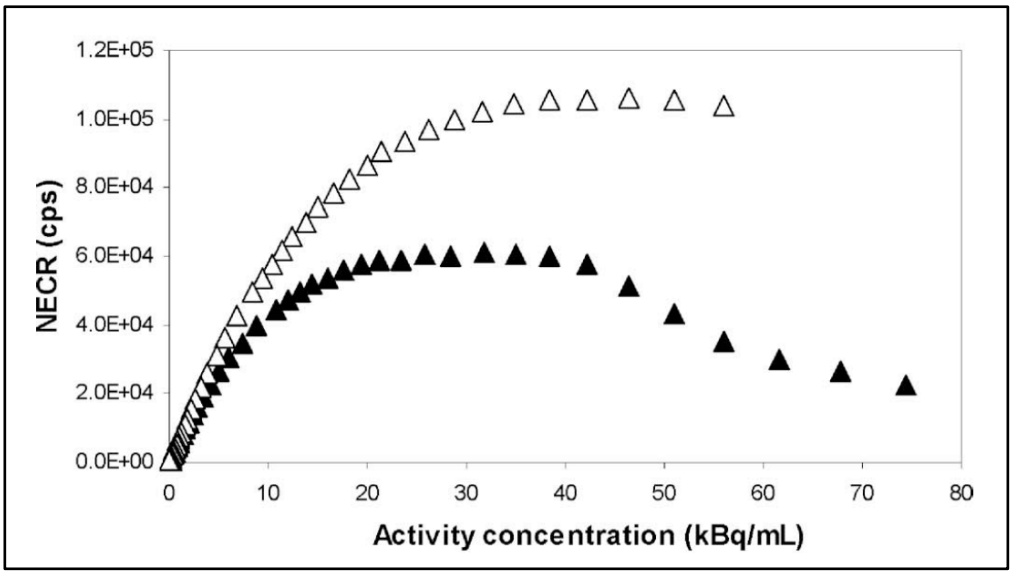


Figure 2.18. Noise equivalent count rate (NECR) curves for a modern PET scanner- the Siemens Biograph16 Hi Rez (Brambilla et al., 2007). The two curves represent slightly different phantom configurations used in the study from which this graph was taken. In either case the NECR curve is approximately linear below about 10 kBq/mL activity concentration.

The possibility therefore exists to use Monte Carlo simulation tools to derive a formula that describes the relationship between collected counts and image noise for brain radiotracers of similar distribution properties to [$^{11}$C]-PK11195. The model would be valid for a given set of conditions corresponding to those of the simulation and subsequent data processing methods, including: scanner geometry, spatial resolution, sensitivity, head phantom properties, and data correction and image reconstruction algorithm. This model would allow rapid calculation of the image voxel or region SNR for a range of existing or hypothetical TSPO tracers, at any time after injection and for any arbitrary frame duration.

## 2.7 Summary

In comparison to the reference radiotracer [$^{11}$C]-PK11195, higher levels of brain uptake and higher ratios of specific to non-specific binding characterise the so-called second generation of TSPO PET tracers. Although PK11195 has been applied with success to quantify the TSPO in the human brain, new tracers are expected to show an improvement in image signal-to-noise ratio with corresponding improvements in the precision of image quantification and also lesion detectability. In addition, new ligands that are labelled with the longer-lived fluorine-18 are expected to yield some improvement in image signal-to-noise ratio over carbon-11 labelled tracers, particularly at later imaging times post injection. Logistical factors favouring the production and distribution of fluorine-18 over carbon-11

radiotracers are also cited as desirable characteristics of any new TSPO agent (Arlicot et al., 2012).

The issue of variation in TSPO binding affinity within the population, which seems to affect many second generation TSPO radiotracers, is essentially a nuisance from an imaging point-of-view. It requires that information of a subject's binding class be known before the full benefit of the new TSPO tracers can be exploited. Such information may be obtained from a blood assay or genetic test prior to PET, although low affinity binders- around ten per cent of the population- would likely not be suitable for scanning with some radiotracers having extremely low affinity to the "low affinity binding sites", such as [$^{11}$C]- PBR28. Nonetheless, if subject binding class is known, then most second generation TSPO PET tracers are still likely to perform better than [$^{11}$C]-PK11195.

Clearly, increasing tracer uptake in the brain will bring about a reduction in relative image noise, which will translate into better precision of binding parameter estimates when using non-linear least squares fitting methods, and less bias in the case of the linear fitting methods. Reductions in non-specific binding will allow more precise determination of binding potential for any method, and possibly improve the minimum detectable increase or decrease in TSPO expression. However, reducing the complexity of the compartmental model used to describe the interaction of tracer and tissue also has the effect of reducing parameter estimate variability. If novel radiotracer 'B' is accurately described by a simple one-tissue model, it should yield more reproducible measurements of binding parameters when compared to radiotracer 'A', which has similar tissue uptake and noise levels, but is better described by a more complex two-tissue model. In this example, tracer 'B' should also be more suitable for analysis with the simplified reference tissue method, since this model assumes that the one-tissue compartmental model is appropriate.

Recent developments in Monte Carlo simulation software for PET, and their applicability to the latest generation of inexpensive personal high-performance computer clusters, provide a tool to study the image signal-to-noise ratio in a range of PET scanning scenarios. Recent reports in the literature and preliminary calculations suggest that it should be feasible to generate a limited number (around forty to fifty) of repeat simulations for several different count levels from a realistic human brain phantom, at count rates commonly encountered in dynamic TSPO PET scanning. This will enable an analytical model describing image SNR under typical scanning conditions for TSPO PET tracers in the human brain to be

developed and validated, and therefore allow predictions to be made on the potential improvements in image quantification that might be expected with other hypothetical TSPO tracers.

# Chapter 3 A Low Cost Computer Cluster for Estimating Image Noise in PET

Recent advances in commodity computer hardware, open source operating systems and software have enabled the development of high performance computer clusters of very low cost and physical size (Adams & Brom, 2008; Becker, 1995). At the same time, the evolution of Monte Carlo software packages has made well validated positron emission tomography (PET) and single photon emission computed tomography (SPECT) simulation tools available to a broader range of applications. Preliminary calculations based on published data, and discussed in 2.4.2 above, have suggested the feasibility of performing around forty to fifty repeated simulations of a low count rate neuro-receptor dynamic brain PET scan, with realistic modelling of the count statistics, attenuation and scatter, within a reasonable time frame, using a modern computer cluster. Fifty repeat data acquisitions has been shown to provide an adequate number of independent samples for the estimation of PET image noise, at very low count levels, via bootstrap resampling techniques (Lartizien et al., 2010).

The overarching motivation for this work was to use Monte Carlo simulation as a tool to study the signal-to-noise ratio of dynamic 18 kilodalton (18kDa) Translocator Protein (TSPO) PET scans of the human brain. To this end, the potential of two high performance computing systems that were operated external to the university and were available for research use were investigated. Both were high performance computer clusters dedicated for scientific research and were shared by multiple users. The first cluster was located away from the university campus and could be accessed via a remote terminal login only. Resources were allocated in units of 'central processing unit (CPU) core hours' and in six month cycles to a number of users, for a broad range of scientific projects, on a competitive basis. An approximate total of one million CPU core hours was available per six month cycle on this system. The second cluster was also located remote from the campus, was dedicated to GEANT4 Monte Carlo radiation transport simulations, and was shared amongst a small number (< 10) of users within a single laboratory. Negotiation for use of the second cluster's resources was done on a less formal basis than for the first system. No remote access was possible with the second cluster.

Pilot investigations showed that both the systems described above were inadequate for the tasks outlined in 1.2 Calculations based on published performance data for the first cluster revealed that the computational resources were sufficient (less than 5% of total available CPU hours over a six month cycle were required), however the large data output file sizes of the PET simulations posed problems with storage space and file transfer from the larger cluster. No actual PET simulations were conducted on this system. Meanwhile, a series of successful PET simulations were carried out on the second cluster using the GEANT4 Application for Tomographic Emission (GATE). However, calculations revealed that memory and CPU capacity on the smaller cluster was insufficient to allow completion of the project within a reasonable time frame (see appendix 7.2). These initial experiences, combined with recent innovations in low-cost computer cluster design, motivated the building of a dedicated cluster to meet the needs of this research.

## 3.1 Feasibility of Designing and Building a Low Cost High Performance Computing Cluster

### 3.1.1 Aim

The aim of this work was to determine the feasibility of designing and building a computer cluster to be used as a tool to study the signal-to-noise ratio of dynamic TSPO PET scans of the human brain. To this end, a series of design objectives for the cluster were set as follows:

- The system must be capable of simulating a realistic dynamic [$^{11}$C]-PK11195 PET scan of the human brain, of sixty minutes duration, including attenuation and scatter modelling, without the use of variance reduction acceleration methods.
- The total simulation time, including up to fifty independent repeats for each frame, must be six weeks or less.
- The total equipment cost must be AUD 10,000 (Australian dollars) or less.

### 3.1.2 Equipment

#### 3.1.2.1 GEANT4 Application for Tomographic Emission

The GEANT4 Application for Tomographic Emission (GATE) Monte Carlo simulation package (Jan et al., 2004) was selected to meet the needs of this research. This choice was justified based on the following considerations:

- GATE is a software tool developed specifically for the Monte Carlo simulation of medical imaging systems: PET, SPECT and more recently, CT (Buvat & Lazaro, 2006; Jan et al., 2011).
- GATE is controlled using a 'macro' script language, and does not require any specialised programming expertise.
- GATE is open source, free of charge and currently maintained by the international 'OpenGATE' collaboration.
- GATE is based on well validated physics models and a general purpose particle physics Monte Carlo software package: GEANT4, which stands for Geometry and Tracking (Agostinelli et al., 2003).
- Several real-world PET systems have been modelled using GATE, and GATE has been shown to provide output data in good agreement with real-world PET systems (Bataille, Comtat, Jan, & Trebossen, 2004; Jan, Comtat, Strul, Santin, & Trebossen, 2005; Karakatsanis et al., 2006; Lamare, Turzo, Bizais, Le Rest, & Visvikis, 2006).
- Recent versions of GATE incorporate an acceleration technique known as 'fictitious interactions', which has been shown to provide an order of magnitude acceleration whilst preserving the statistical properties of the output data (Rehfeld et al., 2009).

Two potential drawbacks of the GATE software are mentioned in several of the reports cited above: simulations are slow to run in comparison to some other Monte Carlo codes, and spatial resolution is consistently underestimated by GATE modelled PET systems. However, methods to overcome these limitations have been reported, including the application of a detector blurring kernel during simulation to address the resolution issue, the above-mentioned fictitious interactions scheme, and the use of multi-core computer clusters to accelerate the simulations (De Beenhouwer et al., 2005; De Beenhouwer, Staelens, Vandenberghe, & Lemahieu, 2007; De Beenhouwer et al., 2006).

#### 3.1.2.2 Desktop Computer: Hardware Components and Operating System

Components for a single desktop computer system were chosen from the catalogues of several local computer retailers. Consideration was given to the various options available at the time of purchase, and components with an apparently favourable cost-to-performance ratio were selected. Specifically, CPU, random access memory (RAM) modules and hard disk drive components were selected such that the ratios of CPU clock speed to cost, CPU clock speed to power consumption and memory capacity to cost were maximised. At the time of assembly, quad-core CPUs appeared to provide the best performance to cost ratio, under the assumption that a quad-core CPU is approximately four times faster than a single core CPU.

The following table (Table 3.1) lists the hardware details of the desktop computer that was assembled for this system. To aid comparison with the literature cited on the costs of various high performance computing systems, historical exchange rate data for the Australian dollar (AUD) and the United States Dollar over the period this study was conducted is given in appendix 7.3.

Table 3.1 Hardware details of single desktop computer system. Scientific Linux is a free-of-charge operating system based on 'Enterprise Linux' and put together by Fermilab (http://www.fnal.gov/) and CERN (http://public.web.cern.ch/public/).

| Component | Manufacturer / Model / Description |
|---|---|
| Motherboard | ASUS M4A77TD AM3 |
| CPU Manufacturer | Advanced Micro Devices Inc. (AMD) |
| CPU Model | Phenom II X4 945, 3.0GHz clock speed, 4 x cores |
| CPU cache memory | 8 Mbytes |
| CPU power rating | 95 W |
| RAM (total) installed | 8 Gbytes |
| RAM type | Double Data Rate type 3 Synchronous Dynamic RAM (DDR3 |
| RAM clock speed | 1333 MHz |
| Hard Disk Drive | 500 Gbytes |
| Power supply rating | 380 watts (430 watts peak) |
| Operating system | Scientific Linux, Version 5.5, 64bit |
| System assembly date | May 2010 |
| Total cost of system | AUD 817.92 |

The total cost reported does not include a monitor, keyboard or mouse, which were acquired free-of-charge from derelict equipment elsewhere. Additional components not listed included a metal 'tower' case, graphics card and Compact Disc Drive, which were included in the hardware package negotiated with the supplier.

#### 3.1.2.3 Digital Brain Phantom

In order to provide a realistic simulation of the human brain, a digital phantom that accurately models the normal human anatomy from the top of the head to the base of the brain is required. The publicly available anatomical model from the McGill University, McConnell Brain Imaging Centre (http://brainweb.bic.mni.mcgill.ca/brainweb/anatomic_normal.html) was chosen for this purpose. Details of the construction of this digital model are described in Collins et al. (1998). In brief, this model was derived from multiple co-registered MRI scans of a single

adult subject, with low noise and high spatial resolution, and consists of a three-dimensional array of 181x217x181 isotropic elements, each of 1 $mm^3$ volume (Collins et al., 1998). Each element is coded with one of ten discrete integers representing the tissue class associated with that location. Ten tissue classes are included in the model: air, cerebrospinal fluid (CSF), grey matter, white matter, fat, muscle, skin, skull, glial tissue in ventricles and other soft tissue. Representative transverse and sagittal planes of the digital phantom for several tissue classes are shown below in Figure 3.1.

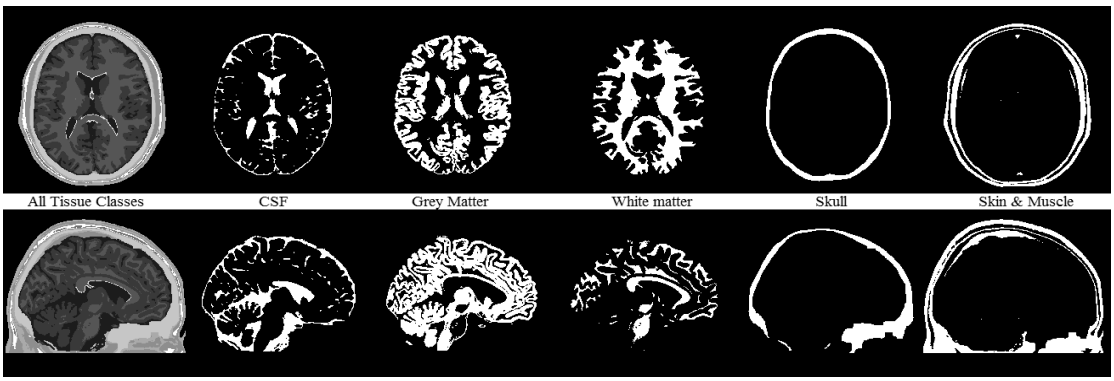


Figure 3.1. Digital anatomical model of the adult human brain from the McGill University McConnell Brain Imaging Centre. Representative transverse (top) and sagittal (bottom) slice is shown for selected tissue classes. A total of ten tissue classes are included in the model. Tissue classes are non-overlapping in this version of the model.

Padding of the digital model with zero-value elements was done to facilitate resampling at a later stage. Some artefactual structures lying external to the head (probably associated with the MRI scan from which the model was derived) were removed. The voxel values and spatial organisation of the tissue classes within the model were not altered from the original version in any way. The final dimensions of the model were: 212 x 264 x 212 voxels, with voxel dimensions of 1 mm x 1 mm x 1 mm. Manipulation of the model and preparation of subsequent phantoms were carried out using the Interactive Data Language software package, version 8.1).

Voxel number and volumes for the ten tissue classes in the final version of the digital model are listed in the table below. The total volume of the phantom, including the air outside the head, was approximately 11.9 litres, while the total tissue volume was approximately 3.85 litres.

Table 3.2. Voxel number and volume (absolute and relative) for each tissue class of the digital model.

| Voxel Value | Tissue Class | Number of Voxels | Volume (mL) | % Total Phantom Volume |
|---|---|---|---|---|
| 0 | Air | 8 017 392 | 8017 | 67.6 |
| 1 | CSF | 357 602 | 358 | 3.013 |
| 2 | Grey Matter | 902 492 | 902 | 7.61 |
| 3 | White Matter | 674 669 | 675 | 5.69 |
| 4 | Fat | 128 428 | 128 | 1.082 |
| 5 | Muscle | 513 751 | 514 | 4.33 |
| 6 | Skin | 531 313 | 531 | 4.48 |
| 7 | Skull | 473 654 | 474 | 3.99 |
| 8 | Glial Matter | 5 987 | 5.99 | 0.0505 |
| 9 | Other Tissue | 259 928 | 260 | 2.19 |

#### 3.1.2.3.1 Attenuation Phantom

In order to model the transport of photons through matter during the simulations, a digital phantom that models the physical properties relevant to photon interactions with matter was required. Included with the GATE software is a material database that contains information on density and elemental composition for a variety of materials that are relevant to particle simulations. Voxels in the digital model corresponding to the tissue class ‘skull’ were assigned the material ‘skull’ from the GATE materials database. Voxels of tissue class ‘air’ were assigned the material ‘air’ from the database. All other tissue classes in the model (grey matter, white matter, fat, muscle, skin and CSF) were assigned the material ‘water’ from the database, which was assumed to closely match the attenuation properties of all soft tissues at 511 keV.

To study the influence of attenuation phantom size on simulation speed, a second phantom was prepared by resampling the original anatomical model to a 2 mm isotropic voxel size. Representative transverse slices of each attenuation phantom are shown below in

Figure 3.2. Reducing phantom size is known to speed up photon tracking in GATE (Rehfeld et al., 2009), and the monotonous distribution of attenuation coefficients in soft tissue and air regions in the attenuation phantom means that the lower spatial resolution is unlikely to adversely affect the photon tracking through these regions.

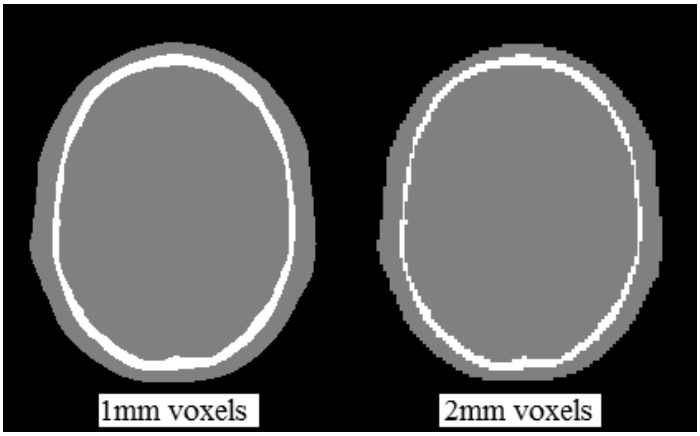


Figure 3.2. Representative transverse slice through the attenuation phantoms generated by assigning each tissue class in the digital model one of three material types from the GATE material database: air, water or skull. A high resolution attenuation phantom was generated using the original model with 1 mm isotropic voxel size. A second lower resolution phantom (right) was generated by resampling the original model down to 2 mm isotropic voxel size.

#### 3.1.2.3.2 Emission Phantom

An emission phantom was prepared by assigning a radioactivity concentration of 10 kBq/mL to each voxel in the digital brain model, except for those classified as 'air. The total activity within the phantom was 38.48 MBq, distributed evenly throughout all soft tissues and skull voxels. The emission phantom was constructed to provide a total emission rate at the higher end of that expected for TSPO brain PET scans. Unlike the attenuation phantom, resampling of the emission phantom to 2 mm voxel size was not considered because preservation of the fine structural details, particularly the grey-white matter interfaces, is potentially more important for modelling realistic radiotracer distributions in the brain.

### 3.1.2.4 PET Scanner Description

A GATE macro script describing the Philips Allegro™ PET scanner was prepared using a published description of this system (Surti & Karp, 2004), and a previously validated GATE model for the Allegro (Lamare et al., 2006) as guides. The script is reproduced in appendix 7.4. Key performance attributes of this system that have been modelled here include:

- Detector dimensions: 4 mm x 6 mm x 20 mm

- Detector material: Gadolinium Oxyorthosilicate (GSO)
- Axial filed-of-view: 18 cm
- Crystal-to-crystal ring diameter: 86.4 cm
- Energy resolution: 18% at 511 keV
- Photopeak window: 420 keV – 700 keV
- Coincidence timing window: 6.5 ns
- Dead time model: paralysable, 210 ns

#### 3.1.2.5 GATE Software Installation

GATE software version 6.0 was downloaded from the website of the international OpenGATE collaboration (http://www.opengatecollaboration.org/) and installed on the single desktop computer system described above.

### 3.1.3 Method

Using the desktop PC system, software and digital phantoms described above, a series of short duration PET simulations were carried out using the GATE software package, version 6.0. PET acquisitions were set to run for 0.15 seconds acquisition time on a single computing core only. The actual time taken to run the simulation was measured using the operating system clock. Care was taken not to run any other programs during the tests that might interfere with the performance of the simulation, other than the default operating system applications. The time taken to initialise the simulations within GATE was measured in separate tests for each tracking algorithm and phantom size, and subtracted from the reported execution times. The average percentage of free memory used during each simulation, as reported by the operating system software, was recorded for each run.

All four tracking algorithms available in this version of GATE were investigated: the original tracking in GATE, known as the ‘parameterized box matrix’ algorithm; the ‘regular matrix’ algorithm; the ‘compressed matrix’ algorithm and the ‘fictitious interactions’ algorithm. There were two attenuation phantoms studied: low resolution 2 mm isotropic voxels, and high resolution 1 mm isotropic voxels. The same digital brain phantom with the uniform source distribution, containing 1 mm isotropic voxels was used for all experiments.

Particle tracking options within GATE were selected to allow tracking of photoelectric and Compton scattered photons using the ‘standard’ energy electromagnetic physics package, which produces relative interaction cross-section errors of less than 10% for photons above

100 keV (Jan et al., 2004). Secondary electrons and x-rays were not simulated. Positrons were not simulated, but rather the back-to-back photon option was used to simulate the 511 keV annihilation photons. This last choice meant that any effects on image resolution or noise due to non-zero positron range were ignored. Simulation of positron interactions was expected to add significantly to the execution time, and was therefore not included.

### 3.1.4 Results

Results for each combination of tracking algorithm and attenuation phantom size are shown in Table 3.3 below. Initialization time for each simulation varied between 11 seconds and 41 seconds, depending on the phantom size and which tracking algorithm was used, and has been subtracted from the execution times reported below.

Table 3.3. GATE simulation time results for each combination of tracking algorithm and phantom size. PET acquisition time was constant for each simulation at 0.15 seconds.

| GATE Tracking Algorithm | Attenuation Phantom Voxel Size | Execution Time (min) | Initialization Time (min) | Memory Usage |
|---|---|---|---|---|
| Parameterized Box Matrix | 1 mm | 274 | 0.68 | 27.5 |
| Parameterized Box Matrix | 2 mm | 140 | 0.22 | 19.4 |
| Compressed Matrix | 1 mm | 101 | 0.27 | 18.3 |
| Compressed Matrix | 2 mm | 83 | 0.18 | 18.2 |
| Regular Matrix | 1 mm | 32.4 | 0.28 | 20.4 |
| Regular Matrix | 2 mm | 25.0 | 0.18 | 18.4 |
| Fictitious Interactions | 1 mm | 16.1 | 0.28 | 20.4 |
| Fictitious Interactions | 2 mm | 13.3 | 0.18 | 18.5 |

### 3.1.5 Discussion

The above timing tests reveal an order of magnitude difference between the fastest and the slowest tracking algorithms available in GATE, for the phantom and source distributions

tested. This finding is consistent with that reported by Rehfeld et al. (2009), who reported a PET simulation speedup of about an order of magnitude, for a similar phantom, using the fictitious interactions algorithm. Reducing spatial sampling of the attenuation phantom from 1 mm to 2 mm results in a 50% reduction in execution time when using the slowest tracking algorithm (parameterized box matrix), and around a 20% reduction in execution time when using all other tracking algorithms.

Initialization times, which are independent of the actual length of the simulation, varied considerably, but were all much less than 1 minute: a time frame that is not considered to be significant with respect to the likely execution times of most PET simulations. Based on these findings, the most efficient tracking algorithm for simulations of similar design to the one studied here is 'fictitious interactions', with the 2 mm attenuation phantom sampling.

A total of $5.77 \times 10^6$ 511 keV photon pairs were simulated during the above timing test ($3.848 \times 10^7 Bq \times 0.15\ s$) over a period of 798 seconds for the most efficient tracking algorithm reported above. This is an average simulation rate of $7.23 \times 10^3$ photon pairs per second achieved on a single CPU core. It should be noted that the actual simulation time for a long dynamic PET scan will be affected by a wide range of factors not explicitly studied in this experiment, including the time course of radioactivity simulated within the phantom, radioactive decay and the duration of the scan. Nonetheless, for a given distribution of radioactivity and attenuating matter, and for a given PET scanner geometry, the execution time is expected to be proportional to the number of photon pairs simulated.

Since the aim of this work was to design a system capable of simulating a dynamic [$^{11}$C]-PK11195 scan of 60 minutes duration with 50 independent repeats, further calculations were carried out to relate the findings of this timing experiment to these requirements. The details of these calculations are presented in appendix 7.5, where it is estimated that the simulation of an hour long dynamic [$^{11}$C]-PK11195 scan requires the simulation of approximately $2.23 \times 10^{10}$ photon pairs in total. At the average rate of $7.23 \times 10^3$ photon pairs per second calculated above, this would take approximately 35.7 days to complete on a single CPU. To meet the target of completing 50 repeated simulations within 6 weeks would therefore require approximately 43 CPU cores, incurring a hardware cost of approximately AUD 9,000 (for example: 11 quad-core CPU systems x AUD 818), using the components tested above.

This extrapolation ignores the extra time and disk storage that might be associated with splitting the simulation and merging the output for a multi-core cluster. Nor does the cost calculation include the Ethernet switch and wires required to connect such a system together. Nonetheless, these findings support the general feasibility of building a system that meets the design goals outlined in 3.1.1.

Memory usage was highest for the parameterized box matrix tracking algorithm with the 1 mm resolution phantom at 27.5% of available memory, which equated to approximately 1.76 Gbytes on this system- the operating system consumed approximately 1.4 Gbytes. GATE memory usage was reduced to 19.4 % (1.24 Gbytes) when using the lower resolution attenuation phantom. Memory usage was consistently around 20% for all other tracking algorithms, and was reduced to around 18% when using the lower resolution phantom with these algorithms.

Memory usage below 25% on this system is preferable, since the system uses a quad-core CPU. If four independent Monte Carlo simulations are to be run simultaneously using this CPU, then each simulation must consume less than 25% of the available memory in order for all four simulations to run concurrently. These results therefore suggest that, for the simulation scenario studied here, a total of 6.5 Gbytes of RAM per CPU is the minimum memory capacity required for a cluster system built on quad-core CPUs such as this one, provided the parameterized box matrix is not used with a 1 mm voxel phantom. In more general terms, a total of around 1.24 Gbytes of memory must be available for each computing core in order to run concurrent simulations of the type studied here. This applies to all tracking algorithms and voxel sizes studied here, with the exception of the parameterized box matrix/1 mm voxel combination.

### 3.1.6 Conclusions

Overall, the results of this experiment suggest that a high performance computer cluster constructed of commodity components, consisting of around 11 quad-core CPUs and 8 Gbytes of RAM per CPU may be constructed for less than AUD 10,000 as of May 2010. This system is expected to take approximately 6 weeks to simulate an hour long [$^{11}$C]-PK11195 dynamic PET scan of the brain with 50 independent repeats per frame.

## 3.2 Investigation of the Effects of Gamma Discard Energy Settings on Execution Time and Scanner Count Rate Response in GATE

### 3.2.1 Introduction

Selection of the fictitious interactions photon tracking algorithm in GATE allows the user to specify a gamma photon discard energy. When a simulated gamma photon within the phantom drops below this energy (following scattering interactions in matter) it is discarded altogether from the simulation. This feature only applies within the phantom, not the detectors. Use of this feature has the potential to speed up the simulation by preventing GATE from spending time tracking low energy photons that are likely to be rejected by the simulated pulse-height analyser (PHA), and are therefore unlikely to contribute to the final image.

However, selecting an inappropriately high discard energy setting could adversely affect the statistical properties of the output data by removing scattered photons that might still be accepted by the PHA. Scatter fractions could therefore be affected. In addition, all low energy photons that reach the detector must still be processed by the (simulated) detector and electronics before reaching the PHA, thereby contributing to system dead-time. Removal of low energy photons therefore has the potential to affect the count rate response of the simulated scanner, and must be carefully investigated for simulation scenarios that involve relatively high phantom activity, or that require highly realistic modelling of the scanner's count rate response.

### 3.2.2 Aim

The aim of this experiment was to investigate the effects of gamma discard energy settings on the execution time, observed energy spectrum and observed count rates (true coincidence, random coincidence, and scatter coincidence rates) at different source activity levels within the simulation of a brain PET scan using GATE.

### 3.2.3 Equipment

The same equipment described in 3.1.2 was used for this experiment. Namely: one single desktop PC running GATE version 6.0 and a digital phantom of the human head modelling the attenuation and source distribution. For this experiment, the digital source

phantom contained a uniform radioactivity distribution throughout the soft tissues of the head, while the total radioactivity within the phantom was varied between 5 MBq and 60 MBq. The GATE macro describing the Philips Allegro™ PET scanner (see appendix 7.4) was used for all simulations.

### 3.2.4 Method

All simulations were performed with the fictitious interactions tracking algorithm switched on. Thirteen different gamma discard energy settings were investigated: 0 keV, 10 keV, 50 keV, 100 keV, 150 keV, 200 keV, 250 keV, 300 keV, 350 keV, 400 keV, 450 keV, 500 keV and 510 keV. Five different source activity levels were also investigated: 5 MBq, 10 MBq, 20 MBq, 40 MBq and 60 MBq. All simulations were run for a minimum total of $7x10^4$ true coincidence counts. The total number of random coincidence counts ranged from $2.8x10^3$ to $3.3x10^4$. The total number of scattered coincidence counts ranged from $4.4x10^2$ up to $3.8x10^4$. The following information was recorded for each simulation: true coincidence rate, random coincidence rate, scatter coincidence rate and single event rate.

An additional series of simulations were conducted with the 20 MBq source phantom only. For each gamma discard setting, the energy spectra of the photons emitted from the phantom, as measured by all the simulated PET detectors, was recorded. A minimum total of $1x10^6$ single events were acquired per discard setting.

A third series of simulations were conducted with the 20 MBq source phantom only. For each gamma discard setting, a PET scan of 1 minute duration was simulated and the execution time was recorded. This series of timing tests was performed separately to the other two series because the data output method used in the first two simulations to obtain the count rate and energy spectrum data (ASCII text output), was different to that used for most other simulations (sinogram output), and was found to have some effect on execution time.

### 3.2.5 Results

Full tabulated results from this experiment are presented in appendix 7.7.

Figure 3.3 shows the relationship between true coincidence rate and phantom activity for a selection of different gamma discard energy settings. It may be seen that discarding photons from the simulation had a more noticeable effect at high activity levels; with an apparent increase in sensitivity to true coincidences as discard energy was increased.

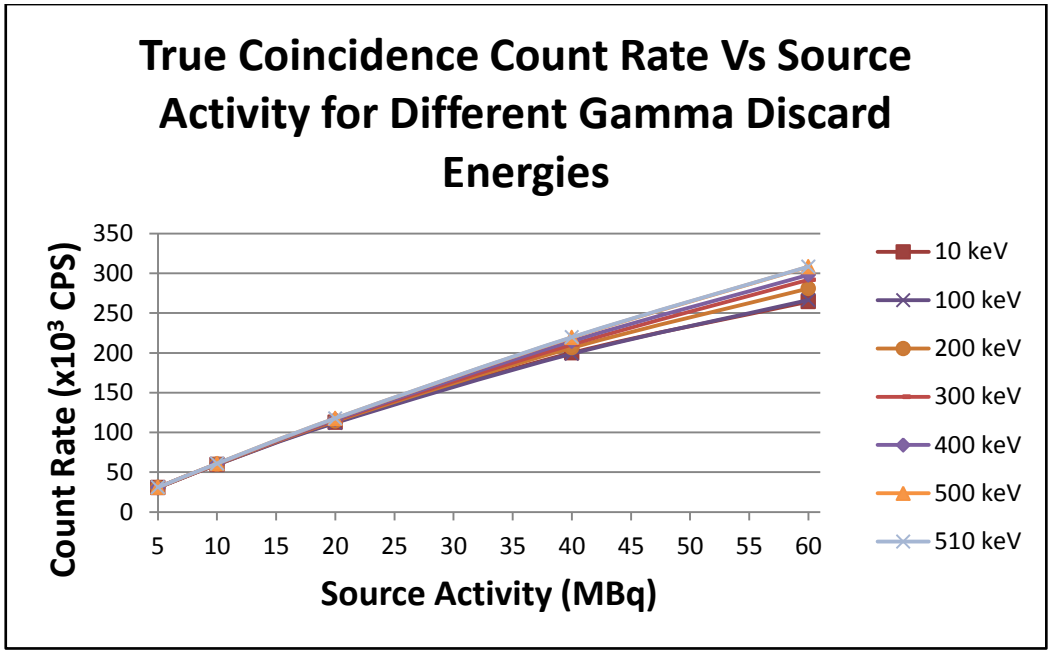


Figure 3.3. True coincidence rates versus source activity for different gamma discard settings (keV). Discarding low energy photons has a more noticeable effect at high activity levels, causing an apparent increase in sensitivity to true coincidences.

Figure 3.4 plots the change in true coincident count rate, relative to the count rate at zero gamma discard energy, as a function of gamma discard energy for each phantom activity level. Discarding photons of 100 keV or lower energy from the simulation resulted in less than 1.3% change in trues rate even at high activity levels. A positive bias in the trues rate was observed for gamma discard energy settings over 100 keV, with the trues rate error increasing as a function of discard energy in an approximately linear fashion for all phantom activities. Above 150 keV discard energy, the higher activity phantoms showed a consistently greater error than the lower activity phantoms at each discard setting.

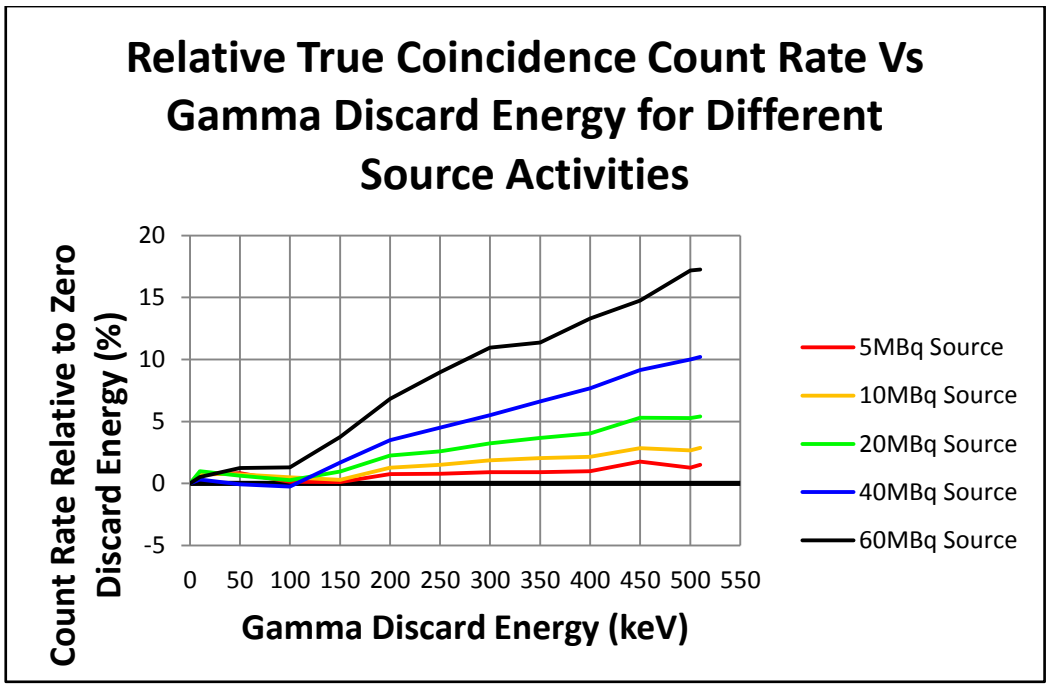


Figure 3.4. Relative true coincidence rate versus gamma discard setting (keV) for different source activities. True coincidence count rate is relative to the trues rate at 0 keV discard setting.

Figure 3.5 plots the rate of random coincidences versus the phantom activity for a selection of gamma discard energy settings. As might be expected, the randoms rate increased with increasing source activity. As for true coincidences, discarding photons from the simulation produces a more noticeable effect at higher activity levels.

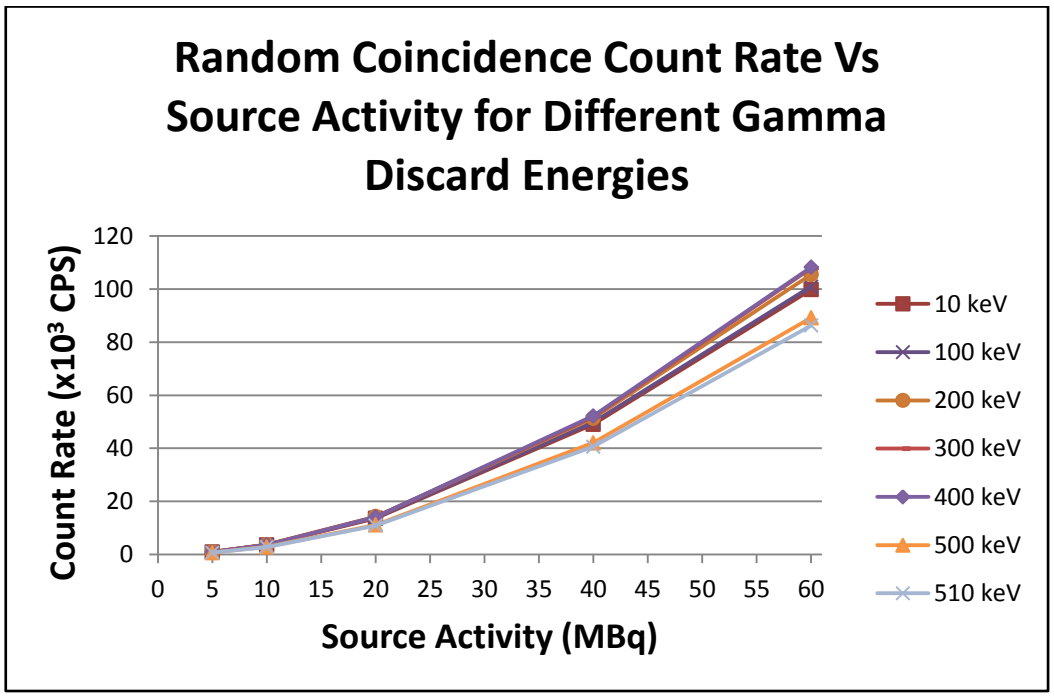


Figure 3.5. Random coincidence rates versus source activity for different gamma discard settings (keV).

Figure 3.6 plots the change in random coincident count rate, relative to the count rate at zero gamma discard energy, as a function of gamma discard energy for each phantom activity level. Discarding photons of 200 keV or lower energy from the simulation resulted in less than 5% error in the observed randoms rate at all activity levels, with a possible negative bias at low source activities. Above 200 keV and under 400 keV discard settings, the error in the randoms rate took on a positive bias for phantom activities above 20 MBq, while the error remained low for phantom activities under 20 MBq. Above 400 keV discard setting, error rates increased rapidly with an apparent negative bias.

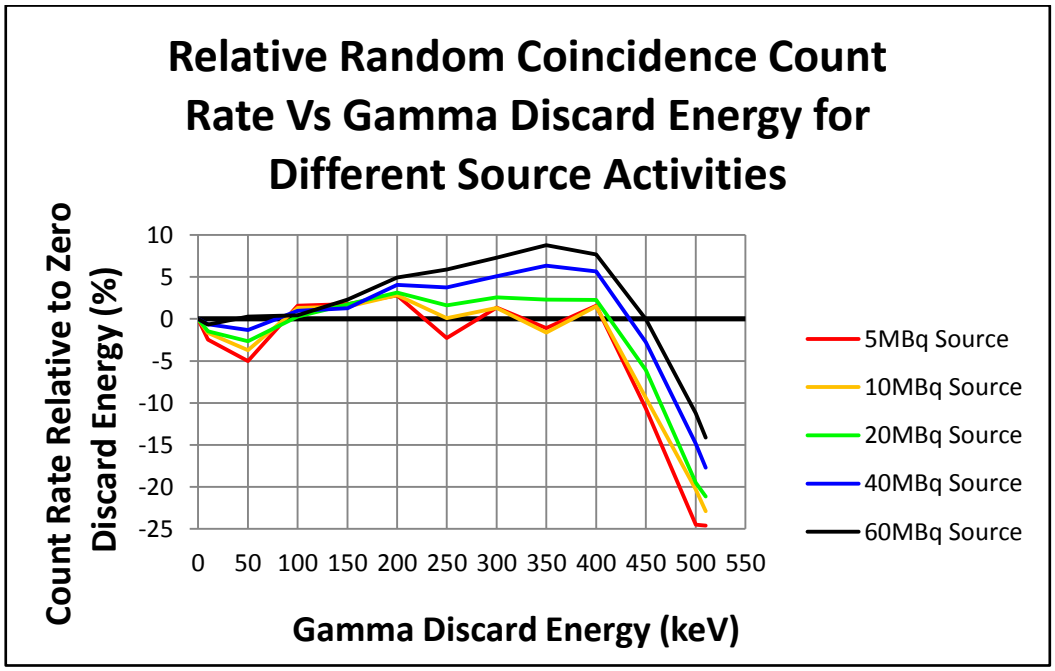


Figure 3.6. Relative random coincidence rate versus gamma discard settings (keV) for different source activities. Random coincidence count rate is relative to the randoms rate at 0 keV discard setting.

Figure 3.7 shows the relationship between scattered coincidence rate and phantom activity for a selection of different gamma discard energy settings. For gamma discard energy settings of 500 keV and above, the scatter count rate was markedly reduced.

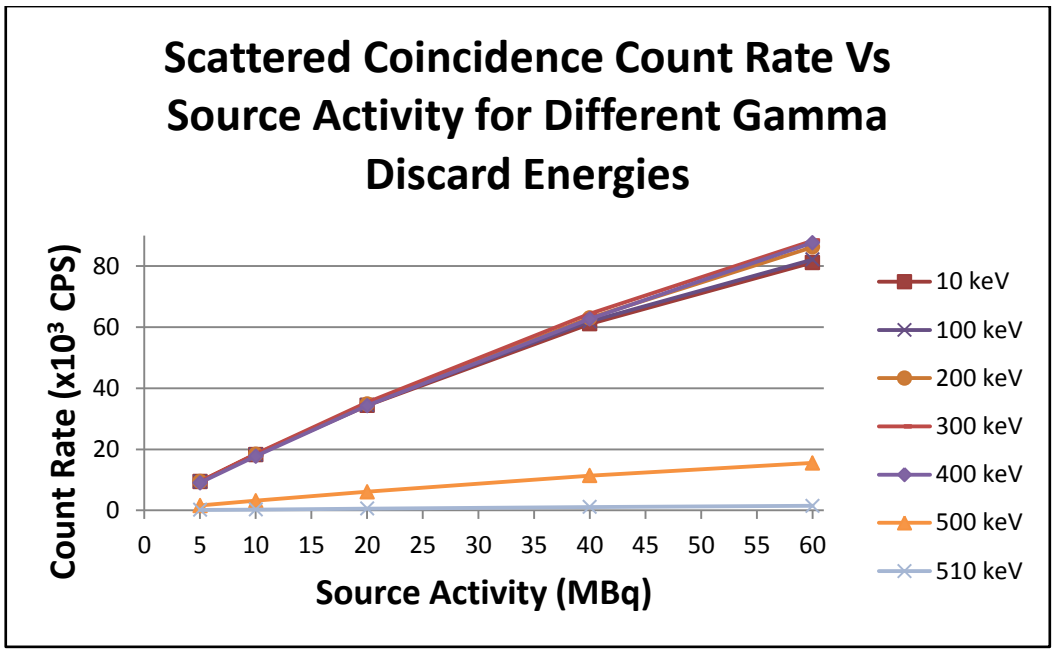


Figure 3.7. Scattered coincidence rates versus source activity for different gamma discard settings (keV).

Figure 3.8 plots the change in scattered coincident count rate, relative to the count rate at zero gamma discard energy, as a function of gamma discard energy for each phantom activity level. A slight positive bias of 3.5% or less was seen in the scatter rate at 100 keV discard energy setting for all phantom activity levels. Above 100 keV discard setting the positive bias rose rapidly for the higher activity phantoms, peaked around 350 keV then dropped rapidly to a negative bias. Error remained at less than 5% for the low (5 MBq and 10 MBq) activity phantoms up to 400 keV discard setting then dropped rapidly to a negative bias along with the high activity phantoms.

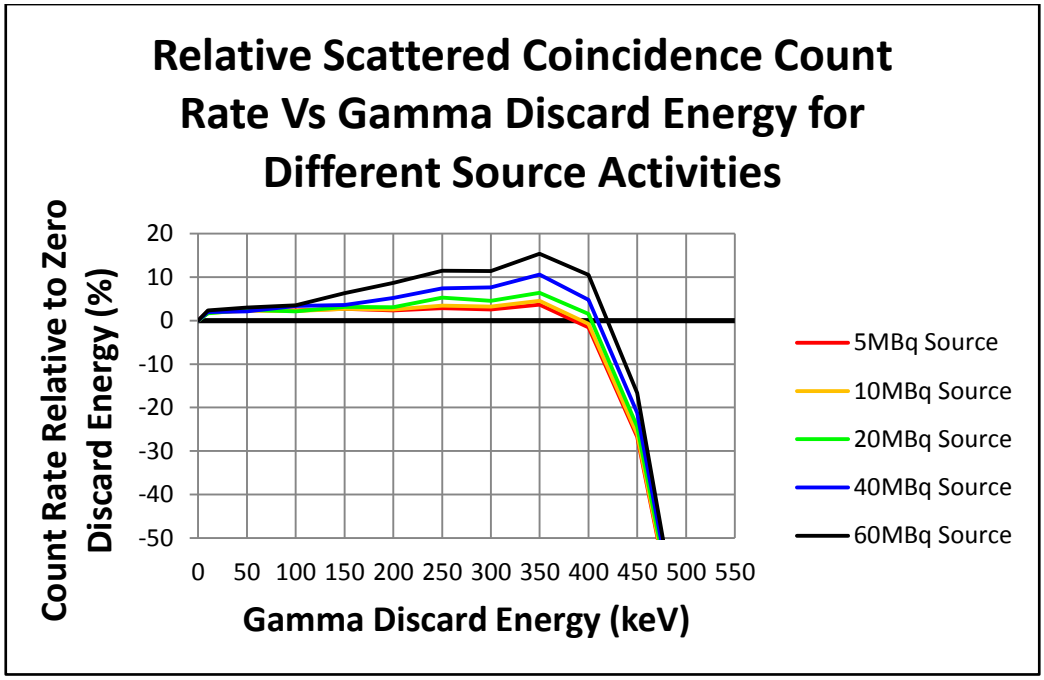


Figure 3.8. Relative scattered coincidence rate versus gamma discard setting (keV) for different source activities. Scatter coincidence count rate is relative to the scatter rate at 0 keV discard setting

Figure 3.9 shows the energy spectra as recorded by the simulated PET scanner for six different gamma energy discard settings. All spectra are displayed with a bin width of 5 keV. All photons emitted from the head phantom that were incident on the simulated detectors are included. Removal of low energy photons from the simulation altered the appearance of the energy spectrum, most obviously at lower energies. A slight effect was also observed within the photopeak region: the height of the 511 keV photopeak was increased slightly for lower energy discard settings and reduced with the 500 keV discard setting. It should be noted that the gamma discard energy setting in GATE applies only to photons tracked through the head phantom and does not apply to photon interactions with the detectors.

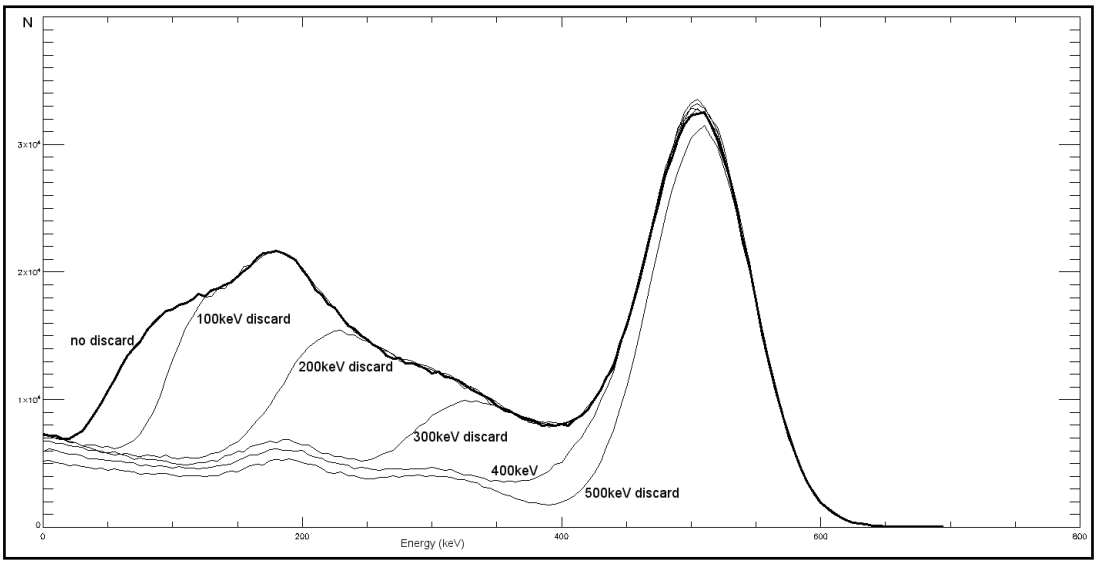


Figure 3.9. Gamma energy spectra of photons (singles) recorded by the simulated PET scanner for six different gamma discard energy settings. The simulated scanner had an energy resolution of 18% at 511 keV. Gamma photon removal applied only to photons being tracked through the phantom and not the detectors.

Execution times for each gamma discard setting are shown in Table 3.4 below. Simulated PET acquisition time was 1.0 seconds and the 20 MBq source phantom was used. Initialization time, which was approximately 11 seconds in each case, was not included in the reported execution times.

Table 3.4. Execution times for each gamma discard energy setting for a 20MBq source phantom and 1.0 second simulated PET acquisition.

| Discard Energy (keV) | Execution Time (min) |
|---|---|
| 0 | 48.0 |
| 10 | 48.0 |
| 50 | 47.1 |
| 100 | 46.5 |
| 150 | 44.25 |
| 200 | 42.8 |
| 250 | 41.0 |
| 300 | 40.0 |
| 350 | 38.8 |
| 400 | 37.4 |
| 450 | 35.7 |
| 500 | 33.9 |
| 510 | 33.3 |

### 3.2.6 Discussion

Absolute counting rate errors associated with the use of the gamma discard function in GATE were less than 5% for all discard settings of 100 keV or lower, at brain phantom activity levels of 60 MBq or less. Above 100 keV discard setting, absolute errors of greater than 5% were observed, especially at higher source activity levels. These findings would seem to counsel against the use of a gamma discard setting above 100 keV for GATE simulations in which high fidelity of count rate response and scatter fractions is required.

The observations with respect to true coincidence count rates can be explained on the basis of system dead time effects. GATE models the system energy resolution and event processing electronics, including the system dead time. The apparent increase in sensitivity to true coincidences as discard energy is increased is likely due to a reduced count rate burden on the system at lower energies. Low activity levels in the phantom, which are already associated with lower count rate burdens, therefore produce smaller apparent gains in sensitivity as discard energy is increased. The same effect may be seen in the energy spectra in Figure 3.9, where the spectra for gamma discard energies of 100 keV to 400 keV show an increased photopeak height compared to the zero discard photopeak. It should be noted that 'true' coincidences here are defined as those coincidence events identified in the GATE simulation as originating from single 511 keV photon pair, and having not undergone a scattering interactions prior to detection. Therefore true coincidences in this context do not include scattered or random coincidences.

The effects of discard energy setting on random and scattered coincidence rates is probably a combination of the dead-time effects noted above, and (at higher discard energies) the direct removal of photons that would otherwise have been accepted by the PHA. The lower energy PHA threshold on the simulated scanner was set to 420 keV (Philips Allegro default setting), and the energy resolution was set to 18% at 511 keV. Therefore the removal of photons greater than about 350 keV resulted in a direct loss of counts that would have been accepted by the PHA as valid, due to the limited energy resolution of the detectors. This effect may also be seen in the energy spectra in Figure 3.9, where a reduced photopeak height is apparent for the 500 keV gamma discard setting.

Execution time analysis revealed only a small advantage to the use of the gamma discard function. Removal of all photons less than 511 keV from the simulation was found to reduce execution time by approximately 30%. However the significant distortions in

observed count rates would seem to make the use of such high discard settings imprudent for the purposes of most simulations. At the discard energy setting of 100 keV, a time saving of approximately 3% was achieved.

### 3.2.7 Conclusions

Given the small error levels associated with the use of 100 keV discard settings in this experiment (less than 3.6% absolute error at all phantom activity levels studied and less than 2.4% error at phantom activities under 20 MBq), the use of 100 keV gamma discard setting might be justified for this combination of phantom geometry, source activity range and scanner parameters. Although the reduction in execution time is expected to be very modest at approximately 3%, over a very long simulation- for example 20 days- this equates to a time saving of around 14 hours, which might still be of practical benefit in some circumstances.

Discarding photons of 250 keV energy or greater from simulations involving high count rates relative to the system dead-time is likely to introduce errors greater than 10%, even if the discard energy setting is well below the lower level energy discrimination threshold. Therefore the use of the gamma discard function in GATE should either be avoided, or validated for each combination of expected phantom activity, discard energy setting, system dead time setting, coincidence timing window, energy resolution, photopeak window width and attenuation phantom.

## 3.3 Design and Assembly of a Low Cost High Performance Computer Cluster

### 3.3.1 Introduction

In 3.1, the feasibility of designing a computer cluster that meets the needs of this research project (see 3.1.1 for specific cluster design goals) was demonstrated. This section discusses in detail the design and assembly of this computer cluster.

### 3.3.2 Components and Budget for the High Performance Cluster

A computer cluster consisting of 10 nodes was assembled using the same components as listed in Table 3.1. The single CPU system assembled from these components, described in 3.1.2.2 and employed for the two experiments described above, was also added to the cluster, and designated the ‘head node’. The remaining 10 nodes were designated the ‘computing

nodes'. Therefore, the cluster contained a total of 11 nodes and 44 computer cores. The components and budget for the 10 compute nodes are given in Table 3.5 below.

Table 3.5. Components and costs for the 10 'compute nodes' of the computer cluster. All components were sourced from a local metropolitan computer component supplier in May 2010. Prices were inclusive of 10% Goods and Services Tax, and delivery to the university campus.

| **Component** | **Quantity** | **Total Cost (AUD)** |
|---|---|---|
| Motherboards | 10 | 1865.10 |
| CPUs | 10 | 919.10 |
| memory (2GByte RAM chips) | 40 | 2920.00 |
| Video Cards | 10 | 400.00 |
| Hard Disk Drives | 10 | 680.00 |
| Network Switch (1Gbps, 16 port) | 1 | 130.00 |
| Power Supply Units | 10 | 700.00 |
| Ethernet Cables | 15 | 70.00 |
| Materials (wood, nails, screws, glue, sandpaper, polyurethane wood finish, nuts & bolts, grounding wires, electrical tape) | | 250.00 |
| | ***Total Cost:*** | ***AUD 7934.20*** |


Figure 3.10. Principal hardware components of one node of the high performance cluster, including: a motherboard, CPU, memory modules, power supply unit. The network switch that allowed communication between the nodes is also shown at the rear.

Adding the component cost of the original 'head node' to the component cost of the 10 nodes detailed above, the total component cost of the cluster was AUD 8,752, including 10% retail taxes. Additional components used but not listed in the budget included: an Ethernet expansion card, a desktop computer monitor, a keyboard, a mouse, 2 multi-outlet power strips and 2 power usage meters with overload and surge protection functionality. These items were recycled from obsolete or derelict equipment in the laboratory. Tools used during the construction of the cluster, also not listed in the budget, included: various screw drivers, pliers, an adjustable spanner, a power drill fitted with 6 cm and 3 cm circular cut-out pieces, a hammer, a paint brush and paint thinner. Approximately 50% of the wooden components used to construct the supporting framework of the cluster were sourced from the 'cut-offs' bin at the local hardware shop, and attracted only a minimal cost.

Labour costs were not explicitly included in the above budget. Design and assembly of the cluster was carried out by the author over a period of approximately 6 weeks. Multiplying this student's weekly average scholarship by 6 yields an approximate labour cost of AUD 3,400, bringing the total cost of building the computer cluster to AUD 12,152.

### 3.3.3 Design and Assembly of the High Performance Cluster

Design of the computer cluster followed closely the design principles of the Microwulf cluster (Adams & Brom, 2008), described in 2.5.3. The following section outlines the design features of the cluster and the methods used for its assembly. Particular emphasis

is given to those areas of the cluster's design that deviate substantially from the Microwulf cluster of Adams and Brom.

Wood was chosen as the material to provide structural support for the cluster because it was low cost, readily available in scrap form and could be manipulated safely with simple tools for which no further training or supervision was required. Specifically, 9 mm thick plywood sheets of size 90 cm x 60 cm were chosen to provide the surface on which to mount the motherboards and all other components. To improve the structural rigidity of the large plywood sheets, hardwood beams of 4 cm x 1.8 cm x 90 cm were attached to the perimeter of the plywood sheets using barbed nails and wood glue. The reinforced platforms were then sanded to remove splinters and sharp edges and, to facilitate the later attachment of components with adhesive products, a polyurethane wood finish was applied. A total of four platforms were constructed in this way. Three of the platforms had holes of 3 cm or 6 cm diameter drilled at various locations to allow the passage of power and communications cables between levels. Legs were added, with adhesive felt pads attached to the lower ends of the legs to dampen any vibrations from the computer equipment and to minimise damage to the bench top on which the cluster was positioned. Altogether, the wooden supporting structure of the cluster measured 90 cm x 60 cm x 90 cm.

Figure 3.11. Wooden supporting structure for the cluster, with first five motherboards installed on lower level. Holes allowing cables to pass through to adjacent levels may be seen on the second and fourth levels.

Although the cluster has been referred to as ‘desktop’ in scale, this cluster was designed to be as large and open as the physical space available on the laboratory bench top would permit. Because the cluster was operated in a general use laboratory rather than a dedicated computer room, quietness of operation was a design priority. No additional cooling fans were installed beyond the small fans already incorporated into the power supply units (PSUs) and CPUs, therefore a larger open design was required to allow air to flow between the four levels. Ease of access to the hardware was also considered a design priority, to allow a hard reset of the boards if required, and to allow monitor and keyboard cables to be attached to the motherboards as necessary, without the need for additional switching hardware. For these reasons, a space of at least 20 cm was allowed between each level.

Each computing node consisted of one motherboard, a power supply unit (PSU), a quad-core CPU, 8 Gbytes of memory and a 250 Gbyte hard disk drive. Each node’s operating system and associated files were stored on its own local hard disk. This allowed for faster booting and resetting of individual nodes as required, and did not require increasing the physical size of the cluster. All other directories and applications, including GATE, were shared from the head node, and were accessed by each computing node via a network file

system (NFS). Unlike the computing nodes, the head node was mounted inside a conventional computer case, and was configured with a CD drive, monitor, keyboard and mouse.

Three power strips were included in the cluster, which drew power from two separate wall sockets. Although it might have been possible to run the cluster from one wall socket (later testing under full load revealed a total power consumption of approximately 1500 watts, or approximately 66% of maximum permissible wall-socket load) two separate sockets were available in the laboratory, so the power supply to the cluster was shared between the two outlets in approximately equal proportion.

Motherboards were mounted on two of the four wooden platforms using adhesive plastic standoffs. Five motherboards were mounted on the lower level and another five on the third level. Each hard disk drive was placed adjacent to the motherboard to which it was attached. The second level of the cluster contained five PSUs: one for each board on the lower level. The network switch and one power strip was also located on the second level. The fourth (top) level contained another five PSUs and another two power strips. Each motherboard and each hard disk drive was grounded to the metal casing of its corresponding PSU using insulated electrical wire and alligator clips.

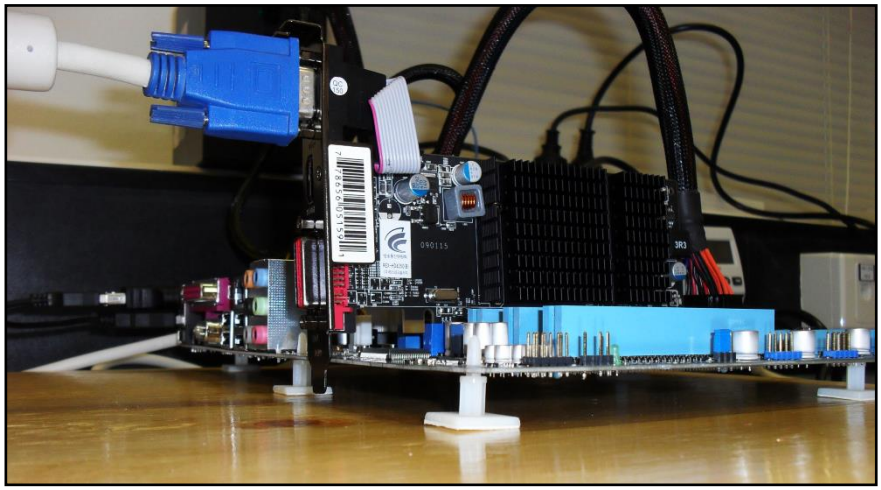

Figure 3.12. Close-up view of motherboard mounted on wooden platform. Adhesive plastic standoffs were used to attach the motherboards to the platforms. Grounding of the motherboards, usually achieved via the metal screws that fix the board to the metal case of a desktop PC, was achieved using separate electrical wires and alligator clips (not shown here).

The following diagrams illustrate the layout and construction of the computer cluster described in the above paragraphs.

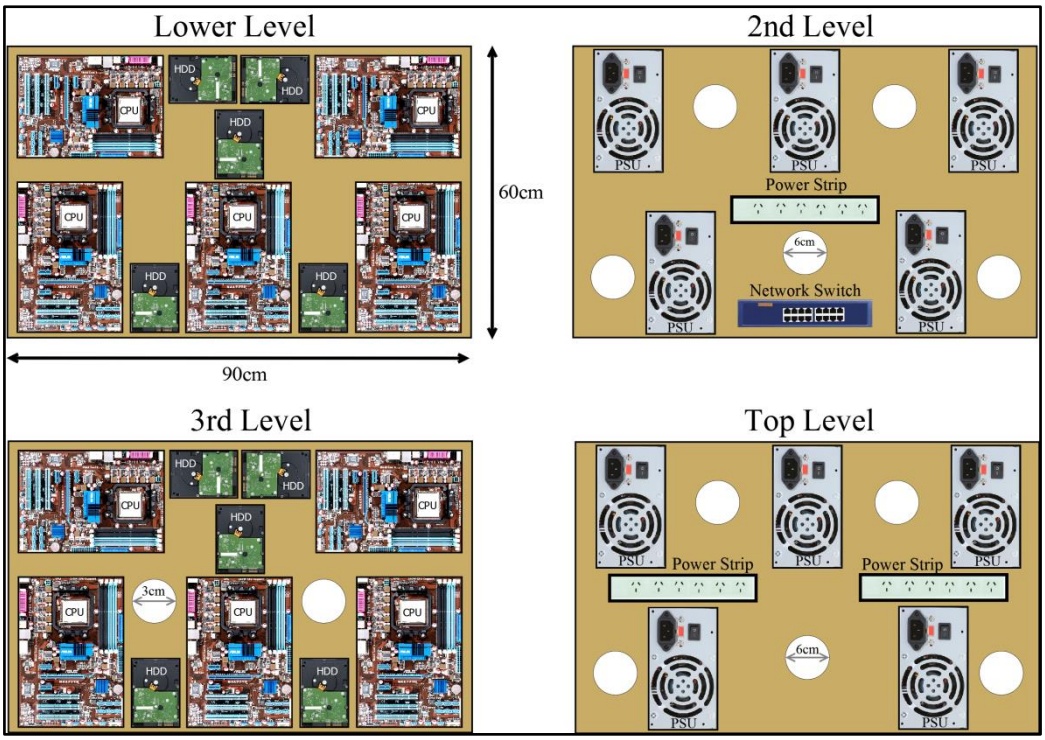


Figure 3.13. Schematic diagram showing the layout of the principal hardware components of the cluster at each level. Holes of 6 cm and 3 cm diameter were drilled at various locations to allow the passage of power cables, Ethernet cables and grounding wires between adjacent levels.

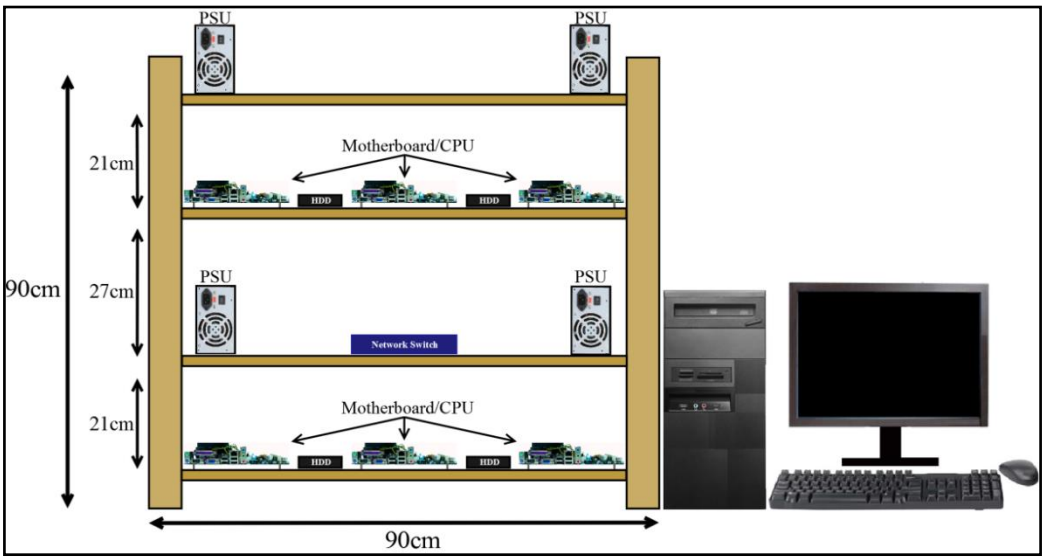


Figure 3.14. Schematic diagram of the cluster as viewed from the front. The head node was housed inside a conventional computer case and contained the same principal hardware components as the compute node. Each node booted from its own hard disk drive. All software and files, other than those associated with the operating system, were shared via a network file system from the head node.

A single Ethernet switch was used to provide all inter-node communications. The performance of the switch was rated at 1 gigabit per second (1Gbps). Inter-node

communication speed has historically been the ‘weak-link’ of the Beowulf-type cluster, with the speed of commodity network hardware typically lagging behind available CPU clock speeds and memory capacity (Becker, 1995; Gropp, 2003; Sterling et al., 1998). It is for this reason that clusters tend to perform poorly at computations requiring frequent or large data transfers between nodes, while performing well at more ‘granular’ tasks, such as Monte Carlo simulations.

It has been suggested (Adams, 2012) that for a cluster to be considered ‘balanced’, the input/output communication speed in bits per second should be equal to the clock speed of the CPU in hertz and the memory capacity in bytes. For the cluster design presented here, this is certainly not the case, with the CPU operating at 3 GHz, with 2 Gbytes of memory per core and 1 Gbps of network bandwidth for each quad core CPU. Therefore, this cluster is out of balance by a factor of 12 with respect to computation speed and communication bandwidth (3 GHz x 4 cores per CPU). It is somewhat more balanced with respect to computation speed and memory, but still weighted 3:2 in favour of computation speed. Although unbalanced, this cluster was designed for the sole purpose of large scale Monte Carlo PET simulations, of the type presented in this chapter. The results of these experiments demonstrated that 2 Gbytes of memory per computer core was sufficient for this purpose, regardless of computation speed. Given that Monte Carlo simulations are well suited to simultaneous and independent execution, and do not normally require any inter-node communication, the limited communication bandwidth of this cluster was deemed an acceptable design compromise.

Many clusters employ job management software to distribute tasks between nodes and perform load-balancing; however no such software was used on this cluster. Instead, independent Monte Carlo simulations, usually expected to run for several days or weeks, were split into jobs of approximately equal computational load directly by the user prior to execution. Jobs were then distributed via remote login software that was available within the operating system. Job splitting and merging software was available within the GATE package, however in the software version used it was not fully compatible with the data output format chosen for these experiments and was not used. In instances where output data had to be summed from multiple computer cores, this was done off-line with user-written code, and generally represented only a small fraction of the total simulation time. For this reason, conventional benchmarking of the cluster’s floating point operation performance was not done.

To allow outside network access, an additional Ethernet card was installed on the motherboard and connected to the campus network. A schematic representation of the network layout for this cluster is presented in Figure 3.15.

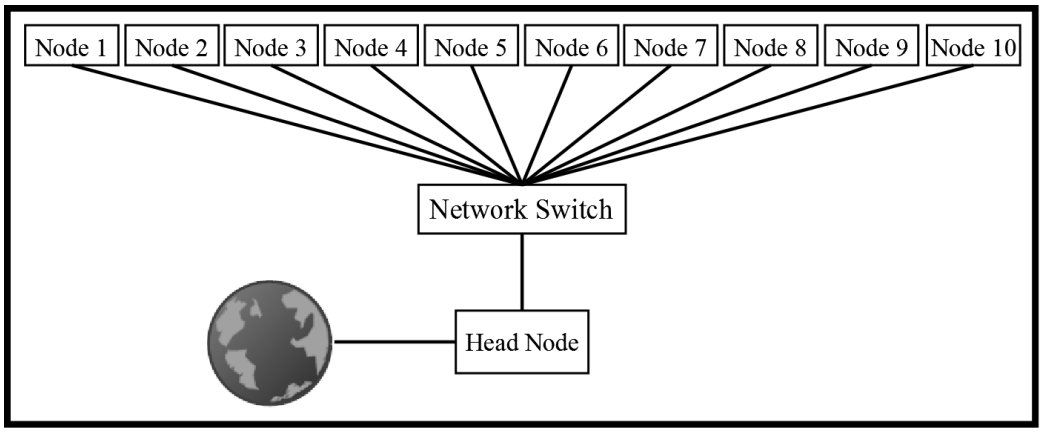


Figure 3.15. Schematic network diagram of the computer cluster. The head node contained an additional network card for access to the external campus network.

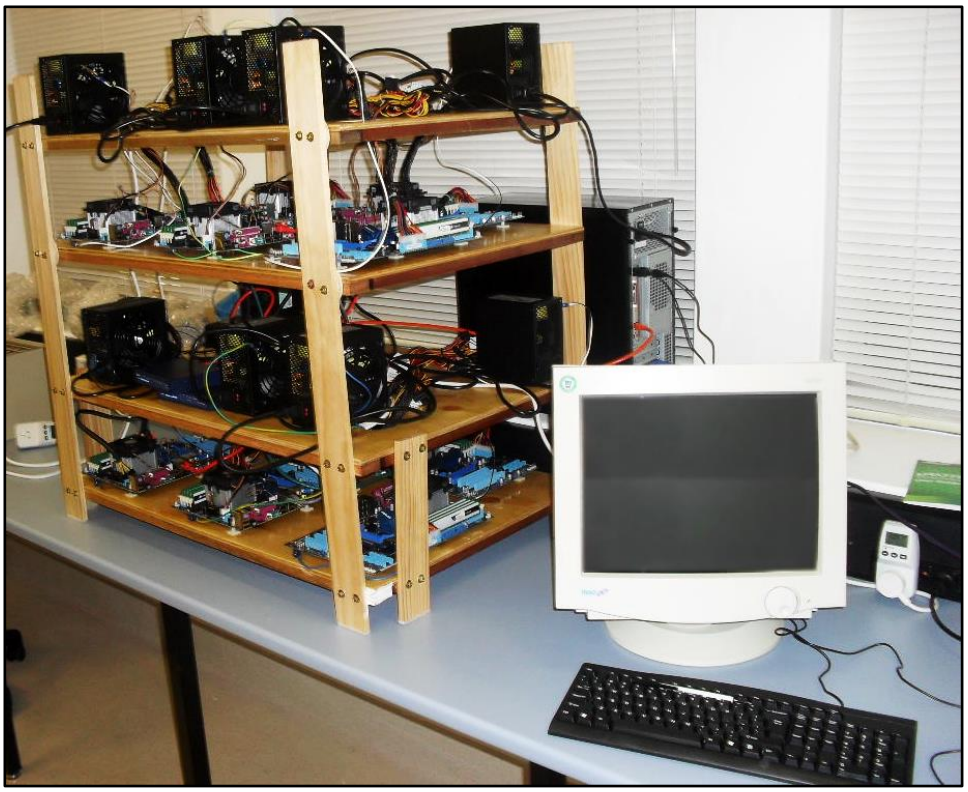

Figure 3.16. Completed computer cluster. The head node (black computer case) may be seen behind the wooden structure containing the ten computing nodes.

### 3.3.4 GATE Installation and Validation

GATE was installed on desktop PC used for the initial timing and memory experiments described in 3.1.2.5. This PC became the head node of the cluster, and all computing nodes accessed exactly the same GATE program and associated libraries from the head node via a shared file system.

To assess the validity of the installation, two benchmark simulations are provided within the GATE software package: the SPECT benchmark and the PET benchmark. Reference output data for both benchmark tests are provided with the GATE distribution. The results obtained from both benchmark simulations on the head node confirmed the validity of the GATE installation. They are presented in appendix 7.6.

#### 3.3.4.1 Performance Assessment of the Computer Cluster

The performance of the 40 computing cores (10 x quad-core nodes) relative to each other was assessed using a simulation task similar to the one described in the above timing experiments, and using the digital attenuation and emission phantoms described in 3.1.2.3.1 and 3.1.2.3.2. A total of 10.26 MBq of activity was distributed within the grey matter, white matter, skin, muscle and other soft tissue voxels of the digital emission phantom, yielding an average tissue concentration of 2.67 kBq/mL. A PET scan of 15 seconds duration was simulated using the fictitious interactions tracking algorithm and 100 keV gamma discard energy. The simulation was run simultaneously, with different random number generator seeds, on each of the 40 computing cores of the cluster. For each simulation, the execution time, total prompt coincidences, total scattered coincidences and total random coincidences were recorded. Total power consumption and memory usage of the cluster under full computational load was also measured.

Results of this test are presented in the plots below (Figure 3.17, Figure 3.18, Figure 3.19 and Figure 3.20). The coefficient of variation (standard deviation divided by the mean) for prompt, scattered and random coincidence counts collected was 0.11%, 0.25% and 0.84% respectively. Coefficient of variation for execution time was 0.97%, with one noticeable outlier, which returned an execution time ≈ 3 standard deviations longer than average. However, this ‘slow’ core produced prompt, random and scattered coincidence totals that were all within ± 1 standard deviation of the corresponding mean values, suggesting that the cause of its reduced speed did not affect the accuracy of the simulation. No correlation was observed between execution time and total prompt counts ($r$ = -0.19).

Setup time for each simulation was approximately 12 seconds, during which time the computer core would load the GATE software and all input data from the head node via the network and initialise the simulation. At the end of each simulation, a burst of network activity lasting approximately 3 to 4 seconds was observed as the output data (3 sinograms of ≈119 Mbytes each plus 6 text files of ≤ 1 kilobyte each) were written out to the hard disk on the head node. To avoid network holdups and potential errors, a conservative delay of 15 seconds was imposed between the start each simulation on different cores, leading to approximately 10 minutes delay between the start of the simulation on the first and the last core. This job splitting overhead was considered insignificant in comparison to the expected length of the simulation; therefore full optimization of this aspect of the cluster's operation was not investigated further.

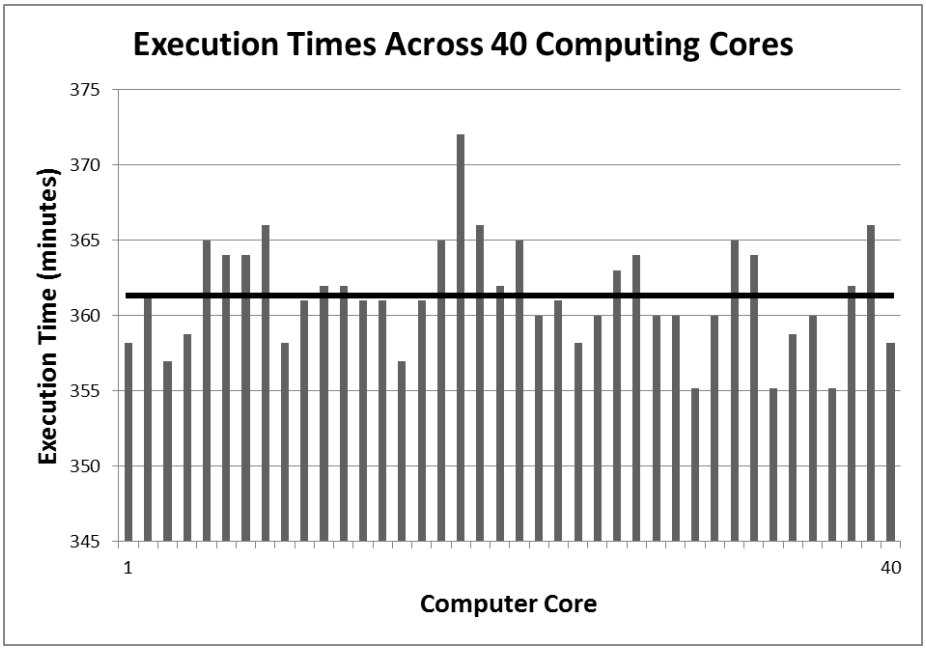


Figure 3.17. Execution time for the brain phantom simulation on 40 computing cores. Average = 361.3 minutes (straight line).

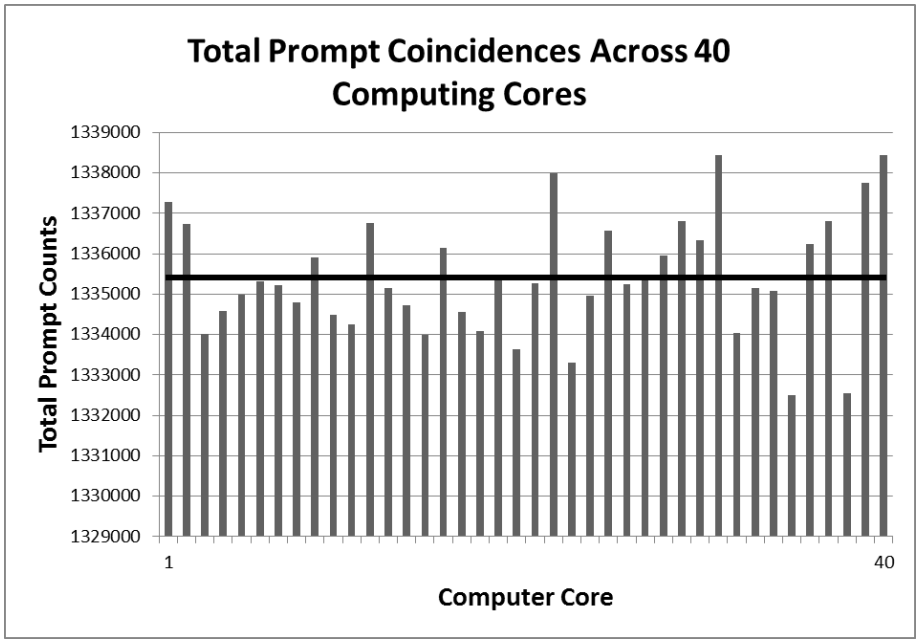


Figure 3.18. Total prompt coincidence events for the brain phantom simulation on 40 computing cores. Average = 1,335,424 counts (straight line).

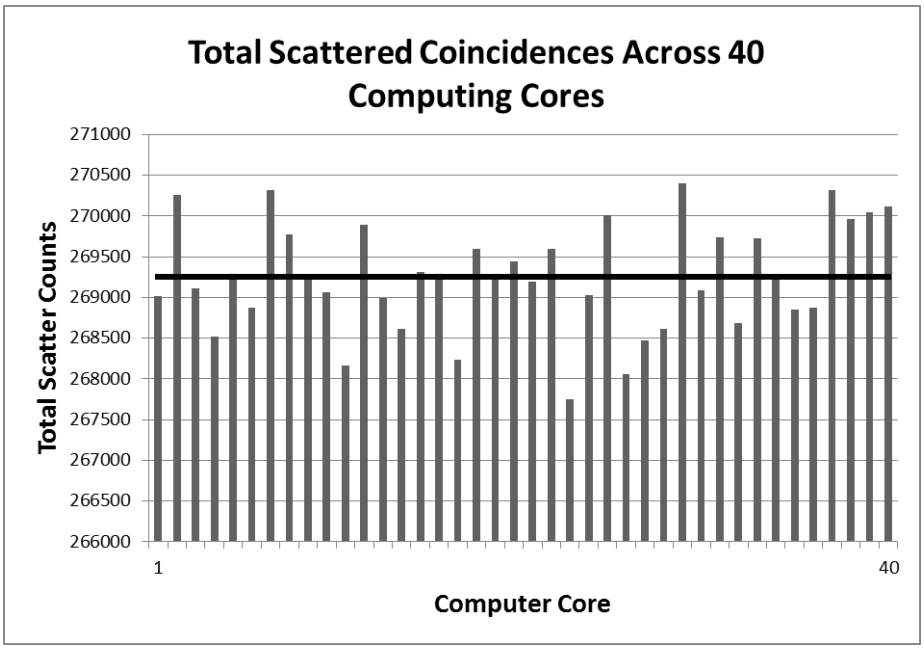


Figure 3.19. Total scattered coincidence events for the brain phantom simulation on 40 computing cores. Average = 269,249 counts (straight line).

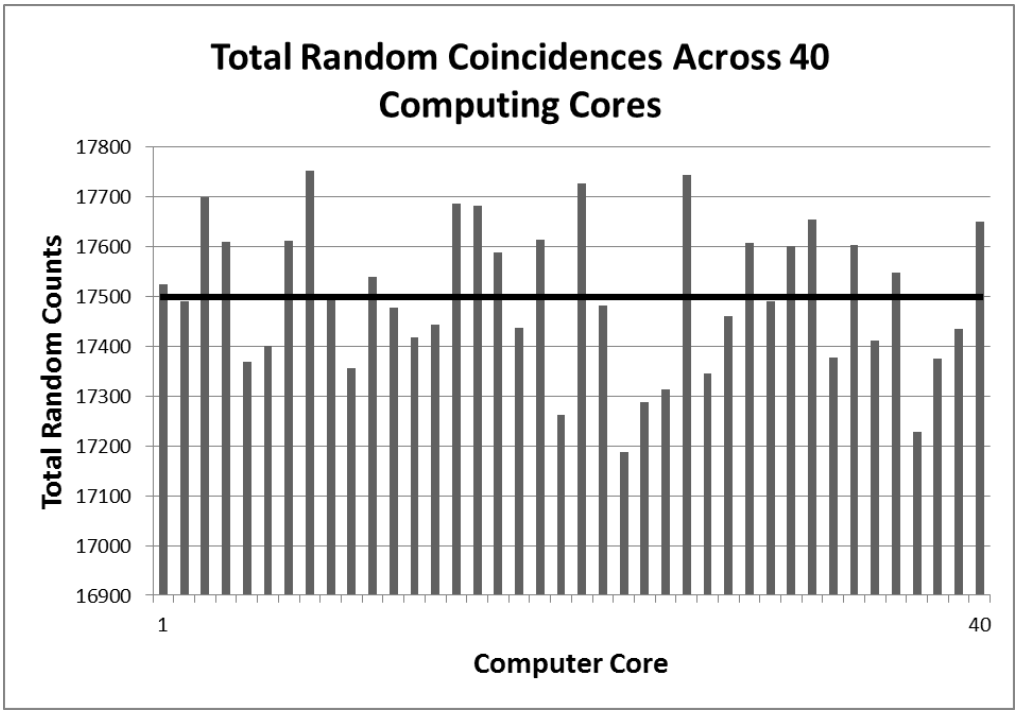


Figure 3.20. Total random coincidence events for the brain phantom simulation on 40 computing cores. Average = 17,499 counts (straight line).

Sample sinogram data output from the test simulations are displayed below in Figure 3.21. The 3D sinograms have been summed over all planes and trimmed to include only the head phantom for display clarity. The prompt sinogram demonstrates a distribution of counts in accordance with that expected from the digital phantom properties used for this test. No correction has been made for attenuation or detector efficiency normalization, and these effects are evident in the prompt sinogram as a reduced level of counts in the central region of the projection profiles (attenuation), and a diagonal 'crosshatch' pattern of varying counts throughout the sinogram (geometric efficiency variation). As expected, the scatter sinogram reveals a background of scattered events that is present across the entire field-of-view, peaking around the central regions of the projection profiles where the object is located. Also as expected, the random coincidence sinogram shows a distribution of events that appears unrelated to the spatial distribution of activity in the phantom.

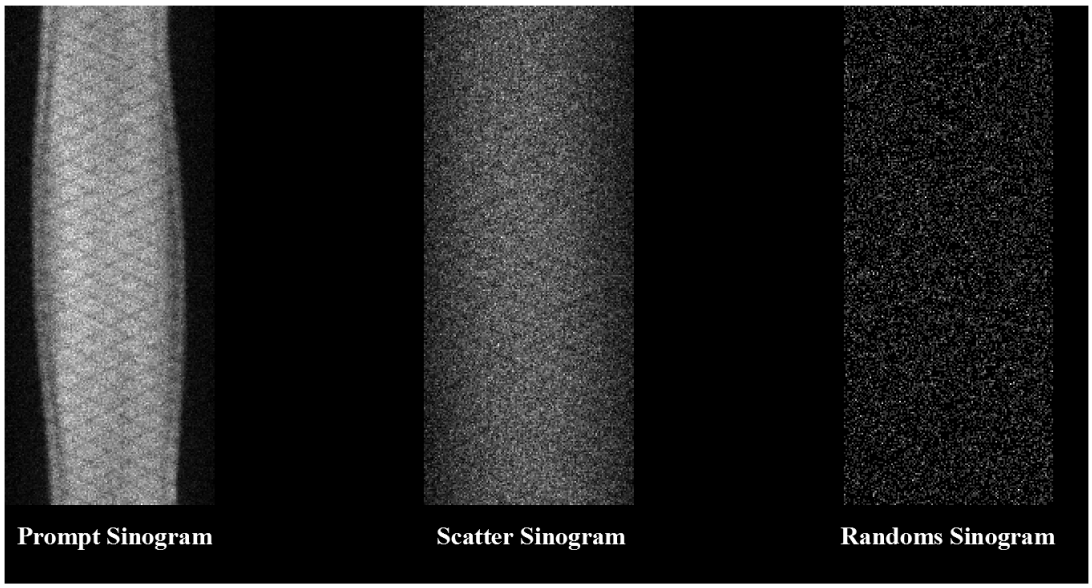


Figure 3.21. Sinogram output data from one core of the test simulation. Sinogram data are summed over all planes and normalised to the maximum value for display purposes.

Power consumption of the entire cluster at full computational load was measured at 1430 watts with the monitor switched off, and 1500 watts with the monitor on. Memory consumption at full load, including operating system requirements, was 59.2 Gbytes or 74% of total installed memory.

The average simulation rate achieved during the above test was $7.1 \times 10^3$ photon pairs per second per core, which is 1.8% slower than the rate achieved on the single CPU core of the head node during previous testing (see 3.1.5). A whole-cluster simulation rate of $2.84 \times 10^5$ photon pairs per second was achieved when all 40 cores were in use. Interestingly, this is approximately 36 times slower than 'real-time' for the 10.26 MBq head phantom tested here ($1.026 \times 10^7 / 2.84 \times 10^5 \approx 36$), suggesting that if the computational speed of the individual computer cores were to increase by a factor of ≈ 36, or if a PET simulation could be efficiently parallelized over a cluster of ≈ 1500 current generation computer cores, then it might be possible to simulate the PET data at the same output rate as a real system.

Referring to the calculations in appendix 7.5, it is estimated that the simulation of an hour long dynamic [$^{11}$C]-PK11195 brain PET scan requires approximately $2.23 \times 10^{10}$ photon pairs, which would take 21.8 hours on 40 CPU cores. Completion of 50 independent repeats could theoretically be accomplished in approximately 45 days, assuming negligible overheads due to job splitting and data output merging. If 40 repeated simulations were considered sufficient for the purpose of estimating image noise in a PET scan, then this could

be easily implemented on this cluster by running the complete scan simulation independently on each core. For the above mentioned dynamic brain simulation task, this would take an estimated 36 days. Each core would run an identical and complete (0 to 60 minutes scan) simulation; therefore data merging and load-balancing problems could be largely avoided.

### 3.3.5 Conclusion

A computer cluster was constructed consisting of 10 computing nodes (40 CPU cores) and one head node (4 CPU cores). The cluster was capable of running a Monte Carlo simulation using the GEANT4 Application for Tomographic Emission software package, including modelling of the attenuation and emission source geometries of the human head. Simulations were run on all 40 computing cores simultaneously, with comparable execution times and output results from each core. A peak simulation rate of $2.84 \times 10^5$ photon pairs per second for a human brain PET simulation, including voxelized emission and attenuation phantoms, was achieved. By extrapolation, the total simulation time for a typical 1 hour [$^{11}$C]-PK11195 PET scan would be $\approx$ 21.8 hours on 40 computer cores. To the best of the author's knowledge, this is the first report of a Microwulf-style computer cluster built specifically for medical imaging related Monte Carlo simulations.

# Chapter 4 Estimating Image Noise in PET using Monte Carlo Simulations

In the previous chapter, a computer cluster was designed and built, capable of running a Monte Carlo simulation of the dynamic acquisition of a [$^{11}$C]-PK11195 positron emission tomography (PET) study, with 40 independent repeats, within a time frame of less than 6 weeks. This chapter details the development and validation of a model that describes the image noise found in dynamic 18 kilodalton (18kDa) Translocator Protein (TSPO) positron emission tomography (PET) scans, including the design of a realistic PET scanner model, the estimation of image noise by repeated measurements and the fitting of an analytical noise model to the data.

## 4.1 Simulation of a Realistic PET System Using GEANT4 Application for Emission Tomography

### 4.1.1 Introduction

Simulation of a PET scan within the GEANT4 Application for Tomographic Emission (GATE) software requires a complete description of the scanner's geometry and electronics. Considerable flexibility exists within GATE to describe the PET geometry, which may correspond closely to an existing real-world system, or to a hypothetical system with no real-world equivalent.

In order to provide meaningful estimates of image noise, a generic PET tomograph with geometry and performance characteristics that closely matched those of current generation clinical PET systems was implemented in GATE. Evaluation of the performance characteristics of the simulated scanner was carried out using simulated equivalents of the standard against which clinical PET scanners are currently tested: the National Electrical Manufacturers Association NU 2-2007 (National Electrical Manufacturers Association, 2007). This section describes the application of these NEMA tests to the simulated PET scanner, and presents the results. Comparison is made with a selection of contemporary clinical PET scanners.

### 4.1.2 Aim

The aim was to develop a PET scanner model within the GATE software package that closely matched the performance of current generation PET scanners in terms of spatial resolution, sensitivity, scatter fraction and noise equivalent count rate (NECR).

### 4.1.3 Equipment

The following equipment was used:

- High performance computer cluster, described in 3.3 .
- GEANT4 Application for Tomographic Emission (GATE) version 6.0
- Software for Tomographic Image Reconstruction (STIR) version 2.1 (Thielemans et al., 2012).
- IDL version 8.1 (Exelis Visual Information Solutions, Boulder, Colorado)

### 4.1.4 Method

#### 4.1.4.1 Simulated PET Scanner and Detector Electronics Description

A cylindrical full-ring PET scanner was described using the GATE macro language. The detectors of the simulated scanner were modelled after the Siemens Biograph 16 HI-REZ (Siemens Healthcare, Knoxville, TN, USA), as described in (Brambilla et al., 2005) and the event processing electronics were modelled after the Siemens Pico-3D™ detector electronics (Martinez, Bercier, Schwaiger, & Ziegler, 2006), also found on the Biograph 16 HI-REZ. However, the inter-block spacing and non-cylindrical geometry of the Biograph were not modelled exactly in the simulated system. The GATE macro describing the scanner geometry is reproduced in appendix 7.8 and the macro describing the event processing electronics is described in appendix 7.9.

Key characteristics of the geometry of the simulated PET scanner are summarised in Table 4.1 below, along with the corresponding characteristics of several modern commercial PET systems: the Siemens Biograph 16 HI-REZ (Brambilla et al., 2005), the older Siemens Biograph equipped with a CPS ECAT Accel tomograph (Erdi, Nehmeh, Mulnix, Humm, & Watson, 2004), the Philips (Philips Medical Systems,) Gemini TF (Surti et al., 2007) and the GE (General Electric Medical Systems) Discovery STE (Teräs, Tolvanen, Johansson, Williams, & Knuuti, 2007).

Table 4.1. Geometrical characteristics of the simulated PET scanner, and four current clinical PET scanners. All real-world scanners listed here are whole body clinical PET/CT systems that are or have been available commercially since 2003. All PET tomographs are based on the block detector design, with the exception of the Philips Gemini which uses a pixelated Anger logic detector module. *LSO = lutetium oxyorthosilicate; LYSO = lutetium yttrium oxyorthosilicate; BGO = bismuth germanate.

| **Characteristic** | **Simulated Scanner** | **Siemens Biograph 16 HI-REZ** | **Siemens Biograph (Accel)** | **Philips Gemini TF** | **GE Discovery STE** |
|---|---|---|---|---|---|
| **Detector material*** | *LSO* | LSO | LSO | LYSO | BGO |
| **Detector dimensions (mm)** | *4* x *4* x *20* | 4 x 4 x 20 | 6.45 x 6.45 x 25 | 4 x 4 x 22 | 4.7 x 6.3 x 30 |
| **Detector block/module configuration** | *13* x *13 detectors* | 13 x 13 detectors | 8 x 8 detectors | 23 x 44 detectors | 8 x 6 detectors |
| **No. detectors (total)** | *24 336* | 24 336 | 9 216 | 28 336 | 13 440 |
| **No. detector rings** | *39* | 39 | 24 | 44 | 24 |
| **Detector ring diameter (cm)** | *86.07* | 83.0 | 82.4 | 90.34 | 88.6 |
| **Axial FOV (cm)** | *16.87* | 16.2 | 16.2 | 18.0 | 15.7 |
| **Acquisition mode** | *3D* | 3D | 3D | 3D | 2D & 3D |

The geometrical characteristics of the simulated scanner are comparable with the real-world systems listed in Table 4.1. The block configuration of the simulated scanner is modelled after the Biograph 16 HI-REZ scanner. A feature of the Biograph PET system is that the outer ring detectors tilt inwards towards the axial centre of the tomograph. This is expected to have negligible effect on sensitivity, therefore to simplify image reconstruction and data corrections for the simulated scanner; this feature was not included in the simulated system. For this reason, the ring diameter and axial field-of-view differ slightly between the

simulated system and the Biograph 16; however they are well within the range of the other PET systems listed. Unlike the Biograph 16, the detectors modelled in the simulated scanner are arranged cylindrically, and the inter-block gaps are the same length as the inter-crystal gaps, again to simplify the image reconstruction procedures.

Scanner operating specifications for the simulated scanner are summarised in Table 4.2 below, along with the corresponding specifications of the same four PET systems listed in Table 4.1.

Table 4.2. Scanner operating specifications of the simulated PET scanner and four current clinical PET scanners. NA = reliable information not available.

| **Characteristic** | **Simulated Scanner** | **Siemens Biograph 16 HI-REZ (Pico3D™)** | **Siemens Biograph (Accel)** | **Philips Gemini TF** | **GE Discovery STE** |
|---|---|---|---|---|---|
| **Energy resolution** | *15%* | 15% | 18% | 11.5% | 17% |
| **Energy window** | *425 – 650 keV* | 425 – 650 keV | 350 – 650 keV | 440 – 665 keV | 425 – 650 keV |
| **Timing resolution** | *500 ps* | 500 ps | 2 ns | 585 ps | 4.875 ns |
| **Coincidence timing window** | *4.5 ns* | 4.5 ns | 6 ns | 6 ns | 9.3 ns (3D) |
| **Dead time** | *136 ns* | 136 ns | 336 ns | NA | NA |

The event processing characteristics of the simulated system were modelled closely after the Siemens Pico-3D™ electronics (Martinez et al., 2006), as found on the Biograph 16 HI-REZ scanner. Event processing parameters such as coincidence timing window and energy resolution are somewhat dependent on the light decay properties of the scintillator crystal, therefore the Pico-3D™ system represents a suitable model for simulating a scanner based on LSO detectors. Two of the systems listed above (Biograph 16 and Gemini TF) are capable of time-of-flight measurement, however this functionality was not included in the

simulated model due to the added complexity of image reconstruction and the limited benefit that time-of-flight confers on human brain studies with current detector technology and timing resolutions (Eriksson et al., 2005).

All prompt coincidence events (i.e. all coincidence events regardless of their origin) were sorted into a 3D sinogram using the GATE sinogram output module. A delayed coincidence window was applied during all simulations to provide an estimate of the random coincidences, and these data were stored in a separate sinogram. Scattered coincidence events were identified by GATE during the simulation and stored in a third sinogram. Corrections for randoms and scatter were applied off-line using methodology described in 4.2. Sinograms were trimmed prior to storage to include only the central 28 cm of the transaxial ($x$,$y$) field-of-view, resulting in final sinogram dimensions of 131 projection profile elements, 312 projection angles and 1521 planes. No axial or angular compression of the 3D sinogram data was applied at this stage.

#### 4.1.4.2 Spatial Resolution Performance Measurement

Spatial resolution of the simulated scanner was measured via a series of point source simulations. A small spherical source of 1 mm diameter and 3.0 MBq activity was simulated in air. Simulated acquisition time was 120 seconds per scan, which ensured a minimum total of $10^6$ coincidence events per scan. Six simulations were performed with the point source located at the following positions relative to the axial ($x$,$y$) and transaxial ($z$) centre of the scanner:

Table 4.3. Locations of the simulated point source measurements relative to the axial and transaxial centre of the scanner.

| $x$ (cm) | $y$ (cm) | $z$ (cm) |
|---|---|---|
| 0 | 1 | 0 |
| 0 | 1 | 4 |
| 0 | 10 | 0 |
| 0 | 10 | 4 |
| 10 | 0 | 0 |
| 10 | 0 | 4 |

Images were reconstructed using version 2.1 of the open source 'Software for Tomographic Image Reconstruction' (STIR) package. Delayed and scattered events were subtracted from the 3D sinogram data prior to reconstruction. Correction for geometrical detector sensitivity variations was applied using a 3D sinogram normalization matrix for the simulated scanner (described in 4.2). Images were reconstructed using the 3D filtered back projection algorithm with a ramp filter and a zoom factor of 2. The 24 most oblique sinogram segments- from a total of 77 segments- were discarded from the data prior to reconstruction. Image matrix dimensions were 131 x 131 x 77 voxels. Voxel dimensions were 0.889 mm x 0.889 mm transaxially and 1.084 mm axially.

The full width at half maximum (FWHM) and full width at tenth maximum (FHTM) in two transverse directions ($x$ and $y$) and in the axial direction ($z$) was calculated for each point source image by interpolation of the point spread profile. Summation of the profiles from two adjacent slices was done prior to measuring the FWHM and FWTM according to the method recommended by NEMA (Daube-Witherspoon et al., 2002; National Electrical Manufacturers Association, 2007).

#### 4.1.4.3 Sensitivity Performance Measurement

Sensitivity of the simulated scanner was measured using an adaptation of the NEMA method for sensitivity measurement of PET systems. A line source containing 2.0 MBq of activity was simulated, with diameter 1.0 mm and length 70 cm. No attenuating material (except the detectors) was included in the simulation. An acquisition of 60 seconds duration was simulated with the line source placed parallel to the axial ($z$) direction and centred axially and transaxially in the scanner. A second acquisition was simulated with the line source displaced 10 cm in the transaxial ($x$) direction. Source decay was included in the simulation with a half-life of 6586 seconds, corresponding to that of the radionuclide fluorine-18. A minimum total of $5 \times 10^5$ prompt coincidence events were collected during each simulation and the random coincidence rate was <1%.

The NEMA NU 2-2007 standard requires the use of concentric cylindrical metal sleeves, with separate acquisitions performed as the sleeves are progressively added or removed, allowing the effects of attenuation to be fully accounted for by linear regression (Bailey, Jones, & Spinks, 1991). Since it is possible within GATE to simulate a line source entirely free from attenuation, and because the addition of attenuating material increases the execution time of the simulations, the aluminium sleeves were not included in the simulation,

and the sensitivity was measured directly from the line source simulation with no attenuating material between the source and the scanner.

#### 4.1.4.4 Scatter Fraction Performance Measurement

Scatter fraction of the simulated scanner was measured using an adaptation of the NEMA method for scatter fraction measurements of PET systems. A line source was simulated containing 1.0 MBq activity, of diameter 3.2 mm and length 70 cm. The line source was embedded in a polyethylene cylinder of diameter 20 cm and length 70 cm and positioned parallel to the phantom axis 4.5 cm off-centre. The polyethylene phantom and line source were positioned in the transaxial centre of the scanner, oriented parallel to the long axis ($z$) of the scanner and centred axially. The rate of random coincidences was <1%. The global scatter fraction ($SF$) was calculated as follows:

$$SF = \frac{S}{T + S} \tag{17}$$

where $S$ is the total number of scattered events, and $T$ is the total number of true events.

The NEMA scatter analysis method, which estimates the scatter contributions to each projection profile and slice by extrapolating the scatter 'tails' across the region of the line source, was not employed here due to the practical difficulties in obtaining a sufficiently long simulated acquisition time with the scatter phantom. Instead, global scatter within the trimmed sinograms (28 cm transaxial FOV) was obtained from a relatively short simulated acquisition containing a total of $2 \times 10^6$ prompt coincidences. The scattered events were identified directly in GATE as non-random coincidence events originating from photons that had undergone one or more scattering interactions within the phantom, and were therefore considered to be an entirely accurate measure of the global scatter.

#### 4.1.4.5 Count Rate Performance Measurements

Counting rate performance parameters were measured by extending the scatter fraction method above (4.1.5.3) in a manner similar to the NEMA method for measuring count rate performance. Twenty-eight simulations were carried out with different source activities in the polyethylene scatter phantom, ranging from 1 MBq to 990 MBq, corresponding to a range of phantom activity concentrations from 0.045 kBq/mL to 45 kBq/mL. A minimum total of $9 \times 10^5$ prompt coincidence events were collected during each simulation. Total scattered coincidence events were identified directly in GATE as for the

scatter fraction measurement described above (4.1.4.4) and total random coincidence events were estimated using the delayed coincidence timing window. The rate of collection for true, random and scattered coincidence events was calculated for each phantom activity concentration. The noise equivalent count rate was calculated for each phantom activity concentration as recommended in the NEMA protocol:

$$NECR = \frac{R_{trues}^2}{R_{trues} + R_{scatter} + k.R_{randoms}} \tag{18}$$

where $R_{subscript}$ refers to the corresponding true, random or scattered count rates, and $k$ is a parameter taking a value of 1 if a noiseless randoms correction method is used, or a value of 2 if a noisy estimate of the randoms is used for data correction.

## 4.1.5 Results

### 4.1.5.1 Spatial Resolution

Sample images reconstructed from the point source simulation, with corresponding axial and transaxial profiles are shown below in Figure 4.1.

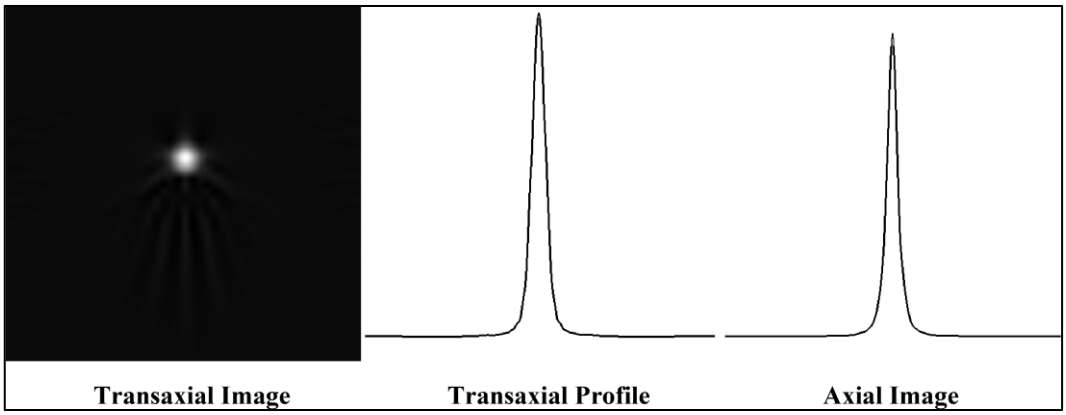


Figure 4.1. Reconstructed image of point source (1 cm radial offset, 0 cm axial offset), with corresponding transaxial profile and axial profile. Image is magnified by a factor of 2.5 for display.

The results of the spatial resolution measurements for the simulated PET scanner are presented below in Table 4.4.

Table 4.4. Spatial resolution results for each source position.

| **Source position (*x*cm,*y*cm,*z*cm)** | **Tangential FWHM (mm)** | **Tangential FWTM (mm)** | **Radial FWHM (mm)** | **Radial FWTM (mm)** | **Axial FWHM (mm)** | **Axial FWTM (mm)** |
|---|---|---|---|---|---|---|
| (0,1,0) | 5.23 | 10.39 | 5.84 | 11.68 | 5.14 | 9.03 |
| (0,1,4) | 5.26 | 10.46 | 5.89 | 11.93 | 5.80 | 10.35 |
| (0,10,0) | 5.35 | 10.22 | 5.49 | 9.91 | 5.97 | 11.48 |
| (0,10,4) | 5.31 | 10.10 | 5.58 | 10.33 | 6.79 | 10.88 |
| (10,0,0) | 5.35 | 10.25 | 5.50 | 9.91 | 5.97 | 11.49 |
| (10,0,4) | 5.34 | 10.14 | 5.76 | 10.85 | 6.71 | 9.88 |

Averaged results for radial, tangential and axial resolution are presented in Table 4.5 below.

Table 4.5. Summary of spatial resolution results.

| | | |
|---|---|---|
| Average tangential FWHM at 1 cm (mm) | 5.25 | |
| Average radial FWHM at 1 cm (mm) | 5.86 | Average at 1 cm = 5.56 |
| Average tangential FWHM at 10 cm (mm) | 5.34 | |
| Average radial FWHM at 10 cm (mm) | 5.58 | Average at 10 cm = 5.46 |
| Average axial FWHM (mm) | 6.06 | |

#### 4.1.5.2 Sensitivity

Results from the sensitivity measurement of the simulated scanner are presented below in Table 4.6.

Table 4.6. Sensitivity results. No attenuating material was included around the simulated line source.

| **0 cm offset** | **10 cm offset** |
|---|---|
| Prompts = 734 539 | Prompts = 770 984 |
| Delayed events = 5277 | Delayed events = 5204 |
| True coincidences = 729 262 | True coincidences = 765 780 |
| Acquisition time = 60s | Acquisition time = 60s |
| Source activity (30s decay) = 1.99979 MBq | Source activity (30s decay) = 1.99979 MBq |
| *Sensitivity = 6.08 kcps/MBq* | *Sensitivity = 6.38 kcps/MBq* |

#### 4.1.5.3 Scatter Fraction

The scatter fraction of the simulated scanner was measured to be 36.8%. A total of 719 341 out of $1.95644 \times 10^6$ prompt coincidences were identified during the simulation as having undergone one or more scattering interactions prior to detection. The random coincidence rate was estimated at 0.35% of the total prompt rate, and was ignored for this calculation.

#### 4.1.5.4 Count Rate Performance

The count rate performance results are plotted below in Figure 4.2. Figure 4.3 shows the same data limited to phantom concentrations below 10 kBq/mL. Within the range of phantom activities studied, the count rate response of the simulated scanner did not reach a peak before the highest activity concentration studied (45 kBq/mL); therefore the peak count rates occur at this concentration for all curves. Figure 4.4 shows count rate performance data for three of the commercial systems described above, for comparison.

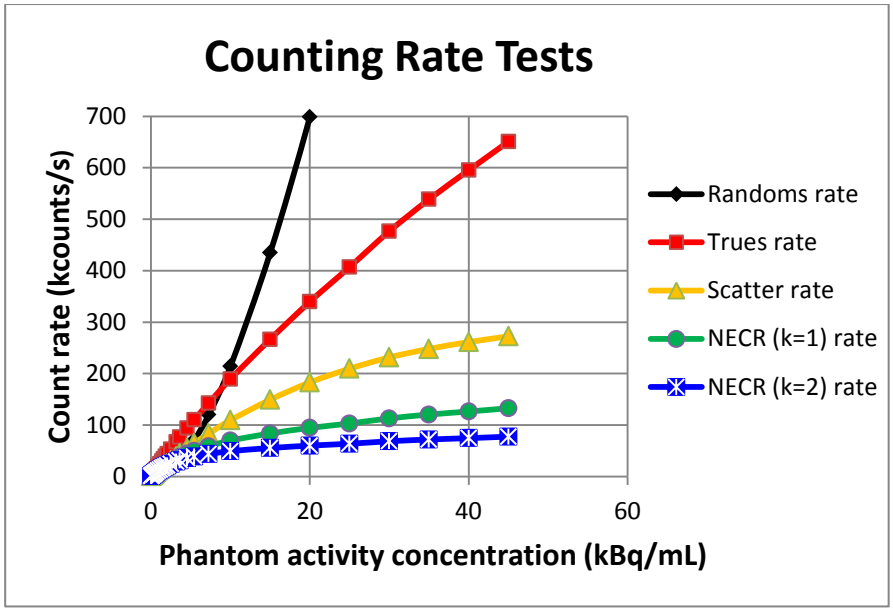


Figure 4.2. Counting rate test results. Noise equivalent count rate (NECR) is shown for k=1 which corresponds to a noiseless randoms correction, and k=2 which corresponds to a noisy randoms correction. The count rate scale (y-axis) is limited to a maximum of 700kcounts/s to allow better appreciation of the curves.

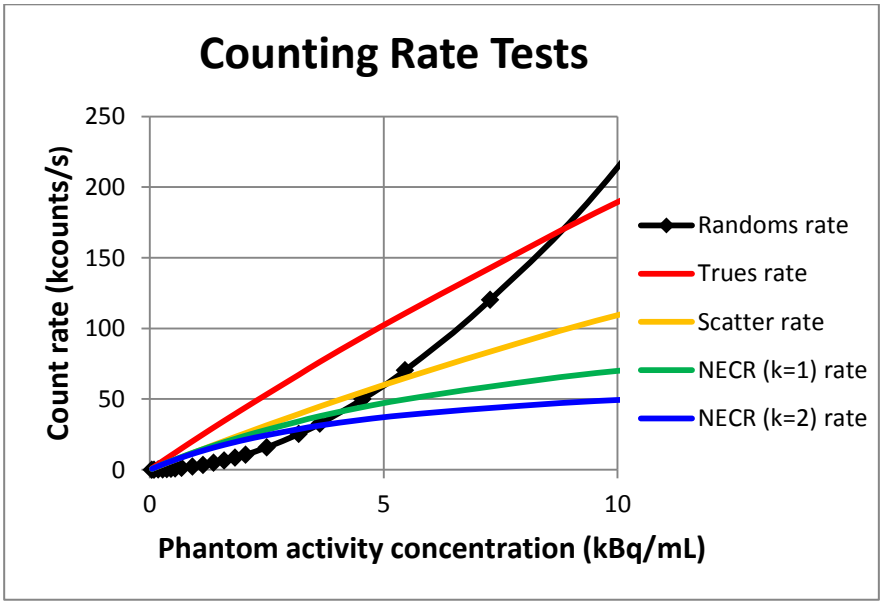


Figure 4.3. Counting rate test results for phantom activity concentration up to 10 kBq/mL only.

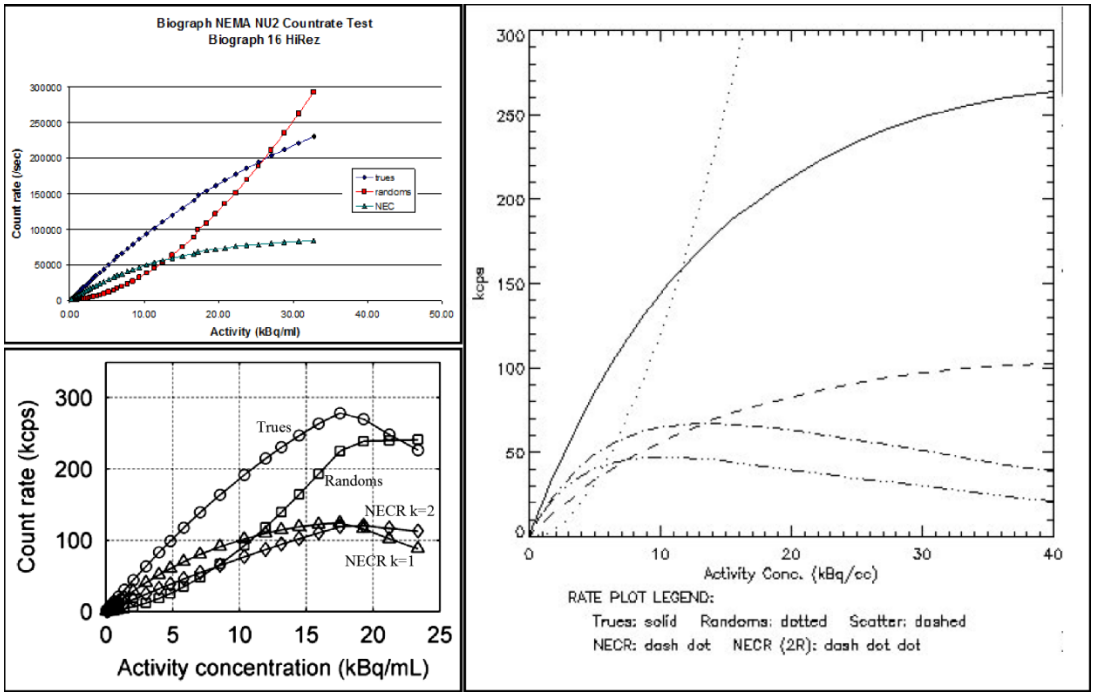


Figure 4.4. Counting rate performance data for the Siemens Biograph 16 HI REZ (top left), Philips Gemini TF (bottom left) and the GE Discovery STE (right). Data for the Siemens and GE systems courtesy of Dr Roger Fulton, University of Sydney. Data for Philips system from (Surti et al., 2007).

### 4.1.6 Discussion

Spatial resolution of the simulated scanner was measured at 5.56 mm FWHM at 1 cm radial offset and 5.46 mm FWHM at 10 cm radial offset. Axial resolution was slightly higher (worse) at 6.06 mm. Although the 10 cm offset resolution is generally expected to be worse than at 1 cm due to parallax effect, this was not evident with these data, however the tangential component of the resolution was slightly worse at 10 cm as expected.

Scatter fraction and sensitivity were measured using a modification of the NEMA NU-2 2007 protocols that enabled the measurements to be made with greater computational efficiency in GATE. The concentric aluminium sleeves normally used during the measurement of absolute sensitivity were not included in the simulation, and the method of calculating scatter fraction was simplified to take advantage of the information about scatter that is available during a GATE simulation. The NEMA recommended methods are intended to overcome the confounding effects of source attenuation and the difficulties inherent in measuring scattered events in real-world PET systems, however these effects may be accounted for exactly within GATE, allowing both the direct measurement of sensitivity free of attenuation effects, and direct access to information about scattered events that is not easily obtainable in reality.

Counting rate performance tests of the simulated scanner produced count rate curves that differ from those of real-world systems at very high counting rates. The dead-time model specified in the GATE simulation was ‘paralysable’ however the parameters were not rigorously validated against any real-world system. The results obtained suggest that, at very high counting rates, the simulated PET system either did not behave in the expected paralysable manner, or that it did not reach saturation before the highest phantom activity concentration investigated (45 kBq/mL). Peak counting rate values therefore correspond to 45 kBq/mL for all curves (the highest activity concentration studied), indicating that the actual peak was not reached during the simulations.

Random coincidence rates also tended to increase more rapidly on the simulated scanner as activity concentration increased. This effect is likely due to the absence of any shielding material in the scanner model causing an increased exposure of the detectors to out-of-filed activity from the 70 cm long scatter phantom. This shortcoming in the modelled scanner is considered to be acceptable for the purposes of brain phantom simulations, where no out-of-field activity is simulated.

Despite the above deviations from the real-world systems, for phantom activity concentrations under 10 kBq/mL the true coincidence and NECR curves are comparable in appearance and scale to those of the real-world systems listed in Table 4.1 (see Figure 4.4). This includes the range of tissue activity concentration expected from [$^{11}$C]-PK11195 brain studies. Therefore a realistic count rate response may be expected from the simulated scanner at activity concentrations under about 10 kBq/mL, and where high levels of out-of-field activity is not included in the simulation. For simulations in which realistic count rate response is desired at activity concentrations above about 10 kBq/mL, or for imaging scenarios in which out-of-field activity is expected to be high, then more accurate modelling of dead-time and axial shielding are required than that implemented here.

Intrinsic radioactivity due to the presence of lutetium-176 in the LSO detectors was not included in this model. Lutetium-176 undergoes radioactive decay and emits a beta particle with a mean energy of 420 keV, and three gamma photons with energies 88 keV, 202 keV and 307 keV, causing an intrinsic background singles counting rate and potentially a background coincidence rate, depending on the energy threshold settings used (Yamamoto, Horii, Hurutani, Matsumoto, & Senda, 2005). Intrinsic activity produces a constant background singles count rate of approximately 850 kcps on the Biograph 16 HI-REZ

(Brambilla et al., 2005), which is considered insignificant at high source activity concentrations, but causes an increase in the random to true coincidences ratio at very low activity concentrations. Although information in the literature is limited, there is some evidence that the detrimental effect on low activity neurological PET studies is minimal. A simulation study investigating the impact of lutetium-176 background on low count rate scans, estimated the minimum concentration at which a 4:1 contrast lesion may be detected at ≈0.148 kBq/mL on a Siemens Biograph 6 scanner, for a 5 minute acquisition time (Karakatsanis & Nikita, 2008). The authors reported only a minor improvement in minimum detectable activity when the lutetium-176 was removed from the simulated scanner. Interestingly, this minimum activity concentration is approximately half the lowest expected concentration for [$^{11}$C]-PK11195 in normal grey matter at 60 minutes post injection (0.36 kBq/mL).

Key performance characteristics of the simulated PET scanner are summarised in Figure 4.5, along with the performance characteristics of the real-world PET scanners listed in Table 4.1.

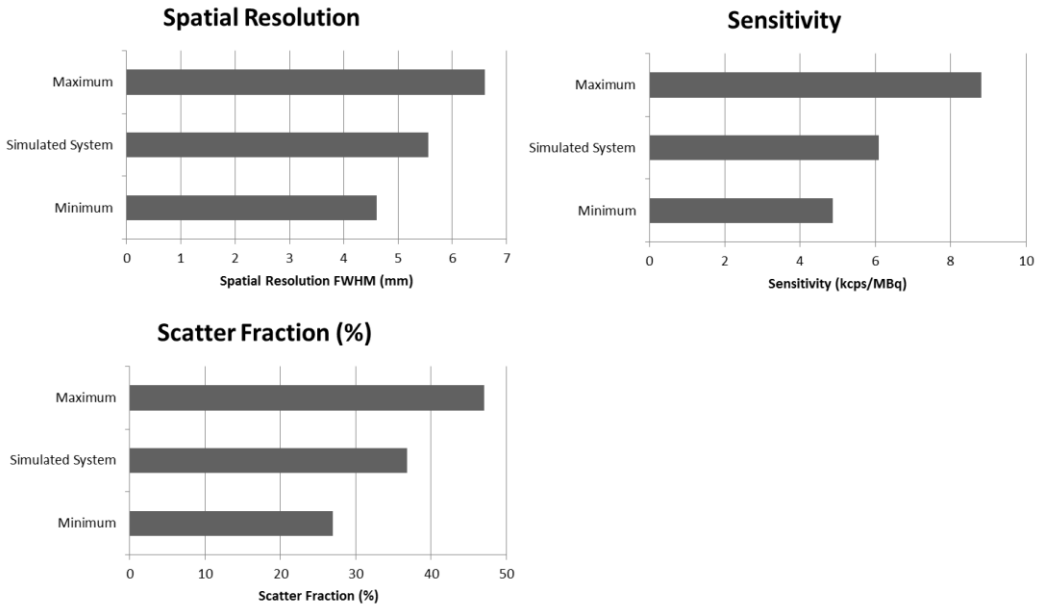


Figure 4.5. Comparison of key performance characteristics of the simulated scanner and the corresponding characteristics of the Siemens Biograph 16 HI-REZ (Brambilla et al., 2005), Siemens Biograph Accel (Erdi et al., 2004), Philips Gemini TF (Surti et al., 2007) and GE Discovery STE (Teräs et al., 2007). Spatial resolution quoted is the average transaxial FWHM at 1 cm radial distance from the centre. Sensitivity quoted is at 0 cm offset from centre.

Overall, the performance of the simulated PET scanner is in broad agreement with the performance of contemporary clinical PET systems, at least in terms of spatial resolution,

sensitivity and scatter fraction. Compared to the Siemens Biograph system (after which the event processing electronics and detector block configurations were modelled), the spatial resolution of the simulated system is slightly worse (5.56 mm versus 4.61 mm) and the sensitivity is slightly better (6.08 kcps/MBq versus 4.87 kcps/MBq). This can probably be attributed to the different geometry of the simulated scanner, which had slightly larger inter-detector gaps, slightly longer axial FOV and smaller inter-block gaps compared to the Biograph 16. In addition, the detectors in the simulated scanner were arranged in a cylindrical array (as are the detectors in the Philips and GE scanners included for comparison) and did not model the inward-facing end blocks of the Biograph 16. This deviation from the real-world system was done in order to simplify the image reconstruction and detector normalization procedures. Given that the overall aim was to closely match the performance of current generation PET scanners, without specific reference to an individual scanner model, then these differences are considered acceptable.

### 4.1.7 Conclusions

A PET scanner system was simulated using the GATE Monte Carlo software package that matched the performance of current generation PET scanners in terms of spatial resolution, sensitivity and scatter fraction. Counting rate performance was also in broad agreement with current generation PET systems at low activity concentrations. The simulated scanner described here produces PET scan data with similar statistical properties to commercial PET systems in current clinical use. For simulations requiring realistic count rate data at activity concentrations above about 10 kBq/mL, or for simulations including high levels of activity outside the field-of-view, then a more accurate dead-time and axial shielding model is required than the one implemented here. Intrinsic radioactivity from lutetium-176 was not included in the model.

## 4.2 Estimation of Image Signal-to-Noise Ratio for TSPO PET Radiotracers Using GATE

### 4.2.1 Introduction

In 2.6.3 the limitations of [$^{11}$C]-PK11195, a PET radiotracer used to image neuroinflammation, were discussed. Accurate and precise quantification of the PET data for this tracer has proven challenging due to a combination of adverse tracer properties and the ubiquitous and sparse distribution of TSPO in the normal brain. New radiotracers for the

TSPO are under development in an attempt to address some of the well documented shortcomings of the tracer $^{11}$C-PK11195: specifically tracers with higher levels of brain tissue uptake and lower non-specific uptake are sought in order to reduce image noise and allow more accurate and precise measurements of neuroinflammation.

This chapter describes how the PET simulation tools developed and validated in Chapter 3 were employed to measure the image variance and signal-to-noise ratio of a typical [$^{11}$C]-PK11195 dynamic PET scan of the human brain.

### 4.2.2 Aim

The overall aim was to measure the image voxel variance and relative noise (coefficient of variation) for each frame in a simulated dynamic [$^{11}$C]-PK11195 PET scan of the human brain, using standard data correction and image reconstruction methods.

### 4.2.3 Equipment

The following equipment was used during this study:

- High performance computer cluster, running the GATE Monte Carlo simulation software (described in 3.3).
- PET scanner description macro in GATE (described in 4.1)
- IDL, version 8.1 (Exelis Visual Information Solutions, Boulder, Colorado)
- PMOD, version 3.17 (PMOD Technologies Ltd., Zurich, Switzerland)

### 4.2.4 Method

#### 4.2.4.1 Generation of a Tissue Time-Activity Curve and Arterial Plasma Input Function for [$^{11}$C]-PK11195

A representative time-activity curve (TAC) for [$^{11}$C]-R-PK11195 in normal human grey matter was obtained from published literature (Kropholler et al., 2005). A plasma input function was also obtained from the same source, as well as a value for plasma to whole blood activity ratio of 1.55, which was reported to be constant for the duration of the scan. A curve describing the plasma parent radioligand fraction for [$^{11}$C]-R-PK11195 in humans was obtained from another source by the same principle author (Kropholler et al., 2009). As is usually the case, correction for radioactive decay had been made on all published curves.

Curve data points were sampled by careful manual measurement of a high-quality reproduction of the published curve images. Tissue TAC data points were time-sampled from the published curve according to a 24 frame dynamic scan schedule similar to the one used by Kropholler et al. in their study. Plasma input function data points were sampled at 10 approximately equally spaced intervals during the initial peak from 0-2 minutes, and another 10 equally spaced intervals from 2-60 minutes. Parent radioligand fraction data points were sampled at 8 points from 0-60minutes. Both plasma curves (plasma input function and parent radioligand fraction) were fitted with a tri-exponential function and resampled to 720 x 5 second samples. All curves were synchronised to the same start time. A whole blood radioactivity curve was then calculated from the plasma input function, parent fraction curve and the plasma to whole blood activity ratio.

A survey of the published literature on human brain imaging with [$^{11}$C]-R-PK11195 revealed a median (reported) injected dose of 370 MBq, and a range of 222 MBq to 888 MBq. The plasma input function and grey matter TAC described above were based on published data for a reported injected dose of 224 MBq, therefore both these curves, and the whole blood TAC, were scaled by a factor of 1.65 to normalise the curves to the median injected dose of 370 MBq (370/224 ≈ 1.65).

The grey matter TAC, arterial plasma input function and whole blood TAC were all loaded into the PMOD kinetic modelling software package (version 3.17). The data were fitted to a compartmental model with one plasma compartment, two-tissue compartments and four rate constants. Fitted parameters were in very close agreement to those obtained by Kropholler et al. (2005), and were: $K_1 = 0.05$, $k_2 = 0.15$, $k_3 = 0.06$, $k_4 = 0.04$. The tissue blood volume fraction was set to a value of 7.1% according to the findings of Kropholler et al. (2005). Residual error between the fitted curve and the original tissue TAC ranged from $-4\text{x}10^{-11}$ to $+1\text{x}10^{-10}$ over the duration of the scan, and visual inspection confirmed that the compartmental model provided a good fit to the data. All curves described above are plotted in Figure 4.6 to Figure 4.8.

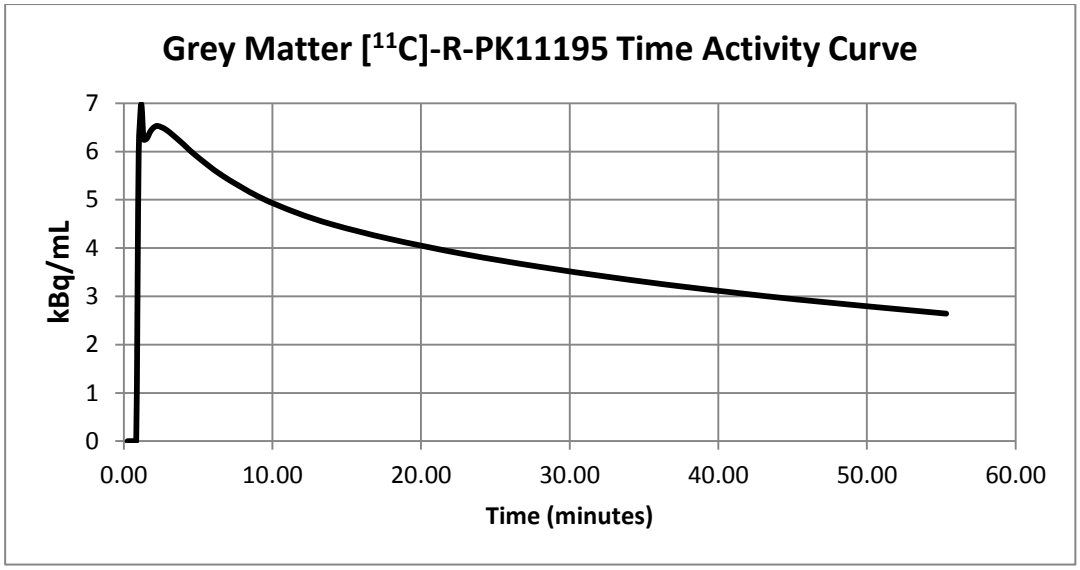


Figure 4.6. Normal human grey matter time-activity curve for [$^{11}$C]-R-PK11195. Curve is decay corrected and fitted to a two-tissue compartment, four-parameter compartmental model using the plasma input function and whole blood curves below. Data from Kropholler et al. (2005).

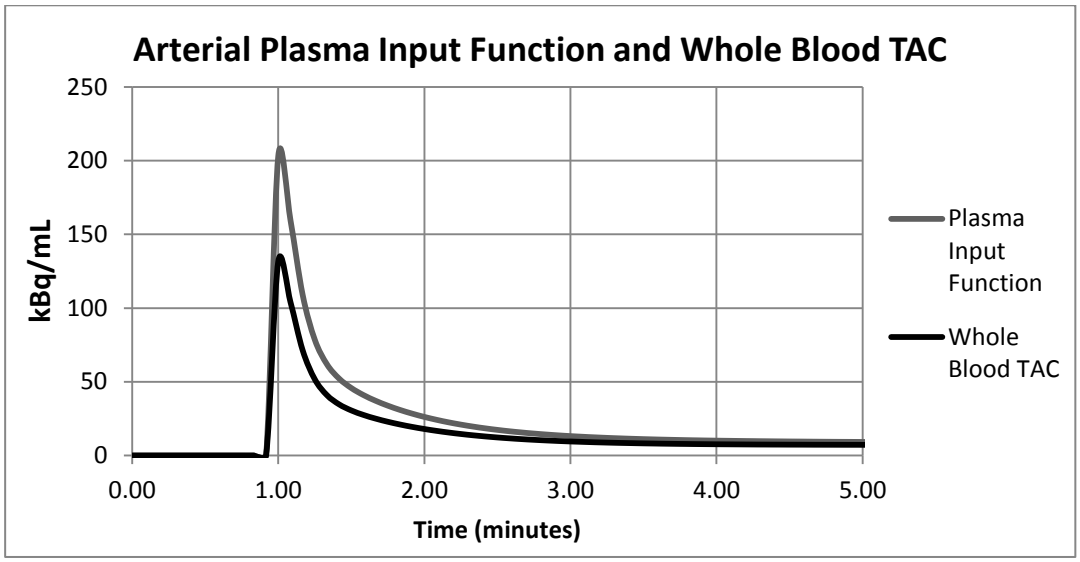


Figure 4.7. Plasma arterial input function and whole blood time-activity curve for [$^{11}$C]-R-PK11195 in humans. For clarity, only data from time 0-5 minutes are displayed. Data from Kropholler et al. (2005).

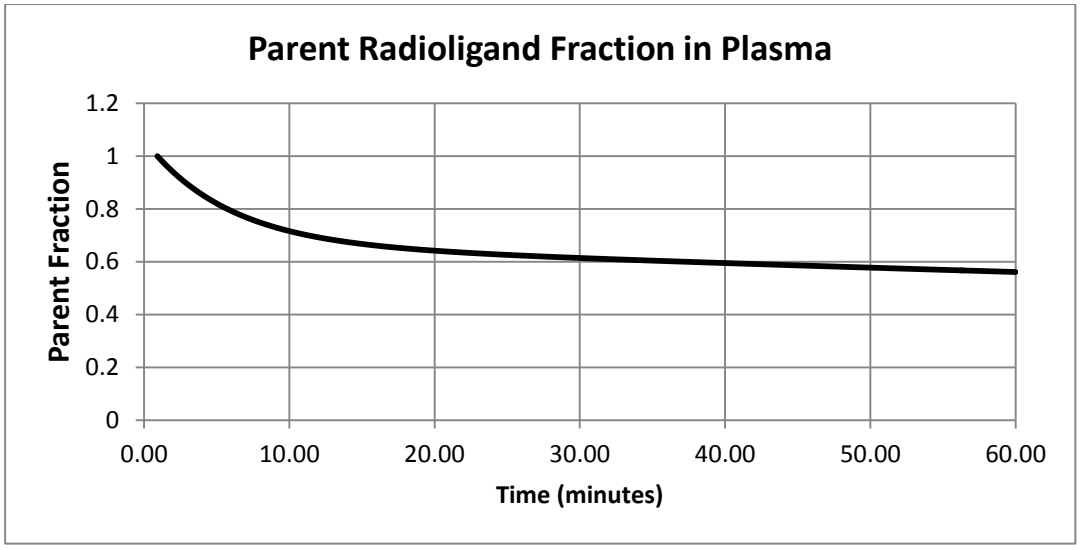


Figure 4.8. Parent fraction in plasma for [$^{11}$C]-R-PK11195 in humans. Data from Kropholler et al. (2009).

#### 4.2.4.2 Simulation of 40 Independent Noise Realisations of a Dynamic [$^{11}$C]-PK11195 PET Scan

A separate emission phantom was constructed for each of the 24 frames of the dynamic scan, using the digital anatomical model described in 3.1.2.3. The volume of each voxel was 1mm$^3$. The value for voxels designated as 'grey matter' (fractional volume of 99.34%) and 'glial matter' (fractional volume of 0.66%) within each phantom was set to the corresponding grey matter tissue TAC concentration for each frame (see Figure 4.6), with a carbon-11 radioactive decay factor to mid-frame time applied. Autoradiographic analysis has shown that [$^3$H]-R-PK11195 binding to normal white matter is approximately half that of normal grey matter (Banati et al., 2000), therefore the tissue concentration of white matter voxels at each frame was set to half the value of the grey matter voxels. All other soft tissue voxels were set to the same concentration as white matter for each frame. The skull was set to zero activity concentration.

Although considerable care was taken to ensure the grey and white matter voxels were set to a realistic activity concentration for [$^{11}$C]-PK11195, less reliable data were available for determining the appropriate concentration for the surrounding non-brain tissues. The following PET images (Figure 4.9 and Figure 4.10) taken from recently published papers demonstrate the uptake of the TSPO tracers [$^{11}$C]-R-PK11195 and [$^{11}$C]-DPA713 in normal human subjects. In the case of PK11195, no regions of conspicuously high uptake in the tissues immediately surrounding the brain are evident. A very small volume of increased uptake in the facial and ocular region is seen on the [$^{11}$C]-DPA713 images and minimal or

absent uptake is evident in the skull. These findings suggest that setting the non-brain voxels of the digital phantom to white matter equivalent uptake values, and setting the skull voxels to zero uptake, is broadly consistent with the known uptake of TSPO tracers in the human head. Since these tissue classes are of no direct interest in the present study, such approximation of their uptake was considered reasonable.

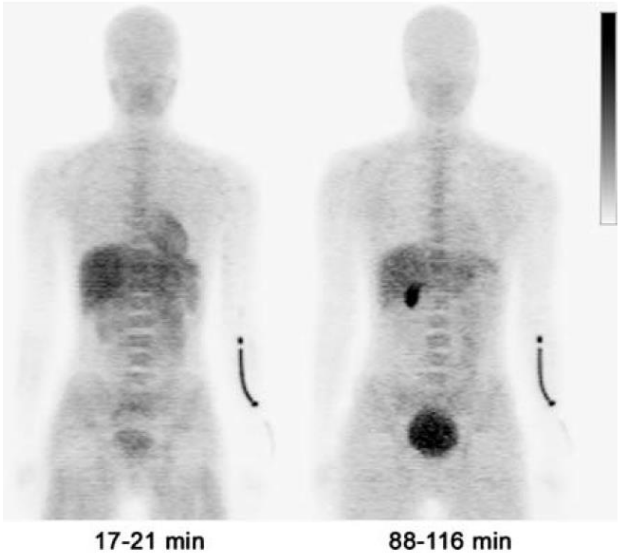


Figure 4.9. Whole body summed coronal images of a healthy male subject, following injection of [$^{11}$C]-R-PK11195 for a dosimetry study (Hirvonen et al., 2010).

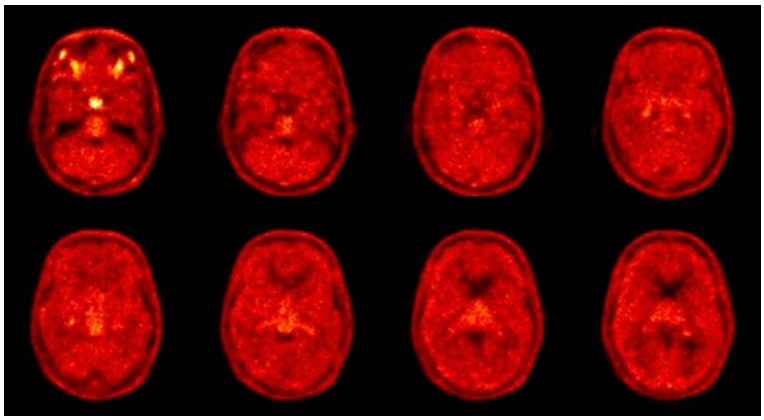

Figure 4.10. Transverse image slices through the lower and middle brain taken following injection of the TSPO radiotracer [$^{11}$C]-DPA713 (Endres et al., 2009).

The attenuation phantom, described in 3.1.2.3.1 was used for all simulations. This phantom models the physical properties, relevant to photon interactions with matter, for all tissues in the digital model. Voxels of the attenuation phantom measured 2 mm x 2 mm x 2 mm and included 3 tissue classes: skull, water and air. The PET scanner model described in 4.1, and in appendix 0 and 7.9, was used for all simulations.

Simulation of the full dynamic [$^{11}$C]-PK11195 scan was carried out using the above 24 emission phantoms and the attenuation phantom. Photon tracking was carried out using the fictitious interactions algorithm, with a gamma energy discard setting of 100 keV. A back-to-back photon pair was simulated for each radioactive decay, assuming a branching ratio equal to 1. Because radioactive decay to each frame was already included in the emission phantoms, no radioactive decay was simulated. Frame duration for the dynamic scan was set (in seconds): 30, 15, 10, 10, 10, 10, 15, 15, 15, 15, 55, 60, 60, 150, 150, 150, 150, 300, 300, 300, 300, 300, 600 and 600.

A total of 40 independent simulations were run, with unique random number generator seeds, for each of the dynamic [$^{11}$C]-PK11195 scan frames. Data output for each frame included a 3D sinogram for prompt, scattered and delayed coincidence events. Simulation of all 40 dynamic scans took 23 days, and produced approximately 350 Gbytes of sinogram output data.

To enable further study of the signal-to-noise properties of novel TSPO radiotracers with higher brain uptake than [$^{11}$C]-PK11195, the above series of simulations were repeated with all phantom activity concentrations increased by a factor of 2. Simulation of all 40 dynamic scans took 48 days to run. In order to extend the range of count densities studied, an additional 30 independent simulations were carried out for an extra frame containing very high total counts, with a grey matter concentration of 5 kBq/mL and an acquisition time of 600 seconds.

To allow a more detailed investigation into the image noise properties of the simulated PET data, an additional 150 independent simulations were run for frame 10 only of the dynamic [$^{11}$C]-PK11195 scan. Frame 10 was chosen because its particular combination of tracer concentration (≈5 kBq/mL) and frame duration (15 seconds) allowed a high number of simulations to be run within a short period of time (≈24 hours for 150 realisations).

#### 4.2.4.3 Validation of Accurate and Realistic Corrections for Non-Uniform Detector Efficiency, Scatter, Randoms and Attenuation

Quantitative PET requires that the data be corrected for the effects of non-uniform detector efficiency, scatter, random events and attenuation, and these corrections are applied in routine clinical practice. Many of these effects are also present in the simulated data. The following sections describe the correction methods employed for the simulated [$^{11}$C]-PK11195 dynamic PET data.

#### 4.2.4.3.1 Detector Normalization

Non-uniform detector efficiency occurs in real-world systems for reasons such as variations and drift in the event processing electronics, variation in crystal composition and mechanical misalignments- none of which apply to the simulated PET scanner in GATE. Geometric effects, whereby line-of-response (LOR) efficiency varies depending on the location of the LOR within the scanner field-of-view and the angles at which photons are incident on the detectors are still applicable to the GATE simulated data. Correction for non-uniform geometric efficiency may be done by direct measurement of all LORs using a uniform source of radioactivity and a long acquisition time, or by summing separate measurements of the various components of LOR sensitivity (Badawi, Lodge, & Marsden, 1998; Badawi & Marsden, 1999). The aim in both cases is to arrive at a measure of relative efficiency for each LOR that is accurate and contains minimal noise.

A simulation was run to directly measure the distribution of relative LOR sensitivity within the simulated PET scanner. To achieve uniform irradiation of all LORs relevant to the brain scan simulations, a cylindrical source measuring 40 cm diameter and 17 cm length, with activity placed around the outer surface only, was implemented in GATE. A total radioactivity 1.0 MBq source activity was specified and no attenuating media were simulated. The plane source was positioned in the centre of the simulated PET scanner, parallel to the long axis and centred axially. The random coincidence rate during simulation was estimated at ≈0.6% of the total coincidence rate. A simulated acquisition time of 70 hours was achieved in 7 days, yielding an average of 27.3 coincidence events per LOR after summing the output sinograms. The relative noise level in the sinograms was deemed to be too high for the purposes of direct normalization of LORs. Sample sinograms from this simulation are presented in Figure 4.11.

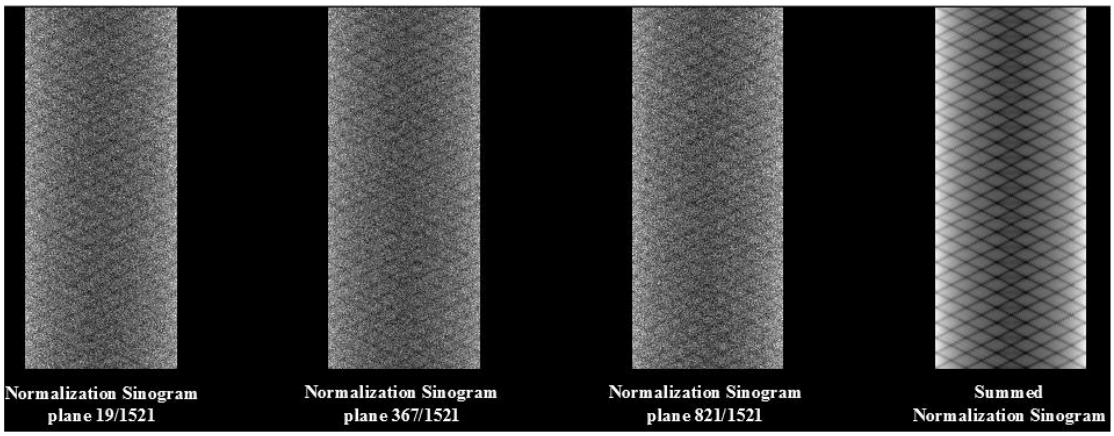


Figure 4.11. Normalization sinograms from a simulation of a uniform cylindrical plane source. Three arbitrarily selected sinogram planes (left). Sinograms were summed over all 1521 planes to yield a high count sinogram for normalization (far right). All sinograms displayed relative to own maximum.

Manipulation and display of the 3D sinogram sensitivity data was carried within IDL and the following empirical observations were made concerning the appearance of the data: that the relative distribution of counts within each sinogram plane follows a pattern that is visually very similar across all 1521 sinograms. Geometric variations are mainly due to LOR position across the transaxial FOV and crystal position within each block, and these factors are expected to be very similar for every sinogram, including the oblique sinograms. This was confirmed by visual assessment of each sinogram plane. The periodic pattern of count variation within each sinogram appeared independent of axial position or segment. Therefore, to increase the count density of the correction matrix and minimise relative noise, all 1521 sinogram planes were summed into a single sinogram. This single high-count sinogram contained an average of $4.15 \times 10^4$ counts per element, with a minimum of $2.72 \times 10^4$ counts and a maximum of $5.99 \times 10^4$ counts. A sensitivity correction factor map was then calculated by dividing each sinogram element into the maximum value ($5.99 \times 10^4$). A sensitivity correction factor for each sinogram plane was then calculated from the in-plane total counts of the original 1521 sinograms. In this way, an essentially noiseless sensitivity normalization map for each 3D sinogram element was produced, relative to the most sensitive element. The minimum correction factor was therefore unity, while the maximum correction factor across the entire 3D sinogram was 3.1897.

#### 4.2.4.3.2 Scatter Correction

Correction for scattered coincidences in PET requires an accurate estimate of the relative contribution of scatter to each LOR. Scattered events are distributed broadly across the entire sinogram, with slightly higher concentration in the vicinity of the object being

scanned. Scattered events can be distinguished (and rejected) on the basis of their energy, however the limited energy resolution of the radiation detectors used in PET means that scatter fractions are usually well above 15% (Meikle & Badawi, 2003). Correction methods generally aim to estimate the scatter contribution as accurately as possible before subtracting the estimate from the data (Phelps, 2006). Because scatter is not measured directly (as is often the case for randoms and attenuation), the propagation of random noise is not usually an issue for most scatter correction methods.

When a GATE Monte Carlo simulation is run, information about the origin of every detected coincidence event is available, including whether or not any scattering took place prior to detection. Thus the scatter sinogram output from each simulation contains 'perfect' information about scatter for every LOR. Subtraction of this scatter data from the prompt sinograms would be a simple and effective method of scatter correction, but would be highly unrealistic with respect to real-world scatter correction methods, where such information is not directly available.

To address this issue, while still taking advantage of the information available from GATE for scatter correction, the 3D scatter output sinograms were averaged over all 40 independent simulations for each frame of the dynamic [$^{11}$C]-PK11195 PET simulation, yielding an estimate of scatter for each frame. The projection profiles were then convolved with a 1-dimensional Gaussian filter kernel (FWHM=3.5 cm) to smooth the scatter estimates and reduce noise. An accurate and low noise estimate of scatter for each frame was then produced by scaling the smoothed scatter sinogram to the (known) total number of scattered events in each frame. Representative scatter profiles and smoothed sinograms produced using this method are displayed in Figure 4.12. During the above processing steps, it was observed that the scatter sinograms were affected by detector sensitivity variation with a pattern similar to that observed during the normalization measurements (see 4.2.4.3.1). Smoothing the scatter sinograms with a 3.5 cm Gaussian filter, which was necessary to remove noise and consistent with the low spatial frequency distribution of scattered events, also distorted the sensitivity variations. Normalization was therefore applied to the scatter sinograms before the smoothing step.

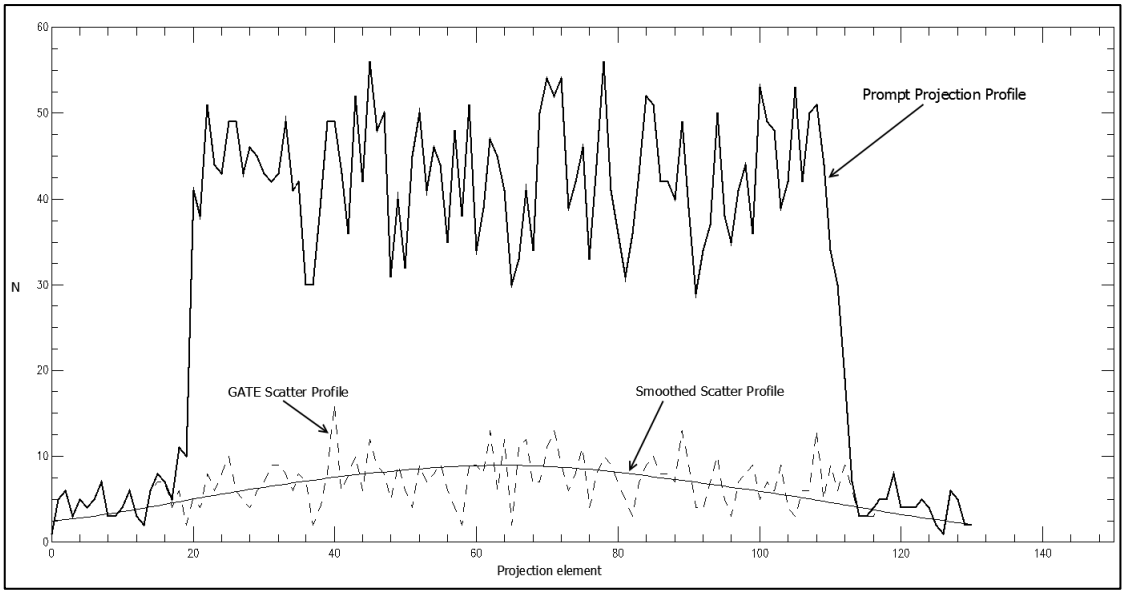


Figure 4.12. Projection profiles through a high-count simulated sinogram, showing prompt coincidence profile, actual scattered events identified during the simulation (dashed line) and a smoothed scatter estimate used for scatter correction.

#### 4.2.4.3.3 Random Event Correction

Random coincidence events are estimated during the simulations via a delayed event coincidence analysis, analogous to the delayed event method used on many PET systems. Delayed events are saved to a separate 3D sinogram for each frame of the simulation. To limit noise propagation during the randoms subtraction, and to approximate the real-world situation where a smooth singles-based randoms estimate is subtracted, a processing method similar to that employed for scatter correction was used: 3D delayed event output sinograms were summed over all 40 independent simulations for each frame of the dynamic simulation, yielding a high-count 3D randoms estimate for each frame. Scaling of the summed sinogram to the total number of random coincidences in each frame was performed prior to subtraction. Random coincidences were generally low for the [$^{11}$C]-PK11195 dynamic simulations, reflecting the low uptake of this tracer in the brain. For example, the peak random:true ratio for the [$^{11}$C]-PK11195 dynamic scan occurred in frame 5 and was ≈ 3.8%.

#### 4.2.4.3.4 Attenuation Correction

Attenuation, in which a 511 keV photon is either absorbed or scattered out of the field-of-view by the object being scanned, causes a reduction in sensitivity for any LOR passing through that object. Attenuation along a LOR can be measured, and a correction factor applied to each LOR, using a variety of techniques. Traditionally in PET, a radioactive

transmission source external to the patient has been used to provide attenuation measurements for each LOR, with reference to a 'blank' transmission scan taken with nothing in the field-of-view. While potentially very accurate, external source methods may propagate a large amount of noise into the PET data, and various methods of smoothing and segmentation are employed to reduce this noise before applying the correction (Meikle, Dahlbom, & Cherry, 1993). More recently, hybrid PET/CT scanners have made use of the computed tomography scan to provide attenuation measurements through the object being scanned, that are essentially noise-free relative to the PET data (Beyer et al., 2000; Zaidi et al., 2007).

For the purpose of attenuation correction of the simulated PET data, attenuation through the digital phantom was measured using a simulated transmission scan. The cylindrical plane source used for the LOR sensitivity normalization simulation served as the transmission source. The same simulation described in 4.2.4.3.1 was run again, with the addition of the digital attenuation phantom in the scanner. Only true coincidence events were collected from the simulation, thereby eliminating scattered coincidences from the data and ensuring that the resulting attenuation measurements represent 'narrow-beam' geometry (Podgorsak, 2006). A total of $5.2 \times 10^8$ true coincidence events were collected during the transmission simulation. The original detector normalization simulation described in 4.2.4.3.1 provided the blank scan necessary for calculating the attenuation along each LOR.

A region of interest was manually selected on the transmission and blank sinograms that included only LORs that were outside the head region, and this was used to normalise the transmission data to the same count level as the blank data. A 3x3x3 averaging kernel was convolved with the transmission and blank sinograms to reduce noise. Integral attenuation coefficient sinograms were then generated as the natural logarithm of the blank/transmission ratio sinograms. Images of the linear attenuation coefficients ($\mu$) within the digital phantom were then reconstructed using the 3D reprojection algorithm in STIR with a ramp filter.

Segmentation of the $\mu$ images into 3 tissue classes (air, soft tissue and bone) was carried out using an adaptation of the method of Meikle et al. (1993). Attenuation coefficients for each tissue class (determined previously, see appendix 7.11) were assigned, and a 2-D Gaussian filter (FWHM = 6 mm) was applied to match the resolution of the segmented images to the PET system. These steps are illustrated below in Figure 4.13. For a detailed

description of the determination of appropriate $\mu$ values for skull and soft tissue, see appendix 7.11.

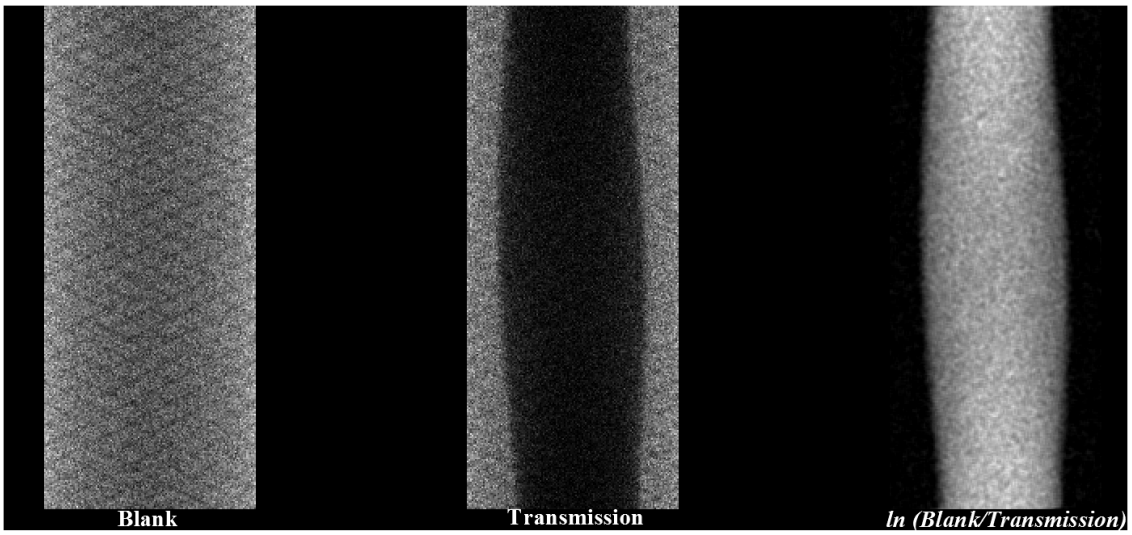


Figure 4.13. Representative attenuation correction sinograms (middle of head phantom).

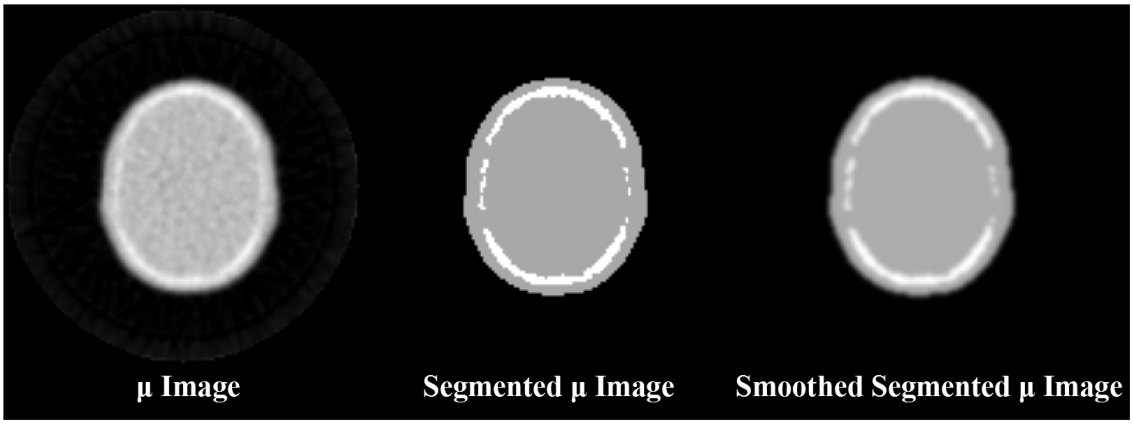


Figure 4.14. Representative images of the digital phantom's linear attenuation coefficients (μ), corresponding to the axial position of the above sinograms. Reconstructed μ image (left) was segmented into 3 voxel classes: air, soft tissue and skull bone (middle image). Smoothing with a 6 mm FWHM Gaussian filter was performed (right).

All correction methods described above apply specifically to the [$^{11}$C]-PK11195 dynamic simulations described in 4.2.4.2. The same attenuation phantom was used in the same position for each simulation; therefore a single transmission scan and attenuation map was required. Corrections to the sinogram data ($S$) were applied prior to image reconstruction using the following algorithm:

$$S_{corrected} = S_{atten\_factor}\left(S_{normalization}\left(S_{prompt} - S_{random}\right) - S_{scatter}\right) \quad (19)$$

Due to the heavy smoothing applied to the scatter sinograms (see 4.2.4.3.2), and the observation of LOR sensitivity variation in the original scatter sinograms, sensitivity normalization was applied to the scatter sinogram prior to smoothing. Therefore normalization is only applied to the randoms-corrected data in the above algorithm. All corrections were applied to the original 3D sinograms without axial or angular compression.

#### 4.2.4.4 Image Reconstruction

All images were reconstructed using the Software for Tomographic Image Reconstruction (STIR), version 2.1. Prior to reconstruction, all pre-corrected 3D sinograms were re-binned to 2D sinograms using the single slice re-binning algorithm (Daube-Witherspoon & Muehllehner, 1987) as implemented in STIR. The 24 most oblique sinogram segments (out of a total of 77 segments) were discarded from the data during re-binning, which corresponded to approximately 11% of total collected counts. Images were reconstructed using the filtered back projection algorithm, with a Hanning filter window, set to a cut-off frequency of 0.7 x Nyquist. Axial sensitivity correction was then applied using correction factors derived from the validation simulation described below (see 4.2.4.5). Finally, a correction for radioactive decay to mid frame time and a quantitative calibration factor (also derived from the validation simulation) was applied. An additional reconstruction was performed using the Ordered Subset Expectation Maximization (OS-EM) algorithm, with 12 iterations and 3 subsets. Post filtering in the form of a 2D Gaussian filter (FWHM=3 mm) was applied to the OS-EM reconstructions. Selection of appropriate OS-EM parameters for the simulated PET data is discussed in appendix 7.13.

#### 4.2.4.5 Validation of Data Correction Methods

Validation of the above data correction methods for brain PET simulations was carried out using a long duration simulated brain scan, with uniform distribution of activity within all tissues of the digital phantom. The activity concentration within each tissue voxel was set to 0.2599 kBq/mL, and an acquisition time of 1700 minutes (28.3 hours) was simulated. No radioactive decay was included in this simulation. Data were corrected and reconstructed according to the methods described. Figure 4.15 below shows the representative images with and without the corrections applied.

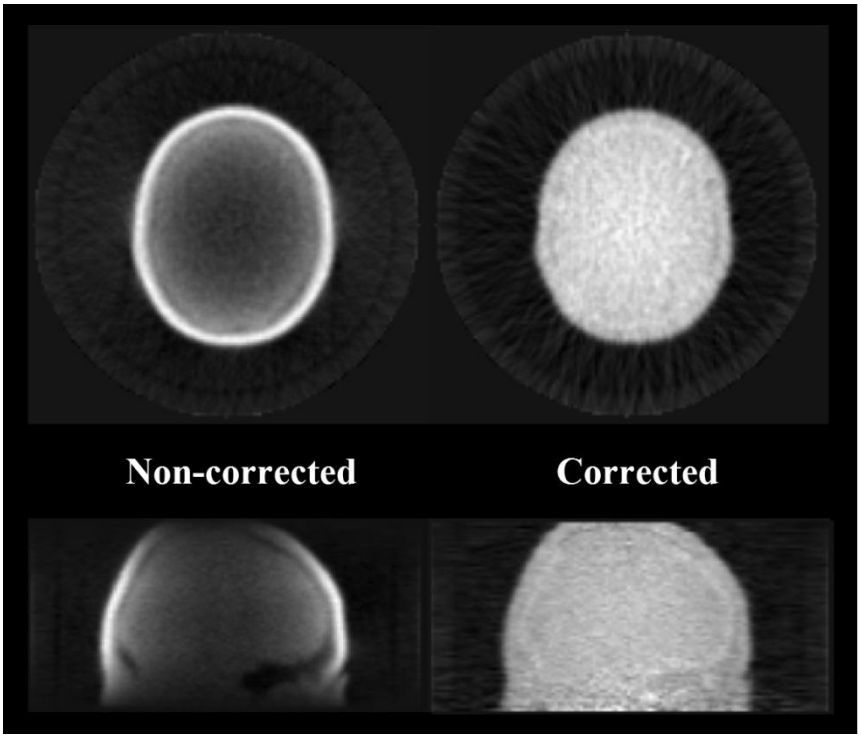


Figure 4.15. Corrected and non-corrected PET images from a long duration/high count simulation. Activity was distributed uniformly through the phantom tissues. Attenuation correction artefacts adjacent to skull regions are evident in the corrected images, otherwise the distribution of counts appears uniform. The count density in the present simulation data is significantly higher than that anticipated for the dynamic [11C]-PK11195 PET simulations.

The corrected image data show a uniform distribution of counts within the soft tissues of the head. Some subtle artefacts at the skull/soft-tissue interfaces are evident on this high-count simulation, most likely due to inaccuracies introduced during the segmentation operation of the attenuation correction. Empirical adjustments were made to the assigned skull attenuation coefficient and smoothing filter parameters to reduce this artefact to the level seen in Figure 4.15. Considering the much lower count density of the dynamic PK11195 data compared with other radioligand studies, and the absence of any direct interest in the skull region in this work, these artefacts were considered acceptable.

Axial sensitivity was measured by summing the total counts for a central region-of-interest within each slice. The axial sensitivity, relative to the most sensitive slice, was plotted (see Figure 4.16).

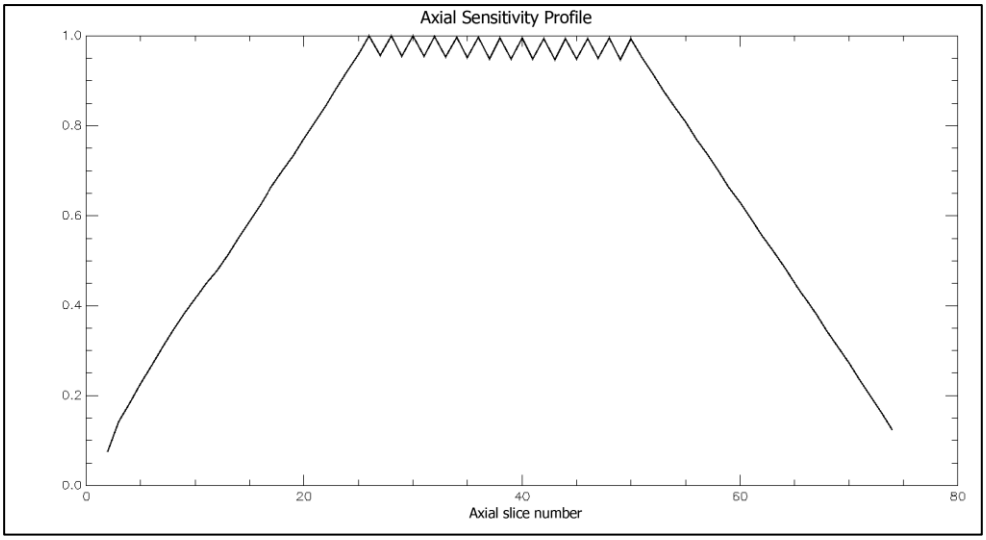


Figure 4.16. Profile of relative axial sensitivity of the simulated PET scanner, after 2D re-binning, and discarding of the most oblique sinogram segments.

## 4.2.5 Data Analysis

### 4.2.5.1 Region of Interest Definition and Estimation of Partial Volume Errors

Partial volume errors (PVE) result from the limited spatial resolution of the PET scanner. Structures that are smaller than about 3x the system FWHM in one or more dimensions are subject to underestimation of their true radioactivity concentration due to blurring of the signal to surrounding regions. Small regions may also be subject to significant 'spill-in' of counts from surrounding activity. Because the grey and white matter regions of the brain contain many volumes that are small relative to the spatial resolution of PET scanners, significant PVE is expected in brain PET studies.

In order to estimate the level of PVE present in the simulated data, and to select voxels for analysis that were (relatively) free from PVE, two separate PET simulations were run using the digital emission phantom and PET scanner model used in all dynamic PET simulations. In the first simulation, only the grey matter voxels contained activity, and in the second simulation, only the white matter voxels contained activity. Activity concentration was set to 10 kBq/mL in both cases. To avoid the complicating effects of scatter and attenuation, no attenuating material was included in the simulations. A long acquisition was simulated to minimise the relative noise in the data. Images were reconstructed using the same filtered back projection algorithm and filter as used for all dynamic PET simulations.

Voxels in the grey matter image that were ≥90% of the expected 'true' value (i.e. ≥ 9 kBq/mL) and did not overlap with voxels from the white matter image that were >10% of the expected value (i.e. ≥ 1kBq/mL) were identified as containing minimal PVE. A total of 7833 'low PVE' grey matter voxels (≈53.64 mL total volume) were identified in this way, located mainly in the posterior and inferior regions of the brain corresponding to the temporal lobes, cerebellar cortex and occipital lobes. Spill in from other non-brain tissues (muscle, skin, fat, skull, CSF) were not considered in this analysis, because these tissues constitute a smaller fraction of the tissue voxels in this phantom (see Figure 3.1), and are either located at a distance from the brain (skin and muscle) or do not contain any activity in the simulations (skull and CSF).

Two smaller regions of interest (ROIs) were defined by selecting subsets of the minimal PVE grey matter voxels. One ROI (253 voxels, 1.73 mL) included left and right medial temporal lobes, while the other ROI (78 voxels, 0.534 mL) included a smaller subset of the medial temporal lobe voxels. These ROIs are illustrated in appendix 7.12 and listed in Table 4.7.

Table 4.7. Grey Matter Regions of Interest.

| Location | Total Volume (mL) |
|---|---|
| Medial temporal lobes (bilateral) | 0.534 |
| Medial temporal lobes (bilateral) | 1.73 |
| Grey matter | 53.64 |

#### 4.2.5.2 Calculation of Image Voxel Variance and Coefficient of Variation

Variance ($\sigma^2$) was calculated for each image voxel ($x$) according to the following equation:

$$\sigma^2 = \frac{\sum_{i=1}^{n}(x_i - \bar{x})^2}{n-1} \tag{20}$$

where $n$ = 40 independent noise realisations. Relative noise, measured by the percentage coefficient of variation (%CoV) was calculated for each voxel as:

$$\%CoV = \frac{100\sqrt{\sigma^2}}{\bar{x}} \tag{21}$$

Average grey matter voxel variance and %CoV were calculated from the images for the large grey matter region of interest in Table 4.7.

### 4.2.6 Results

Variance and coefficient of variation images for frame 10 (early short duration frame) and frame 14 (later frame with higher total counts) for the [$^{11}$C]-PK11195 simulation are shown below in Figure 4.17 to Figure 4.24. A bright line of 1-pixel width was observed running the axial length of the images. The source of this artefact was not clear, however a similar artefact was reported in the STIR user's manual (Thielemans, K. et al., STIR User's Guide Version 2.1) and is therefore thought to be an image reconstruction artefact. Switching between different projector algorithms did not affect the appearance of the artefact. Since it appears to affect only one pixel in each slice, and the ROIs used for analysis did not intersect it, the artefact was ignored.

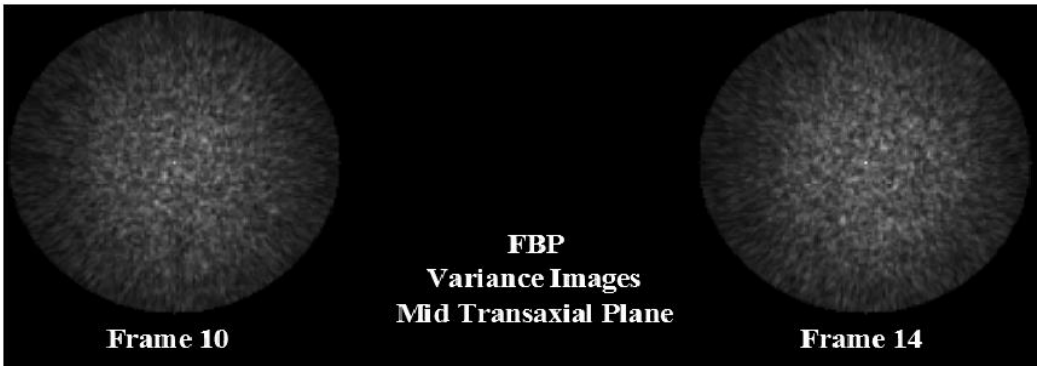


Figure 4.17. Variance images for filtered back projection reconstruction, one transaxial slice. Each image is scaled to own maximum.

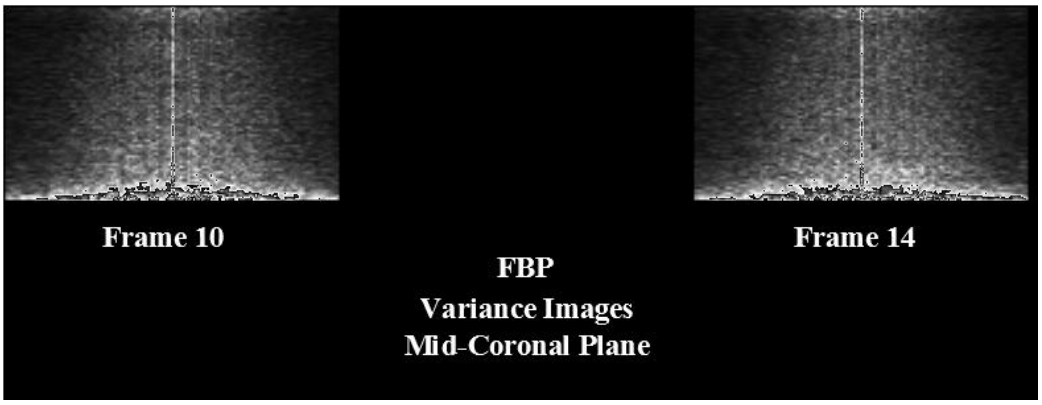


Figure 4.18. Variance images for filtered back projection reconstruction, one coronal slice. Images displayed to same scale as corresponding transaxial slice above.

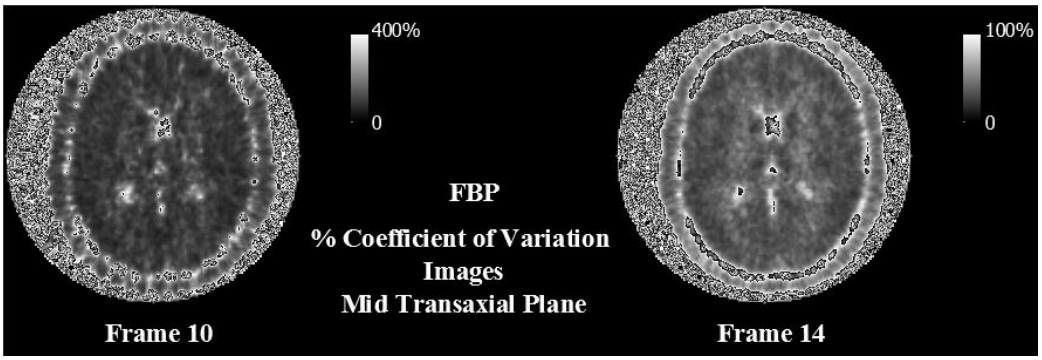


Figure 4.19. Percentage coefficient of variation images for filtered back projection reconstruction, one transaxial slice.

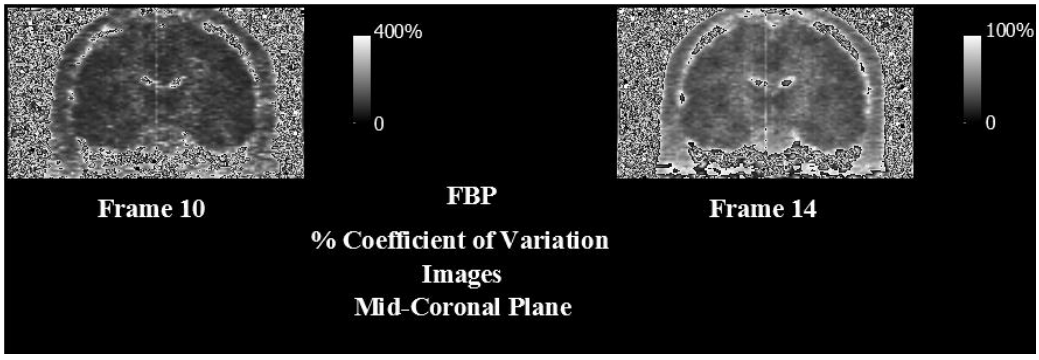


Figure 4.20. Percentage coefficient of variation images for filtered back projection reconstruction, one coronal slice.

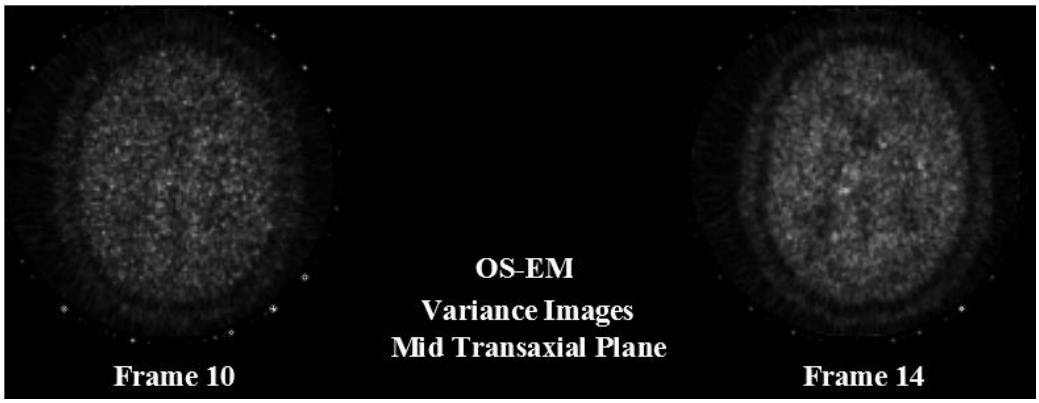


Figure 4.21. Variance images for OS-EM reconstruction, one transaxial slice. Each image is scaled to own maximum.


Figure 4.22. Variance images for OS-EM reconstruction, one coronal slice. Images displayed to same scale as corresponding transaxial slice above.

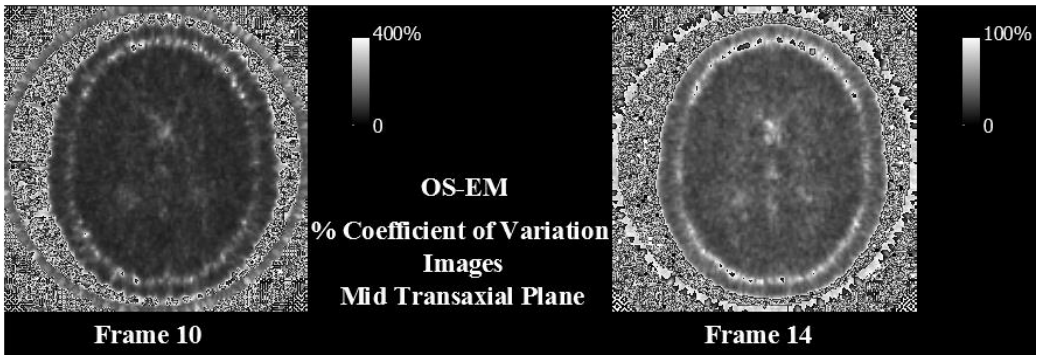


Figure 4.23. Percentage coefficient of variation images for OS-EM reconstruction, one transaxial slice.

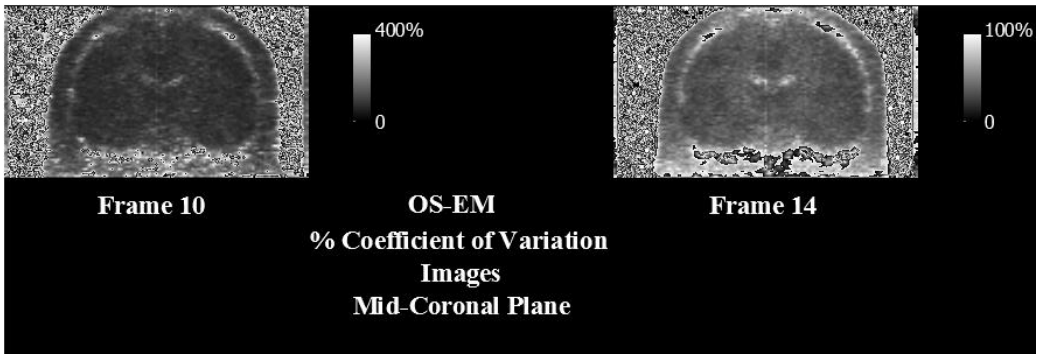


Figure 4.24. Percentage coefficient of variation images for OS-EM reconstruction, one coronal slice.

Relative voxel noise, measured by the percentage coefficient of variation (%CoV) averaged over all grey matter voxels, ranged from 123% (frame 4, PK11195 dynamic simulation, FBP) to 24% (frame 18, double PK11195 uptake simulation, FBP). Relative noise is plotted against frame number for both dynamic simulations (PK11195 and double uptake PK11195) and both reconstruction algorithms (FBP, OS-EM) in Figure 4.25 below.

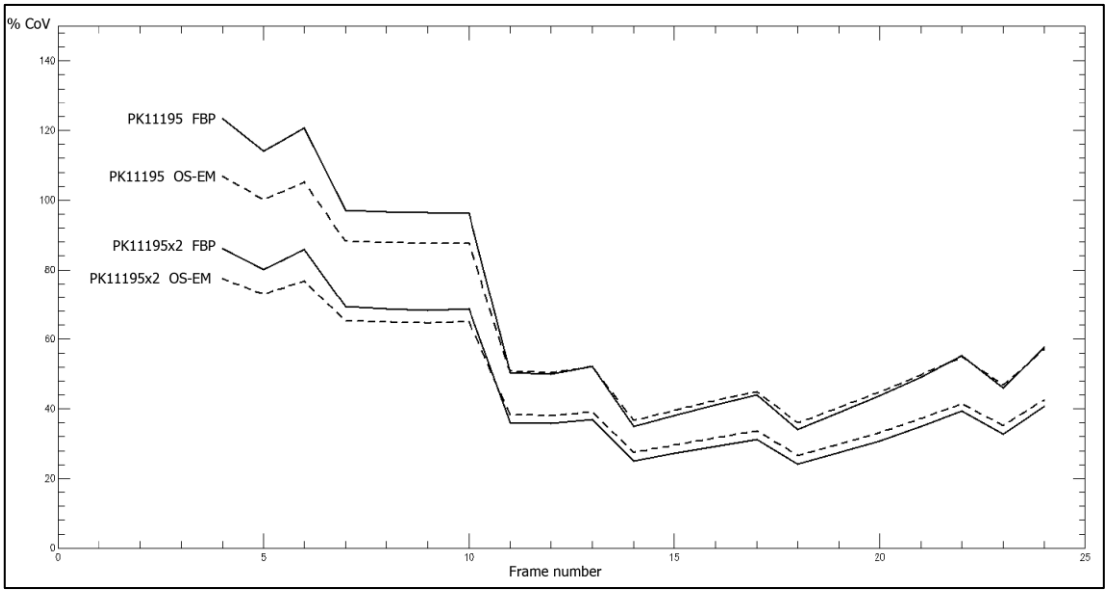


Figure 4.25. Relative noise (% coefficient of variation) averaged over grey matter voxels for both dynamic scan simulations and both reconstruction algorithms.

Relative noise was highest in the early frames, which were of shorter duration. As frame duration increased, %CoV decreased. Radioactive decay of carbon-11 caused an increase in relative noise towards the end of the simulations. OS-EM yielded lower relative noise during the early frames compared to FBP, however this advantage appears to be lost in higher count frames, where OS-EM produced slightly higher CoV than FBP from frame 11 onwards.

Relative noise for the two ROIs (small and medium size) is plotted against frame number in Figure 4.26 and Figure 4.27. These data represent the uncertainty associated with ROI averaged counts, and as such are expected to contain much lower levels of relative noise than that found at the voxel level. Again, OS-EM produced lower CoV at low count frames, but not at higher count frames.

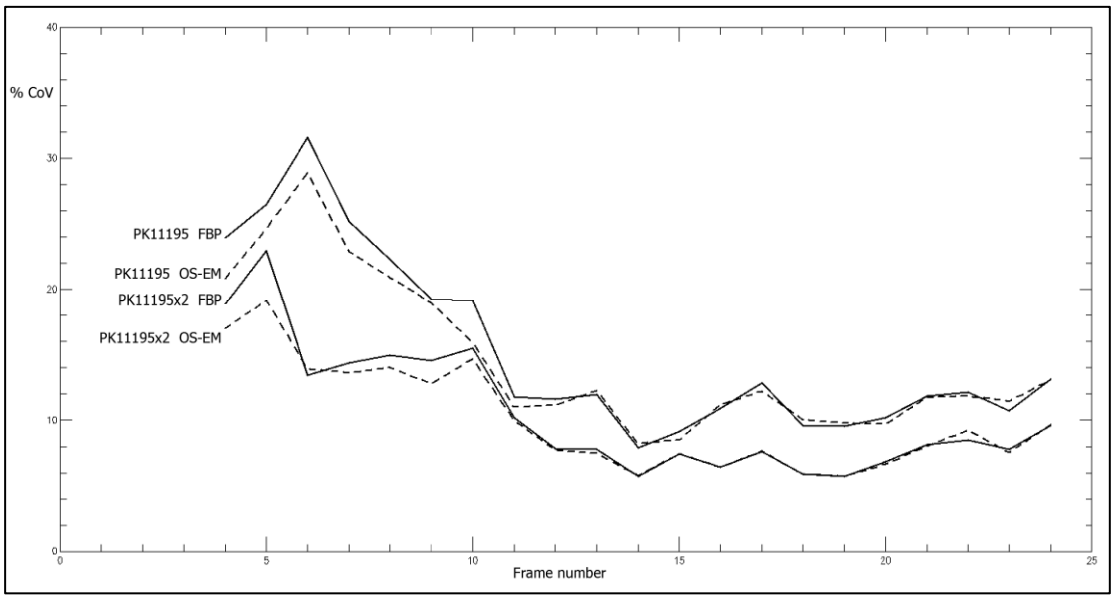


Figure 4.26. Relative noise (% coefficient of variation) for a small (0.53mL) temporal lobe grey matter ROI, for both dynamic scan simulations and both reconstruction algorithms.

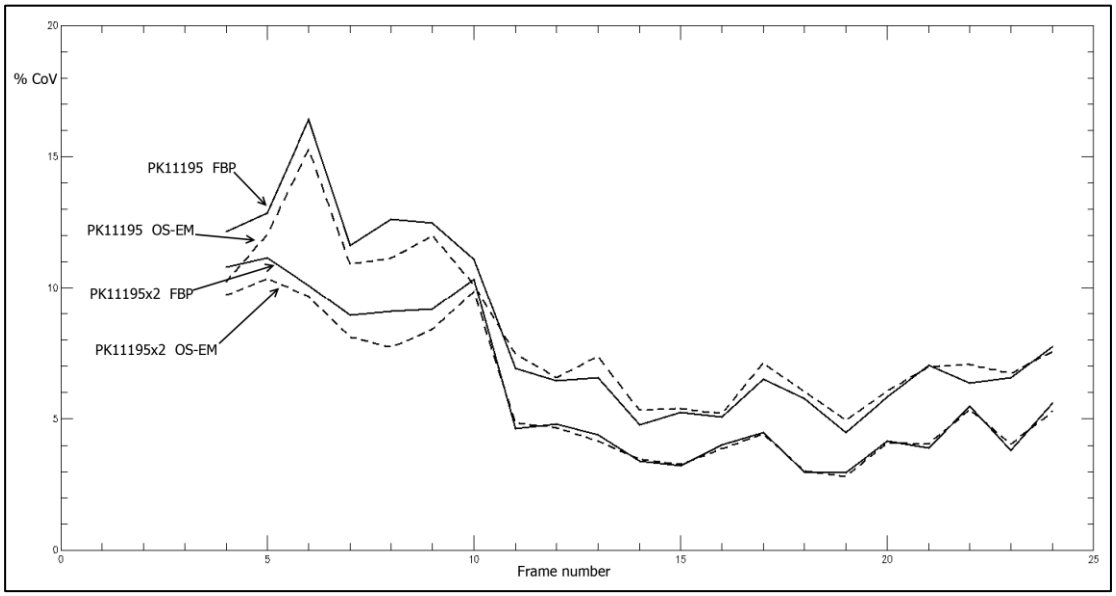


Figure 4.27. Relative noise (% coefficient of variation) for a medium (0.1.73mL) temporal lobe grey matter ROI, for both dynamic scan simulations and both reconstruction algorithms.

### 4.2.7 Discussion

Image noise in PET depends fundamentally upon the number of counts collected during the scan. However, various other factors, such as the corrupting influence of attenuation, scatter and random coincidences, image reconstruction algorithm and associated parameters and the use of smoothing filters, also strongly influence the final relative and absolute noise levels within each image voxel. Relative noise tends to increase towards the centre of the image, due to the effects of attenuation. Voxel variance may be correlated with the regional distribution of activity, depending upon which reconstruction algorithm is used. The results of this investigation are consistent with these known properties of image noise in PET.

Relative voxel noise, expressed as average voxel %CoV, ranged from 24% to 123%. As expected, this relative noise was highest during the short duration frames at the start of the dynamic scan, decreasing to a minimum as frame duration increased, then rising again towards the end of the scan due to the combined effects of radioactive decay and clearance of the tracer from the tissues. Image reconstruction also plays an important role in determining the noise properties, with OS-EM yielding lower relative noise than FBP during early low count frames, but offering no apparent advantage at higher count frames. An important difference between OS-EM and FBP is the non-negativity constraint that applies to OS-EM but not to FBP (Hutton et al., 2006), which has been shown to produce a positive bias for very low count data (Rahmim, Cheng, Blinder, Camborde, & Sossi, 2005). This could also affect the measurement of relative noise, and is investigated further in 4.3.

Image variance was closely related to the underlying activity concentration for the OS-EM reconstructions, allowing the distribution of tracer to be distinguished in the variance images. This is consistent with previously reported findings with this algorithm (Nuyts, 2002; Schmidtlein et al., 2010). In contrast, FBP produces much more uniform variance distribution in the transaxial plane, with a slight increase in variance towards the transaxial centre of the scanner. This is also consistent with previously reported findings, and the properties of the FBP algorithm. Coefficient of variation images for the OS-EM algorithm therefore show a more uniform distribution, with the exception of the zero-activity regions (skull and CSF), which have higher relative noise than surrounding regions. Relative noise in the FBP images is inversely related to the tracer distribution: lower uptake regions (white matter, CSF and skull) appear brighter than the higher uptake grey matter.

Coronal images reveal higher variance and relative noise towards the axial edges, consistent with the 3D sensitivity profile for this simulated scanner and the use of sinogram re-binning and 2D reconstruction algorithms.

It is important to note that this study was limited in scope to the particular combination of PET scanner geometry, data processing and reconstruction algorithms used. Although care was taken to model the performance of current generation clinical systems as closely as possible, there are many factors not investigated here that could affect the level and distribution of noise in the final image data. Scanner sensitivity has been identified as a potential area of technological improvement for the next generation of PET tomographs (Eriksson et al., 2005) and at the time of writing there is at least one commercially available whole body PET system with an 21.8 cm axial field of view and substantially better sensitivity than the previous generation system which it replaced (Jakoby, Bercier, Watson, Bendriem, & Townsend, 2009). More sophisticated image reconstruction approaches could also have a substantial effect on the relative image noise. For example algorithms incorporating system point-spread function information into the reconstruction (Panin, Kehren, Michel, & Casey, 2006), have been shown to improve both the spatial resolution and noise properties of the images. Both of these recent advances could be expected to have a positive influence on the noise properties of low count PET studies such as [$^{11}$C]-PK11195. Further research would be needed to clarify this.

Another important limitation of this study was the use of only 40 repeated measures to estimate the noise. Limitations related to the speed of Monte Carlo simulations- 71 days total simulation time for all dynamic scans- as well as data storage- 700 Gbytes of original sinogram data- and image reconstruction requirements, made it impractical to run a greater number of simulations. Therefore the noise estimates may themselves be subject to a certain amount of ‘noise’. Furthermore, the overall aim of this research was to investigate the effects of novel TSPO tracer properties on quantification with kinetic modelling, which could potentially require a new series of noise estimates and dynamic simulations for each tracer studied. This fact motivated further analysis of the noise data collected, with the aim of developing an analytical model that could predict the relative image noise for any likely combination of tracer uptake and acquisition time, with due reference to the limitations discussed in the previous paragraph.

### 4.2.8 Conclusions

A dynamic [$^{11}$C]-PK11195 PET scan, and a dynamic PET scan at twice the tissue radioactivity concentration of [$^{11}$C]-PK11195, was simulated. Image noise (variance and coefficient of variation) was calculated for each voxel, and for two grey matter regions of interest. Relative noise in image voxels ranged from 24% to 123% over the two dynamic simulations. The two reconstruction algorithms studied (2D FBP and 2D OS-EM) yielded differences in relative image noise that was most apparent at low count frames. Spatial distribution of variance and coefficient of variation also differed between the two reconstructions, in a manner consistent with previously published findings.

Variance and coefficient of variation estimates were based on a limited number (40) of independent repeated simulations, and are therefore subject to uncertainty. In the context of estimating the effects of image noise on compartmental modelling parameter estimation, the ability to estimate image noise in dynamic PET acquisitions for a variety of TSPO brain tracers, without the need to perform lengthy simulations for each one, is desirable. Methods that allow estimation of image noise, for a variety of tracer uptake and acquisition durations, using the data from the 40 repeated simulations, require further investigation.

## 4.3 Development and Validation of a Mathematical Model for Image Noise

### 4.3.1 Introduction

In 4.2, Monte Carlo simulations were employed to estimate the image noise in a dynamic [$^{11}$C]-PK11195 PET scan. Variance and coefficient of variation were calculated for voxels and two regions of interest in grey matter. Although this method can provide useful insights into image noise properties, a major limitation is the length of time required to run the simulations- in this instance approximately 10 weeks for two 60 minute dynamic simulations- using a modern computer cluster with 40 cores. The primary interest of this research was to study the effects of image noise on parameter estimation with compartmental modelling, for a variety of tissue activity concentrations and dynamic frame durations. Estimation of image noise using the Monte Carlo approach for every tracer at each frame time would be impractical. Therefore additional methods were required to allow estimation of image noise, using the data obtained so far, for other similar tracers.

Bootstrap resampling methods, whereby a set of pseudo-repeat PET sinograms are derived from either a single noisy dataset, or from a limited number of repeated acquisitions, have been advocated for this purpose (Buvat, Benali, & Di Paola, 2000; Dahlbom, 2002; Haynor & Woods, 1989; Lartizien et al., 2010). These methods are attractive in that they can provide a large number of (pseudo-)repeated PET sinograms from which a highly precise estimation of noise may be calculated. One drawback of the bootstrap approach is the potentially large volume of data that is generated, and the computational burden of performing image reconstructions on each replicate dataset.

On the other hand, analytical models of image noise have been proposed (Budinger et al., 1978) that attempt to relate the relative image noise to the number of collected counts. Analytical models may be criticised on the grounds that they must make assumptions about the source and propagation of noise, including from the reconstruction algorithm. However, unlike other methods that rely on noise estimation from repeated measurements, they have the advantages of being computationally very efficient and requiring negligible data storage. They are also readily applicable to kinetic modelling and parameter estimation tasks: indeed an analytical noise model is often employed for calculating the weighting factors for each point on the tissue time-activity curve during least-squares fitting of kinetic parameters, and to provide an estimate of TAC noise during Monte Carlo simulations of kinetic modelling (Yaqub et al., 2004).

In view of the above limitations, further analysis of the image noise data obtained from the [$^{11}$C]-PK11195 and the 'double uptake' [$^{11}$C]-PK11195 simulations was carried out. It was hypothesised that the very low count rates experienced in the majority of frames would give rise to a relatively linear noise equivalent count rate (NECR) response from the scanner over the expected range of activity concentrations. It was further hypothesised that the image noise at the voxel and region levels could be adequately described by a Gaussian probability density function. If so, then an analytical model could potentially provide a reliable and accurate estimate of image noise, for any combination of tissue activity concentration and acquisition time.

### 4.3.2 Aim

The broad aim of this study was to use the repeated simulation data (see 4.2) to develop and validate an analytical model relating the relative image noise in grey matter

voxels to the grey matter activity concentration and PET acquisition time, for [$^{11}$C]-PK11195 and radiotracers of similar uptake in the brain.

## 4.3.3 Method

### 4.3.3.1 Assessment of Normality of Image Noise

It is usually assumed that the PET image voxel and ROI average values are normally distributed about the 'true' value and are therefore described adequately by a Gaussian probability density function. This might not always be the case, for example very low count image frames reconstructed with conventional OS-EM are known to have a skewed distribution due to the non-negativity constraint of this reconstruction algorithm (Rahmim et al., 2005). This has implications when using a measured or calculated standard deviation ($\sigma$) or coefficient of variation to predict image voxel variation, for example when studying the effects of noise on quantitative compartmental modelling.

To assess the validity of the assumption of normality for the PET data used in this study, skewness and kurtosis of grey matter voxels were calculated for each frame 10 of the $^{11}$C-PK11195 dynamic PET simulation. A larger number of simulation runs (n=191) was performed for frame 10. This was done separately from the (n=40) runs used for calculating the image noise in each frame. Frame 10 represents an early, short duration frame of 15 seconds, from 130 to 145 seconds post injection. The non-decay corrected grey matter voxel concentration of tracer in frame 10 was 5.4 kBq/mL. Frame 10 was chosen because the very low counts were expected to increase the likelihood of observing non-normality in the OS-EM reconstructed images. Also, the low count frame could be simulated in a reasonably short time, allowing a much higher number of noise realisations than was feasible for other frames. Images were reconstructed using both the FBP and OS-EM algorithms, with the same parameters used for the dynamic PK11195 simulation data.

Analysis of normality was carried out by converting each image voxel to a z-score, with respect to its mean value over the 191 noise realisations. Skewness and kurtosis were then calculated for all grey matter voxels, for each frame and for both reconstruction algorithms.

### 4.3.3.2 Fitting an Analytical Model to the Image Noise Data

The relationship between relative image noise, defined as the average coefficient of variation (CoV) of all grey matter voxels, and the grey matter tissue activity concentration

(kBq/mL), was investigated graphically. Because the relative noise also depends upon the frame acquisition time, activity concentration in grey matter was multiplied by the frame duration, yielding a quantity for each frame with units of kBq.s/mL. This quantity could also be interpreted as "nuclear disintegrations per mL of grey matter tissue", and in the absence of significant count rate losses, is expected to be in approximate proportion to the total true coincidence counts collected. The average grey matter CoV was then plotted against the above activity-time quantity for each frame in the simulated PK11195 and double uptake dynamic scans. Curve fitting was then applied to yield a model that predicts image noise, given grey matter activity concentration and frame time.

It is generally accepted that image noise in PET is more closely related to the total noise equivalent counts rather than total true coincidence counts, and that for filtered back projection reconstruction, image noise is proportional to the square root of the NEC (Strother et al., 1990). The NEC takes into account the effects of scatter and random coincidences in increasing the relative noise of the PET data. Since NEC is dependent on the object and the concentration of activity in all tissues (not just in one region), it is not necessarily predictable given only a regional (e.g. grey matter) tissue concentration. Initially, it was assumed that at the low activity concentrations studied, the NECR curve would not deviate significantly from a hypothetical linear (loss-less) count rate response of the scanner. The fitted model therefore did not explicitly take into account the count rate experienced during each frame. In other words, it was assumed that a frame containing $x$ kBq/mL acquired for $y$ seconds would produce the same relative image noise as a frame containing $y$ kBq/mL acquired for $x$ seconds. To investigate the validity of this assumption, the actual NECR curve for the simulated data was measured using the raw output data from each simulated frame, and compared to a hypothetical linear count rate response of the scanner. The effect of incorporating this additional NEC data into the noise model was also investigated.

#### 4.3.3.3 Validation of the Analytical Noise Model for Estimating the Precision of Kinetic Parameters

To assess the performance of the fitted noise model in predicting %CoV, the frame 10 (with $n$=191 realisations) simulated data were analysed and the measured %CoV for the voxels and three ROIs were compared to that predicted by the model equations. The $n$=191 data were acquired separately from the data on which the model is based, but were processed and reconstructed in exactly the same way.

The ultimate purpose of the analytical noise model is to allow an investigation into the effects of changing TSPO tracer uptake in the brain on relative image noise, and subsequent effects on the precision of estimated compartmental kinetic parameters. Therefore, the noise model was applied to the task of estimating the noise-induced variance of compartmental modelling parameters, and its performance was assessed against the original noisy data produced by the GATE simulations.

The noise-free reference grey matter TAC for [$^{11}$C]-PK11195 that was used in the original GATE simulations, with known kinetic parameters, was taken and noise (σ) was calculated for each point using the analytical noise model. The values for σ, and the original noise-free TAC, were read into the PMOD 'Biomedical Image Quantification Software' package (version 3.17, PMOD Technologies, Zurich, Switzerland). Simulations were then run ($n$=40), using the in-built Monte Carlo simulation tool in PMOD and the supplied σ values, to estimate the noise-induced variance of the fitted kinetic parameters. Noise-induced variance was then estimated directly from a TAC of the 40 original GATE simulated [$^{11}$C]-PK11195 noise realisations. Comparison of the kinetic parameter variance produced by the noise model against the original GATE data was made. A two-tissue compartment, four-parameter model was fitted to the TACs using the least squares fitting routine within PMOD. In keeping with the previously published kinetic analysis of this tracer (Kropholler et al., 2005), the $K_1/k_2$ ratio was fixed, and three parameters were fitted: $K_1$, $k_3$ and $k_4$. The above procedures were repeated for FBP and OSEM reconstructed data and their corresponding noise models.

## 4.3.4 Results

### 4.3.4.1 Assessment of Normality of Image Noise

The plots below (Figure 4.28 and Figure 4.29) illustrate the distribution of voxel values for frame 10 of the PK11195 dynamic simulation, for the large number of noise realisations ($n$=191). Voxel deviations from the mean were normalised to the standard deviation (i.e. converted to z-scores). Mean and standard deviation were determined for each voxel from the 191 independent noise realisations.

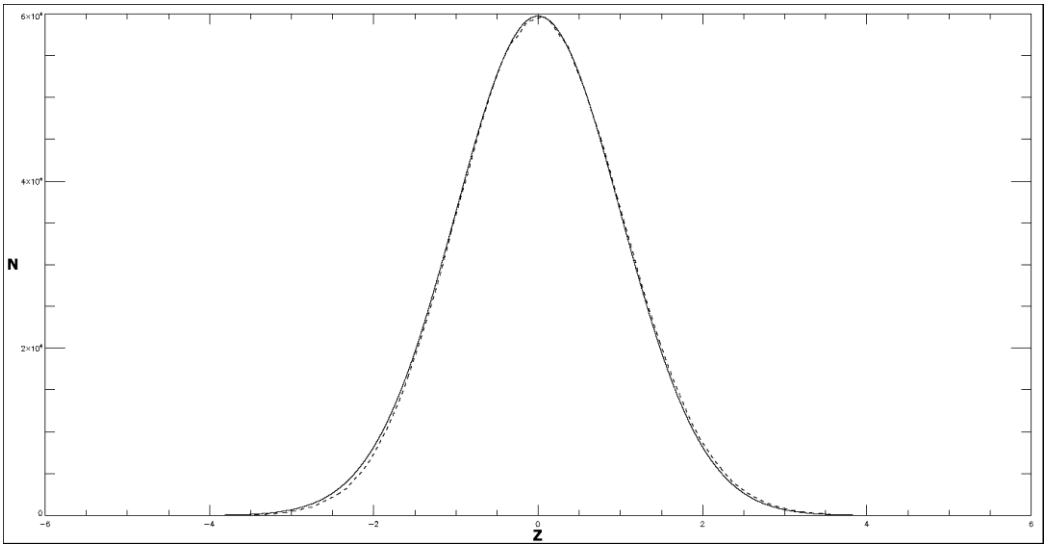


Figure 4.28. Histogram showing the distribution of voxel values (z-scores) for the n=191 frame 10 images, reconstructed using filtered back projection (dashed line). Skewness = 0.059, kurtosis = -0.029. A Gaussian function of the same σ and height is plotted (solid line) for comparison.

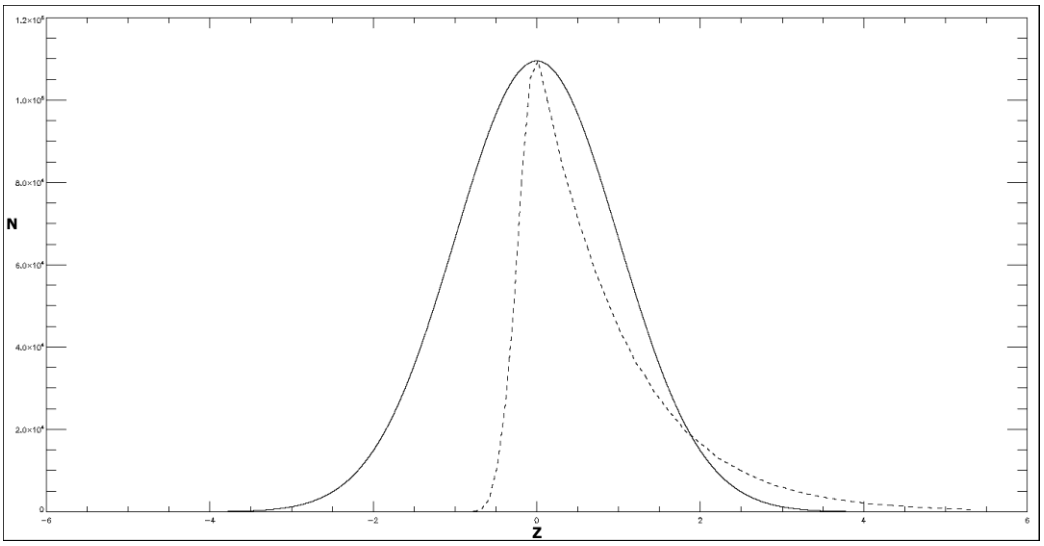


Figure 4.29. Histogram showing the distribution of voxel values (z-scores) for the n=191 frame 10 images, reconstructed using OS-EM (dashed line). Skewness = 1.77, kurtosis = 4.44. A Gaussian function of the same σ and height is plotted (solid line) for comparison.

A strong positive skew was readily apparent in the OS-EM reconstructed data, and confirmed by the calculated skewness value of 1.77 (Gaussian skewness = 0). No skew was observed for the FBP reconstructed data, which showed good agreement with the overlayed Gaussian function. Skewness for the FBP voxels was calculated to be 0.059. The above analysis was repeated for each frame of the (*n*=40) dynamic PK11195 simulation, and the results are plotted below in Figure 4.30. Values for skewness and kurtosis for each frame are presented in Table 4.8. A positive skew was identified in every frame reconstructed with OS-

EM (skewness range: 0.55 to 1.1), with skewness increasing as total counts decreased. In contrast, FBP produced a relatively flat distribution of skewness for the range of total counts studied (range: 0.0084 to 0.061).

Table 4.8. Skewness and kurtosis (from z-score normalised images) for each frame of the dynamic PK11195 PET simulation.

| FBP Skewness | FBP Kurtosis | OSEM Skewness | OSEM Kurtosis |
|---|---|---|---|
| 0.0585 | -0.125 | 1.12 | 2.041 |
| 0.0518 | -0.163 | 1.056 | 1.80 |
| 0.0615 | -0.139 | 1.12 | 2.0073 |
| 0.0521 | -0.155 | 1.019 | 1.57 |
| 0.0491 | -0.129 | 1.023 | 1.57 |
| 0.0507 | -0.137 | 1.036 | 1.63 |
| 0.0546 | -0.141 | 1.030 | 1.64 |
| 0.0256 | -0.143 | 0.723 | 0.674 |
| 0.0208 | -0.157 | 0.717 | 0.633 |
| 0.0190 | -0.151 | 0.731 | 0.658 |
| 0.0163 | -0.131 | 0.566 | 0.363 |
| 0.0127 | -0.143 | 0.600 | 0.412 |
| 0.0159 | -0.140 | 0.627 | 0.464 |
| 0.0107 | -0.154 | 0.644 | 0.494 |
| 0.00838 | -0.144 | 0.548 | 0.338 |
| 0.0149 | -0.143 | 0.613 | 0.437 |
| 0.0344 | -0.158 | 0.678 | 0.554 |
| 0.0203 | -0.135 | 0.707 | 0.673 |
| 0.0241 | -0.161 | 0.761 | 0.749 |
| 0.0272 | -0.166 | 0.676 | 0.525 |
| 0.0240 | -0.166 | 0.782 | 0.809 |

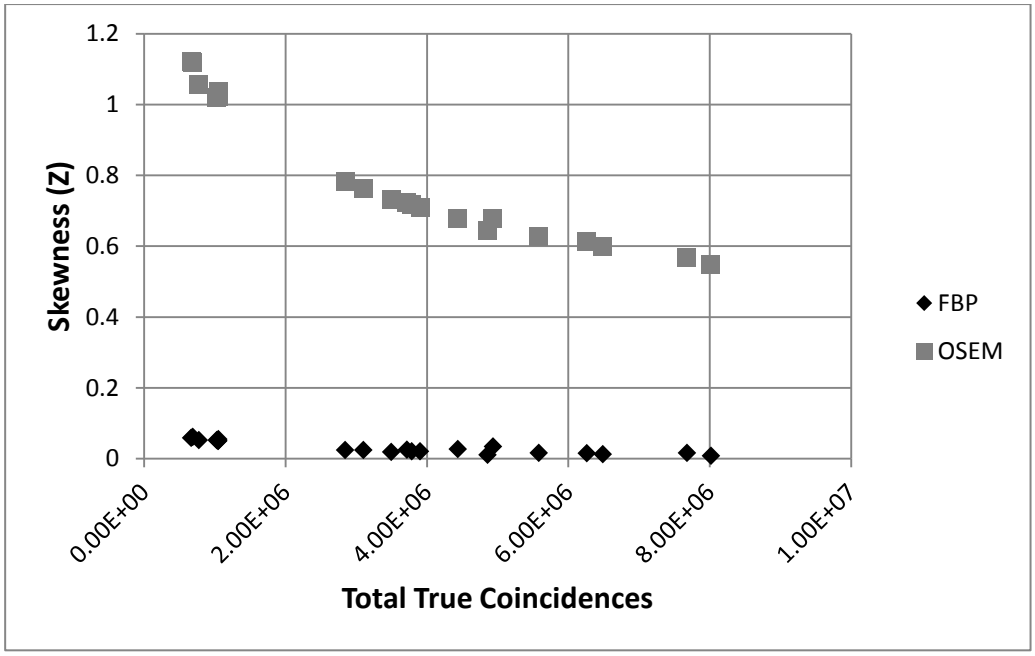


Figure 4.30. Skewness of z-score images plotted against total true coincidences, for each frame of the PK11195 simulation. OS-EM reconstructed image data show a strong positive skew. This plot suggests a non-linear inverse relationship between skewness and collected counts for the OS-EM data.

#### 4.3.4.2 Fitting an Analytical Model to the Image Noise Data

Average voxel coefficient of variation was plotted against the quantity defined as the product of activity concentration and frame duration, for both the FBP and OS-EM reconstructions. The appropriateness of a 'power law' relationship between these two variables was suggested by the appearance of the plotted data, and confirmed by plotting the curve on logarithmic axes, which resulted in straight lines (see Figure 4.31 to Figure 4.33). An equation of the form: $y = ax^b$, was therefore fitted to the data points, where $y$ = % coefficient of variation and $x$ = the activity concentration x frame duration. The parameters $a$ and $b$ were determined using an iterative curve fitting routine, written in IDL, which sought to minimise the sum of squared differences between the data points and the fitted curve. Figure 4.32 (FBP data) and Figure 4.33 (OS-EM data) show the results of this analysis. The actual functions that resulted from the curve fitting procedures were:

$$\%CoV_{FBP} = 802.063(concentration \times time)^{-0.485484} \quad (22)$$

$$\%CoV_{OS-EM} = 541.915(concentration \times time)^{-0.417817} \quad (23)$$

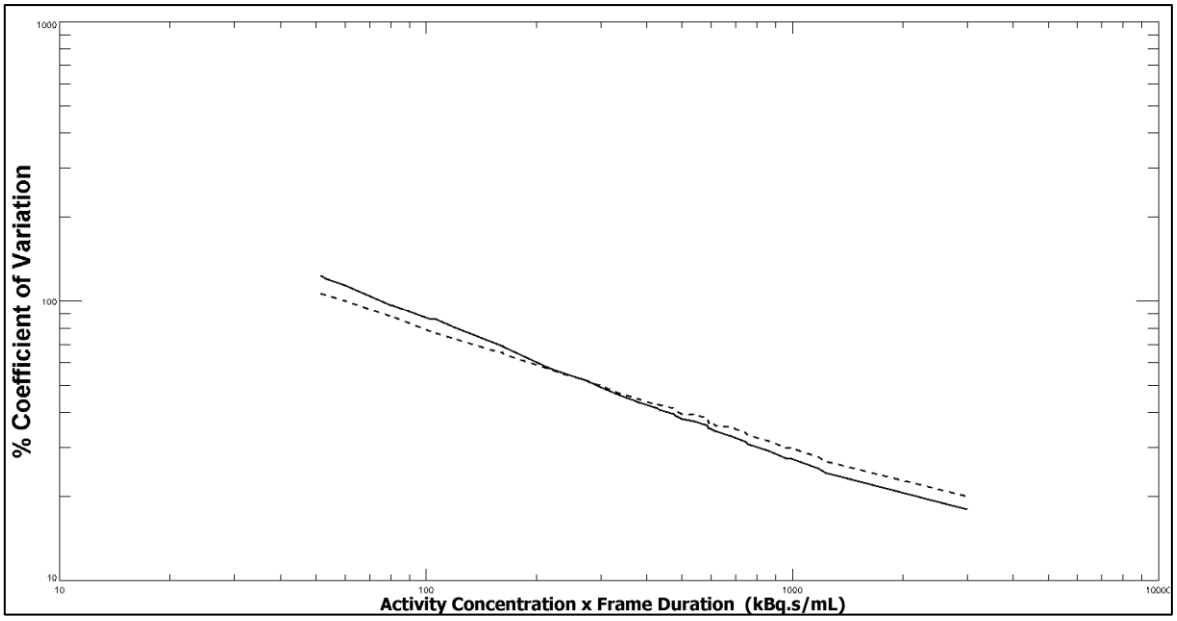


Figure 4.31. Log-log plot of average voxel coefficient of variation versus the product of activity concentration and frame duration for FBP reconstructions (solid line) and OS-EM (dashed line). The linearity of this plot suggests that a power law might be an appropriate mathematical description of the relationship between the two variables.

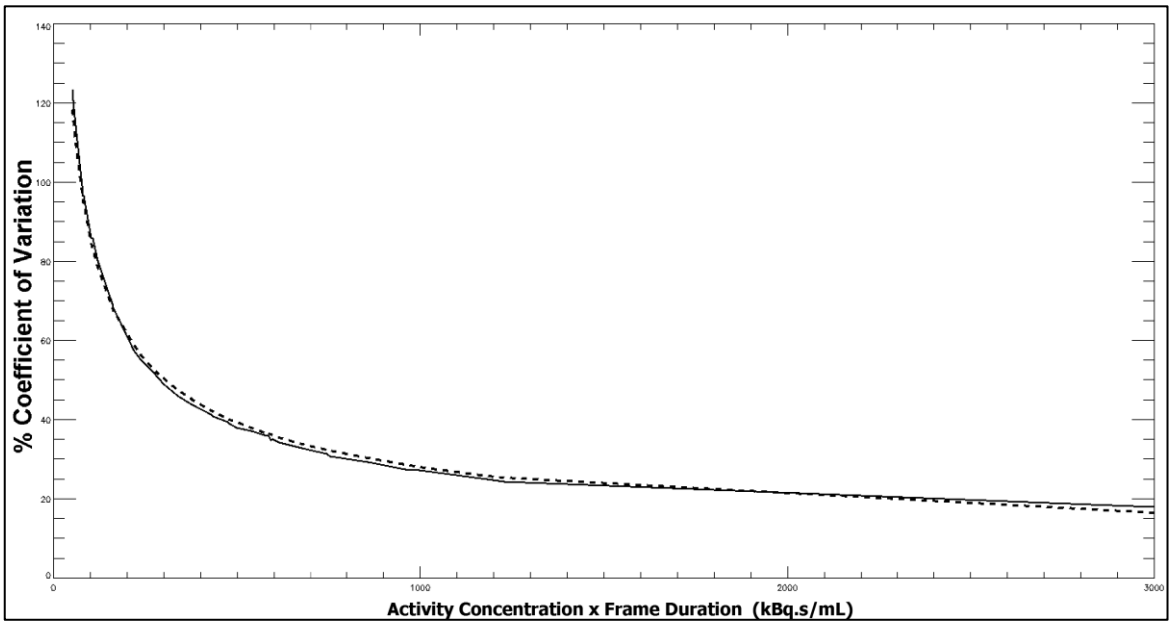


Figure 4.32. Average voxel coefficient of variation versus the product of activity concentration and frame duration for FBP reconstructions (solid line). A curve of the form: $y = ax^b$ was fitted to the data points using an iterative curve fitting procedure (dashed line).

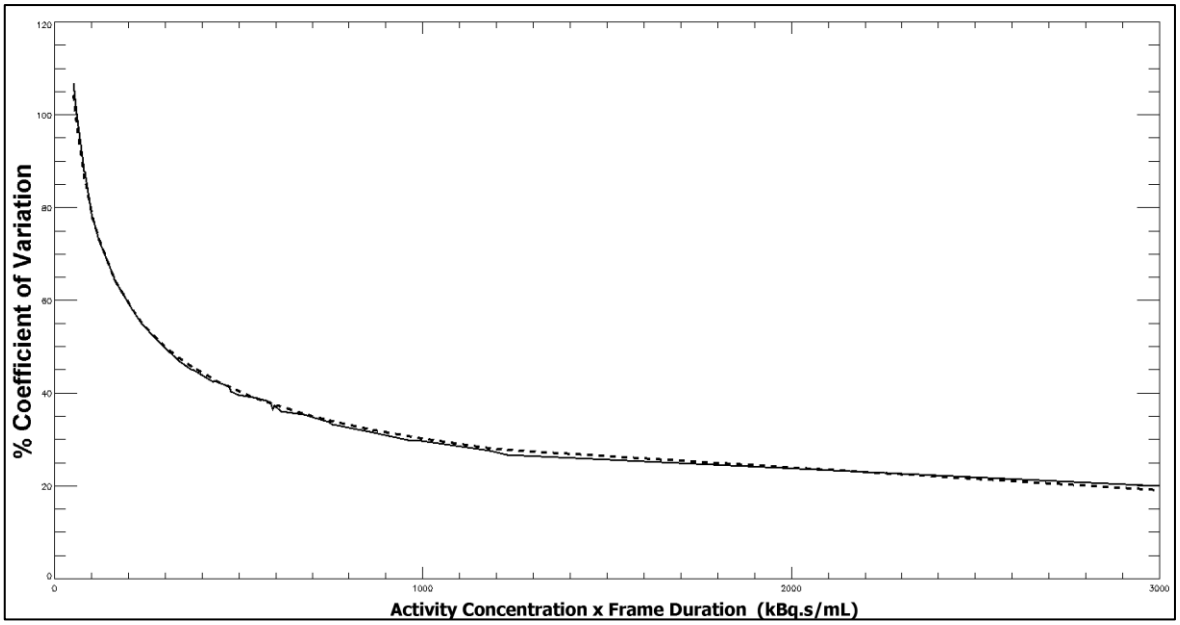


Figure 4.33. Average voxel coefficient of variation versus the product of activity concentration and frame duration for OS-EM reconstructions (solid line). A curve of the form: $y = ax^b$ was fitted to the data points using an iterative curve fitting procedure (dashed line).

In order to investigate the assumption that the image noise was not influenced by count rate dependent effects, the NECR for each dynamic frame simulation was calculated using the count rate data available from GATE. Figure 4.34 below shows the NECR curves plotted as a function of grey matter activity concentration. A hypothetical 'ideal' true coincidence count rate response curve, extrapolated from the first three (low count rate) true count rate points, is also plotted for comparison. The ratio between the NECR (k=1) curve and the ideal trues curve is plotted in Figure 4.35.

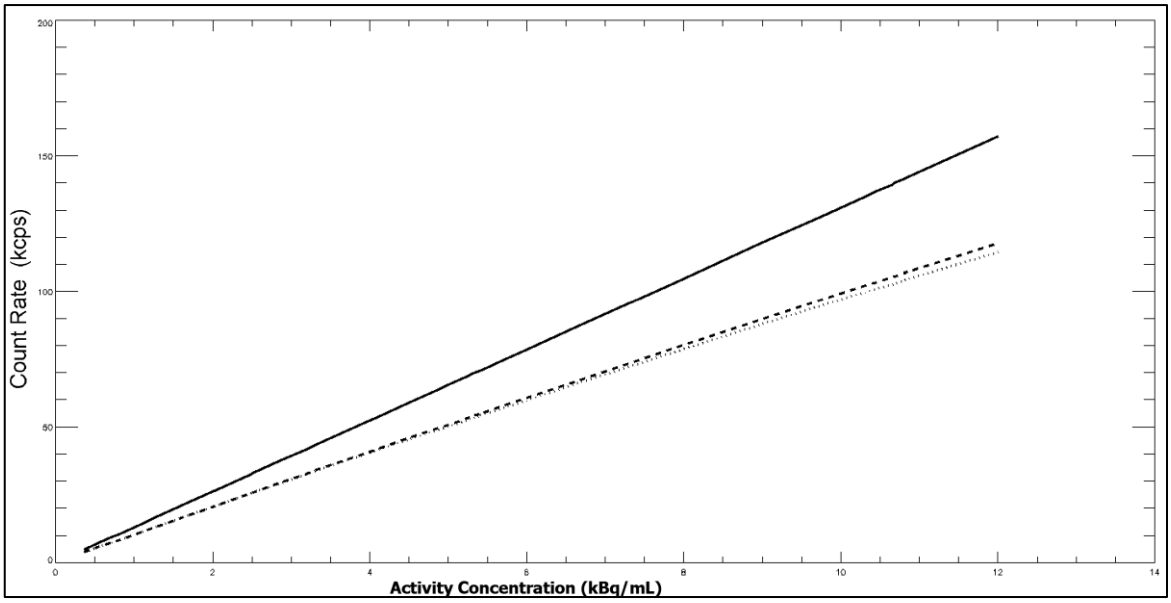


Figure 4.34. Counting rate response for all dynamic simulation frames, plotted as a function of phantom grey matter activity concentration. NECR curves (dashed and dotted lines for noiseless and noisy randoms subtraction respectively) are plotted along with a hypothetical 'ideal' linear true counting rate response curve (solid line).

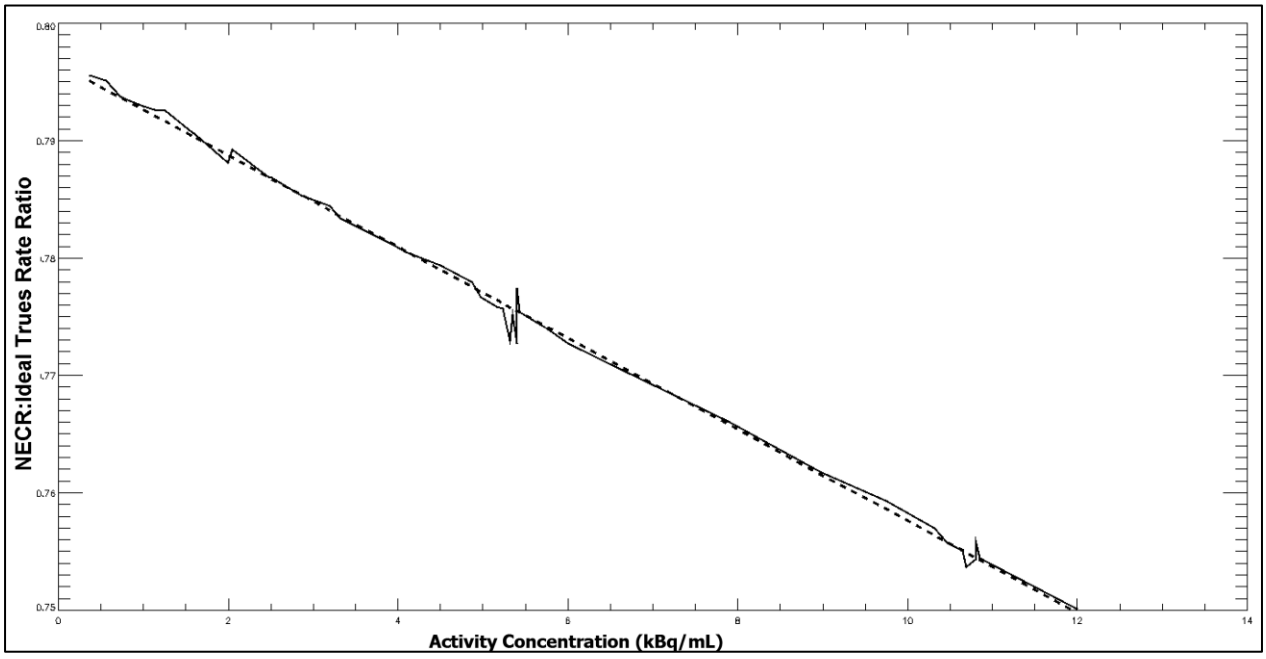


Figure 4.35. Plot showing the ratio of NECR (noisless randoms subtraction) to ideal linear response curve, versus phantom grey matter activity concentration (solid line). Fluctuations in the curve at around 5.5 kBq/mL and 11 kBq/mL are due to the noise associated with the very short frame durations from which these data points are derived. A straight line with a slope of -0.003892 and a y-intercept of 0.7965 was fitted to the data points by linear regression (dashed line). The y-intercept is ≈ 1-scatter fraction, which averaged 20.17% over all simulated dynamic frames.

The NECR curves were approximately linear at the count rates observed during these simulations. The ratio of NECR to the ideal trues rate line (NECR:$trues_{ideal}$) varied in a linear fashion from 0.7955 to 0.7501 over the same range of count rates. Fitting of a straight line to the NECR:$trues_{ideal}$ ratio data yielded a slope of -0.003892 and a y-intercept of 0.7965 (or ≈ 1- scatter fraction). The scatter fraction was measured directly from the raw data for each frame and ranged from 19.86% to 20.39% (average = 20.17%).

Although the deviation of the NECR curve from the ideal true curve is modest, the effect probably cannot be considered negligible even at the very low count rates observed during these simulations. Therefore the noise model described in 4.3.4.1 (Equations 14 and 15) was modified to take the NECR:$trues_{ideal}$ ratio into consideration. The NECR modified noise model takes the form of:

$$\%CoV = a\left[concentration \times time \times \left(NECR / Trues_{ideal}\right)\right]^{b} \tag{24}$$

In this model, the NECR:$trues_{ideal}$ ratio, which is always less than 1, acts to reduce the tissue concentration to the equivalent level that would produce the same relative noise if scatter, randoms and dead-time were non-existent.

The results of fitting the new noise model to the data are plotted in Figure 4.36. The actual functions that resulted from the curve fitting procedures were:

$$\%CoV_{FBP} = 853.103\left(concentration \times time \times NECR / Trues_{ideal}\right)^{-0.499869} \tag{25}$$

$$\%CoV_{OS-EM} = 507.787\left(concentration \times time \times NECR / Trues_{ideal}\right)^{-0.407806} \tag{26}$$

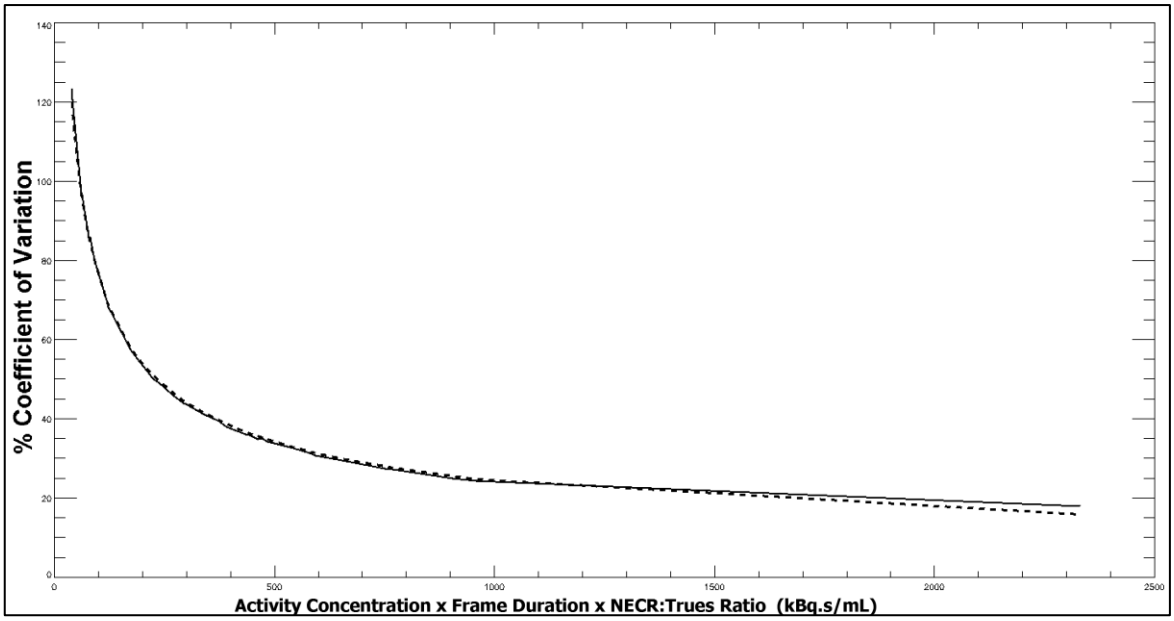


Figure 4.36. Average voxel coefficient of variation versus the product of activity concentration, frame duration and NECR:trues$_{ideal}$ ratio for FBP reconstructions (solid line), and the fitted function (dashed line). The 'activity concentration x time' quantity for each frame has been multiplied by the NECR:trues$_{ideal}$ ratio for that frame.

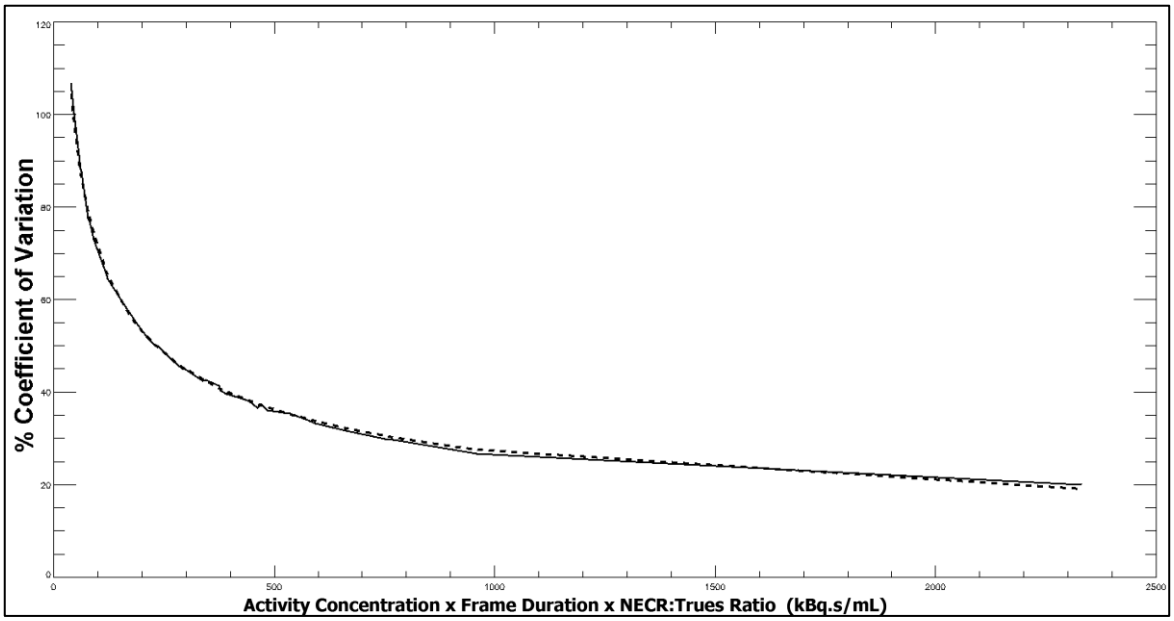


Figure 4.37. Average voxel coefficient of variation versus the product of activity concentration, frame duration and NECR:trues$_{ideal}$ ratio for OS-EM reconstructions (solid line), and the fitted function (dashed line). The 'activity concentration x time' quantity for each frame has been multiplied by the NECR:trues$_{ideal}$ ratio for that frame.

Table 4.9 shows the fitted curve parameters for the %CoV for each region of interest, for both reconstruction parameters (FBP and OS-EM) and both noise models (simple and NECR modified). Fitted curves are displayed for each region of interest, for the NECR modified model only (Figure 4.38 to Figure 4.43). For the ROI levels, only the parameter '*a*'

was fitted, due to the greater uncertainty associated with each data point. The value for parameter '*b*' was taken from the value determined from the voxel average %CoV analysis, for the corresponding reconstruction algorithm. The value for parameter '*a*' was consistently 6.8% lower when fitted to the NECR modified model than the simpler model for FBP reconstructed data, and was consistently 9.6% lower for the OS-EM reconstructed data. The value of parameter '*b*' was close to -0.5 for the filtered back projection data, indicating that for this reconstruction algorithm the relative image noise is proportional to $1/\sqrt{counts}$ . A lower value for '*b*' of around 0.42 was obtained for the OS-EM reconstructions, as well as consistently lower values for '*a*' when compared to filtered back projection data. These lower parameter values yield a lower but flatter noise curve, suggesting that OS-EM yields lower relative image noise than FBP at low counts, but with a less rapid improvement as counts increase. This is evident in the log-log plot (Figure 4.31), where the OS-EM data is lower (less noisy) than the FBP data at less than 270 kBq.s/mL, but is higher (more relative noise) than FBP data above this point.

Table 4.9. Fitted noise model parameters. Curve fitted to an equation of the form: $y = ax^b$. SSD = sum of squared differences.

| Region Level | Reconstruction Algorithm | Simple Noise Model Parameter *a* | NECR Noise Model Parameter *a* | Simple noise model Parameter *b* | NECR noise model Parameter *b* | Simple Model Curve Fit SSD | NECR Model Curve Fit SSD |
|---|---|---|---|---|---|---|---|
| Voxel | FBP | 802.063 | 747.414 | -0.485484 | -0.496169 | $10^{-11}$ | $10^{-7}$ |
| | OS-EM | 541.915 | 489.804 | -0.417817 | -0.418934 | $10^{-11}$ | $10^{-8}$ |
| Grey Matter ROI | FBP | 22.3283 | 20.8069 | *-0.485484* | *-0.496169* | $10^{-11}$ | $10^{-12}$ |
| | OS-EM | 16.9189 | 15.2919 | *-0.417817* | *-0.418934* | $10^{-10}$ | $10^{-12}$ |
| Medium ROI | FBP | 102.914 | 95.902 | *-0.485484* | *-0.496169* | $10^{-11}$ | $10^{-11}$ |
| | OS-EM | 69.6704 | 62.9706 | *-0.417817* | *-0.418934* | $10^{-10}$ | $10^{-11}$ |
| Small ROI | FBP | 184.308 | 171.75 | *-0.485484* | *-0.496169* | $10^{-10}$ | $10^{-10}$ |
| | OS-EM | 122.723 | 110.921 | *-0.417817* | *-0.418934* | $10^{-10}$ | $10^{-10}$ |

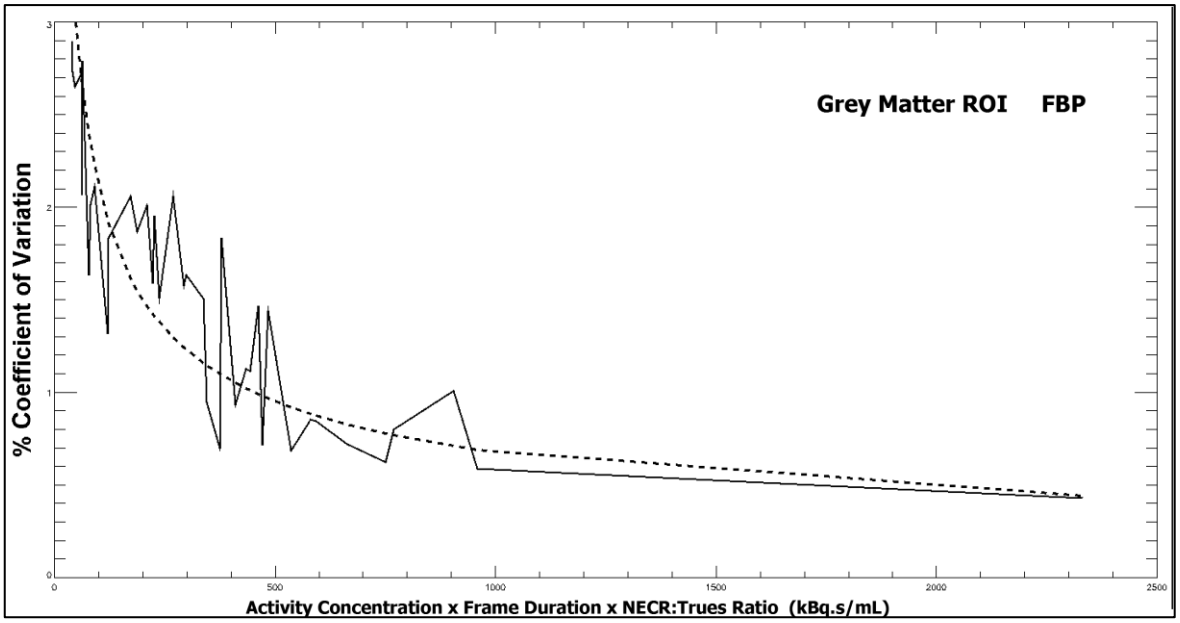


Figure 4.38. Grey matter ROI coefficient of variation versus the product of activity concentration, frame duration and NECR:$trues_{ideal}$ ratio for FBP reconstructions (solid line), and the fitted function (dashed line).

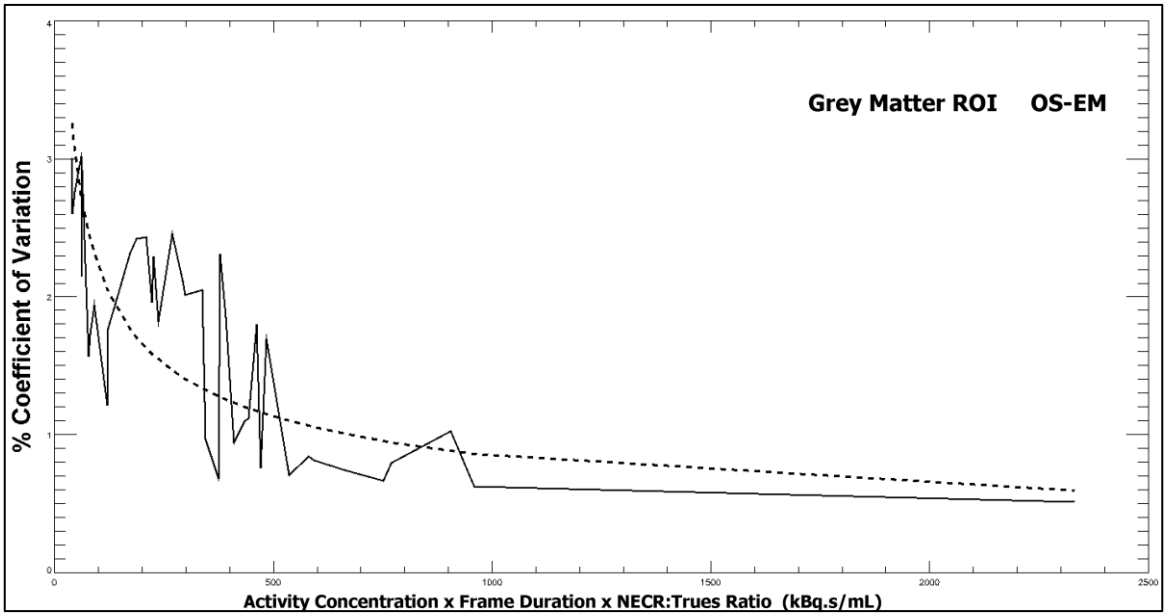


Figure 4.39. Grey matter ROI coefficient of variation versus the product of activity concentration, frame duration and NECR:$trues_{ideal}$ ratio for OS-EM reconstructions (solid line), and the fitted function (dashed line).

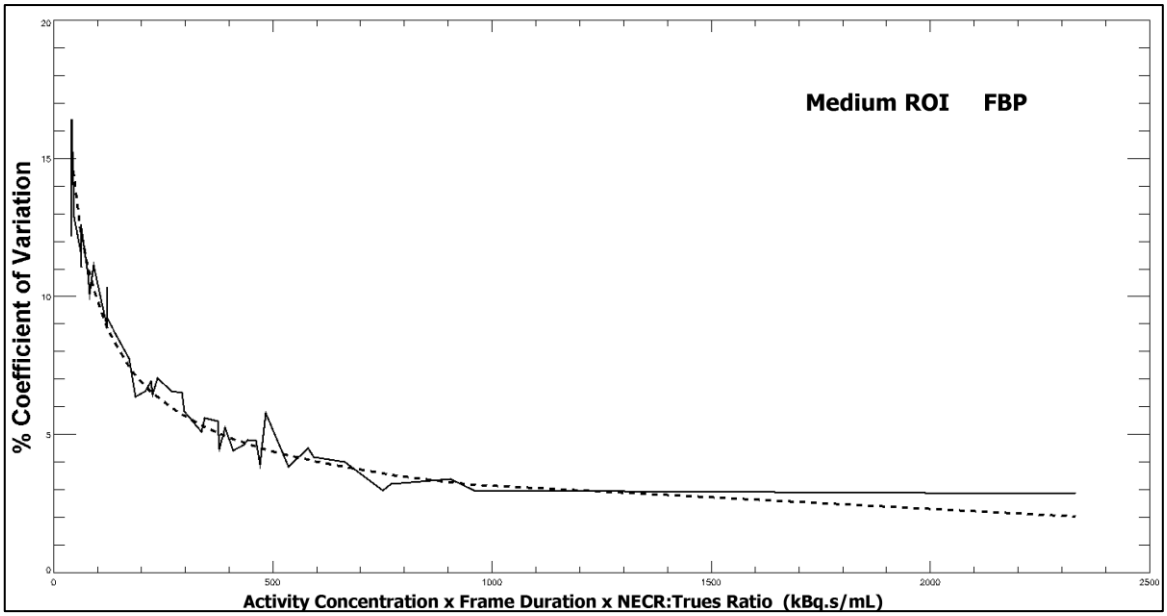


Figure 4.40. Medium sized ROI (temporal lobes) coefficient of variation versus the product of activity concentration, frame duration and NECR:$trues_{ideal}$ ratio for FBP reconstructions (solid line), and the fitted function (dashed line).

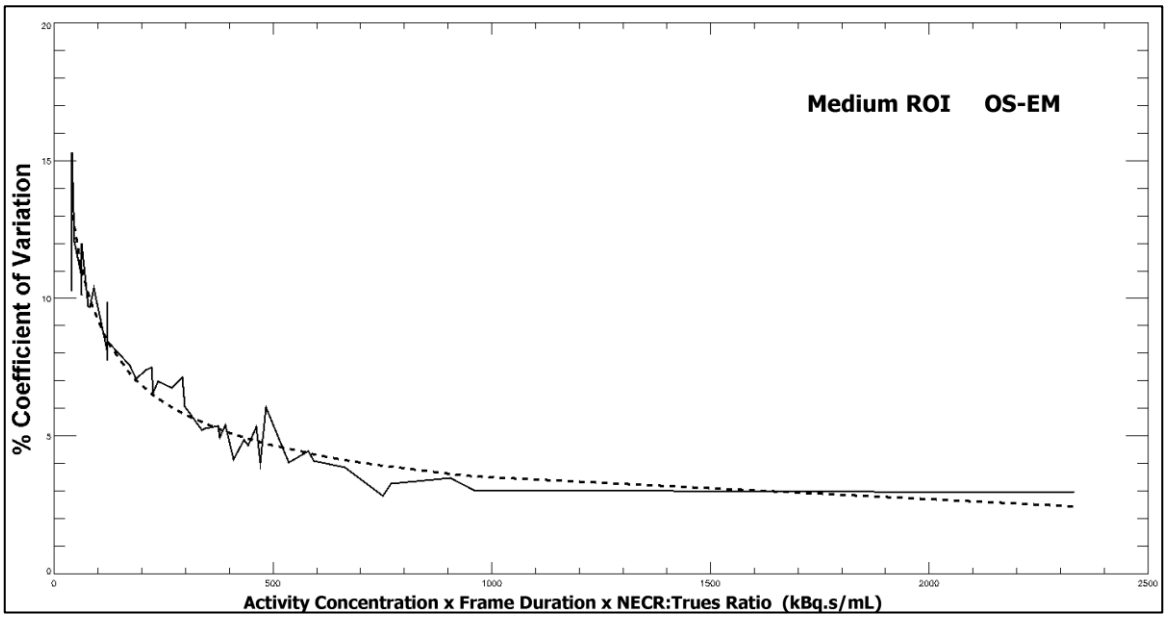


Figure 4.41. Medium sized ROI (temporal lobes) coefficient of variation versus the product of activity concentration, frame duration and NECR:$trues_{ideal}$ ratio for OS-EM reconstructions (solid line), and the fitted function (dashed line).

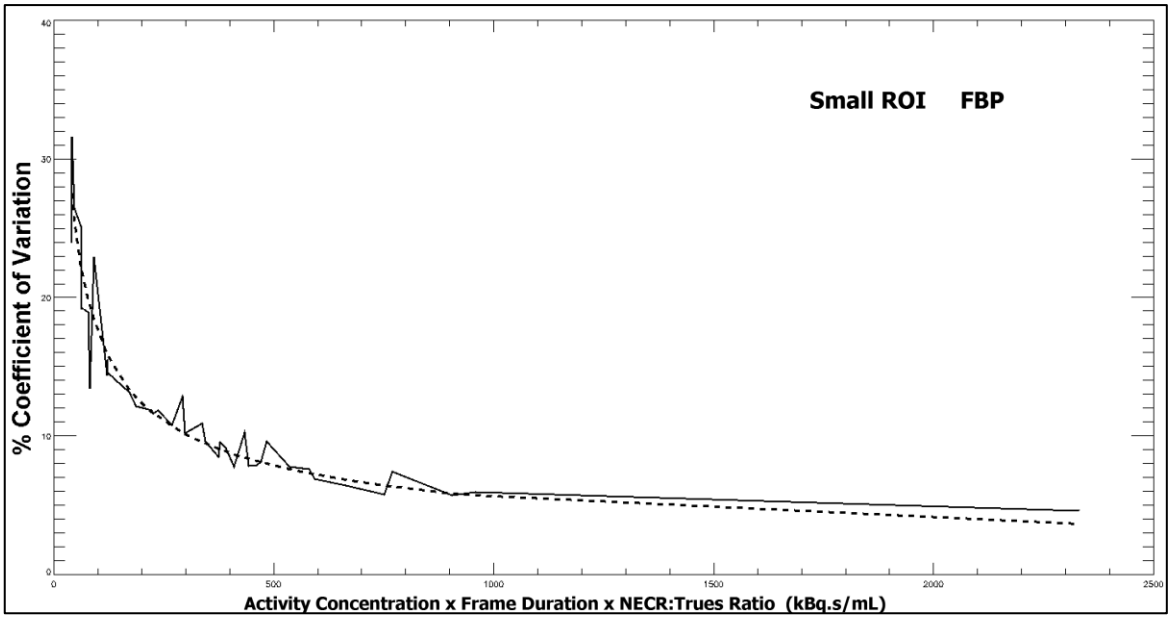


Figure 4.42. Small sized ROI (temporal lobes) coefficient of variation the product of activity concentration, frame duration and NECR:$trues_{ideal}$ ratio for FBP reconstructions (solid line), and the fitted function (dashed line).

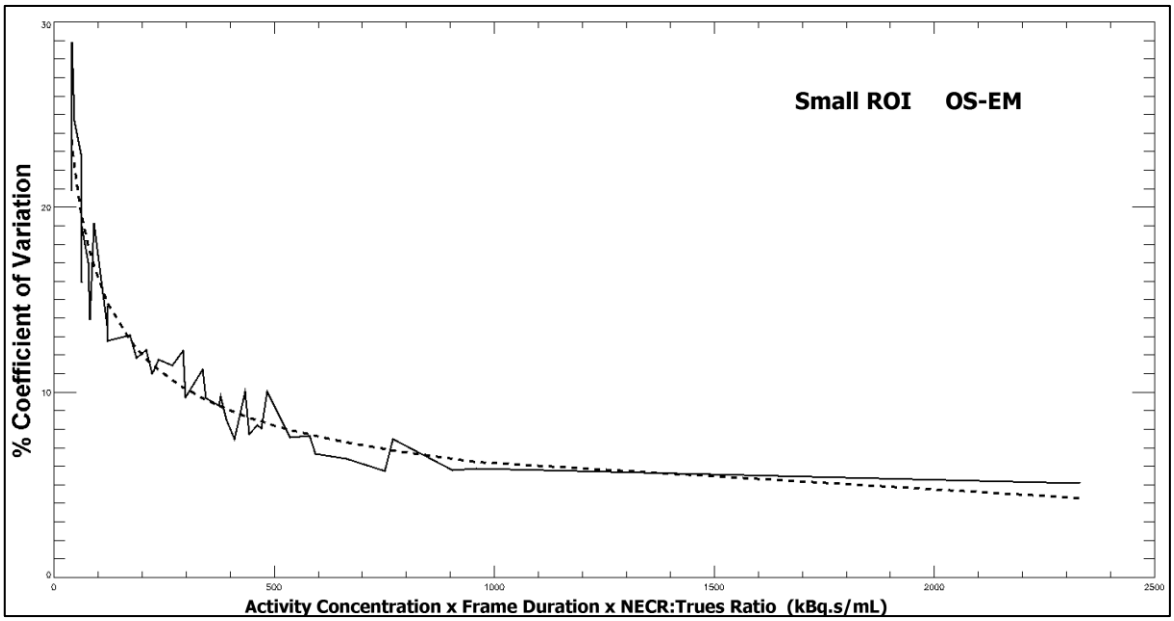


Figure 4.43. Small sized ROI (temporal lobes) coefficient of variation versus the product of activity concentration, frame duration and NECR:$trues_{ideal}$ ratio for OS-EM reconstructions (solid line), and the fitted function (dashed line).

#### 4.3.4.3 Validation of Noise Model for Estimating the Precision of Kinetic Parameters

To assess the performance of the fitted noise model in predicting %CoV, the frame 10 (with $n$=191 realisations) simulated data were analysed and the measured %CoV for the voxels and three ROIs were compared to that predicted by the model equations. The results of

this analysis showed that both models returned values for %CoV that were in close agreement with the measure values. Results are shown in Figure 4.44 and Figure 4.45 below.

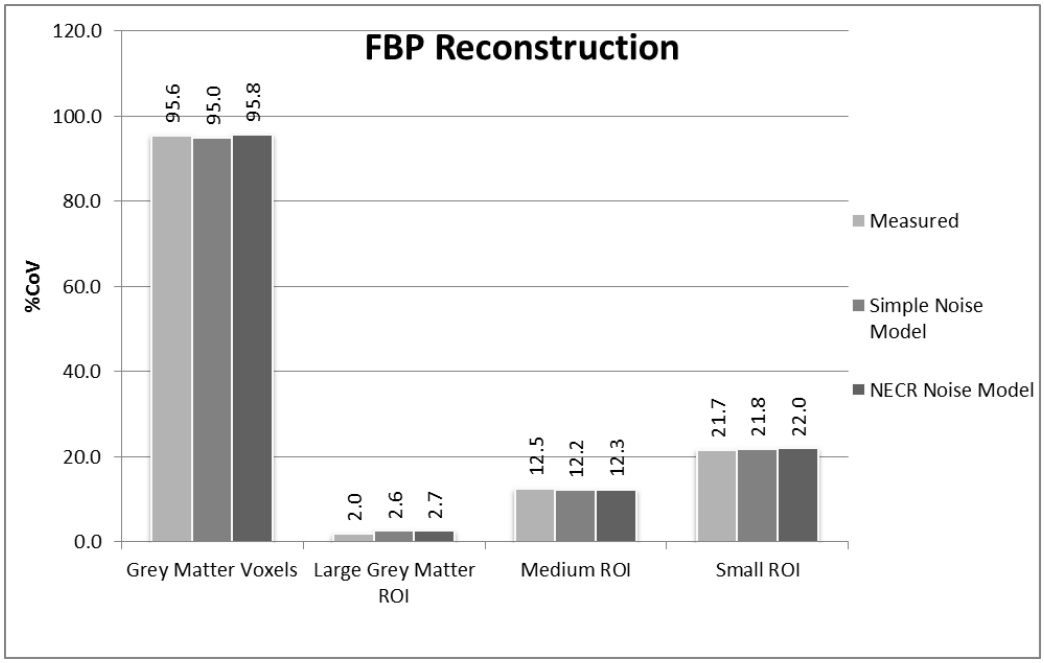


Figure 4.44. Comparison of measured %CoV for frame 10 ($n$=191 realisations) with %CoV predicted by both the simple noise model, and the 'NECR noise model', for images reconstructed with FBP.

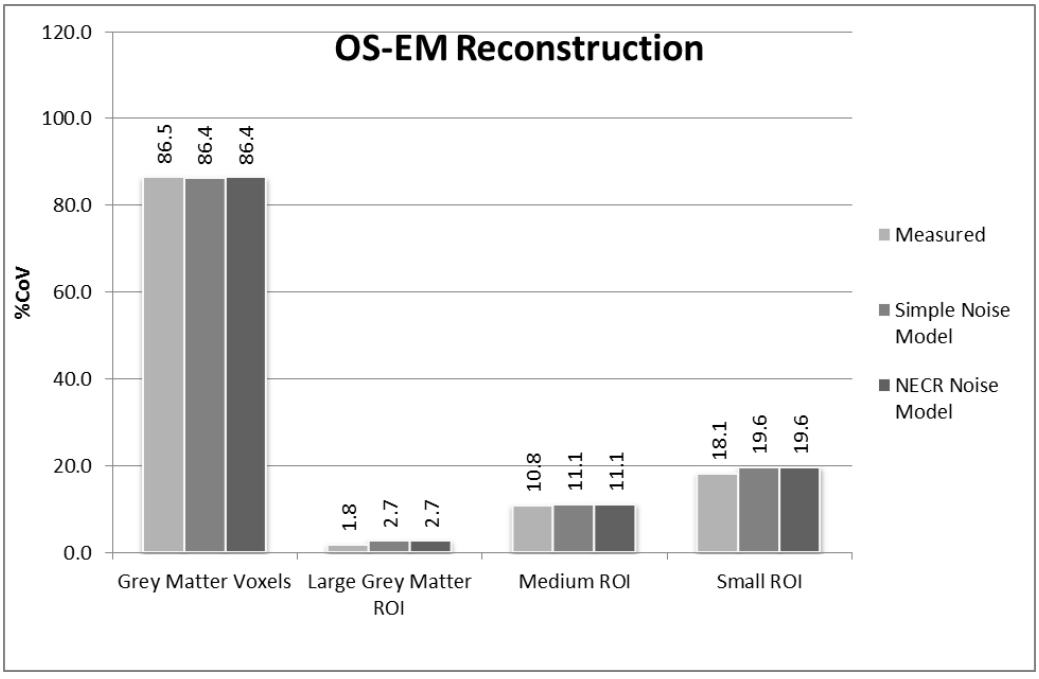


Figure 4.45. Comparison of measured %CoV for frame 10 ($n$=191 realisations) with %CoV predicted by both noise models, for images reconstructed with FBP.

Validation of the noise model, for the task of estimating noise-induced kinetic parameter variance, was done by comparing the variance of kinetic parameter estimates predicted by the noise model with the variance of kinetic parameters obtained from the actual ($n$=40 realisations) GATE simulated TACs. The NECR modified noise model was used to add noise to the reference TACs. Although the noise model predicts the %CoV for both FBP and OS-EM reconstructed images, the positive bias observed in the images reconstructed with OS-EM resulted in TAC values that differed somewhat from the original noise free reference TAC, making it difficult to compare the variances of fitted kinetic parameters. Therefore no further analysis was carried out on the OS-EM image data, and all results reported from here on are for FBP reconstructions only.

Table 4.10. Variance of estimated kinetic parameters. Noise was added to the reference TAC using the NECR noise model.

| Kinetic Parameter | Reference Value | Parameter Variance (noisy GATE data) | Parameter Variance (modelled noise added) | F-Ratio |
|---|---|---|---|---|
| ***Large Grey Matter ROI*** | | | | |
| K1 | | 2.924E-07 | 3.861E-07 | *1.32* |
| k2 | 0.15 | | | |
| k3 | 0.06 | 1.099E-07 | 1.316E-07 | *1.20* |
| k4 | 0.04 | 1.421E-06 | 1.660E-06 | *1.17* |
| | | | | |
| ***Medium ROI*** | | | | |
| K1 | 0.05 | 9.663E-06 | 1.074E-05 | *1.11* |
| k2 | 0.15 | | | |
| k3 | 0.06 | 3.053E-06 | 3.399E-06 | *1.11* |
| k4 | 0.04 | 3.752E-05 | 3.864E-05 | *1.03* |
| | | | | |
| ***Small ROI (1TCM)*** | | | | |
| K1 | 0.0417 | 2.922E-05 | 2.244E-05 | *1.30* |
| k2 | 0.0648 | 1.355E-04 | 1.087E-04 | *1.25* |

Comparison of the variances of the estimated kinetic parameters was carried out using the $F$-ratio of variances (Table 4.10). All $F$-ratios were found to be lower than a critical value of 1.506 ($p$=0.1), therefore no statistical evidence was found that the two methods produced different variances of the fitted parameters. It should be noted that statistics like the $F$-ratio for comparing variances are very sensitive to departures from normality in the data (Johnson, Freund, & Miller, 2011), and that they do not provide assurance that the two variances are equal. Rather, they provide evidence that the variances are not different. Kinetic parameter coefficients of variation for each noise estimation method are plotted in Figure 4.46, Figure 4.47 and Figure 4.48 below.

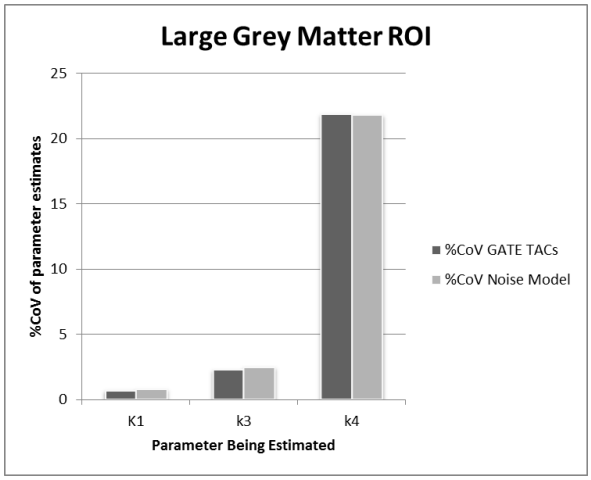


Figure 4.46. Coefficient of variation of kinetic parameters ($K_1$, $k_3$ and $k_4$) for the large grey matter ROI using the noise model and GATE simulation data.

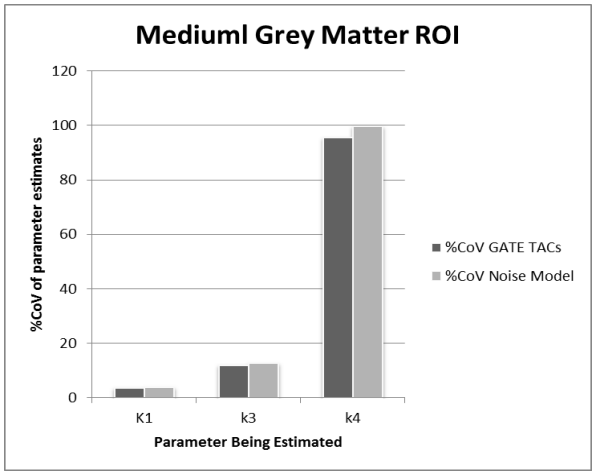


Figure 4.47. Coefficient of variation of kinetic parameters ($K_1$, $k_3$ and $k_4$) for the medium grey matter ROI using the noise model and GATE simulation data.

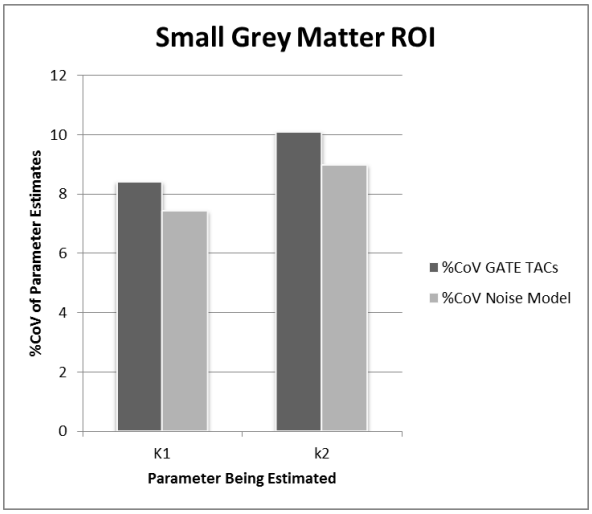


Figure 4.48. Coefficient of variation of kinetic parameters ($K_1$, $k_3$ and $k_4$) for the small grey matter ROI using the noise model and GATE simulation data.

### 4.3.5 Discussion

A positive skew of voxel values was identified for the OS-EM reconstructed data (see Figure 4.29), and the skewness was shown to be inversely correlated with the number of true coincident counts collected. This effect has been reported previously (Rahmim et al., 2005), and was attributed to the subtraction of random and scatter coincidences prior to reconstruction, which is likely to produce negative values at low (<10) average counts per sinogram element. Statistical reconstruction algorithms like ML-EM assume Poisson statistical properties of the input data, a consequence of which being that negative values are not allowed, and are usually truncated to zero. This effectively adds counts to the sinogram, causing an overestimation bias in the reconstructed images. Since the FBP algorithm makes no assumption about the noise properties of the data, negatives are allowed and no bias is produced.

The findings of this study confirm these properties of both reconstruction algorithms. Further, it may be seen that at the count rate levels expected from [$^{11}$C]-PK11195, and even for the hypothetical 'double uptake' [$^{11}$C]-PK11195 tracer, overestimation bias is likely to be present if the OS-EM algorithm is used with pre-corrected sinogram data. Solutions to this problem exist, for example incorporating all the data corrections directly into the reconstruction algorithm as in the case of the 'Ordinary Poisson Expectation Maximisation' algorithm (Politte, 1991), or using alternative algorithms that tolerate negative sinogram values such as the 'Shifted Poisson Expectation Maximisation' algorithm (Ahn & Fessler, 2004). Further research into the application of statistical image reconstruction in the context of low count TSPO PET imaging is warranted, particularly considering the potentially favourable image noise properties of such algorithms at low counts.

Average voxel coefficient of variation varied with respect to the product of grey matter activity concentration and frame time in a non-linear manner. A mathematical 'power law' function was fitted to the plotted data points. A good quality fit was obtained for both FBP and OSEM data- assessed visually and by the sum of squared differences ($\leq 10^{-11}$). An implicit, and somewhat unrealistic, assumption made during the analysis of these data was that the relative noise in the images was not influenced by count rate dependent effects, or in other words, that the NECR curve was linear and the effects of scatter, randoms and dead-time losses were negligible. Therefore, further analysis was carried out in which the activity

concentration in grey matter was scaled by a factor that took into account the noise equivalent count rate at each frame.

Although theoretically more appealing, the ratio of NECR to ideal true count rate response was relatively flat over the range of activity concentrations studied (slope ≈ -0.0039), and the modified 'NECR noise model' produced curve fits of similar quality and appearance (but slightly different in scale) to the simpler noise model. The image noise data available therefore did not allow a rigorous assessment of the accuracy of the modified 'NECR noise model', however for studies in which the NECR curve does deviate substantially from the ideal count rate response line, it could potentially yield more accurate estimates of relative image noise.

The fitted noise models allow image voxel noise, and noise for three regions of interest, to be calculated rapidly for any arbitrary grey matter tissue activity concentration. This makes the models especially useful as an adjunct to compartmental modelling for image quantification of TSPO PET tracers, where it is desirable to know the noise at each point in a tissue TAC. It is important to note that the models are limited to the specific PET geometry, and the data processing and reconstruction algorithms that were used to generate the data. In addition, the models are only applicable to approximately uniform distributions of activity (i.e. not to focal 'hot' lesions) and only within the range of activity concentrations studied (≈0.36 – 12 kBq/mL).

In addition to the problem of overestimation bias, the non-normality of the OS-EM reconstructed image data might limit the accuracy of the analytical noise model in the context of compartmental modelling. Although the noise model predicts the voxel (or region) %CoV, it does not predict the skewness, and a Gaussian distribution is typically assumed. The noise model may still be suitable for estimating appropriate weighting factors for the least-squares fitting of compartmental model parameters, where it has been shown that the effect of using of incorrect but 'reasonable' weighting factors on bias and precision of estimated [$^{11}$C]-PK11195 kinetic parameters is negligible (Yaqub et al., 2004). Due to the difficulties of obtaining quantitatively accurate TACs with the OS-EM algorithm and the data available, OS-EM was not investigated further in this work.

Analysis of the variance of estimated kinetic parameters for a compartmental modelling task showed that the fitted analytical noise model could provide very similar estimates of parameter uncertainty to the 40 GATE simulation noise realisations for a [$^{11}$C]-

PK11195 dynamic study. There was no statistical evidence that the two methods produced different variances ($p$=0.1).

The effect of intrinsic radioactivity from lutetium-176, found in the commonly used PET detector materials of LSO and LYSO, was not investigated here. As discussed in 4.1.6, intrinsic singles counts increase the random coincidence rate and may become a significant source of noise when imaging at very low activity concentrations. Further research into the effects of intrinsic detector count rates on minimum detectable activity concentrations is required to address this issue, especially in the context of the low brain tissue concentration of TSPO radiotracers like [$^{11}$C]-PK11195.

### 4.3.6 Conclusions

Relative image noise at the voxel and ROI level was found to be well represented by a Gaussian function, with minimal skewness and kurtosis, for images reconstructed with filtered back projection. Images reconstructed with the ordered subset expectation maximization algorithm demonstrated a strong positive skew of voxel values, with a dependence on total collected counts, and was therefore not well described by a Gaussian function. Any noise model that assumes a normal distribution of image values is therefore potentially inaccurate for OS-EM reconstructed images.

The average voxel %CoV varied according to the product of phantom activity concentration and acquisition time. A power law, of the form $y=ax^b$ was found to fit the data well, with the parameter '$b$' taking the value -0.485484 for FBP reconstructions, and -0.417817 for OS-EM reconstructions. Information about the NECR for each simulated dynamic frame was incorporated into the noise model, however the ratio of NECR to an ideal linear count rate response was found to vary over a narrow range (0.75 – 0.8) for all count rates in the simulations, and the effect on the noise model was therefore small.

Validation of the analytical noise model for the purpose of studying the effects of TAC noise on compartmental parameter estimation was achieved by comparing the precision of parameter estimates derived from the original 40 independent [$^{11}$C]-PK11195 GATE simulations, with 40 synthetic noisy [$^{11}$C]-PK11195 TACs generated using the noise model. There was no statistical evidence that the variances of fitted kinetic parameters were different, therefore it was concluded that the analytical noise model provides an accurate estimation of TAC noise, within the range of tissue activity concentrations studied.

# Chapter 5 Investigation of the Factors that Affect Quantitative Reliability for TSPO PET

## 5.1 Introduction

Quantitative positron emission tomography (PET) imaging with the 18 kilodalton (18kDa) Translocator Protein (TSPO) ligand [$^{11}$C]-PK11195 has proven challenging, due to low brain uptake and high non-specific binding. To place the low brain uptake of [$^{11}$C]-PK11195 in the context of other commonly encountered (non-TSPO related) neurological radiotracers, the tissue Time Activity Curves (TACs) in humans for four different neurological positron emission tomography (PET) radiotracers were obtained from the following published sources:

- [$^{18}$F]-Fluoro-DOPA (FDOPA) in normal striatum (Huang & Hoffman, 1991).
- *N*-methyl-[$^{11}$C]-2-(4-methylaminophenyl)-6-hydroxybenzothiazole (also known as Pittsburgh Compound-B, or 'PIB') in the posterior cingulate in an Alzheimer's Disease patient (Price, Ziolko, & Mathis, 2005).
- 2-[$^{18}$F]-fluorodeoxy-D-glucose (FDG) in normal brain cortex (Graham, 2002).
- [$^{11}$C]-R-PK11195 in normal grey matter (Kropholler et al., 2005).

The last reference provided the TAC for the Monte Carlo simulations reported in this study. A second TAC was generated for PK11195 with the kinetic parameter '$k_3$' increased by a factor of 2.5, which approximates the pathological situation corresponding to a moderately increased level of neuroinflammation, using the published kinetic parameters of Kropholler et al. (2005).

A wide range of injected doses are reported in the literature- especially for the carbon-11 labelled tracers examined here- therefore to facilitate a meaningful comparison, all fluorine-18 tracer TACs were normalised to an injected dose of 185 MBq and all carbon-11 tracer TACs were normalised to an injected dose of 555 MBq. Where a range of injected doses was specified by the authors, an average figure was assumed for the displayed TAC. All TACs described above are plotted on the same axes in Figure 5.1. Data are not decay corrected.

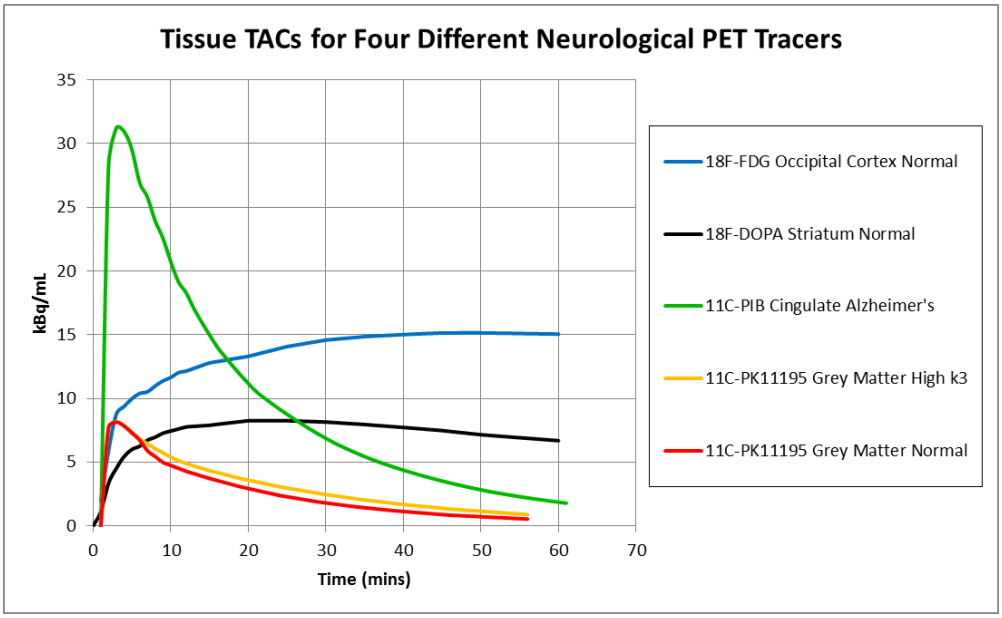


Figure 5.1. Typical tissue time-activity (including radioactive decay) curves for four neurological PET tracers, including [$^{11}$C]-PK11195. All curves normalised to an injected dose of 185 MBq for fluorine-18 and 555 MBq for carbon-11.

The above TACs illustrate that the level of brain radioactivity concentration for [$^{11}$C]-PK11195 is substantially lower than for the other non-TSPO brain imaging tracers. Relative image noise is therefore expected to be higher, especially at later time points after injection. Non-specific binding of [$^{11}$C]-PK11195 in brain tissue is also known to be high, relative to the specific binding, which further complicates the quantification of TSPO density with this tracer.

The use of a carbon-11 radiolabel also contributes to the lower tissue activity concentration values observed at later time points when compared to fluorine-18 labelled tracers. Although patient radiation dosimetry considerations may permit the injection of higher doses of carbon-11 TSPO tracers (Brown et al., 2007; Hirvonen et al., 2010), there are other factors that limit the quantity of tracer that may be injected, such as staff radiation safety (Towson, 2003), cyclotron production yield, and the need to inject a sufficiently small mass of ligand consistent with tracer principles (Hume et al., 1998). For these reasons, injected doses above 800 MBq are uncommon, and may not completely compensate for the loss of counts due to decay.

Expression of the TSPO molecule in the brain occurs in response to neuroinflammation, both on the outer mitochondrial membranes of resident microglia, and also on invading blood-borne cells in the case of focal blood-brain barrier disruption. Autoradiographic quantification of [$^{3}$H]-R-PK11195 binding in Multiple Sclerosis (MS)

affected brain tissue was reported (Banati et al., 2000) and revealed an increase in binding of between 3.5 – 7 times over healthy control brain tissue. The 7:1 ratio of binding was only found in focal MS plaques associated with the presence of macrophages and probable blood-brain barrier disruption, whereas the 3.5:1 ratio of binding was reported for the white matter of MS patients compared to healthy controls. Another study reported specific binding of [$^{3}$H]-PK11195 in the temporal lobe tissue of elderly Alzheimer's Disease subject to be approximately twice that of age-matched normal controls (Diorio, Welner, Butterworth, Meaney, & Suranyi-Cadotte, 1991). Similarly, autoradiography data (Kumlien, Hilton-Brown, Spannare, & Gillberg, 1992) provides evidence of a two-fold increase in specific [$^{3}$H]-PK11195 binding in the temporal lobes of epilepsy patients. By comparison, a study of the binding of [$^{3}$H]-2-(4-Methylaminophenyl) Benzothiazole (an amyloid binding compound similar in structure to Pittsburgh compound-B) to post-mortem brain tissue homogenate demonstrated a ten-fold increase in frontal lobe grey matter binding for subjects with Alzheimer's disease over normal controls, 94% of which was specific binding to amyloid (Klunk et al., 2003).

These data indicate that increases in TSPO expression in the brain that might be expected in the presence of disease are relatively subtle (e.g. <3 fold), in comparison to the other successful 'positive signal' PET tracers like amyloid imaging agents, particularly for non-focal pathology without blood-brain-barrier disruption. The effects of trying to detect a subtle increase in TSPO expression in the presence of low image SNR are illustrated in the following figure, taken from a recently published paper on the use of [$^{11}$C]-Vinpocetine as a TSPO tracer for measuring TSPO expression in normal ageing and Alzheimer's disease (Gulyas et al., 2011):

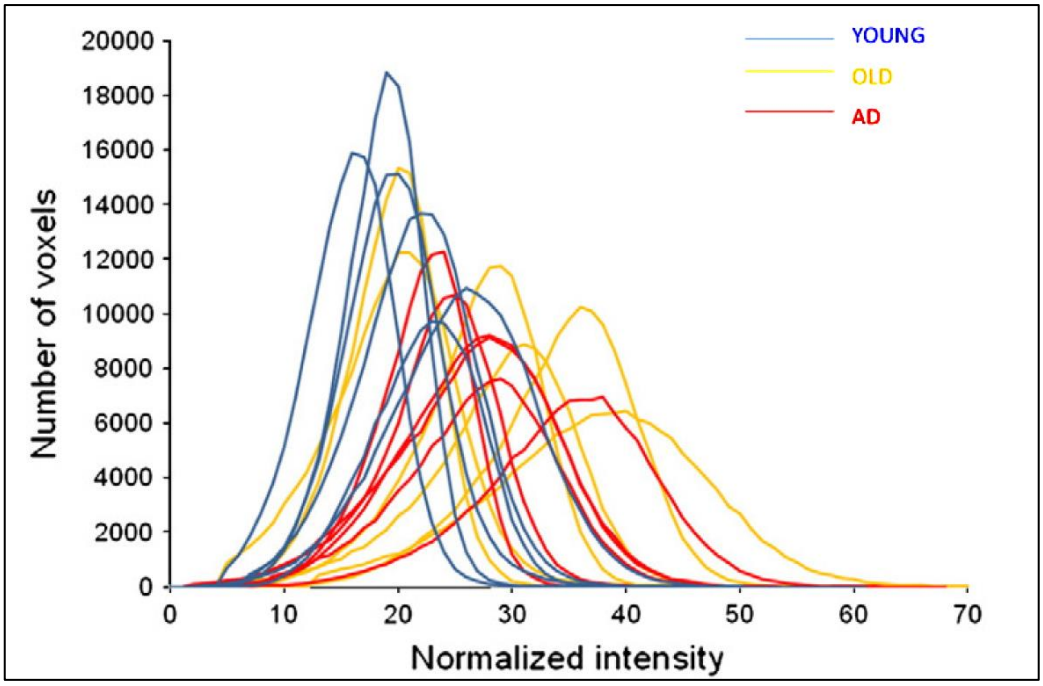


Figure 5.2. Spectra of voxel intensity values, normalised to injected dose and body weight, for young healthy adults, subjects with Alzheimer's disease and age-matched non-demented subjects. Figure taken from Gulyas et al., 2011.

Considerable overlap in voxel values between the three subject groups is apparent, due to a combination of statistical noise as well as inter-individual physiological variations and non-TSPO-specific tissue uptake, but also due to the (probable) modest difference in TSPO expression between the three groups. Precision of quantitative measurements of TSPO expression are therefore highly relevant, both in terms of the sensitivity of the test to pathological changes in an individual subject or patient, and also in terms of obtaining statistically powerful group comparisons in studies with limited subject numbers.

In the preceding chapters, considerable attention was devoted to the task of developing computational tools for the ultimate purpose of estimating the relative voxel noise that is present in [$^{11}$C]-PK11195 PET scans of the human brain. This chapter describes experiments where these tools were employed for their intended purpose.

## 5.2 Aim

The aim of this study was to investigate the effects of varying brain tracer concentration, region-of-interest size, radionuclide half-life and kinetic model complexity on the precision of kinetic parameter estimation, in the context of TSPO PET imaging.

## 5.3 Method

A noise-free reference tissue TAC was defined using the reference [$^{11}$C]-R-PK11195 TAC from 4.2.4.1, described by a two-tissue compartment four-parameter compartmental model, referred to hereafter as the '2TCM'. The 'ground truth' parameter values of $K_1$, $k_2$, $k_3$ and $k_4$ for this reference TAC were known. A second reference TAC was generated by fitting a one-tissue compartment two-parameter compartmental model (1TCM) to the above reference TAC. Although not a perfect fit to the original TAC, this second TAC served as a reference for which the values of the two kinetic parameters ($K_1$ and $k_2$) that described it were known. Both reference TACs and their corresponding kinetic parameters are presented in the following graphs and table (Figure 5.3 Figure 5.4, Table 5.1).

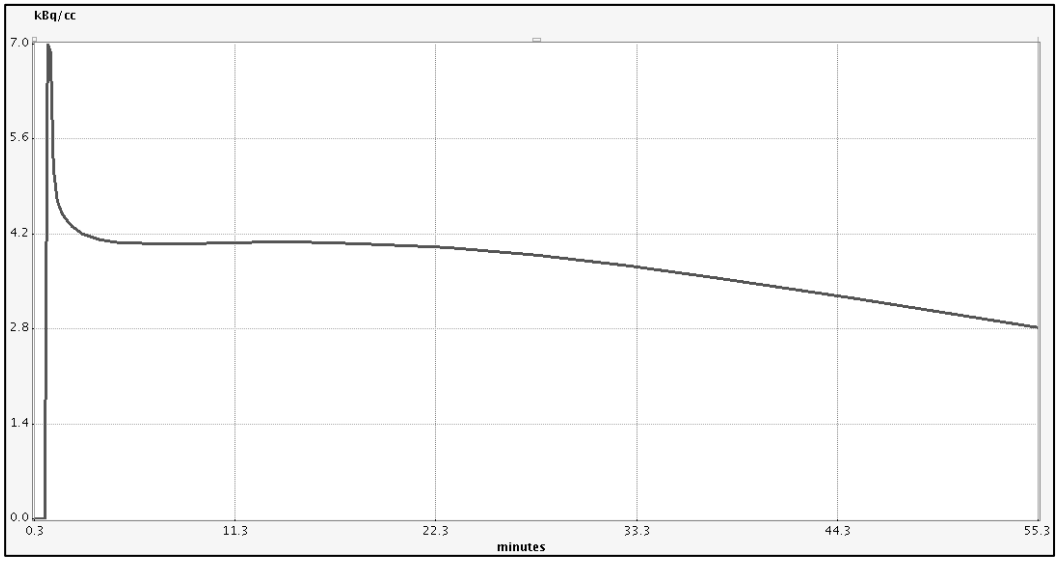


Figure 5.3. Noise-free reference TAC, described by a 2TCM.

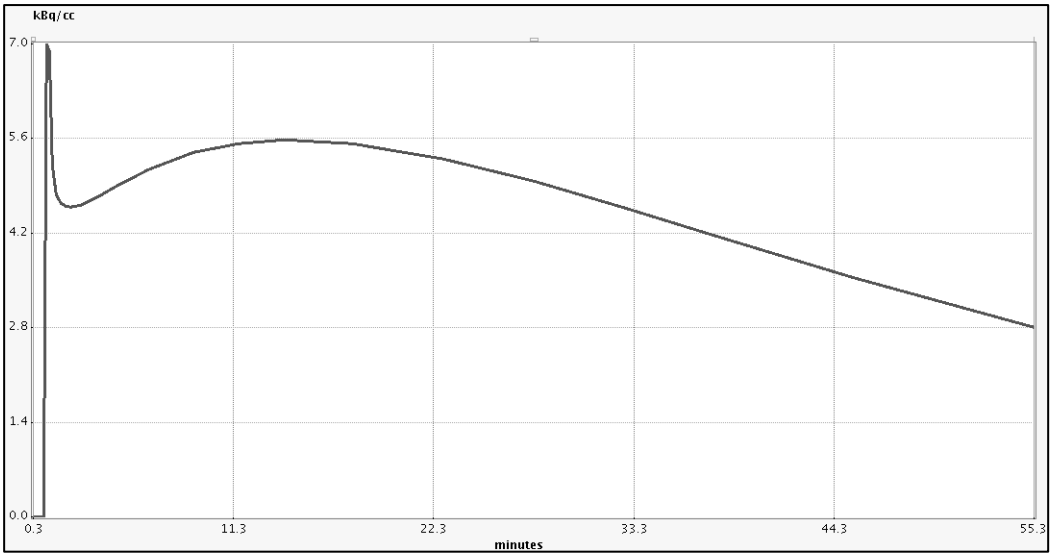


Figure 5.4. Noise-free reference TAC, described by a 1TCM.

Table 5.1. Reference TAC kinetic parameter values. $V_B$ = blood volume fraction. $V_T$ = total distribution volume. *ND* = Not Defined. Blood volume was set to 7.1% according to the findings of Kropholler et al. (2005).

| **Model** | $V_B$ | $K_1$ | $k_2$ | $k_3$ | $k_4$ | $V_T$ | $k_3/k_4$ |
|---|---|---|---|---|---|---|---|
| 2TCM | 0.071 | 0.05 | 0.15 | 0.06 | 0.04 | 0.8333 | 1.5 |
| 1TCM | 0.071 | 0.05 | 0.06 | *ND* | *ND* | 0.8333 | *ND* |

In order to study the effects of image noise on the precision of kinetic parameter estimation, the empirically determined models for grey matter TSPO image noise were used to calculate a standard deviation for each point on the TACs, based on the tissue activity concentration (after radioactive decay to mid-frame) and the frame acquisition time. All noise models used were of the type that incorporated the NECR information (see 4.3.4.2). The same 24 frame temporal sampling schedule used during the GATE simulations was assumed (see 4.2.4.1). In this way, TAC noise was calculated for both 2TCM and 1TCM TACs, for all combinations of the following variables, at the levels indicated in the following table (Table 5.2). Image reconstruction with the filtered back projection algorithm was assumed for all the subsequent analysis.

Table 5.2. Variables considered for their effect on TAC noise and precision of estimated kinetic parameters.

| Variable | Levels |
|---|---|
| Tissue tracer concentration relative to PK11195 reference TAC | 0.5, 1, 2, 3, 5 |
| ROI size | 54mL (large), 1.7mL (medium), 0.53mL (small) |
| Radionuclide half-life | 20.38 min (carbon-11), 109.8 min (fluorine-18) |
| Injected dose | fluorine-18 = 185 MBq only, carbon-11 = 370 MBq and 555 MBq |

Tissue activity concentration was determined by a TAC scaling factor relative to the reference PK11195 TAC, with values ranging from 0.5 to 5. The ROI sizes refer to the 3 ROIs for which the noise model was defined, and are shown in appendix 7.12. Radionuclide half-life was included at two levels, chosen to correspond to the two most commonly encountered radionuclides in TSPO PET tracers: carbon-11 and fluorine-18. The difference in branching ratio between the two radionuclides, which is <3%, was not taken into account in this study.

Analysis of the injected doses reported in the literature for carbon-11 and fluorine-18 labelled TSPO tracers in humans, from 1995 to 2010, showed a median carbon-11 dose of 370 MBq and an average of 433 MBq, with a range of 222 MBq to 888 MBq (Figure 5.5). The distribution was very spread-out, with peaks occurring at around 300MBq, 400MBq, 700MBq and 900MBq. A much narrower spread of injected doses was reported for fluorine-18 labelled TSPO tracers, with a median dose of 173 MBq and a mean of 183 MBq. Therefore the noise calculations corresponding to the fluorine-18 half-life assumed an injected dose of 185 MBq (5 mCi), while for carbon-11, two injected doses were studied: 370 MBq (10 mCi) and 555 MBq (15 mCi).

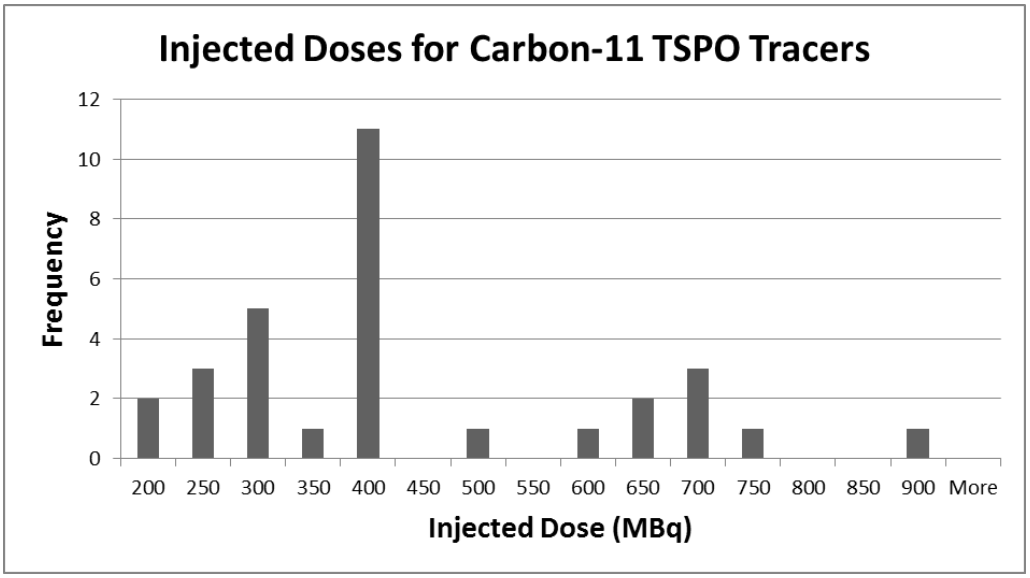


Figure 5.5. Histogram of injected doses reported in the literature for all carbon-11 labelled TSPO tracers, from 1995 to 2010.

A total of 45 noise profiles were therefore generated for each of the 2 reference TACs (90 noise profiles altogether), with each vector containing the standard deviation at each frame point for a given combination of tissue activity concentration, ROI size, radionuclide half-life and injected dose.

Each TAC and noise profile was read into the PMOD software package, along with the original [$^{11}$C]-PK11195 arterial input function used in the GATE simulations (see 4.2.4.1). Simulations for each noise profile were run using the in-built Monte Carlo simulation tool in PMOD, for 1000 runs each. In the case of the 2TCM reference TAC, the parameters $K_1$, $k_3$ and $k_4$ were estimated at each run, while a constant $K_1/k_2$ ratio of ⅓ was assumed. Fixing the $K_1/k_2$ ratio is based on the findings of Kropholler et al. (2005) that fixing the $K_1/k_2$ ratio to that of whole cortex grey matter improves PK11195 parameter estimate reliability for noisy data. The ratio of 1/3 was taken from the known 2TCM reference parameters in Table 5.1 ($K_1$=0.05 and $k_2$=0.15). For comparison, the published grey matter values of Kropholler et al. were $K_1$=0.06 and $k_2$=0.16). For the 1TCM reference, both parameters $K_1$ and $k_2$ were estimated at each run.

The following steps were carried out by the PMOD Monte Carlo program during each simulation. First, an initial fit of the kinetic parameters to the noise free reference TAC produced reference parameter values (i.e. the true values for each parameter) against which all subsequent estimations would be compared. Next, 1000 noisy TACs were generated using

the supplied noise profile for each frame time point. Third, the kinetic parameters were fit to each noisy TAC in turn. From the 1000 fitted parameter values, the coefficients of variation for each fitted kinetic parameter, and for the derived parameters total distribution volume ($V_T$) and $k_3/k_4$ ratio (2TCM only) were calculated for each combination of tissue activity, ROI size and radionuclide. An example of the 1TCM reference TAC, with two noise profiles added, is shown in Figure 5.6 below.

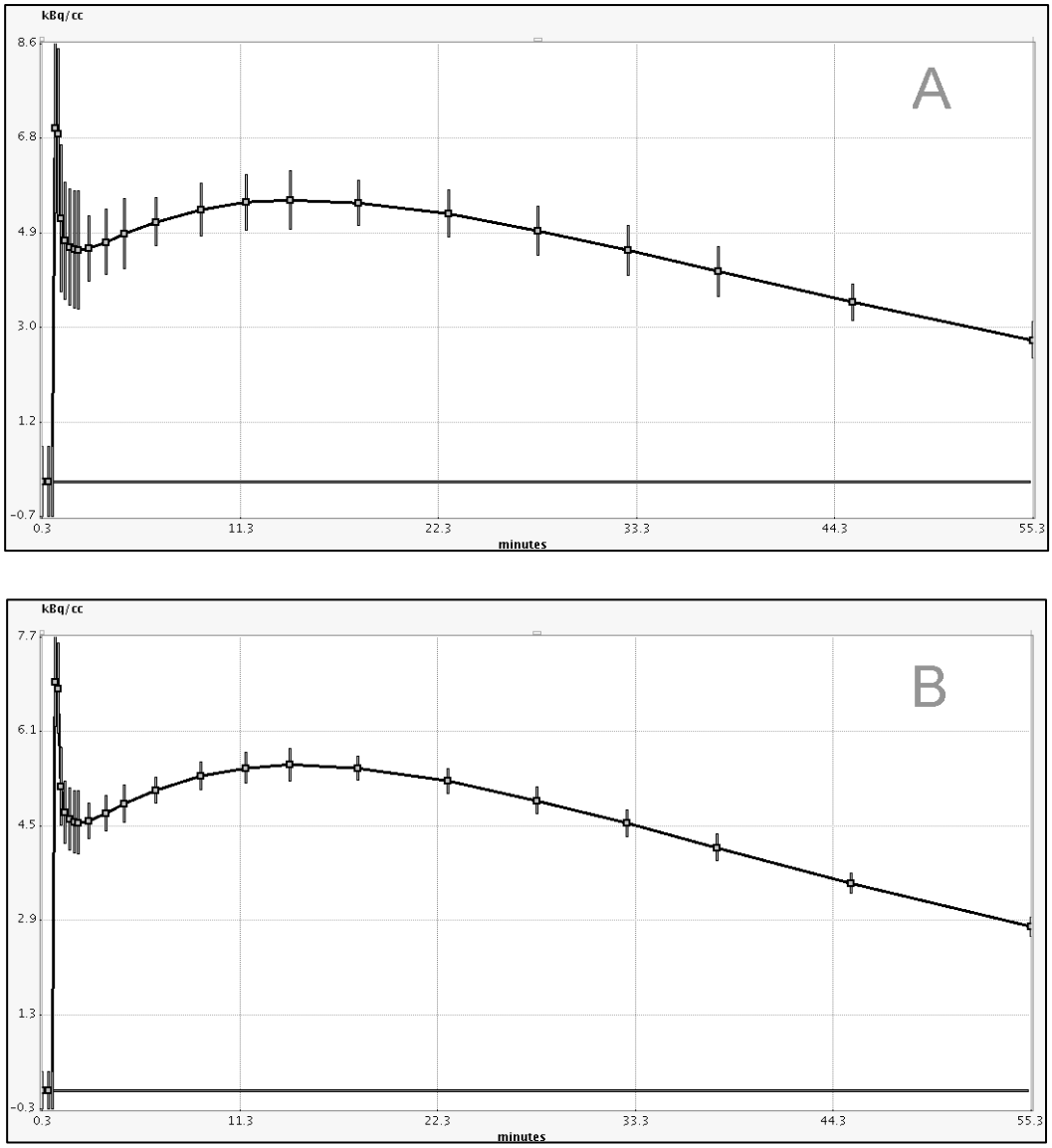


Figure 5.6. Reference TACs (1TCM) showing the calculated standard deviations at each frame (error bars) for a carbon-11 half-life and small ROI size. Noise associated with tissue activity concentrations of 1 x PK11195 (A) and 5 x PK11195 (B) are shown.

## 5.4 Results

In Figure 5.7, the coefficient of variation for the ratio of $k_3/k_4$ is plotted against tissue activity concentration for the large region of interest. The low relative noise associated with the large ROI produced high precision (<5 %CoV) estimates of this binding parameter. An injected dose of 555 MBq of carbon-11 tracer produced very similar precision of parameter estimates to 185 MBq of fluorine-18, while reducing the carbon-11 injected dose to 370 MBq reduced the precision (i.e. increases CoV) by approximately 20%.

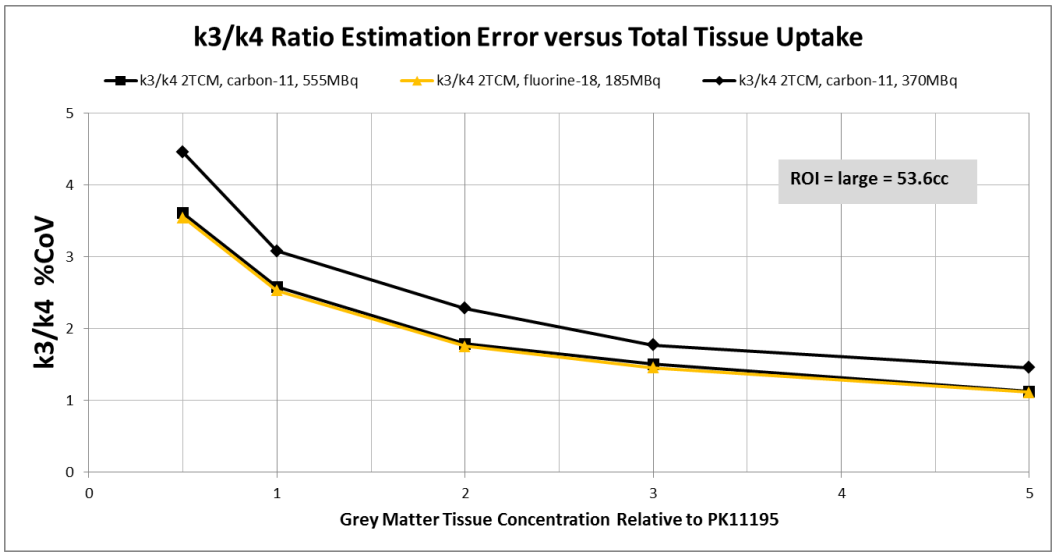


Figure 5.7. Coefficient of variation of $k_3/k_4$ ratio versus relative grey matter tissue activity concentration for a large ROI, for 185 MBq of fluorine-18, 370MBq and 555Mq of carbon-11.

In Figure 5.8 below, the coefficient of variation for the binding parameter known as total distribution volume ($V_T$) is plotted against tissue activity concentration for the same large region of interest. Since $V_T$ may be calculated from both the 2TCM and the 1TCM, the results for both compartmental models are plotted on the same axes for comparison. Again, fluorine-18 and carbon-11 produced similar precision of parameter estimates at injected doses of 185 MBq and 555 MBq respectively, with a small (≈20%) reduction in precision for the lower carbon-11 dose of 370 MBq. Reducing the complexity of the kinetic model from 2TCM to 1TCM, resulted in an increase in precision (i.e. reduction in CoV) of $V_T$ by ≥ 70% at each point. This is consistent with the smaller number of parameters that must be fitted to the 1TCM compared to the 2TCM.

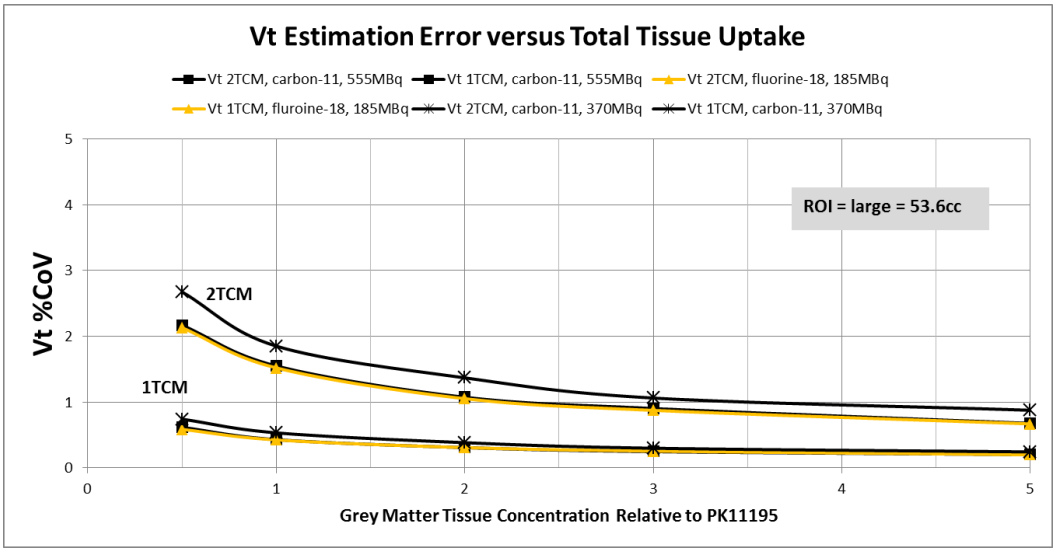


Figure 5.8. Coefficient of variation of total distribution volume ($V_T$) versus relative grey matter tissue activity concentration for a large ROI, for 185 MBq of fluorine-18, 370MBq and 555Mq of carbon-11.

Evidence that the precision of $V_T$ and $k_3/k_4$ ratio, for the large ROI, are well correlated is presented in Figure 5.9 below. A correlation coefficient of $r > 0.99$ was obtained in each case. Fitting a straight line to each plot yielded a $y$-intercept of 0 and proportionality constant equal to 1.67.

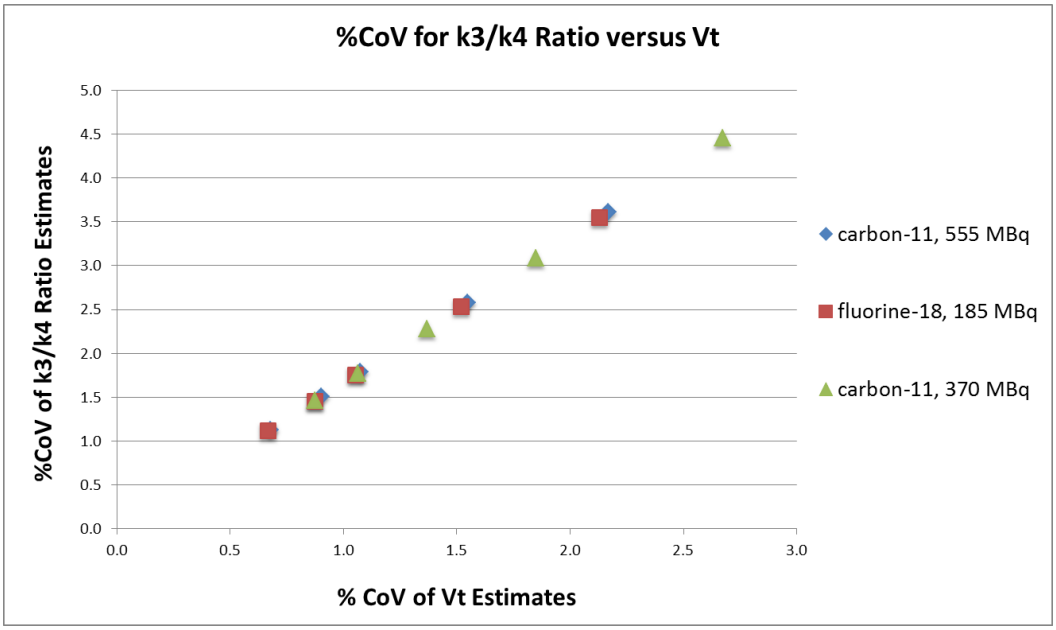


Figure 5.9. %CoV of $V_T$ plotted against %CoV of $k_3/k_4$ ratio for each radionuclide and injected dose.

It is worth pointing out that the accuracy of the parameter estimates is not in question here, and is expected to be high in the case of both compartmental models, because a separate reference TAC was defined for each model. In other words, the appropriateness of a 1TCM or

2TCM is not being evaluated here, only the *precision* of the parameter estimates in each case. To confirm and illustrate this point, the bias of the average parameter estimates, for $k_3/k_4$ ratio and $V_T$, is plotted against the % coefficient of variation for each of the compartment models and injected doses (Figure 5.10). Bias was defined as the relative difference between the average fitted parameters values (averaged over the 1000 simulation runs) and the known true parameter values, expressed as a percentage. Despite some small fluctuations in the parameter values about the true value, and a slight increase in the spread of parameters values as noise increases, a maximum absolute error of only 0.11% was observed.

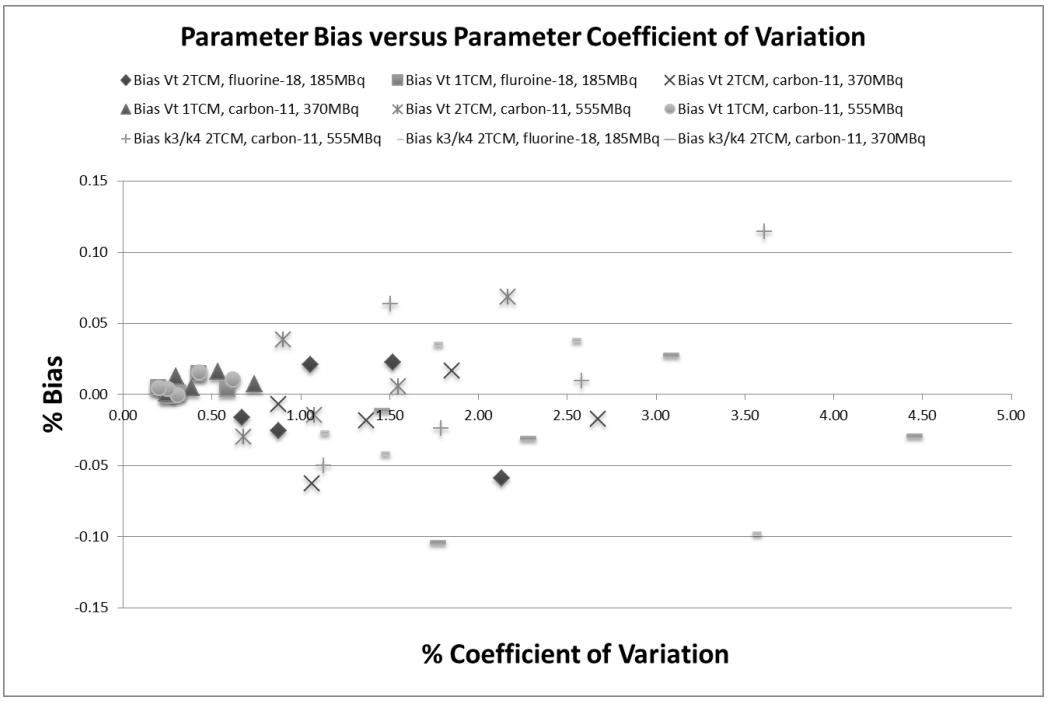


Figure 5.10. Bias, defined as the percentage difference of the average estimated parameter (over 1000 simulation runs) from the known true value of that parameter, plotted against %CoV.

In Figure 5.11 Figure 5.16, the coefficient of variation for the derived parameters of total distribution volume ($V_T$) and $k_3/k_4$ ratio are plotted against tissue activity concentration for the remaining ROI sizes that were investigated. Missing data points correspond to those combinations of variables that returned a parameter %CoV $>10^2$, or where the noise level was too high to produce any meaningful estimates of the kinetic parameters.

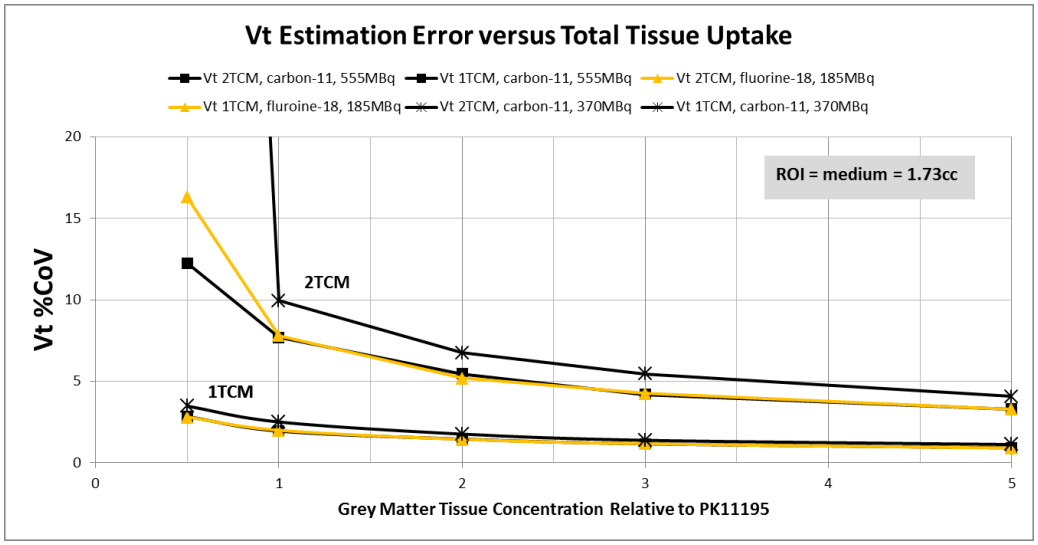


Figure 5.11. Coefficient of variation of total distribution volume ($V_T$) versus relative grey matter tissue activity concentration for a medium size ROI.

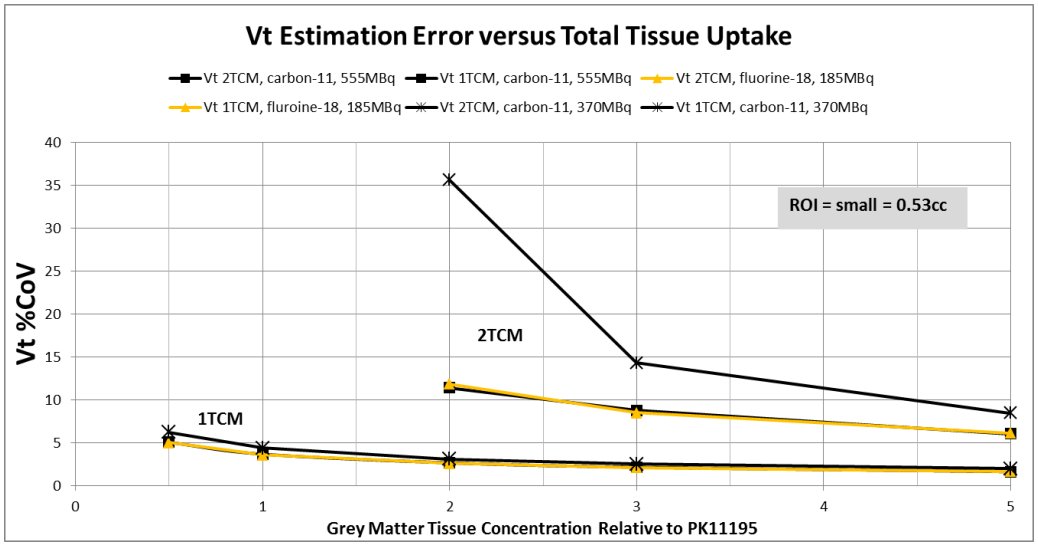


Figure 5.12. Coefficient of variation of total distribution volume ($V_T$) versus relative grey matter tissue activity concentration for a small size ROI.

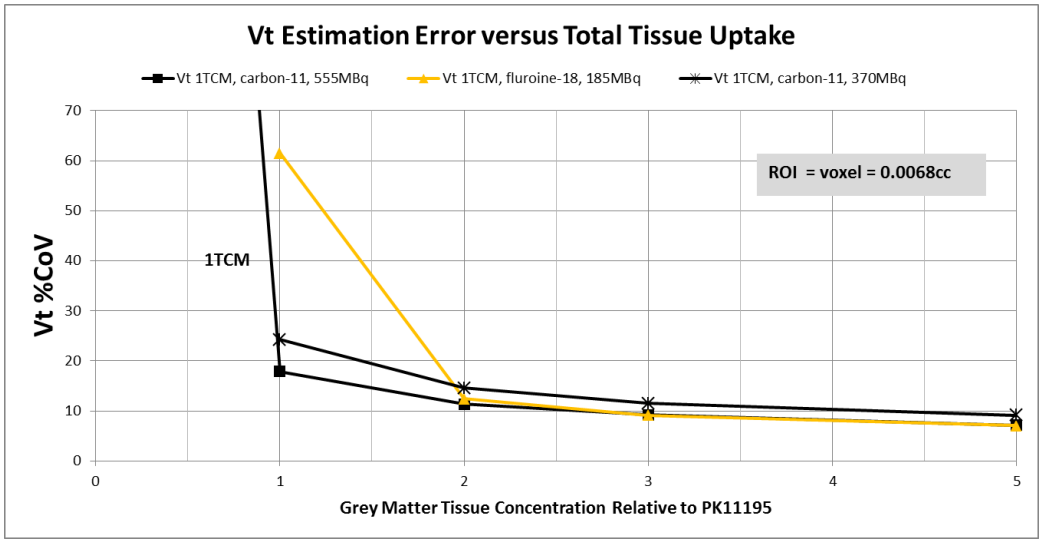


Figure 5.13. Coefficient of variation of total distribution volume ($V_T$) versus relative grey matter tissue activity concentration for voxel-level noise.

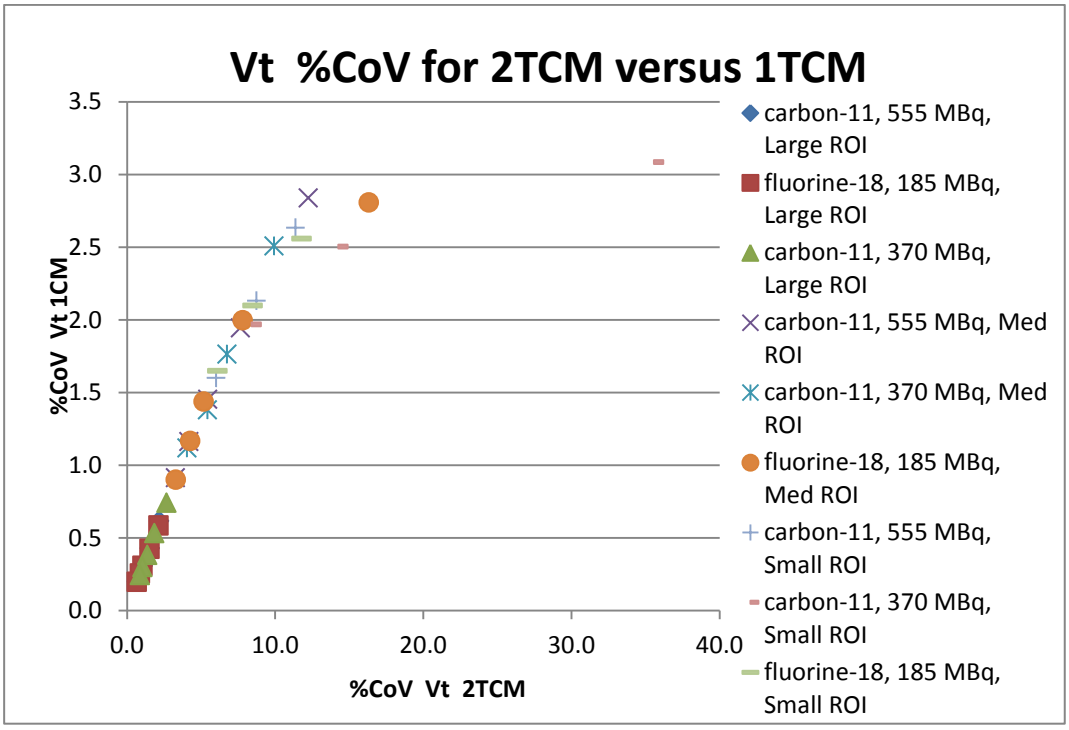


Figure 5.14. Ratio of total distribution volume ($V_T$) %CoV for the 2TCM versus the 1TCM. Average ratio of 2TCM CoV to 1TCM CoV was 0.78.

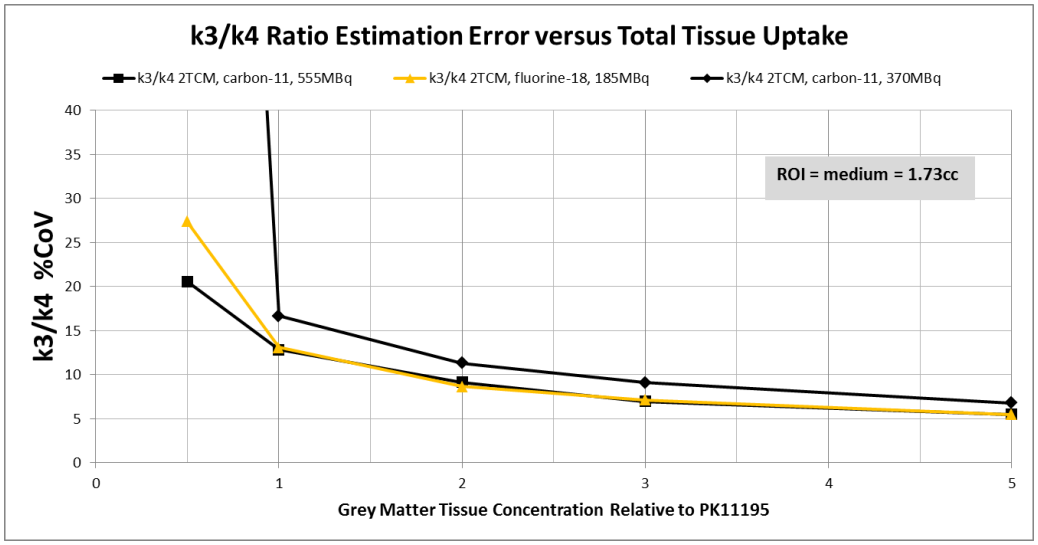


Figure 5.15. Coefficient of variation of $k_3/k_4$ ratio versus relative grey matter tissue activity concentration for a medium size ROI. The $k_3/k_4$ ratio is defined only for a 2TCM.

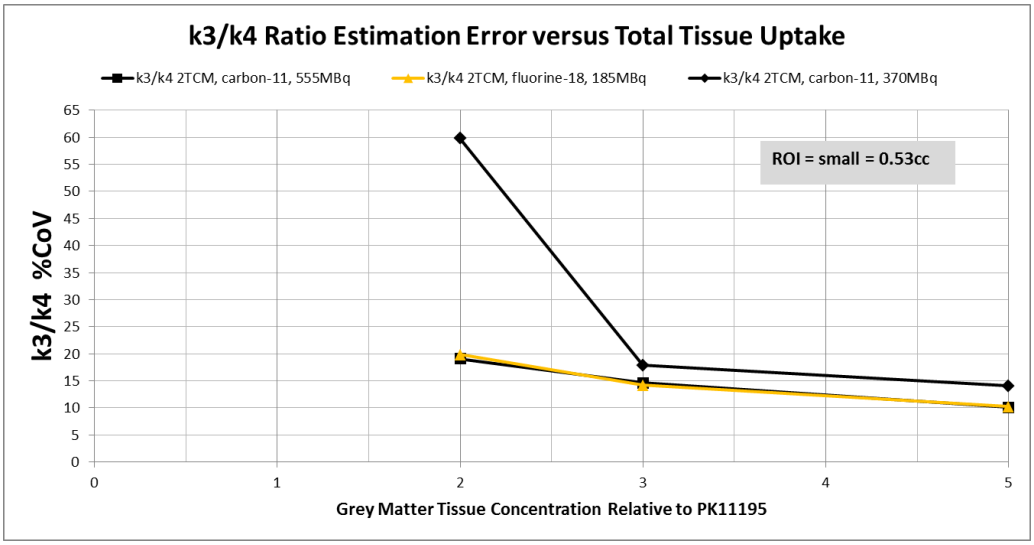


Figure 5.16. Coefficient of variation of $k_3/k_4$ ratio versus relative grey matter tissue activity concentration for a small size ROI.

For the binding parameter of $V_T$, the simpler 1TCM returned consistently more precise estimates than the more complex 2TCM (Figure 5.11 and Figure 5.12). The 1TCM produced estimates of $V_T$ with a CoV that were, on average, 78% lower for each tissue concentration and half-life studied (Figure 5.14). Interestingly, the 1TCM was able to produce an estimate of $V_T$ with similar precision to the 2TCM, but with approximately $1/10^{th}$ the level of tissue activity concentration, for medium and large ROIs. A similar comparison was not available for the small ROI, because the 2TCM was unable to produce reliable parameter estimates at this noise level (%CoV $>10^3$), however, the 1TCM was able to estimate $V_T$, with a precision of ≤6.2 %CoV even for the small ROI, and at each tissue activity level and half-life studied.

Voxel-level noise was too high to obtain reliable parameter estimates from the 2TCM, and the 1TCM only produced reliable (<15% CoV) estimates at tissue concentrations equal to or greater than PK11195.

It is important to note that this study is not directly concerned with the suitability of the parameter $V_T$ for the purposes of quantifying TSPO density with a particular ligand, but only with the precision with which this parameter (and others) may be estimated.

The effect of ROI size on parameter %CoV is illustrated in the plot below (Figure 5.17), for the three ROIs studied. Region of interest size has a large and non-linear effect on parameter %CoV. Although this effect is clearly important, choice of ROI size is usually dictated by other factors.

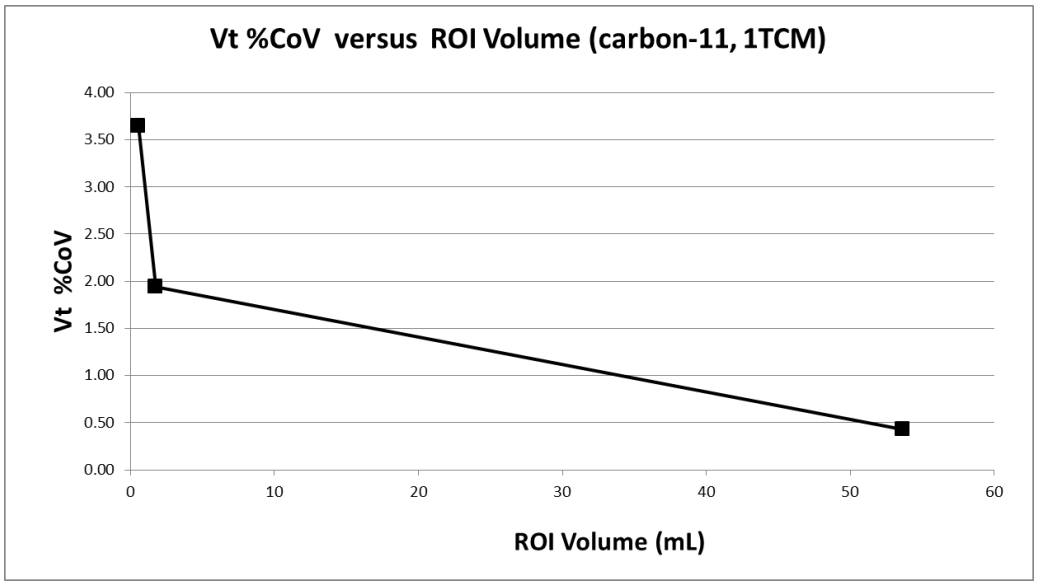


Figure 5.17. Precision of $V_T$ estimates versus ROI volume, for the 1TCM and carbon-11 (555MBq) radionuclide.

## 5.5 Discussion

New PET radioligands for the TSPO are typically evaluated with respect to the prototypical ligand [$^{11}$C]-PK11195, with the aim of addressing the well documented shortcomings of this tracer. In particular, the low brain penetration of PK11195 and high non-specific binding have combined to limit the precision with which changes in TSPO expression in the brain may be quantified with PET. Therefore new TSPO tracers with higher brain uptake, and lower non-specific binding than PK11195 are sought for the primary purpose of improving the precision of TSPO quantification. This study sought to investigate

and quantify the effects of varying brain tracer concentration, region-of-interest size, radionuclide half-life and kinetic model complexity on the precision of kinetic parameter estimation, in the context of TSPO PET imaging, and to evaluate their relative influence on this precision.

The grey matter time-activity curve and plasma input function for [$^{11}$C]-PK-R-11195 were used as kinetic 'templates' for this study, however new TSPO PET ligands are not necessarily expected to follow the kinetic example of PK11195 in this way. Kinetic properties (tissue uptake, clearance rates etc.) themselves can influence the relative image noise at each time point in the TAC, by determining how much radioactivity is present in tissue at each time. Therefore by keeping the shape of the tissue TAC constant[1] for each combination of variables studied, the effects of tissue activity, radionuclide half-life and compartmental model complexity could be studied in isolation from this potentially confounding factor.

Tissue radioactivity concentration was studied here by simply scaling each point in the tissue TAC by a factor relative to the original [$^{11}$C]-R-PK11195 TAC. Using this approach, the tissue activity concentration may be conceived of as an increase (or decrease) due to different tracer uptake properties, or to injecting a higher (or lower) dose of tracer. It could potentially be thought of as relating to improved (or reduced) scanner sensitivity, insofar as a change in sensitivity translates directly to a change in the NECR performance of the system at the relevant counting rates. Since the aim of this study was not to investigate the performance of specific TSPO PET tracers, but rather to draw more general conclusions about the factors that might affect TSPO PET quantification, the above two methodological simplifications were considered to be justified.

The results obtained from this study indicate that there is a non-linear, inverse relationship between tissue activity concentration and kinetic parameter %CoV. At the injected dose levels studied, both radionuclides provide broadly similar parameter precision, with the higher carbon-11 dose of 555 MBq yielding very similar parameter precision to an injected dose of 185MBq of Fluorine-18. The lower carbon-11 injected dose of 370MBq is associated with slightly higher (≈ 20%) parameter %CoV. It can be concluded from this that, at typically injected doses and for dynamic scans lasting 60 minutes or less, and all else being

[1] Two reference tissue TACs were used in this study, which were slightly different in shape due to the different compartmental model parameters used to describe them. However they both followed the general shape of the original PK11195 grey matter TAC closely, so may be considered 'constant' for the purposes of this argument.

equal, fluorine-18 labelled tracers yield the same precision estimates of kinetic parameter as carbon-11 labelled tracers. In terms of equivalence of parameter precision, 555 MBq of carbon-11 tracer is approximately equivalent to 185 MBq of fluorine-18 tracer.

A survey of the TSPO PET literature from 1995 to 2010 suggested that there was considerable variation in the injected dose of carbon-11 labelled TSPO tracers, ranging from 222 MBq to 888 MBq. The results obtained here suggest that, all else being equal, such a wide range of injected doses could lead to significant differences in kinetic parameter CoVs. Therefore, for carbon-11 labelled TSPO tracers, careful consideration should be given to the injected dose with consideration given to the expected scan duration and even the sensitivity of the PET scanner. Radiation dosimetry for the carbon-11 labelled TSPO ligands is expected to be comparable to other carbon-11 labelled tracers (5.1 μSv/MBq mean effective dose for [$^{11}$C]-R-PK11195 (Hirvonen et al., 2010) and 6.6 μSv/MBq mean effective dose for [$^{11}$C]-PBR28 (Brown et al., 2007)). Further research into the effects of injected dose, over a wider range than studied here, is warranted.

Other factors not studied here may favour fluorine-18 as the preferred choice of radiolabel, such as the economic or logistical advantages of manufacturing and distributing tracers to remote imaging sites. The longer half-life of fluorine-18 also makes it more suited to imaging beyond 1 hour post injection. Radiotracers with high affinity, for example, often require longer imaging times to measure receptor parameters than similar tracers of lower affinity, due to the increased time required to properly capture the uptake, equilibrium and washout phases of the ligand-receptor interaction (Laruelle et al., 2003).

Complexity of compartmental model had a strong influence on the precision of the binding parameters. For example, the 1TCM yielded CoV of $V_T$ estimates that were at least 70% lower than for the 2TCM, while the 1TCM CoV of $V_T$ estimates were at least 80% lower than 2TCM estimates of $k_3/k_4$ ratio (see Figure 5.11 and Figure 5.12).

These findings suggest that model complexity is a greater determinant of quantitative precision than the image noise (i.e. due to brain uptake, or total counts collected). Similar findings were reported by Koeppe et al. who investigated the in-vivo kinetic behaviour of [$^{11}$C]-flumazenil, a radioligand for the central benzodiazepine receptor (Koeppe et al., 1991). The authors reported that the: “variability in the estimates of the receptor-related parameters is far more dependent upon the model configuration employed”, and noted parameter CoV was reduced to levels “as good as or better than” those seen in other PET brain scanning

procedures, including $^{18}$F-FDG metabolism studies (typically associated with very high brain uptake of tracer), when a simple two-parameter 1TCM was employed. Therefore the findings of the present study are entirely consistent with what is known about the effects of model complexity on parameter precision.

In the example cited above, a 1TCM was found to be a suitable model for the receptor binding characteristics of [$^{11}$C]-flumazenil principally because the tracer's high rate of specific binding, and low levels of non-specific binding, meant that the *specific* component of the total distribution volume ($V_T$) was dominant, and could therefore provide a reasonable estimate of $B_{max}$ (receptor density). Additionally, the 1TCM was found to provide a better fit to the TAC for brain regions containing high concentrations of the target receptor, due to the relatively rapid equilibration of the free and specifically bound tissue compartments with respect to the PET scan duration and the $K_1$ and $k_2$ transport rates- which is a requirement for simplifying a 2TCM to a 1TCM. Regions with a lower concentration of target receptor were not described as well with the 1TCM.

The significance of these findings for TSPO PET lies in the ongoing research to find a replacement ligand for [$^{11}$C]-PK11195. As discussed in the introduction to this chapter (see 5.1), the density of TSPO expression in the normal human brain is low, and the increase in TSPO expression typically associated with neurological disease is relatively modest. This suggests that the specific distribution volume ($V_3$) of any TSPO ligand will likely be a small fraction of the total distribution volume ($V_T$) for all except those ligands with extremely low non-specific binding, thereby ruling out analysis with a simple 1TCM.

If a 2TCM is required, then the results of this study indicate that reasonably precise estimates of $k_3/k_4$ ($\leq$ 20% CoV) may be obtained for small regions of interest (0.53 mL) if tissue radioactivity concentration is increased by at least a factor of 2 over that observed with 555 MBq of [$^{11}$C]-PK11195 (see Figure 5.16). This could be achieved, for example, through the use of a TSPO ligand that demonstrates approximately twice the brain uptake of PK11195. Fitting of 3 parameters was also assumed (fixed $K_1/k_2$ ratio) in this analysis.

Alternatively, if a (hypothetical) TSPO ligand could be found with kinetic properties conducive to analysis with a 1TCM, the findings of the present study suggest that this would go as far or further towards improving quantitative precision than measures aimed only at increasing brain tissue radioactivity concentration (e.g. higher brain uptake ligands or higher injected dose). Referring to the findings of Koeppe et al. (1991), and considering of the

established principles of tracer kinetic modelling (Huang & Phelps, 1986; Laruelle et al., 2003), radiotracers that may be described with "simple models" that are suitable for estimating the process of interest should, as far as possible, have:

- extremely low non-specific binding
- tissue kinetics that are related only to the process of interest
- low extraction fraction- to reduce dependence of the measured parameters on blood flow
- rapid equilibration of the free and specifically bound tissue compartments with respect to the PET scan duration, and the $K_1$ and $k_2$ transport rates, allowing these compartments to be merged into a single tissue compartment
- trapping of the tracer in a slow turnover compartment after tracer has gone through the process of interest
- high specificity to the process of interest
- fast plasma clearance to reduce blood volume effects and to reduce time required to reach equilibrium

The above requirements are often contradictory and can be difficult to satisfy completely in one tracer. Lipophilicity is an important property in that it is associated with the ability of a ligand to cross the blood-brain barrier (Clark, 2003). Affinity for the target is an important ligand property. From a kinetic modelling perspective, the required ligand affinity depends on the concentration of target sites, with low concentration of target generally requiring relatively higher affinity ligands, and vice-versa (Laruelle et al., 2003). Maximising the ratio of specific to non-specific binding is crucially important to achieving reliable quantification, and this ratio increases as $B_{max}$ (target receptor density) and ligand affinity increase, and as non-specific binding decreases. To the extent that the TSPO may be considered a 'low receptor density' target in comparison to other PET receptor targets, then high affinity and low non-specific binding are arguably more important than for other PET tracers, especially if a TSPO tracer is to be considered for 1TCM analysis. However, if higher ligand affinity is also associated with higher lipophilicity, then this could lead to higher non-specific binding, potentially negating any benefit. All else being equal, an increase in ligand affinity will generally require an increase in scan duration to properly capture the uptake, equilibrium and washout phases of the kinetics, which would further favour the use of fluorine-18 as the preferred radiolabel for TSPO tracers. Therefore, the low target density of

TSPO in the brain, and the (possibly) subtle changes in TSPO density that accompany disease, make this a particularly challenging target for quantification.

Several groups have reported on the use of the simplified reference tissue model (SRTM) (Lammertsma & Hume, 1996) for the analysis of [$^{11}$C]-PK11195 PET data. Kinetic models based on reference tissues have several advantages: they do not require an arterial plasma input function, making PET procedure less invasive and less labour-intensive, and they may be applied to individual image voxels for parametric image generation (Gunn, Lammertsma, Hume, Myers, et al., 1997). Despite the difficulty associated with defining an anatomically discrete TSPO reference region (i.e. free from specific binding), success has been reported with the application of clustering techniques for defining a subset of brain tissue reference voxels (Turkheimer et al., 2007; Yaqub et al., 2012). Reference tissue models were not investigated in this study, however in light of the findings already discussed, it is worth noting that an underlying assumption of the SRTM is that the tracer kinetics in the target region are described by a 1TCM (Ikoma et al., 2008; Lammertsma & Hume, 1996). Bias introduced by the violation of this (and other) assumptions is likely to be present consistently across subjects, and has been considered by some to be an acceptable trade-off for the other advantages (non-invasiveness, parametric images etc.) of the reference tissue methods (Banati, 2002; Kropholler et al., 2006).

In the event that a TSPO tracer were found that could satisfy the requirements for analysis with a simple 1TCM, the results of the present study indicate that a *reduction* in brain tissue uptake relative to [$^{11}$C]-PK11195 might be acceptable, at least in terms of obtaining reliable parameter estimates at the ROI level. For example, a TSPO ligand that shows lower brain uptake than PK11195 might produce more precise binding parameter estimates if it could be adequately described by a 1TCM. However, a limitation of the noise model used in this study is relevant here: no account was taken of the effects of intrinsic radioactivity in the PET detectors, nor was the minimum detectable activity (with or without intrinsic radioactivity) investigated for the simulated scanner and image reconstruction algorithm used. Further research is therefore required to answer the question: what is the lowest actual tissue activity concentration that may be used to derive quantitative kinetic parameters for TSPO PET, and how does scanner sensitivity and intrinsic detector radioactivity affect this minimum level? This is related to the issue of the effects of variable injected doses of carbon-11 labelled TSPO tracers discussed above, and could potentially be studied in combination with this issue.

The issue of inter-subject variation in the apparent affinity of many 'second generation' TSPO ligands was not included in this analysis. A recent study (Guo, 2012) predicted the performance of several second generation TSPO radioligands ($^{18}$F-PBR111, $^{11}$C-PBR28 and $^{11}$C-DPA713) using a biomathematical model. In-silico (i.e. computer modelling) and in-vitro information about the tracers was used to predict tissue TACs, a noise model (derived empirically from real ROI TACs) was applied, and binding parameter CoV was estimated for each tracer. Improved performance of all second generation ligands was predicted in terms of within-subject reproducibility of parameter estimates, and for between-subjects disease characterisation type tasks. Nonetheless, the variable binding affinity of the second generation ligands required that the subject's binding class be known prior to analysis.

The present study bears some similarity to the one cited above, in that the potential of new TSPO tracers was evaluated in terms of predicted kinetic parameter precision. In the present study, consideration was given to the more general factors that influence the precision, whereas the study by Guo et al. dealt with specific second generation TSPO ligands, and the implications of the predicted parameter precision on their performance in longitudinal and disease characterisation studies. Given the findings presented here- that compartmental model complexity has a large influence on the precision of kinetic parameter estimates; potential exists to extend the work of both studies by using the biomathematically predicted tissue TACs for a large range of potential TSPO tracers to search for ligands that might meet the criteria for radiotracers amenable to analysis with simple models. Further validation and extension of the noise models derived in this work might also be useful, to cover a wider range of tissue uptake and counting rate scenarios.

Pursuing new TSPO radioligands, predominantly on the basis of higher brain uptake than PK11195 in healthy subjects, has been criticised on pharmacological grounds (Luus et al., 2010). Evidence for more than one binding site for different TSPO ligands, and the possibility of additional TSPO binding sites found only in activated microglia, suggests that increased uptake in normal brain tissue alone is not necessarily indicative of a better ligand for measuring TSPO expression in disease. Luus et al. further argue that early screening of potential TSPO ligands may have missed potentially useful ones on the basis that they showed low affinity for the TSPO in the non-activated state. The motivation for finding a replacement for [$^{11}$C]-PK11195 is to find a more sensitive marker of inflammatory disease in the brain, therefore the level of brain uptake is only one important factor that needs to be

considered, not only from a pharmacological point-of-view, but (as the findings of this study indicate) from an imaging quantification point-of-view.

## 5.6 Conclusions

The aim of this study was to investigate, within the context of TSPO PET imaging, the effects of varying brain tracer concentration, ROI size, half-life and kinetic model complexity on precision of kinetic parameters. The radioactivity concentration in brain tissue influences TSPO binding parameter precision in a non-linear manner, with more tissue 'uptake' being associated with more precise parameter estimates. This was true for all ROI sizes, injected doses and nuclide half-lives studied. Radionuclide half-life (20 or 110 minutes) is less important in determining parameter precision, however injected dose has an influence and further research into the effects of carbon-11 injected dose on quantitative precision for TSPO tracers is warranted.

Complexity of the compartmental model used to analyse the PET data has a large influence on precision of binding parameters, with simpler models (i.e. fewer compartments and parameters) producing more precise estimates of binding parameters. Estimates of the binding parameter $V_T$ were on average 78% lower for the 1TCM compared to the 2TCM.

The findings of this study support the idea that adequate quantification of TSPO expression in the brain might be achievable in principle, using a tracer with less brain uptake than [$^{11}$C]-PK11195, if a simple one-tissue compartment two-parameter compartmental model could provide an adequate description of the observed brain tissue kinetics. However, given the already low tissue activity concentrations observed with [$^{11}$C]-PK11195, the issue of minimum detectable activity, in the presence or absence of intrinsic detector radioactivity, and in combination with scanner sensitivity and optimization of image reconstruction algorithms requires further investigation to clarify this point.

This study suggests that in the pursuit of more reliable TSPO binding quantification, a more holistic approach should be taken that considers the various tracer kinetic properties that might improve image signal-to-noise ratio, and that lend themselves to analysis with a simple one-tissue compartmental model, rather than considerations of total brain uptake or non-specific binding as isolated factors. Similarly, if accurate predictions of tracer kinetics may be made from in-vitro data, as recent reports suggest, then an emphasis on the likely kinetic properties of novel TSPO ligands should be applied during screening.

# Chapter 6 Major Conclusions and Future Work

## 6.1 Major Conclusions

The overall aim of this research was to investigate the effects of image signal-to-noise ratio on TSPO PET quantification. To this end, novel computational tools were developed and validated. This research describes for the first time the application of a purpose-built Microwulf 'personal desktop' cluster for large scale Monte Carlo simulations in medical imaging. The favourable cost-to-performance ratio of modern commodity computer components was exploited to achieve computational speeds on a single 'desktop' cluster that until recently were available only from large scale shared resource systems.

Prior to this research, the relative contribution of model complexity to the reliability of parameter estimation compared with factors that more directly affect relative image noise (such as scanner sensitivity, radioactive half-life and injected dose) was unknown. This research has demonstrated that even at the relatively high image noise levels found in dynamic 18 kilodalton (18kDa) Translocator Protein (TSPO) positron emission tomography (PET) scanning, high precision of kinetic parameters is obtainable *if* the ligand kinetics in brain tissue may be adequately described by a simple one-tissue compartment kinetic model. Going from a 2 tissue compartment model to a 1 tissue compartment model has a similar effect on parameter precision as increasing tissue concentration (or scanner sensitivity, or injected dose- at least as far as these things are related linearly) by a factor of about 10. The significance of these findings relates to the search for better TSPO PET radioligands: it is important to consider total brain uptake and non-specific binding in conjunction with the tissue kinetic properties of novel TSPO ligands, rather than as isolated factors.

### 6.1.1 High Performance Computer Clusters

The first aim of this thesis was to investigate the potential of modern computer clusters and Monte Carlo simulation software as tools for measuring image noise in PET. Investigation was made of several different options available, including shared resource compute facilities and personal 'desktop' (a.k.a. Microwulf) clusters. Recent advances in personal computer (PC) hardware, and the evolution and proliferation of Beowulf-type commodity clusters made the personal 'desktop' cluster option attractive in terms of performance and cost. The feasibility of performing a full dynamic [$^{11}$C]-PK11195 PET scan

simulation, with 40 independent repeats of each frame, using the GEANT4 Application for Tomographic Emission (GATE) Monte Carlo simulator, within a time period of less than 6 weeks, was demonstrated using a cluster assembled from relatively inexpensive components. As far as the author is aware, this is the first reported use of a Microwulf type computer cluster in medical imaging research.

### 6.1.2 Image Noise in PET

A model of a PET tomograph was developed within the GATE simulation environment, to allow study of the effects of PET image noise in as realistic a manner as possible. The simulated scanner was modelled after several current generation clinical (human) PET systems in terms of detector geometry, material, size and performance. Validation was accomplished using modifications of the NEMA PET quality acceptance protocols for scanner resolution, sensitivity, scatter fraction and noise equivalent counting rate performance. Results indicated that performance of the simulated scanner was within the range of current generation PET systems.

An analytical model that describes the image noise, at the voxel level and for several ROIs, as a function of tissue activity concentration and acquisition time, for radiotracers with uptake similar to [$^{11}$C]-PK11195 in the brain, was empirically derived. Using the 'gold standard' of Monte Carlo noise measurements, the model was validated for the purposes of estimating kinetic parameter precision of a dynamic [$^{11}$C]-PK11195 scan. It was concluded that the analytical noise models derived from Monte Carlo noise measurements provided accurate estimates of image noise in dynamic TSPO PET studies, for any combination of tissue activity concentration and acquisition time.

### 6.1.3 Image Noise and Kinetic Parameter Precision for TSPO PET

The effects of brain tissue activity concentration, ROI size, radioactive half-life, injected dose and compartmental model complexity were investigated for their effects on the precision of TSPO quantification. Precision of binding parameter estimates was greatly improved when tissue activity concentration was increased, and when the compartmental model complexity was reduced from a two-tissue compartment four-parameter to a one-tissue compartment two-parameter model. Binding parameters of equivalent precision were produced for carbon-11 and fluorine-18 tracers over an hour-long dynamic scan, assuming an injected dose of 185 MBq for the fluorine-18 tracer and 555 MBq for the carbon-11 tracer.

Research aimed at finding a replacement for [$^{11}$C]-PK11195 has focussed on candidate ligands that show increased brain uptake (due usually to higher $K_1$ or higher ligand affinity) than PK11195 and lower non-specific binding, in order to maximise image signal-to-noise. This research confirms that these are reasonable goals, however it has highlighted the equal important role of kinetic model simplicity (i.e. the number of parameters that must be estimated) in influencing the precision of binding parameter estimates. For example, less than 10% coefficient of variation of the binding parameter of total distribution volume ($V_T$) was achieved even at tissue concentrations one-half that of [$^{11}$C]-PK11195. These findings suggest that ultimately, the usefulness of a TSPO tracer, at least in terms of the precision with which binding parameters may be estimated, is determined as much by the simplicity of the compartmental model that can describe it's kinetics in the brain, as it is by the degree of uptake into the brain.

The findings of this research therefore indicate that a broader consideration of the kinetic properties of novel TSPO radioligands is at least as important as the current focus on obtaining higher brain uptake, in the search for the next generation of TSPO PET tracers. The significant advantage, in terms of quantitative *precision*, conferred by the use of a one-tissue, two-parameter compartmental model rather than a more complex two-tissue, four-parameter model, should favour the use of TSPO ligands whose kinetics in the human brain might be adequately described with such a simple model, even if such a ligand should demonstrate similar or even lower brain uptake than the current reference ligand [$^{11}$C]-PK11195. This implies a ligand with low non-specific binding, and a relatively rapid exchange of ligand from free to specifically bound compartments, even if this comes at the expense of slightly lower brain uptake than that of other candidate ligands. As far as the author is aware, no such TSPO ligands have been reported to date.

## 6.2 Future Research

From the outcomes of this research, the following areas are identified as either methodological improvements or as further avenues of inquiry.

The use of low-cost commodity clusters in medical imaging research is an area of potential growth, due to the unprecedented cost-to-performance ratio of current systems. The peak simulation rate obtained from the cluster described in this thesis was approximately 36 times slower than 'real-time', for a high-resolution digital brain phantom containing 10.26 MBq, including attenuation modelling, but neglecting the parallel execution overheads.

Assuming that demand for efficient and realistic Monte Carlo simulations continues, these findings suggests that efficient job-splitting and output data merging will become an important area of research. Although these issues were effectively 'side-stepped' during this project (due to the relatively small data merging overheads with respect to the lengthy simulations that were undertaken), the issue is likely to become more important as processor speed increases or as the number of computing nodes employed in parallel is increased.

Image reconstruction algorithm is well known to play an important role in determining image noise properties, and further research into the effects of image reconstruction algorithm and parameters in the context of TSPO brain PET imaging is warranted. The use of the relatively simple single-slice re-binning approach in this work could be extended to more commonly used Fourier re-binning approach, or to fully 3D reconstruction algorithms. Of particular interest are the findings that OS-EM produced a strongly skewed distribution of image voxel values at count levels typically found in all frames of a dynamic [$^{11}$C]-PK11195 study. The use of direct '4D' reconstruction algorithms is an area that has also been shown to improve the quantification of binding parameters (Angelis et al., 2011; Matthews, Angelis, Kotasidis, Markiewicz, & Reader, 2010), but was not investigated here.

The limits of PET with respect to activity detectability at very low count rates requires further exploration, particularly in the context of intrinsic lutetium-176 activity that is found in the detectors of many contemporary PET tomographs. The findings of this research suggest that adequate precision of binding parameters may be obtained even at lower tissue concentrations than that found with [$^{11}$C]-PK11195, providing that the tissue kinetics may be adequately described with a one-tissue compartmental model. However the question of minimum detectable activity was not explored in this study, nor did the noise model developed for this study take account the effects of intrinsic detector radioactivity. A Monte Carlo investigation of detection and quantification limits at low count rates, including accurate modelling of lutetium-176 background and TSPO tracer distributions, could help to answer this question.

Effects of positron range on image quality were ignored in this research. Simulation of positron interactions within the GATE software is possible, but requires much longer computation times than was considered feasible. Although the range in tissue for carbon-11 and fluorine-18 positrons is expected to be small with respect to the spatial resolution of the

scanner simulated (<2 mm versus 6 mm), any effects due to this non-zero range would not have been captured in the data from this study.

# Chapter 7 Appendices

## 7.1 Appendix 1: Nomenclature of the 18kDa Translocator Protein

The 18kDa Translocator Protein, abbreviated to TSPO, is also known as the Peripheral Benzodiazepine Receptor, usually abbreviated to PBR. It has also been referred to in the literature as the Peripheral Benzodiazepine Binding Site, or PBBS (Banati, 2002). The designation 'PBR' originated because it was first discovered in organs outside the central nervous system (i.e. in the periphery) and was found to bind Diazepam (Valium™), a well-known drug and ligand for the *central* benzodiazepine receptor. Although the term 'PBR' was used for many years, '18kDa Translocator Protein' was proposed as a more accurate alternative (Papadopoulos et al., 2006) and has gained currency in recent years. For consistency, the term 'TSPO' is preferred in this thesis.

## 7.2 Appendix 2: Pilot Study on a High Performance Computer Cluster

A high performance cluster (referred to as the 'second cluster' in 3.1 ) consisting of 23 nodes (42 computing cores total) was studied to assess the feasibility of performing large scale PET simulations for the purpose of determining the signal-to-noise ratio of dynamic brain PET scans. Each node consisted of either a dual core or quad core CPU, and was equipped with 2 Gbytes of memory.

A simulation using the GATE software and the digital emission and attenuation phantoms described in 3.1.2.3, 3.1.2.3.1 and 3.1.2.3.2 was run. A total of 35 MBq of activity was distributed within the soft tissues of the digital phantom. The scanner description macro given in appendix 7.4 was used. A PET acquisition of 0.001 seconds was run using one core of a quad-core computing node on the cluster. The simulation was then repeated by duplicating the first simulation and running it in parallel with the first simulation on the same quad-core node. Likewise three simultaneous simulations were run on the same quad-core node. Finally four simultaneous simulations were run on the same node. The time taken and memory used by each run was recorded, and the results are presented below.

| Cores Used | Execution Time (seconds) | Memory Used (Gbytes) | Swap Space Used (Gbytes) |
|---|---|---|---|
| 1 | 39 | 1.16 | 0.21 |
| 2 | 40 | 1.94 | 0.17 |
| 3 | 46 | 1.94 | 1.10 |
| 4 | >200 | 1.94 | 1.94 |

The results above indicate that memory on this node is insufficient to support four independent simultaneous GATE simulations. Swap space (hard disk drive space used by the operating system to supplement the memory) was able to compensate for this inadequacy when three simulations were run concurrently, but with a noticeable increase in execution time. Four simulations were not able to be run within a reasonable time frame and the program was terminated after 200 seconds. Examination of the cluster hardware revealed that

only 18 out of a total of 42 CPU cores could be utilised due to this memory limitation. By extrapolation, completion of 50 repeated acquisitions of 10 minutes duration would require approximately 2.4 years execution time using this system- well outside the goal of 6 weeks or less.

## 7.3 Appendix 3: Historical Exchange Rate of Australian to U.S. Dollars

The cost of constructing the high performance computing cluster in this project is expressed in Australian dollars (AUD), because all components were sourced within Australia. To facilitate comparison with other cluster systems cited from the literature, all of which are quoted in U.S. dollars (USD or $US), the following historical exchange rate plot is provided. Data was obtained from the Reserve Bank of Australia web site in January 2013 (Reserve Bank of Australia, 2013) http://www.rba.gov.au/statistics/hist-exchange-rates/index.html and covers the period over which this research was undertaken. Exchange rates are averaged over calendar month intervals.

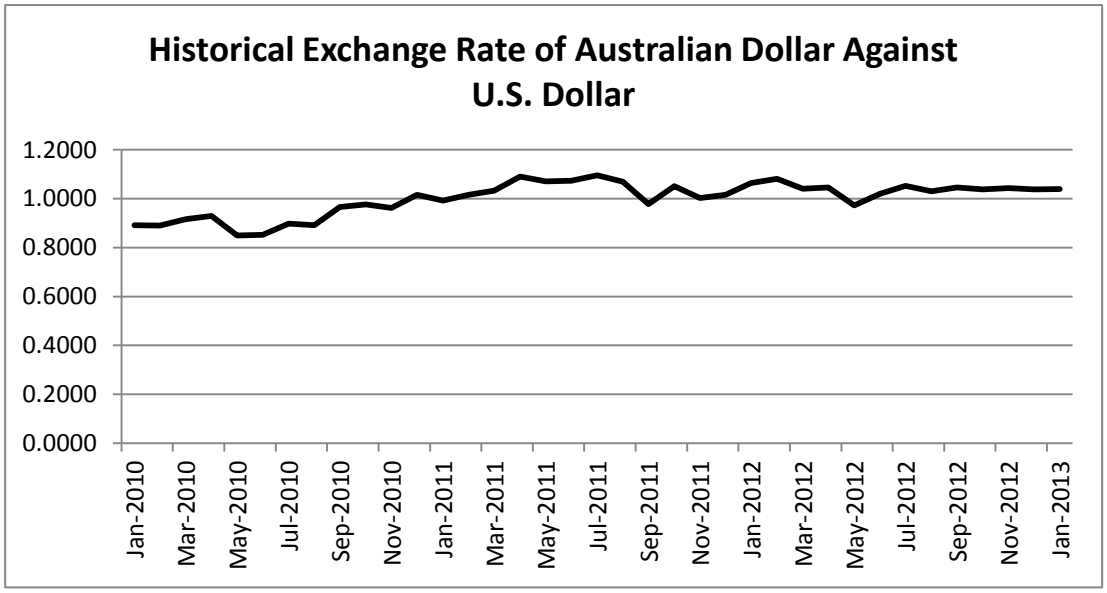

## 7.4 Appendix 4: GATE Description Macro for the Philips Allegro PET Scanner

The following GATE script describing the Philips Allegro PET scanner was used during the initial timing, memory and fictitious interactions experiments. This script was modified from one supplied courtesy of Dr. G. O'Keeffe, Centre for PET at Austin Health, Melbourne.

```
# sub-routine for setup of the Philips Allegro PET system:

#     W O R L D
/gate/world/geometry/setXLength 1.2 m
/gate/world/geometry/setYLength 1.2 m
/gate/world/geometry/setZLength 1.2 m
/gate/world/setMaterial Air

#     D E T E C T O R
/gate/world/daughters/name cylindricalPET
/gate/world/daughters/insert cylinder
/gate/cylindricalPET/setMaterial Air
/gate/cylindricalPET/geometry/setRmax 52. cm
/gate/cylindricalPET/geometry/setRmin 28. cm
/gate/cylindricalPET/geometry/setHeight 24.02 cm
/gate/cylindricalPET/vis/forceWireframe

#     S H I E L D I N G
/gate/cylindricalPET/daughters/name Shielding
/gate/cylindricalPET/daughters/insert cylinder
/gate/Shielding/setMaterial Lead
/gate/Shielding/geometry/setRmax 46.132 cm
/gate/Shielding/geometry/setRmin 28. cm
/gate/Shielding/geometry/setHeight 2.86 cm
/gate/Shielding/vis/forceSolid
#/gate/Shielding/vis/forceWireframe
/gate/Shielding/vis/setColor white

#     R E P E A T   S H I E L D I N G
/gate/Shielding/repeaters/insert linear
/gate/Shielding/linear/setRepeatNumber 2
/gate/Shielding/linear/setRepeatVector 0. 0. 21.16 cm


#     D E T E C T O R  =  R S E C T O R
/gate/cylindricalPET/daughters/name rsector
/gate/cylindricalPET/daughters/insert box
/gate/rsector/geometry/setXLength 40 mm
/gate/rsector/geometry/setYLength 94.5 mm
/gate/rsector/geometry/setZLength 18.3 cm
/gate/rsector/setMaterial Glass
/gate/rsector/placement/setTranslation  45.2 0 0 cm
/gate/rsector/vis/forceWireframe

#     M O D U L E
/gate/rsector/daughters/name module
```

```
/gate/rsector/daughters/insert box
/gate/module/geometry/setXLength 20. mm
/gate/module/geometry/setYLength 94.5 mm
/gate/module/geometry/setZLength 18.3 cm
/gate/module/setMaterial PTFE
/gate/module/placement/setTranslation  -10. 0 0 mm
/gate/module/vis/forceWireframe

#      C R Y S T A L
/gate/module/daughters/name crystal
/gate/module/daughters/insert box
/gate/crystal/geometry/setXLength 20. mm
/gate/crystal/geometry/setYLength 4 mm
/gate/crystal/geometry/setZLength 6 mm
/gate/crystal/setMaterial GSO
/gate/crystal/placement/setTranslation 0 0 0 mm

#     L A Y E R   G S O
/gate/crystal/daughters/name GSO
/gate/crystal/daughters/insert box
/gate/GSO/geometry/setXLength 20. mm
/gate/GSO/geometry/setYLength 4 mm
/gate/GSO/geometry/setZLength 6 mm
/gate/GSO/placement/setTranslation 0 0 0 mm
/gate/GSO/setMaterial GSO

#  R E P E T I T I O N   C R Y S T A L
/gate/crystal/repeaters/insert cubicArray
/gate/crystal/cubicArray/setRepeatNumberX 1
/gate/crystal/cubicArray/setRepeatNumberY 22
/gate/crystal/cubicArray/setRepeatNumberZ 29
/gate/crystal/cubicArray/setRepeatVector 0. 4.3 6.3 mm

#  R E P E T I T I O N   R S E C T O R
/gate/rsector/repeaters/insert ring
/gate/rsector/ring/setRepeatNumber 28

# Sub-routine for digitizer setup of Allegro PET scanner:

/gate/digitizer/Singles/insert adder
/gate/digitizer/Singles/insert readout
/gate/digitizer/Singles/readout/setDepth 1
/gate/digitizer/Singles/insert blurring
/gate/digitizer/Singles/blurring/setResolution 0.18
/gate/digitizer/Singles/blurring/setEnergyOfReference 511. keV

/gate/digitizer/Singles/insert deadtime
/gate/digitizer/Singles/deadtime/setDeadTime 210. ns
/gate/digitizer/Singles/deadtime/setMode paralysable
/gate/digitizer/Singles/deadtime/chooseDTVolume module

/gate/digitizer/Singles/insert timeResolution
/gate/digitizer/Singles/timeResolution/setTimeResolution 3. ns
/gate/digitizer/Singles/timeResolution/verbose 0

/gate/digitizer/Singles/insert thresholder
/gate/digitizer/Singles/thresholder/setThreshold 0.420 MeV
/gate/digitizer/Singles/insert upholder
```

```
/gate/digitizer/Singles/upholder/setUphold 0.700 MeV

#     C O I N C I D E N C E     S O R T E R
/gate/digitizer/Coincidences/setWindow 6.5 ns
/gate/digitizer/Coincidences/minSectorDifference 7
```

## 7.5 Appendix 5: Estimating the Simulation Time for [$^{11}$C]-PK11195 with GATE.

The plot below is reproduced from published data on the brain kinetics of [$^{11}$C]-PK11195 in normal grey matter (Kropholler et al., 2005). Data shown are not decay corrected and therefore show the actual tissue radioactivity concentration as a function of time since injection. Distribution of uptake for this radiotracer is known to be approximately uniform throughout the grey matter of the brain in normal subjects.

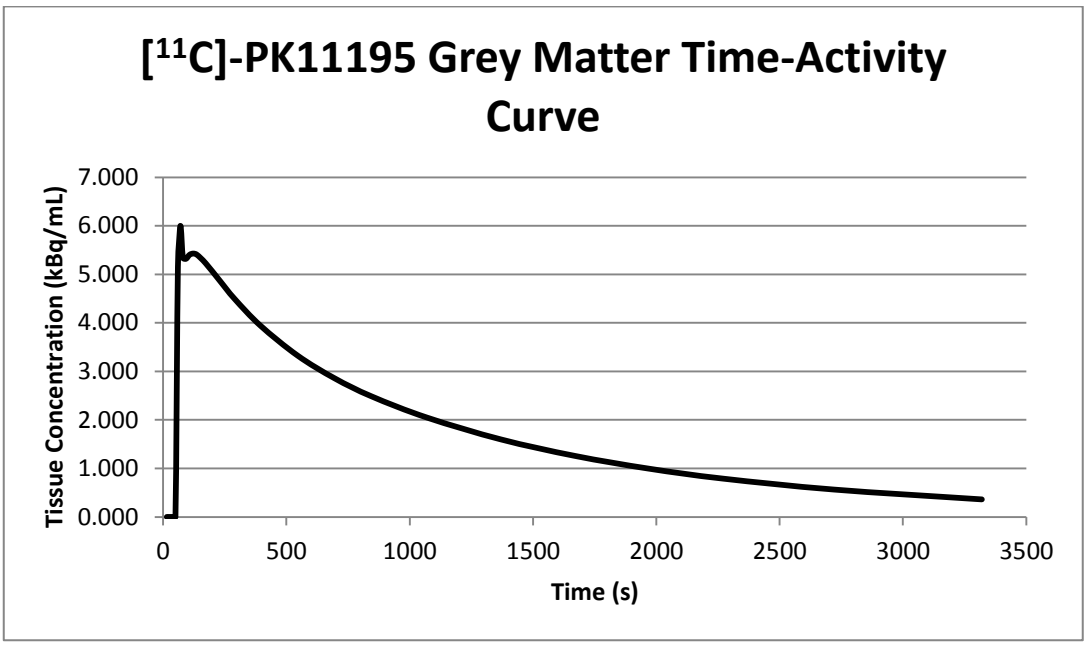


The same data are shown in the table below, divided into 24 discrete time frames as for a typical dynamic PET acquisition. The final column shows the calculated total number of radioactive disintegrations for each frame. For the purposes of this calculation a somewhat unrealistic assumption was made that all tissues within the head have the same radioactive time-activity curve as grey matter. Although this is approximately true for this tracer with respect to brain tissue, it is unlikely to be so for non-brain tissues such as skull, CSF, muscle and skin. However since these non-brain tissues are of limited interest in this work, assigning them incorrect tissue values is unlikely to alter the findings significantly. Radioactive decay within frames was assumed to be zero for these calculations- i.e. constant mid-frame time activity concentrations were assumed.

| Frame | Mid frame Time[s] | Frame Duration[s] | Decay Corrected for carbon-11 | Non Decay Corrected | Total Disintegrations |
|---|---|---|---|---|---|
| 1 | 15 | 30 | 0.000 | 0.000 | 0.00E+00 |
| 2 | 37.5 | 15 | 0.000 | 0.000 | 0.00E+00 |
| 3 | 50 | 10 | 0.001 | 0.001 | 5.33E+04 |
| 4 | 60 | 10 | 5.337 | 5.158 | 1.98E+08 |
| 5 | 70 | 10 | 6.244 | 6.002 | 2.31E+08 |
| 6 | 80 | 10 | 5.594 | 5.346 | 2.06E+08 |
| 7 | 92.5 | 15 | 5.607 | 5.320 | 3.07E+08 |
| 8 | 107.5 | 15 | 5.744 | 5.404 | 3.12E+08 |
| 9 | 122.5 | 15 | 5.819 | 5.429 | 3.13E+08 |
| 10 | 137.5 | 15 | 5.841 | 5.403 | 3.12E+08 |
| 11 | 172.5 | 55 | 5.766 | 5.229 | 1.11E+09 |
| 12 | 230 | 60 | 5.546 | 4.868 | 1.12E+09 |
| 13 | 290 | 60 | 5.297 | 4.494 | 1.04E+09 |
| 14 | 395 | 150 | 4.930 | 3.942 | 2.28E+09 |
| 15 | 545 | 150 | 4.530 | 3.327 | 1.92E+09 |
| 16 | 695 | 150 | 4.238 | 2.859 | 1.65E+09 |
| 17 | 845 | 150 | 4.012 | 2.486 | 1.43E+09 |
| 18 | 1070 | 300 | 3.752 | 2.048 | 2.36E+09 |
| 19 | 1370 | 300 | 3.470 | 1.598 | 1.84E+09 |
| 20 | 1670 | 300 | 3.237 | 1.258 | 1.45E+09 |
| 21 | 1970 | 300 | 3.036 | 0.995 | 1.15E+09 |
| 22 | 2270 | 300 | 2.857 | 0.790 | 9.12E+08 |
| 23 | 2720 | 600 | 2.625 | 0.565 | 1.30E+09 |
| 24 | 3320 | 600 | 2.364 | 0.362 | 8.35E+08 |
| | | | | ***Average:*** | ***9.29E+08*** |
| | | | | ***Total:*** | ***2.23E+10*** |

Notwithstanding the assumptions mentioned above, it may be seen that the total number of nuclear disintegrations for an hour long dynamic scan is approximately $2.23 \times 10^{10}$. Assuming a nuclear decay branching ratio $\approx 1$ for carbon-11, the number of 511 keV photon pairs required to be simulated is also $2.23 \times 10^{10}$.

## 7.6 Appendix 6: GATE Benchmark Results

A single installation of the GEANT4 Application for Tomographic Emission (GATE), version 6.0, was used throughout these experiments. To test the validity of this GATE installation, two benchmark simulations are provided within the software package. The benchmark programs were run on the single desktop system described in 3.1.2.2 which also served as the head node of the computer cluster used in all subsequent experiments described in this thesis. Output results from the benchmark simulations are presented below, along with the corresponding reference values for each variable.

| SPECT Benchmark Variable | Reference mean | Value Obtained | % Difference |
|---|---|---|---|
| Emitted Particles | 17999920 | 18004800 | 0.03 |
| Detected Counts | 35758 | 36029 | 0.76 |
| Primary Photons % | 35.6 | 36.000 | 1.12 |
| Scatter Phantom | 53.3 | 52.9 | -0.75 |
| Scatter Table | 3.0 | 2.9 | -3.33 |
| Scatter Collimator | 0.34 | 0.38 | 11.76 |
| Scatter Crystal | 6.4 | 6.6 | 3.12 |
| Scatter Backcompartment | 1.2 | 1.2 | 0.00 |
| Scatter Order 1 | 48.2 | 48.7 | 1.04 |
| Scatter Order 2 | 26.4 | 26.4 | 0.00 |
| Scatter Order 3 | 12.8 | 12.7 | -0.78 |
| Scatter Order 4 | 6.6 | 6.5 | -1.52 |
| Scatter Order >4 | 6.0 | 5.6 | -6.67 |

| PET Benchmark Variable | Reference mean | Value | % Difference |
|---|---|---|---|
| Total Decays | 36812600 | 36812600 | 0.000 |
| Random coincidences | 23536 | 24297 | 3.233 |
| Unscattered coincidences | 312725 | 332501 | 6.324 |
| Scattered coincidences | 370116 | 374648 | 1.224 |
| Simulated O-15 half-life (s) | 121.85 | 123.003 | 0.946 |

Results of the benchmark simulations are in broad agreement with the supplied reference values. For the SPECT simulation, scatter within the collimator and ‘order>4’ scattering show more than 5% absolute difference from the reference values. For the PET

simulation, unscattered coincidences are 6.3% higher than the reference value. All other PET variables show a difference of less than 5% from the reference mean values.

## 7.7 Appendix 7: Effects of Gamma Discard Energy Setting on Observed Count Rates

Full results from the experiment described in 3.2 are presented in the following table. Global counts are reported, including all planes, segments and lines of response of the simulated PET scanner.

| Activity (MBq) | Acq time (sec) | Gamma Discard (keV) | Total Singles | Singles Rate (/sec) | Total Trues | Trues Rate (/sec) | Total Scatters | Scatter Rate (/sec) | Total Randoms | Randoms Rate (/sec) |
|---|---|---|---|---|---|---|---|---|---|---|
| *5.0* | *4.0* | *0* | 2379036 | 594759 | 122104 | 30526 | 36838 | 9210 | 3764 | 941 |
| *5.0* | *4.0* | *10* | 2378724 | 594681 | 122968 | 30742 | 37608 | 9402 | 3671 | 918 |
| *5.0* | *4.0* | *50* | 2379259 | 594815 | 123115 | 30779 | 37727 | 9432 | 3575 | 894 |
| *5.0* | *4.0* | *100* | 2380830 | 595208 | 122266 | 30567 | 37705 | 9426 | 3824 | 956 |
| *5.0* | *4.0* | *150* | 2384445 | 596111 | 122235 | 30559 | 37827 | 9457 | 3831 | 958 |
| *5.0* | *4.0* | *200* | 2382878 | 595720 | 123020 | 30755 | 37704 | 9426 | 3869 | 967 |
| *5.0* | *4.0* | *250* | 2387296 | 596824 | 123059 | 30765 | 37897 | 9474 | 3678 | 920 |
| *5.0* | *4.0* | *300* | 2384958 | 596240 | 123196 | 30799 | 37764 | 9441 | 3814 | 954 |
| *5.0* | *4.0* | *350* | 2388644 | 597161 | 123226 | 30807 | 38181 | 9545 | 3723 | 931 |
| *5.0* | *4.0* | *400* | 2366136 | 591534 | 123320 | 30830 | 36250 | 9063 | 3824 | 956 |
| *5.0* | *4.0* | *450* | 2257263 | 564316 | 124244 | 31061 | 26977 | 6744 | 3363 | 841 |
| *5.0* | *4.0* | *500* | 2082365 | 520591 | 123668 | 30917 | 6379 | 1595 | 2842 | 711 |
| *5.0* | *4.0* | *510* | 2044374 | 511094 | 123938 | 30985 | 630 | 158 | 2838 | 710 |
| *10.0* | *2.0* | *0* | 2350831 | 1175416 | 118388 | 59194 | 35793 | 17897 | 7276 | 3638 |
| *10.0* | *2.0* | *10* | 2350567 | 1175284 | 119331 | 59666 | 36406 | 18203 | 7156 | 3578 |
| *10.0* | *2.0* | *50* | 2350947 | 1175474 | 119255 | 59628 | 36613 | 18307 | 7004 | 3502 |
| *10.0* | *2.0* | *100* | 2353379 | 1176690 | 118959 | 59480 | 36563 | 18282 | 7370 | 3685 |
| *10.0* | *2.0* | *150* | 2358299 | 1179150 | 118736 | 59368 | 36746 | 18373 | 7381 | 3691 |
| *10.0* | *2.0* | *200* | 2360122 | 1180061 | 119891 | 59946 | 36697 | 18349 | 7482 | 3741 |
| *10.0* | *2.0* | *250* | 2366925 | 1183463 | 120176 | 60088 | 37027 | 18514 | 7282 | 3641 |
| *10.0* | *2.0* | *300* | 2365394 | 1182697 | 120582 | 60291 | 36948 | 18474 | 7371 | 3686 |
| *10.0* | *2.0* | *350* | 2371181 | 1185591 | 120806 | 60403 | 37405 | 18703 | 7159 | 3580 |
| *10.0* | *2.0* | *400* | 2349732 | 1174866 | 120941 | 60471 | 35527 | 17764 | 7386 | 3693 |
| *10.0* | *2.0* | *450* | 2242242 | 1121121 | 121767 | 60884 | 26468 | 13234 | 6592 | 3296 |
| *10.0* | *2.0* | *500* | 2069836 | 1034918 | 121544 | 60772 | 6318 | 3159 | 5798 | 2899 |
| *10.0* | *2.0* | *510* | 2032399 | 1016200 | 121797 | 60899 | 622 | 311 | 5611 | 2806 |
| *20.0* | *1.0* | *0* | 2298899 | 2298899 | 111696 | 111696 | 33805 | 33805 | 13824 | 13824 |
| *20.0* | *1.0* | *10* | 2298242 | 2298242 | 112793 | 112793 | 34357 | 34357 | 13619 | 13619 |
| *20.0* | *1.0* | *50* | 2297778 | 2297778 | 112378 | 112378 | 34634 | 34634 | 13458 | 13458 |
| *20.0* | *1.0* | *100* | 2303084 | 2303084 | 111988 | 111988 | 34519 | 34519 | 13865 | 13865 |
| *20.0* | *1.0* | *150* | 2314052 | 2314052 | 112770 | 112770 | 34873 | 34873 | 14064 | 14064 |
| *20.0* | *1.0* | *200* | 2319953 | 2319953 | 114201 | 114201 | 34840 | 34840 | 14259 | 14259 |
| *20.0* | *1.0* | *250* | 2330269 | 2330269 | 114581 | 114581 | 35582 | 35582 | 14047 | 14047 |
| *20.0* | *1.0* | *300* | 2330702 | 2330702 | 115298 | 115298 | 35329 | 35329 | 14181 | 14181 |
| *20.0* | *1.0* | *350* | 2339510 | 2339510 | 115794 | 115794 | 35969 | 35969 | 14144 | 14144 |

| | | | | | | | | | | |
|---|---|---|---|---|---|---|---|---|---|---|
| *20.0* | *1.0* | *400* | 2321227 | 2321227 | 116199 | 116199 | 34310 | 34310 | 14137 | 14137 |
| *20.0* | *1.0* | *450* | 2217036 | 2217036 | 117602 | 117602 | 25559 | 25559 | 12982 | 12982 |
| *20.0* | *1.0* | *500* | 2048070 | 2048070 | 117585 | 117585 | 6118 | 6118 | 11130 | 11130 |
| *20.0* | *1.0* | *510* | 2011397 | 2011397 | 117739 | 117739 | 617 | 617 | 10902 | 10902 |
| *40.0* | *0.5* | *0* | 2189781 | 4379562 | 99694 | 199388 | 29938 | 59876 | 24691 | 49382 |
| *40.0* | *0.5* | *10* | 2186826 | 4373652 | 100008 | 200016 | 30534 | 61068 | 24538 | 49076 |
| *40.0* | *0.5* | *50* | 2185893 | 4371786 | 99611 | 199222 | 30563 | 61126 | 24367 | 48734 |
| *40.0* | *0.5* | *100* | 2198805 | 4397610 | 99431 | 198862 | 30934 | 61868 | 24932 | 49864 |
| *40.0* | *0.5* | *150* | 2213064 | 4426128 | 101370 | 202740 | 31013 | 62026 | 25006 | 50012 |
| *40.0* | *0.5* | *200* | 2229392 | 4458784 | 103170 | 206340 | 31504 | 63008 | 25687 | 51374 |
| *40.0* | *0.5* | *250* | 2244977 | 4489954 | 104165 | 208330 | 32147 | 64294 | 25617 | 51234 |
| *40.0* | *0.5* | *300* | 2253290 | 4506580 | 105195 | 210390 | 32216 | 64432 | 25942 | 51884 |
| *40.0* | *0.5* | *350* | 2267017 | 4534034 | 106278 | 212556 | 33109 | 66218 | 26258 | 52516 |
| *40.0* | *0.5* | *400* | 2252305 | 4504610 | 107356 | 214712 | 31353 | 62706 | 26089 | 52178 |
| *40.0* | *0.5* | *450* | 2155848 | 4311696 | 108816 | 217632 | 23586 | 47172 | 24003 | 48006 |
| *40.0* | *0.5* | *500* | 1996989 | 3993978 | 109665 | 219330 | 5694 | 11388 | 21027 | 42054 |
| *40.0* | *0.5* | *510* | 1962507 | 3925014 | 109869 | 219738 | 558 | 1116 | 20315 | 40630 |
| *60.0* | *0.3* | *0* | 1873941 | 6246470 | 78901 | 263003 | 23801 | 79337 | 30140 | 100467 |
| *60.0* | *0.3* | *10* | 1875460 | 6251533 | 79316 | 264387 | 24350 | 81167 | 29936 | 99787 |
| *60.0* | *0.3* | *50* | 1876475 | 6254917 | 79890 | 266300 | 24521 | 81737 | 30220 | 100733 |
| *60.0* | *0.3* | *100* | 1888003 | 6293343 | 79922 | 266407 | 24641 | 82137 | 30275 | 100917 |
| *60.0* | *0.3* | *150* | 1909019 | 6363397 | 81854 | 272847 | 25302 | 84340 | 30834 | 102780 |
| *60.0* | *0.3* | *200* | 1931883 | 6439610 | 84280 | 280933 | 25869 | 86230 | 31622 | 105407 |
| *60.0* | *0.3* | *250* | 1949071 | 6496903 | 85977 | 286590 | 26523 | 88410 | 31914 | 106380 |
| *60.0* | *0.3* | *300* | 1965378 | 6551260 | 87555 | 291850 | 26505 | 88350 | 32336 | 107787 |
| *60.0* | *0.3* | *350* | 1975625 | 6585417 | 87876 | 292920 | 27451 | 91503 | 32786 | 109287 |
| *60.0* | *0.3* | *400* | 1970291 | 6567637 | 89405 | 298017 | 26303 | 87677 | 32456 | 108187 |
| *60.0* | *0.3* | *450* | 1889522 | 6298407 | 90535 | 301783 | 19830 | 66100 | 30135 | 100450 |
| *60.0* | *0.3* | *500* | 1754179 | 5847263 | 92452 | 308173 | 4656 | 15520 | 26751 | 89170 |
| *60.0* | *0.3* | *510* | 1724467 | 5748223 | 92523 | 308410 | 447 | 1490 | 25880 | 86267 |

## 7.8 Appendix 8: GATE Description Macro for the Generic PET Scanner

The following GATE macro script describes the geometry of the PET scanner that was introduced in Chapter 4, and used for all subsequent experiments presented in this thesis. As the comments (lines beginning with #) at the top of the macro indicate, the scanner description was adapted from one supplied with the GATE software distribution (version 6.0) attributed to Sébastien Jan. It uses the 'ecat' layout option available in GATE to simulate the geometry of a PET scanner using the block detector design.

```
# Sub-routine for setup of an ecat clinical PET scanner
# geometry in GATE.
# Adapted from the macro supplied with GATE V6.0 by S. Jan
# A cylindrical scanner with 16.8cm axial FOV and
# 4mmx4mmx20mm LSO crystals arranged in blocks of
# 13x13 crystals, with 1/3mm crystal and block spacing and
# with 86.07cm cylinder diameter is implemented here.
# This geometry is intended to be similar to, but not exactly
# replicate, the geometry of current generation CTI/Siemens
# clinical (human) PET systems, such as the Biograph(TM)16
# PET/CT scanner.
#
# C. Constable Feb 2011.
#
#*****************************************************************

#     W O R L D

/gate/world/geometry/setXLength 1.5 m
/gate/world/geometry/setYLength 1.5 m
/gate/world/geometry/setZLength 1.5 m

#     E C A T

/gate/world/daughters/name ecat
/gate/world/daughters/insert cylinder
/gate/ecat/setMaterial Vacuum
/gate/ecat/geometry/setRmax 45.0355 cm
/gate/ecat/geometry/setRmin 43.0355 cm
/gate/ecat/geometry/setHeight 16.8667 cm
/gate/ecat/vis/forceWireframe

#     B L O C K

/gate/ecat/daughters/name block
/gate/ecat/daughters/insert box
/gate/block/placement/setTranslation 440.355 0.0 0.0 mm
/gate/block/geometry/setXLength 20.0 mm
/gate/block/geometry/setYLength 56.0 mm
/gate/block/geometry/setZLength 56.0 mm
/gate/block/setMaterial Air
/gate/block/vis/forceWireframe
```

```
#     C R Y S T A L

/gate/block/daughters/name crystal
/gate/block/daughters/insert box
/gate/crystal/geometry/setXLength 20.0 mm
/gate/crystal/geometry/setYLength 4.0 mm
/gate/crystal/geometry/setZLength 4.0 mm
/gate/crystal/setMaterial LSO
/gate/crystal/vis/setColor yellow

#     R E P E A T    C R Y S T A L

/gate/crystal/repeaters/insert cubicArray
/gate/crystal/cubicArray/setRepeatNumberX 1
/gate/crystal/cubicArray/setRepeatNumberY 13
/gate/crystal/cubicArray/setRepeatNumberZ 13
/gate/crystal/cubicArray/setRepeatVector 0. 4.33333 4.33333 mm

#     R E P E A T    BLOCK

/gate/block/repeaters/insert linear
/gate/block/linear/setRepeatNumber 3
/gate/block/linear/setRepeatVector 0. 0. 56.33333 mm
/gate/block/repeaters/insert ring
/gate/block/ring/setRepeatNumber 48

#     A T T A C H    S Y S T E M
/gate/systems/ecat/block/attach block
/gate/systems/ecat/crystal/attach crystal

#     A T T A C H    C R Y S T A L  SD
/gate/crystal/attachCrystalSD
```

## 7.9 Appendix 9: GATE Description Macro for the PET Detector Electronics

The following GATE macro script describes the event processing electronics of the PET scanner that was introduced in Chapter 4, and used for all subsequent experiments presented in this thesis. As the comments (lines beginning with #) at the top of the macro indicate, the electronics were modelled after the Siemens Pico-3D PET detector electronics (Martinez et al., 2006).

```
# Sub-routine for digitizer setup of the ECAT type PET scanner.
# Digitizer parameters are chosen to model the published
# performance characteristics
# of the Siemens/CTI Pico3D (TM) electronics as found on Siemens
# Biograph/Hi-Rez(TM) type PET scanners. Specifically, a timing
# window of 4.5ns, timing resolution of 500ps, dead-time of
# 136ns, an energy threshold of 425keV and an energy resolution
# of 15% are modelled.
#
# C. Constable, Feb 2011.
#

/gate/digitizer/convertor/verbose 0

#     A D D E R
/gate/digitizer/Singles/insert adder

#       R E A D O U T
/gate/digitizer/Singles/insert readout
/gate/digitizer/Singles/readout/setDepth 1

#      E N E R G Y   B L U R R I N G

# settings for LSO block detector at 511 keV with
# 92% quantum efficiency...

/gate/digitizer/Singles/insert crystalblurring
/gate/digitizer/Singles/crystalblurring/setCrystalResolutionMin
0.12
/gate/digitizer/Singles/crystalblurring/setCrystalResolutionMax
0.18
/gate/digitizer/Singles/crystalblurring/setCrystalQE 0.92
/gate/digitizer/Singles/crystalblurring/setCrystalEnergyOfReferenc
e 511. keV

#       E N E R G Y   W I N D O W
/gate/digitizer/Singles/insert thresholder
/gate/digitizer/Singles/thresholder/setThreshold 425. keV
/gate/digitizer/Singles/insert upholder
/gate/digitizer/Singles/upholder/setUphold 650. keV

#       T I M I N G   R E S O L U T I O N
/gate/digitizer/Singles/insert timeResolution
/gate/digitizer/Singles/timeResolution/setTimeResolution 500. ps
```

```
#       D E A D    T I M E
/gate/digitizer/Singles/insert deadtime
/gate/digitizer/Singles/deadtime/setDeadTime 136. ns
/gate/digitizer/Singles/deadtime/setMode paralysable
/gate/digitizer/Singles/deadtime/chooseDTVolume block


#     C O I N C I    S O R T E R
/gate/digitizer/Coincidences/setWindow 4.5 ns
/gate/digitizer/Coincidences/setOffset 0. ns
/gate/digitizer/Coincidences/describe

/gate/digitizer/name delay
/gate/digitizer/insert coincidenceSorter
/gate/digitizer/delay/setWindow 4.5 ns
/gate/digitizer/delay/setOffset 600. ns
/gate/digitizer/delay/describe


/gate/digitizer/name finalCoinc
/gate/digitizer/insert coincidenceChain
/gate/digitizer/finalCoinc/addInputName delay
/gate/digitizer/finalCoinc/addInputName Coincidences
/gate/digitizer/finalCoinc/usePriority true
/gate/digitizer/finalCoinc/describe
```

## 7.10 Appendix 10: GATE Physics Macro

The following GATE macro script describes physics processes of the PET scanner that was introduced in Chapter 4, and used for all subsequent experiments presented in this thesis.

```
# Sub-routine that sets up the physics processes for
# PET simulations
# involving a clinical(human) scanner.
# Standard tables for photoelectric and compton interactions used.
#
#
# Modified April 2010 for ecat simulations.
# Modified Nov 2010 to meet GATE v6.0 requirements.
#
# C. Constable.
#


/gate/physics/addProcess PhotoElectric
/gate/physics/addProcess Compton
/gate/physics/addProcess GammaConversion
/gate/physics/addProcess LowEnergyRayleighScattering

/gate/physics/addProcess ElectronIonisation
/gate/physics/addProcess Bremsstrahlung
/gate/physics/addProcess PositronAnnihilationStd

/gate/physics/addProcess MultipleScattering e+
/gate/physics/addProcess MultipleScattering e-

/gate/physics/processList Enabled
/gate/physics/processList Initialized

# Cuts- adapted from 'GATE/...../examples' for an ecat system...

/gate/physics/Gamma/SetCutInRegion      crystal 1.0 mm
/gate/physics/Electron/SetCutInRegion   crystal 1.0 cm
/gate/physics/Positron/SetCutInRegion   crystal 1.0 cm


#/gate/physics/Gamma/SetCutInRegion      phantom 0.5 mm
#/gate/physics/Electron/SetCutInRegion   phantom 30.0 cm
#/gate/physics/Positron/SetCutInRegion   phantom 0.1 mm

#/gate/physics/SetMaxStepSizeInRegion    phantom 0.01 mm



# if fictitious interactions used in a voxelized phantom, then:

/gate/physics/addProcess Fictitious
```

## 7.11 Appendix 11: Measurement of Linear Attenuation Coefficient s for Skull and Water in GATE

In order to validate the use of 'skull' and 'water' materials from the GATE materials database for PET simulations, measurements of their respective linear attenuation coefficients ($\mu$) were made and compared to published values. These measurements also provided the *a-priori* values for $\mu$ that were used in the segmentation of the attenuation image.

A series of simulations were run in which the attenuation of varying lengths of 'water' and 'skull' materials was measured in GATE. The following diagram illustrates the geometrical arrangement of source, detector and attenuating media for this simulation.

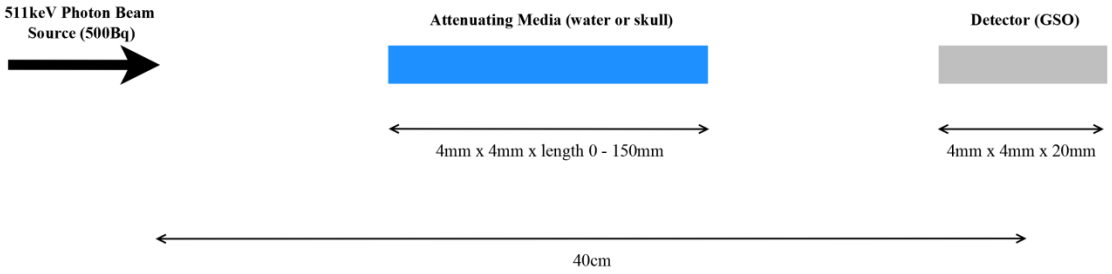


A one-dimensional beam source emitting 511 keV photons was placed 40 cm distant from a radiation detector. In between the source and detector, a length of absorbing material was simulated with the same cross-sectional dimensions as the detector (i.e. 4 mm x 4 mm). For each material (water and skull), 8 simulations were run corresponding to the following lengths of attenuating medium: 0 cm (no attenuation), 2 cm, 4 cm, 6 cm, 8 cm, 10 cm, 12 cm and 15 cm. As for all dynamic PET scan simulations reported in this thesis, the fictitious interactions tracking algorithm was used with a 100 keV gamma discard setting. A scintillation detector composed of Gadolinium oxyorthosilicate (GSO) was simulated, measuring 4 mm x 6 mm x 20 mm. Energy resolution of the detector was set to 18% at 511 keV, and an energy acceptance window of 420 – 700 keV was applied. No detector dead time was included in this simulation. A minimum total of 40,000 counts were collected for each combination of material and length.

The output data from these simulations are plotted below. The natural logarithm of the ratio of counts at zero attenuation to counts at each absorber thickness was calculated, and $\mu$ for both materials was determined by linear regression as follows: water $\mu$ = 0.09596 $cm^{-1}$, skull $\mu$ = 0.1457 $cm^{-1}$. The value for water μ thus calculated is very close to that reported in the literature for soft tissue at 511 keV (Meikle et al., 1993). A recent study investigating

attenuation correction for cerebral PET reported the average skull linear attenuation coefficient at 511 keV across 325 subjects was 0.143 $cm^{-1}$ (Catana et al., 2010). These findings indicate that GATE can provide highly realistic modelling of the attenuation of soft tissue and skull bone.

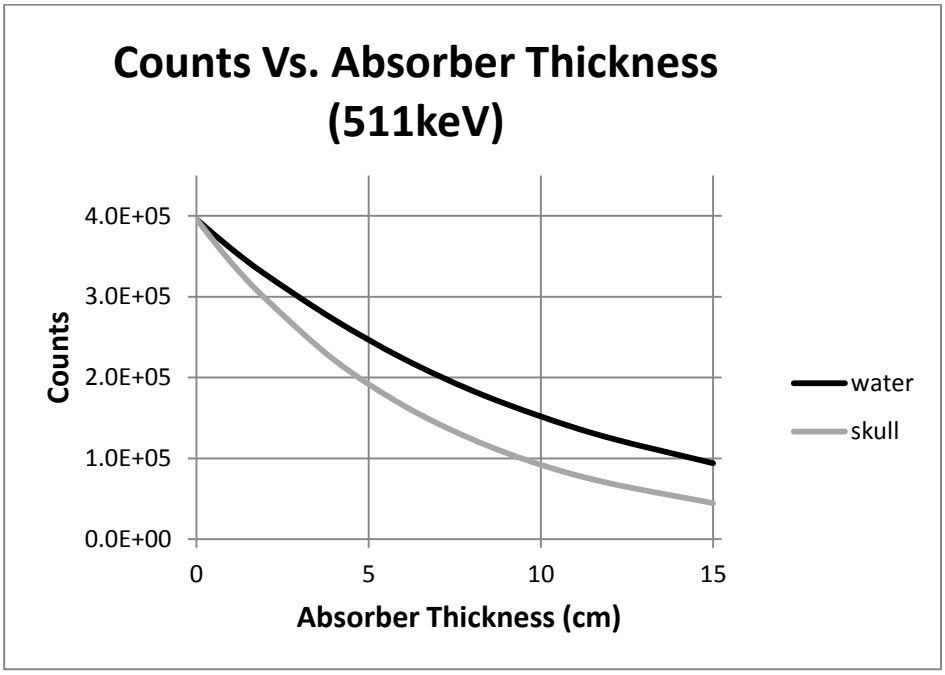

## 7.12 Appendix 12: Grey Matter Regions-of-Interest

Three grey matter regions-of-interest (ROIs), described in 4.2.5.1 are displayed below. Regions-of-interest are displayed in white, superimposed on the entire grey matter voxel volume (displayed in grey). Regions were selected from grey matter voxels that contained minimal partial volume error, defined as less than 10% loss of counts from grey matter, and no more than 10% 'spill-in' of counts from white matter voxels. Spill out and spill in were estimated from separate high-count simulations of grey-matter-only and white-matter-only emission phantoms.

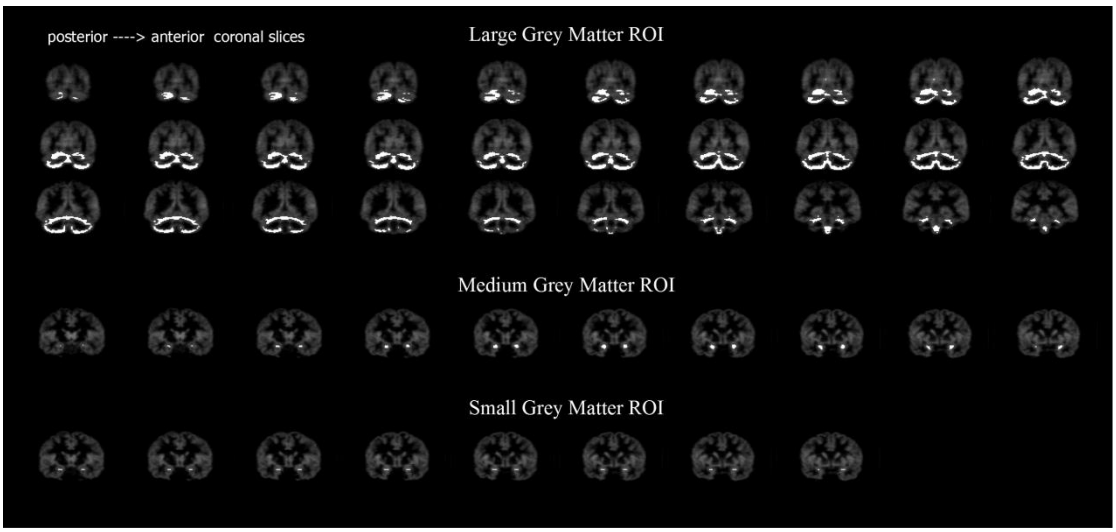

## 7.13 Appendix 13: Parameter Selection for OS-EM Reconstruction of GATE Simulated [$^{11}$C]-PK11195 Scans

Ordered subset expectation maximisation (OS-EM) reconstruction was used in addition to filtered back projection to reconstruct the dynamic [$^{11}$C]-PK11195 PET simulation. Selection of an appropriate number of iterations was made by examining the mean-squared error and the grey matter to white matter contrast ratio, as a function of maximum likelihood expectation maximization (ML-EM) iteration number, for two sample frames of the simulation. Frame 10 was chosen as an example of a low count density frame, while frame 14 was chosen due to its relatively high count density. Post reconstruction filter width (FWHM) was chosen by attempting to match the spatial resolution of the OS-EM reconstructions to the filtered back projection (FBP) reconstructions of a point source simulation.

Transverse image plane number 38, for frame 14, is shown below for increasing iteration number. The minimum mean squared error for frame 10 (low count frame) occurred at iteration number 3, and for frame 14 (high counts) at iteration number 5. The contrast ratio for grey:white matter reached a plateau, defined as ≤1% change, for frame 10 at iteration number 37, and for frame 14 at iteration number 35. On the basis of these findings, all frames of the [$^{11}$C]-PK11195 dynamic simulation were reconstructed with the OS-EM algorithm, using 12 iterations and 3 subsets.

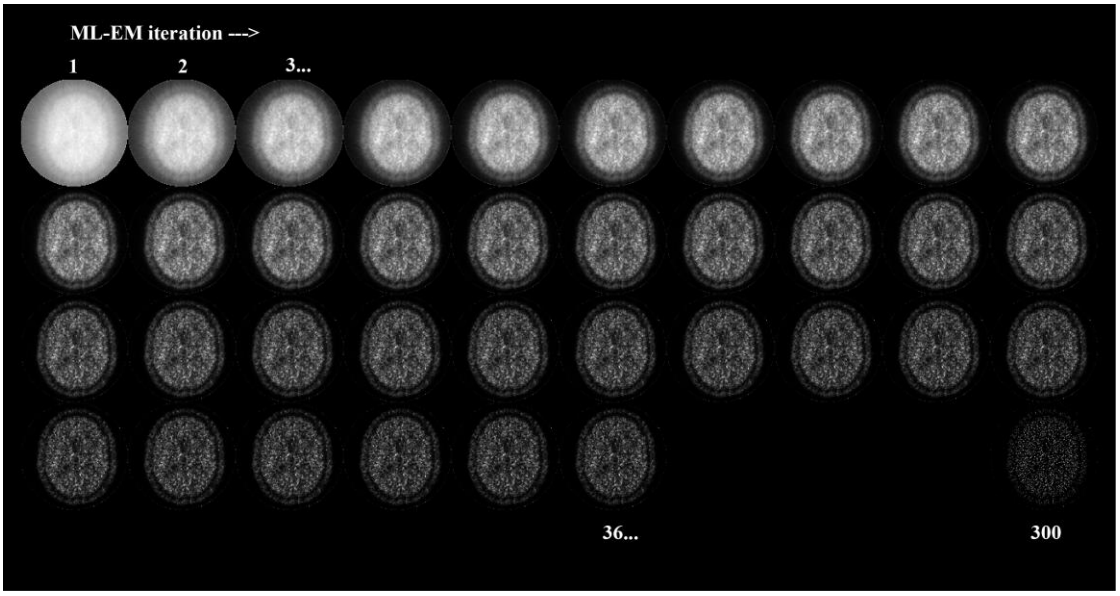

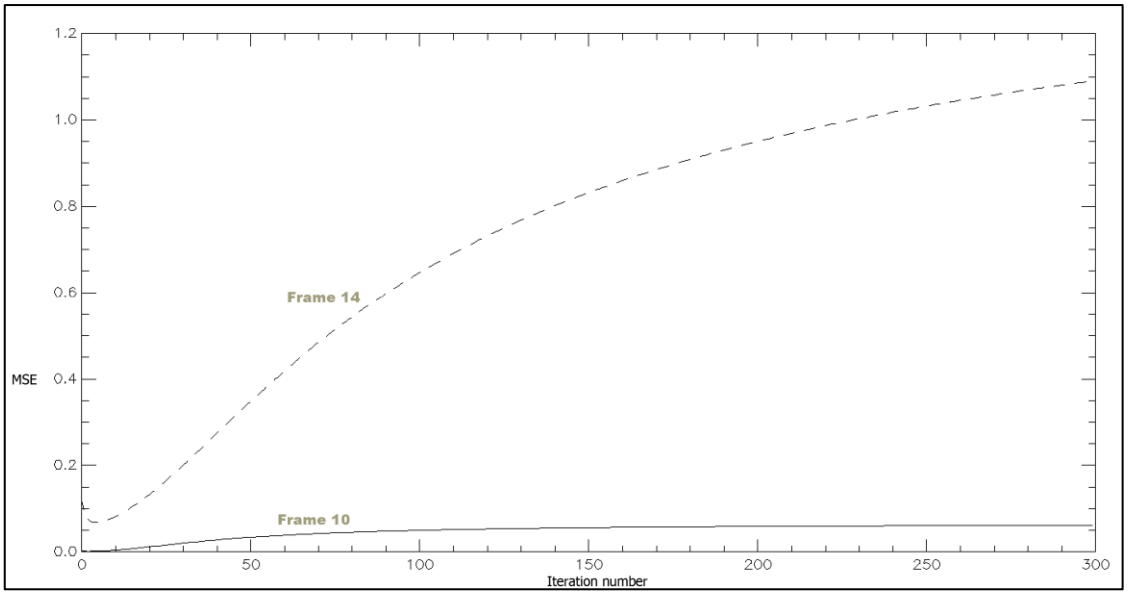


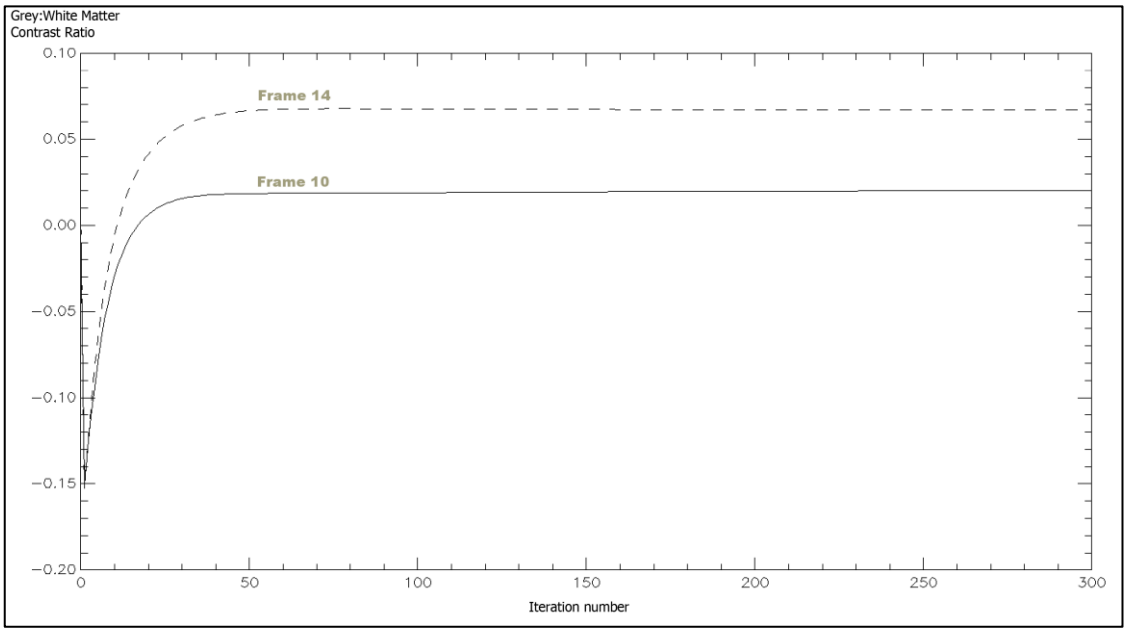


In an attempt to match the spatial resolution of the two reconstruction algorithms used (FBP and OS-EM), their outputs for a point source image reconstruction were analysed. Application of a 3 mm Gaussian post reconstruction filter was found to closely match the spatial resolution (transverse FWHM) of the OS-EM to the FBP reconstruction. The results of this analysis are presented in the table below.

| | **Radial offset 1 cm FWHM (mm)** | **Radial offset 10 cm FWHM (mm)** |
|---|---|---|
| **FBP (Hanning, 0.7)** | 6.09 | 6.25 |
| **OS-EM (3 mm filter)** | 5.96 | 6.20 |

# Chapter 8 References


Adams, J. C. (2012). Microwulf: A Personal, Portable Beowulf Cluster, from http://www.calvin.edu/~adams/research/microwulf/

Adams, J. C., & Brom, T. H. (2008). *Microwulf: A Beowulf Cluster For Every Desk.* Paper presented at the Sigcse'08: Proceedings of the 39th Acm Technical Symposium on Computer Science Education.

Agostinelli, S., Allison, J., Amako, K., Apostolakis, J., Araujo, H., Arce, P., . . . Zschiesche, D. (2003). GEANT4-a simulation toolkit. [Review]. *Nuclear Instruments & Methods in Physics Research Section a-Accelerators Spectrometers Detectors and Associated Equipment, 506*(3), 250-303. doi: 10.1016/s0168-9002(03)01368-8

Ahn, S., & Fessler, J. A. (2004). Emission image reconstruction for randoms-precorrected PET allowing negative sinogram values. *IEEE Trans Med Imaging, 23*(5), 591-601.

Amdahl, G. M. (1967). Validity of the Single Processor Approach to Achieving Large Scale Computing Capabilities, Reprinted from the AFIPS Conference Proceedings, Vol. 30 (Atlantic City, N.J., Apr. 18–20), AFIPS Press, Reston, Va., 1967, pp. 483–485, when Dr. Amdahl was at International Business Machines Corporation, Sunnyvale, California. *IEEE Solid-State Circuits Newsletter, 12*(3), 19-20.

Angelis, G. I., Matthews, J. C., Kotasidis, F. A., Markiewicz, P. J., Lionheart, W. R., & Reader, A. J. (2011, 23-29 Oct. 2011). *Evaluation of a direct 4D reconstruction method using GLLS for estimating parametric maps of micro-parameters.* Paper presented at the Nuclear Science Symposium and Medical Imaging Conference (NSS/MIC), 2011 IEEE.

Arlicot, N., Vercouillie, J., Ribeiro, M. J., Tauber, C., Venel, Y., Baulieu, J. L., . . . Guilloteau, D. (2012). Initial evaluation in healthy humans of F-18 DPA-714, a potential PET biomarker for neuroinflammation. [Article]. *Nuclear Medicine and Biology, 39*(4), 570-578. doi: 10.1016/j.nucmedbio.2011.10.012

Badawi, R. D., Lodge, M. A., & Marsden, P. K. (1998). Algorithms for calculating detector efficiency normalization coefficients for true coincidences in 3D PET. *Physics in Medicine and Biology, 43*(1), 189-205. doi: 10.1088/0031-9155/43/1/012

Badawi, R. D., & Marsden, P. K. (1999). Developments in component-based normalization for 3D PET. *Physics in Medicine and Biology, 44*(2), 571-594. doi: 10.1088/0031-9155/44/2/020

Bailey, D. L., Jones, T., & Spinks, T. J. (1991). A method for measuring the absolute sensitivity of positron emission tomographic scanners. *Eur J Nucl Med, 18*(6), 374-379.

Banati, R. (2002). Visulalising microglial activation in vivo. *Glia, 40*(2), 206-217.

Banati, R. (2003). Neuropathological imaging: in vivo detection of glial activation as a measure of disease and adaptive change in the brain (Vol. 65, pp. 121-131): British Medical Bulletin.

Banati, R. B., Goerres, G. W., Myers, R., Gunn, R. N., Turkheimer, F. E., Kreutzberg, G. W., . . . Duncan, J. S. (1999). [11C](R)-PK11195 positron emission tomography imaging of activated microglia in vivo in Rasmussen's encephalitis. *Neurology, 53*(9), 2199-2203.

Banati, R. B., Newcombe, J., Gunn, R. N., Cagnin, A., Turkheimer, F., Heppner, F., . . . Myers, R. (2000). The peripheral benzodiazepine binding site in the brain in multiple sclerosis: quantitative in vivo imaging of microglia as a measure of disease activity. *Brain, 123*(Pt 11), 2321-2337.

Basu, S., Zaidi, H., Houseni, M., Bural, G., Udupa, J., Acton, P., . . . Alavi, A. (2007). Novel quantitative techniques for assessing regional and global function and structure based on modern imaging modalities: Implications for normal variation, aging and diseased states. [Review]. *Seminars in Nuclear Medicine, 37*(3), 223-239. doi: 10.1053/j.semnuclmed.2007.01.005

Bataille, F., Comtat, C., Jan, S., & Trebossen, R. (2004). Monte Carlo simulation for the ECAT HRRT using GATE. In J. A. Seibert (Ed.), *2004 IEEE Nuclear Science Symposium Conference Record, Vols 1-7* (pp. 2570-2574).

Becker, D. J. S., T.; Savarese, D.; Dorband, J. E.; Ranawake, U. A. (1995). *BEOWULF: A Parallel Workstation for Scientific Computation.* Paper presented at the International Conference on Parallel Processing (ICPP)

Bentourkia, M., & Zaidi, H. (2006). Tracer Kinetic Modeling in Nuclear Medicine: Theory and Applications. In H. Zaidi (Ed.), *Quantitative Analysis in Nuclear Medicine Imaging.* (pp. 391-413). New York: Springer.

Bernassau, J. M., Reversat, J. L., Ferrara, P., Caput, D., & Lefur, G. (1993). A 3D model of the peripheral benzodiazepine receptor and its implication in intra mitochondrial cholesterol transport. *J Mol Graph, 11*(4), 236-244.

Beyer, T., Townsend, D. W., Brun, T., Kinahan, P. E., Charron, M., Roddy, R., . . . Nutt, R. (2000). A combined PET/CT scanner for clinical oncology. *J Nucl Med, 41*(8), 1369-1379.

Bourne, R. (2010). *Fundamentals of Digital Imaging in Medicine*. London: Springer-Verlag.

Boutin, H., Chauveau, F., Thominiaux, C., Kuhnast, B., Gregoire, M. C., Jan, S., . . . Katsifis, A. (2007). In vivo Imaging of brain lesions with C-11 CLINME, a new PET radioligand of peripheral benzodiazepine receptors. [Article]. *Glia, 55*(14), 1459-1468. doi: 10.1002/glia.20562

Brambilla, M., Matheoud, R., Secco, C., Sacchetti, G., Comi, S., Rudoni, M., . . . Inglese, E. (2007). Impact of target-to-background ratio, target size, emission scan duration, and activity on physical figures of merit for a 3D LSO-based whole body PET/CT scanner. [Article]. *Medical Physics, 34*(10), 3854-3865. doi: 10.1118/1.2776242

Brambilla, M., Secco, C., Dominietto, M., Matheoud, R., Sacchetti, G., Inglese, E., . . . Inglese, E. (2005). Performance characteristics obtained for a new 3-dimensional lutetium oxyorthosilicate-based whole-body PET/CT scanner with the National Electrical Manufacturers Association NU 2-2001 standard. *Journal of Nuclear Medicine, 46*(12), 2083-2091.

Brasse, D., Kinahan, P. E., Lartizien, C., Comtat, C., Casey, M., & Michel, C. (2005). Correction methods for random coincidences in fully 3D whole-body PET: impact on data and image quality. *J Nucl Med, 46*(5), 859-867.

Brown, A. K., Fujita, M., Fujimura, Y., Liow, J. S., Stabin, M., Ryu, Y. H., . . . Innis, R. B. (2007). Radiation dosimetry and biodistribution in monkey and man of 11C-PBR28: a PET radioligand to image inflammation. *J Nucl Med, 48*(12), 2072-2079.

Budinger, T. F., Derenzo, S. E., Greenberg, W. L., Gullberg, G. T., & Huesman, R. H. (1978). Quantitative Potentials of Dynamic Emission Computed Tomography. [Article]. *Journal of Nuclear Medicine, 19*(3), 309-315.

Buvat, I., Benali, H., & Di Paola, R. (2000). Characterizing the noise properties of reconstructed emission images from a single noisy sinogram using a bootstrap approach. [Meeting Abstract]. *Journal of Nuclear Medicine, 41*(5), 401.

Buvat, I., Castiglioni, I., Feuardent, J., & Gilardi, M. C. (2005). Unified description and validation of Monte Carlo simulators in PET. [Article]. *Physics in Medicine and Biology, 50*(2), 329-346. doi: 10.1088/0031-9155/50/2/011

Buvat, I., & Lazaro, D. (2006). Monte Carlo simulations in emission tomography and GATE: An overview. *Nuclear Instruments & Methods in Physics Research Section a-Accelerators Spectrometers Detectors and Associated Equipment, 569*(2), 323-329. doi: 10.1016/j.nima.2006.08.039

Cagnin, A., Brooks, D. J., Kennedy, A. M., Gunn, R. N., Myers, R., Turkheimer, F. E., . . . Banati, R. B. (2001). In-vivo measurement of activated microglia in dementia.[Erratum appears in Lancet. 2001 Sep 1;358(9283):766]. *Lancet, 358*(9280), 461-467.

Cagnin, A., Kassiou, M., Meikle, S. R., & Banati, R. B. (2006). In vivo evidence for microglial activation in neurodegenerative dementia. *Acta Neurol Scand Suppl, 185*, 107-114.

Cagnin A, M. R., Gunn RN, Turkheimer FE, Cunningham VJ, Brooks DJ, Jones T, Banati RB. (2001). Imaging activated microglia in the ageing human brain. In H. S. Gjedde A, Knudsen GM, Paulson OB (Ed.), *Physiological imaging of the brain with PET* (pp. 361–367). San Diego: CA: Academic Press.

Cagnin, A., Rossor, M., Sampson, E. L., Mackinnon, T., & Banati, R. B. (2004). In vivo detection of microglial activation in frontotemporal dementia. *Annals of Neurology, 56*(6), 894-897.

Camsonne, R., Crouzel, C., Comar, D., Maziere, M., Prenant, C., Sastre, J., . . . Syrota, A. (1984). Synthesis of N-(C-11) methyl, N-(methyl-1 propyl), (chloro-2 phenyl)-1 Isoquinoleine Carboxamide-3 (PK-11195) - A New Ligand For Peripheral Benzodiazepine Receptors. *Journal of Labelled Compounds & Radiopharmaceuticals, 21*(10), 985-991.

Carson, R. (2003). Tracer Kinetic Modeling in PET. In P. E. Valk, D. L. Bailey, D. Townsend & M. Maisey (Eds.), *Positron Emission Tomography: Basic Science and Clinical Practice*. London: Springer-Verlag.

Catana, C., van der Kouwe, A., Benner, T., Michel, C. J., Hamm, M., Fenchel, M., . . . Sorensen, A. G. (2010). Toward implementing an MRI-based PET attenuation-correction method for neurologic studies on the MR-PET brain prototype. *J Nucl Med, 51*(9), 1431-1438. doi: 10.2967/jnumed.109.069112

Charbonneau, P., Syrota, A., Crouzel, C., Valois, J. M., Prenant, C., & Crouzel, M. (1986). Peripheral-type Benzodiazepine Receptors in the Living Heart Characterized by Positron Emission Tomography. [Article]. *Circulation, 73*(3), 476-483.

Chauveau, F., Boutin, H., Van Camp, N., Dolle, F., Tavitian, B., Chauveau, F., . . . Tavitian, B. (2008). Nuclear imaging of neuroinflammation: a comprehensive review of [11C]PK11195 challengers. [Research Support, Non-U.S. Gov't Review]. *European Journal of Nuclear Medicine & Molecular Imaging, 35*(12), 2304-2319.

Chauveau, F., Van Camp, N., Dolle, F., Kuhnast, B., Hinnen, F., Damont, A., . . . Tavitian, B. (2009). Comparative evaluation of the translocator protein radioligands 11C-DPA-713, 18F-DPA-714, and 11C-PK11195 in a rat model of acute neuroinflammation. [Comparative Study Research Support, Non-U.S. Gov't]. *Journal of Nuclear Medicine, 50*(3), 468-476.

Cherry, S. R., Sorenson, J. A., & Phelps, M. E. (2003). *Physics in Nuclear Medicine* (3rd ed.). Philadelphia: Saunders.

Clark, D. E. (2003). In silico prediction of blood–brain barrier permeation. *Drug Discovery Today, 8*(20), 927-933. doi: http://dx.doi.org/10.1016/S1359-6446(03)02827-7

Collins, D. L., Zijdenbos, A. P., Kollokian, V., Sled, J. G., Kabani, N. J., Holmes, C. J., & Evans, A. C. (1998). Design and construction of a realistic digital brain phantom. *IEEE Trans Med Imaging, 17*(3), 463-468.

Cray Duly Launches Its $2.2m to $31m Parallel T3D. (1993). *Computer Business Review*. Retrieved from CBR Online website: http://www.cbronline.com/news/cray_duly_launches_its_22m_to_31m_parallel_t3d

Dahlbom, M. (2002). Estimation of image noise in PET using the Bootstrap method. *Ieee Transactions on Nuclear Science, 49 I*(5), 2062-2066. doi: 10.1109/tns.2002.803688

Daube-Witherspoon, M. E., Karp, J. S., Casey, M. E., DiFilippo, F. P., Hines, H., Muehllehner, G., . . . Sossi, V. (2002). PET performance measurements using the NEMA NU 2-2001 standard. *Journal of Nuclear Medicine, 43*(10), 1398-1409.

Daube-Witherspoon, M. E., & Muehllehner, G. (1987). Treatment of axial data in three-dimensional PET. *J Nucl Med, 28*(11), 1717-1724.

De Beenhouwer, J., Kruecker, D., Staelens, S. G., Ferrer, L., Chatziioannou, A. F., & Rannou, F. R. (2005). *Distributed computing platform for PET and*

*SPECT simulations with GATE.* Paper presented at the Nuclear Science Symposium Conference Record, 2005 IEEE.

De Beenhouwer, J., Staelens, S., Vandenberghe, S., & Lemahieu, I. (2007). *Acceleration of GATE SPECT simulations.* Paper presented at the Nuclear Science Symposium Conference Record, 2007. NSS '07. IEEE.

De Beenhouwer, J., Staelens, S. G., D'Asseler, Y., & Lemahieu, I. (2006). *Optimizing the Scalability of Parallelized GATE Simulations.* Paper presented at the Nuclear Science Symposium Conference Record, 2006. IEEE.

Debruyne, J. C., Van Laere, K. J., Versijpt, J., De Vos, F., Eng, J. K., Strijckmans, K., . . . De Reuck, J. L. (2002). Semiquantification of the peripheral-type benzodiazepine ligand C-11 PK11195 in normal human brain and application in multiple sclerosis patients. [Article]. *Acta Neurologica Belgica, 102*(3), 127-135.

Debruyne, J. C., Versijpt, J., Van Laere, K. J., De Vos, F., Keppens, J., Strijckmans, K., . . . De Reuck, J. L. (2003). PET visualization of microglia in multiple sclerosis patients using C-11 PK11195. [Article]. *European Journal of Neurology, 10*(3), 257-264.

Diorio, D., Welner, S. A., Butterworth, R. F., Meaney, M. J., & Suranyi-Cadotte, B. E. (1991). Peripheral benzodiazepine binding sites in Alzheimer's disease frontal and temporal cortex. *Neurobiol Aging, 12*(3), 255-258.

Doorduin, J., de Vries, E. F. J., Dierckx, R. A., & Klein, H. C. (2008). PET Imaging of the Peripheral Benzodiazepine Receptor: Monitoring Disease Progression and Therapy Response in Neurodegenerative Disorders. [Review]. *Current Pharmaceutical Design, 14*(31), 3297-3315.

Edison, P., Archer, H. A., Gerhard, A., Hinz, R., Pavese, N., Turkheimer, F. E., . . . Brooks, D. J. (2008). Microglia, amyloid, and cognition in Alzheimer's disease: An [11C](R)PK11195-PET and [11C]PIB-PET study. *Neurobiology of Disease, 32*(3), 412-419.

Endres, C. J., Pomper, M. G., James, M., Uzuner, O., Hammoud, D. A., Watkins, C. C., . . . Kassiou, M. (2009). Initial Evaluation of C-11-DPA-713, a Novel TSPO PET Ligand, in Humans. [Article]. *Journal of Nuclear Medicine, 50*(8), 1276-1282. doi: 10.2967/jnumed.109.062265

Erdi, Y. E., Nehmeh, S. A., Mulnix, T., Humm, J. L., & Watson, C. C. (2004). PET performance measurements for an LSO-based combined PET/CT scanner using the National Electrical Manufacturers Association NU 2-2001 standard. *J Nucl Med, 45*(5), 813-821.

Eriksson, L., Townsend, D., Eriksson, M., Casey, M. E., Schmand, M., Conti, M., . . . Nutt, R. (2005). Potential for a fifth generation PET scanner for oncology. In B. Yu (Ed.), *2005 IEEE Nuclear Science Symposium Conference Record, Vols 1-5* (pp. 1996-2000). New York: Ieee.

Espana, S., Herraiz, J. L., Vicente, E., Vaquero, J. J., Desco, M., & Udias, J. M. (2009). PeneloPET, a Monte Carlo PET simulation tool based on PENELOPE: features and validation. *Phys Med Biol, 54*(6), 1723-1742. doi: 10.1088/0031-9155/54/6/021

Farde, L., Ehrin, E., Eriksson, L., Greitz, T., Hall, H., Hedstrom, C. G., . . . Sedvall, G. (1985). Substituted benzamides as ligands for visualization of dopamine receptor binding in the human brain by positron emission tomography. [Research Support, Non-U.S. Gov't]. *Proceedings of the National Academy of Sciences of the United States of America, 82*(11), 3863-3867.

Finnie, S. (2007). Mac vs. PC cost analysis: How does it all add up? *Computerworld*. Retrieved from http://www.computerworld.com/s/article/9023959/

Fujita, M., Imaizumi, M., Zoghbi, S. S., Fujimura, Y., Farris, A. G., Suhara, T., . . . Innis, R. B. (2008). Kinetic analysis in healthy humans of a novel positron emission tomography radioligand to image the peripheral benzodiazepine receptor, a potential biomarker for inflammation. *Neuroimage, 40*(1), 43-52.

Garnett, E. S., Firnau, G., & Nahmias, C. (1983). Dopamine visualized in the basal ganglia of living man. [Research Support, Non-U.S. Gov't]. *Nature, 305*(5930), 137-138.

Gerhard, A., Pavese, N., Hotton, G., Turkheimer, F., Es, M., Hammers, A., . . . Brooks, D. J. (2006). In vivo imaging of microglial activation with [11C](R)-PK11195 PET in idiopathic Parkinson's disease. *Neurobiology of Disease, 21*(2), 404-412.

Gerhard, A., Schwarz, J., Myers, R., Wise, R., & Banati, R. B. (2005). Evolution of microglial activation in patients after ischemic stroke: a [11C](R)-PK11195 PET study. *Neuroimage, 24*(2), 591-595.

Graham, M. M. M., M.; Spence, A.M.; O'Sullivan, F.; Lewellen, T.K.; Link, J.M. and Krohn, K.A. (2002). The FDG lumped constant in normal human brain. *Journal of Nuclear Medicine, 43*(9), 1157-1166.

Groom, G. N., Junck, L., Foster, N. L., Frey, K. A., & Kuhl, D. E. (1993). Positron Emission Tomography of C-11 PK 11195 Binding to Peripheral

Benzodiazepine Receptors in Alzheimers-Disease. [Meeting Abstract]. *Journal of Nuclear Medicine, 34*(5), P116-P117.

Groom, G. N., Junck, L., Foster, N. L., Frey, K. A., & Kuhl, D. E. (1995). PET of Peripheral Benzodiazepine Binding Sites in the Microgliosis of Alzheimer's Disease. *Journal of Nuclear Medicine, 36*(12), 2207-2210.

Grootoonk, S., Spinks, T. J., Sashin, D., Spyrou, N. M., & Jones, T. (1996). Correction for scatter in 3D brain PET using a dual energy window method. *Phys Med Biol, 41*(12), 2757-2774.

Gropp, W. (2003). *Beowulf cluster computing with Linux* (W. Gropp, E. Lusk & T. L. Sterling, Trans. 2nd ed. ed.). Cambridge, Mass. :: MIT Press.

Gulyas, B., Toth, M., Schain, M., Airaksinen, A., Vas, A., Kostulas, K., . . . Halldin, C. (2012). Evolution of microglial activation in ischaemic core and pen-infarct regions after stroke: A PET study with the TSPO molecular imaging biomarker C-11 vinpocetine. [Article]. *Journal of the Neurological Sciences, 320*(1-2), 110-117. doi: 10.1016/j.jns.2012.06.026

Gulyas, B., Vas, A., Toth, M., Takano, A., Varrone, A., Cselenyi, Z., . . . Halldin, C. (2011). Age and disease related changes in the translocator protein (TSPO) system in the human brain: Positron emission tomography measurements with C-11 vinpocetine. [Article]. *Neuroimage, 56*(3), 1111-1121. doi: 10.1016/j.neuroimage.2011.02.020

Gunn, R. N., Lammertsma, A. A., & Cunningham, V. J. (1998). Parametric imaging of ligand-recpetor interactions using a reference tissue model and cluster analysis. In R. E. D.-W. Carson, M. E.; Herscovitch, P. (Ed.), *Quantitative Function Brain Imaging with Positron Emission Tomography* (pp. 401-406). San Diego: Academic Press.

Gunn, R. N., Lammertsma, A. A., Hume, S. P., & Cunningham, V. J. (1997). Parametric imaging of ligand-receptor binding in PET using a simplified reference region model. [Article]. *Neuroimage, 6*(4), 279-287. doi: 10.1006/nimg.1997.0303

Gunn, R. N., Lammertsma, A. A., Hume, S. P., Myers, R., Bloomfield, P. M., & Cunningham, V. J. (1997). A simplified reference region approach to parametric imaging of ligand receptor binding in PET. [Meeting Abstract]. *Journal of Nuclear Medicine, 38*(5), 875-875.

Guo, Q. O., D.R.; Rabiner, E.A.; Turkheimer, F.E.; Gunn,R. (2012). Identifying improved TSPO PET imaging probes through biomathematics: The impact of multiple TSPO binding sites in vivo. *NeuroImage, 60*, 902-910.

Hammoud, D. A., Endres, C. J., Chander, A. R., Guilarte, T. R., Wong, D. F., Sacktor, N. C., . . . Pomper, M. G. (2005). Imaging glial cell activation with [11C]-R-PK11195 in patients with AIDS. *Journal of Neurovirology, 11*(4), 346-355.

Harrison, R. (2011, 07/15/2011). SimSET Home Page, 2013, from http://depts.washington.edu/simset/html/simset_main.html

Haynor, D. R., Harrison, R. L., & Lewellen, T. K. (1991). The Use of Importance Sampling Techniques to Improve the Efficiency of Photon Tracking in Emission Tomography Simulations. *Medical Physics, 18*(5), 990-1001.

Haynor, D. R., & Woods, S. D. (1989). Resampling Estimates of Precision in Emission Tomography. *Ieee Transactions on Medical Imaging, 8*(4), 337-343.

Herholz, K., Herscovitch, P., & Heiss, W.-D. (2004). *NeuroPET- PET in Neuroscience and Clinical Neurology*. Berlin: Springer-Verlag.

Hevesy, G. (1923). The absorption and translocation of lead by plants. A contribution to the application of the method of radioactive indicators in the investigation of the change of substance in plants. [Article]. *Biochemical Journal, 17*(4-5), 439-445.

Hirvonen, J., Roivainen, A., Virta, J., Helin, S., Nagren, K., & Rinne, J. O. (2010). Human biodistribution and radiation dosimetry of C-11-(R)-PK11195, the prototypic PET ligand to image inflammation. [Article]. *European Journal of Nuclear Medicine and Molecular Imaging, 37*(3), 606-612. doi: 10.1007/s00259-009-1298-3

Hoffman, E. J., & Phelps, M. E. (1986). Positron Emission Tomography: Principles and Quantitation. In M. E. Phelps, J. C. Mazziota & H. R. Schelbert (Eds.), *Positron Emission Tomography and Autoradiography: Principles and Application for the Brain and Heart.* New York: Raven Press.

Holdsworth, C. H. L., C.S.; Janecek, M.; Dahlbom, M. and Hoffman, E.J. (2002). Performance Analysis of an Improved 3-D PET Monte Carlo Simulation and Scatter Correction. *IEEE TRANSACTIONS ON NUCLEAR SCIENCE, 49*(1), 83-89.

Huang, S.-C., & Phelps, M. E. (1986). Principles of Tracer Kinetic Modeling in Positron Emission Tomography and Autoradiography. In M. E. Phelps, J. C. Mazziota & H. R. Schelbert (Eds.), *Positron Emission Tomography*

*and Autoradiography: Principles and Applications for the Brain and Heart.* (pp. 287-346). New York: Raven Press.

Huang, S.-c. Y., Dan-chu; Barrio, Jorge R.; Grafton, Scott ; Melega, William P.;, & Hoffman, J. M. S., N; Mazziotta, John C. and Phelps, Michael E. . (1991). Kinetics and Modeling of L-6-[18F]Fluoro-DOPA in Human Positron Emission Tomographic Studies. *Journal of Cerebral Blood Flow and Metabolism, 11*, 898-913.

Huang, S. C. (2000). Anatomy of SUV. *Nuclear Medicine and Biology, 27*, 643-646.

Hume, S. P., Gunn, R. N., & Jones, T. (1998). Pharmacological constraints associated with positron emission tomographic scanning of small laboratory animals. *European Journal of Nuclear Medicine, 25*(2), 173-176.

Hume, S. P., Myers, R., Bloomfield, P. M., Opackajuffry, J., Cremer, J. E., Ahier, R. G., . . . Lammertsma, A. A. (1992). Quantitation of Carbon-11-Labelled Raclopride in Rat Striatum Using Positron Emission Tomography. [Article]. *Synapse, 12*(1), 47-54. doi: 10.1002/syn.890120106

Hutton, B. F., Nuyts, J., & Zaidi, H. (2006). Iterative Reconstruction Methods. In H. Zaidi (Ed.), *Quantitative Analysis in Nuclear Medicine Imaging* (pp. 107-140). New York: Springer.

Ikoma, Y., Watabe, H., Shidahara, M., Naganawa, M., & Kimura, Y. (2008). PET kinetic analysis: error consideration of quantitative analysis in dynamic studies. *Annals of Nuclear Medicine, 22*(1), 1-11. doi: 10.1007/s12149-007-0083-2

Imaizumi, M., Briard, E., Zoghbi, S. S., Gourley, J. P., Hong, J., Musachio, J. L., . . . Fujita, M. (2007). Kinetic evaluation in nonhuman primates of two new PET ligands for peripheral benzodiazepine receptors in brain. *Synapse, 61*(8), 595-605.

Jakoby, B. W., Bercier, Y., Watson, C. C., Bendriem, B., & Townsend, D. W. (2009). Performance Characteristics of a New LSO PET/CT Scanner With Extended Axial Field-of-View and PSF Reconstruction. *Ieee Transactions on Nuclear Science, 56*(3), 633-639. doi: 10.1109/tns.2009.2015764

Jan, S., Benoit, D., Becheva, E., Carlier, T., Cassol, F., Descourt, P., . . . Buvat, I. (2011). GATE V6: a major enhancement of the GATE simulation

platform enabling modelling of CT and radiotherapy. *Phys Med Biol, 56*(4), 881-901. doi: 10.1088/0031-9155/56/4/001

Jan, S., Comtat, C., Strul, D., Santin, G., & Trebossen, R. (2005). Monte Carlo simulation for the ECAT EXACT HR plus system using GATE. *Ieee Transactions on Nuclear Science, 52*(3), 627-633. doi: 10.1109/tns.2005.851461

Jan, S., Santin, G., Strul, D., Staelens, S., Assié, K., Autret, D., . . . Morel, C. (2004). GATE: a simulation toolkit for PET and SPECT. *Phys Med Biol, 49*(19), 4543-4561.

Johnson, R., Freund, J., & Miller, I. (2011). *Probability and Statistics for Engineers* (8th ed.): Pearson Education Inc.

Junck, L., Olson, J. M. M., Ciliax, B. J., Koeppe, R. A., Watkins, G. L., Jewett, D. M., . . . Young, A. B. (1989). PET Imaging of Human Gliomas With Ligands for the Peripheral Benzodiazepine Binding-site. [Article]. *Annals of Neurology, 26*(6), 752-758.

Karakatsanis, N., Sakellios, N., Tsantilas, N. X., Dikaios, N., Tsoumpas, C., Lazaro, D., . . . Nikita, K. (2006). Comparative evaluation of two commercial PET scanners, ECAT EXACT HR+ and Biograph 2, using GATE. *Nuclear Instruments & Methods in Physics Research Section a-Accelerators Spectrometers Detectors and Associated Equipment, 569*(2), 368-372. doi: 10.1016/j.nima.2006.08.110

Karakatsanis, N. A., & Nikita, K. S. (2008). *A study of the parameters affecting minimum detectable activity concentration level of clinical LSO PET scanners.* Paper presented at the BioInformatics and BioEngineering, 2008. BIBE 2008. 8th IEEE International Conference on.

Kassiou, M., Meikle, S. R., & Banati, R. B. (2005). Ligands for peripheral benzodiazepine binding sites in glial cells. *Brain Res Brain Res Rev, 48*(2), 207-210.

Keyes, J. W. (1995). SUV: Standard Uptake or Silly Useless Value? *Journal of Nuclear Medicine, 36*, 1836-1839.

Klunk, W. E., Wang, Y., Huang, G. F., Debnath, M. L., Holt, D. P., Shao, L., . . . Mathis, C. A. (2003). The binding of 2-(4'-methylaminophenyl)benzothiazole to postmortem brain homogenates is dominated by the amyloid component. *Journal of Neuroscience, 23*(6), 2086-2092.

Koeppe, R. A., Holthoff, V. A., Frey, K. A., Kilbourn, M. R., & Kuhl, D. E. (1991). Compartmental Analysis of C-11 Flumazenil Kinetics for the

Estimation of Ligand Transport Rate and Receptor Distribution Using Positron Emission Tomography. [Article]. *Journal of Cerebral Blood Flow and Metabolism, 11*(5), 735-744.

Kreisl, W. C., Fujita, M., Fujimura, Y., Kimura, N., Jenko, K. J., Kannan, P., . . . Innis, R. B. (2010). Comparison of C-11 -(R)-PK 11195 and C-11 PBR28, two radioligands for translocator protein (18 kDa) in human and monkey: Implications for positron emission tomographic imaging of this inflammation biomarker. *Neuroimage, 49*(4), 2924-2932. doi: 10.1016/j.neuroimage.2009.11.056

Kropholler, M. A., Boellaard, R., Elzinga, E. H., van der Laken, C. J., Maruyama, K., Kloet, R. W., . . . Lammertsma, A. A. (2009). Quantification of (R)- C-11 PK11195 binding in rheumatoid arthritis. [Article]. *European Journal of Nuclear Medicine and Molecular Imaging, 36*(4), 624-631. doi: 10.1007/s00259-008-0987-7

Kropholler, M. A., Boellaard, R., Schuitemaker, A., Folkersma, H., van Berckel, B. N. M., & Lammertsma, A. A. (2006). Evaluation of reference tissue models for the analysis of C-11 (R)-PK11195 studies. *Journal of Cerebral Blood Flow and Metabolism, 26*(11), 1431-1441. doi: 10.1038/sj.jcbfm.9600289

Kropholler, M. A., Boellaard, R., Schuitemaker, A., van Berckel, B. N. M., Luurtsema, G., Windhorst, A. D., & Lammertsma, A. A. (2005). Development of a tracer kinetic plasma input model for (R)-[11C]PK11195 brain studies. *Journal of Cerebral Blood Flow & Metabolism, 25*(7), 842-851.

Kumlien, E., Hilton-Brown, P., Spannare, B., & Gillberg, P. G. (1992). In vitro quantitative autoradiography of [3H]-L-deprenyl and [3H]-PK 11195 binding sites in human epileptic hippocampus. *Epilepsia, 33*(4), 610-617.

Lamare, F., Turzo, A., Bizais, Y., Le Rest, C. C., & Visvikis, D. (2006). Validation of a Monte Carlo simulation of the Philips Allegro/GEMINI PET systems using GATE. *Phys Med Biol, 51*(4), 943-962.

Lammertsma, A. A., & Hume, S. P. (1996). Simplified reference tissue model for PET receptor studies. [Article]. *Neuroimage, 4*(3), 153-158. doi: 10.1006/nimg.1996.0066

Lartizien, C., Aubin, J. B., & Buvat, I. (2010). Comparison of Bootstrap Resampling Methods for 3-D PET Imaging. [Article]. *Ieee Transactions on Medical Imaging, 29*(7), 1442-1454. doi: 10.1109/tmi.2010.2048119

Laruelle, M., Slifstein, M., & Huang, Y. (2003). Relationships between radiotracer properties and image quality in molecular imaging of the brain with positron emission tomography. *Molecular Imaging & Biology, 5*(6), 363-375.

Laruelle, M., Slifstein, M., & Huang, Y. Y. (2002). Positron emission tomography: imaging and neurotransporter availability. [Review]. *Methods, 27*(3), 287-299. doi: 10.1016/s1046-2023(02)00085-3

Lockhart, A., Davis, B., Matthews, J. C., Rahmoune, H., Hong, G. Z., Gee, A., . . . Brown, J. (2003). The peripheral benzodiazepine receptor ligand PK11195 binds with high affinity to the acute phase reactant alpha 1-acid glycoprotein: implications for the use of the ligand as a CNS inflammatory marker. [Article]. *Nuclear Medicine and Biology, 30*(2), 199-206.

Luus, C., Hanani, R., Reynolds, A., & Kassiou, M. (2010). The development of PET radioligands for imaging the translocator protein (18 kDa): What have we learned? [Review]. *Journal of Labelled Compounds & Radiopharmaceuticals, 53*(7-8), 501-510. doi: 10.1002/jlcr.1752

Mackenzie, I. R. A. (2000). Activated microglia in dementia with Lewy bodies. [Article]. *Neurology, 55*(1), 132-134.

Martinez, M. J., Bercier, Y., Schwaiger, M., & Ziegler, S. I. (2006). PET/CT Biograph (TM) Sensation 16 - Performance improvement using faster electronics. [Article]. *Nuklearmedizin-Nuclear Medicine, 45*(3), 126-133.

Matthews, J. C., Angelis, G. I., Kotasidis, F. A., Markiewicz, P. J., & Reader, A. J. (2010, Oct. 30 2010-Nov. 6 2010). *Direct reconstruction of parametric images using any spatiotemporal 4D image based model and maximum likelihood expectation maximisation*. Paper presented at the Nuclear Science Symposium Conference Record (NSS/MIC), 2010 IEEE.

Meikle, S., & Badawi, R. D. (2003). Quantitative Techniques in PET. In P. E. Valk, D. L. Bailey, D. W. Townsend & M. Maisey (Eds.), *Positron Emission Tomography: Basic Science and Clinical Practice* (pp. 115-146). London: Springer-Varlag.

Meikle, S. R., Dahlbom, M., & Cherry, S. R. (1993). Attenuation correction using count-limited transmission data in positron emission tomography. *J Nucl Med, 34*(1), 143-150.

National Electrical Manufacturers Association. (2007). NEMA Standards Publication NU 2-2007: Performance Measurements of Positron

Emission Tomographs (Vol. NU 2-2007). Rosslyn, Virginia: National Electrical Manufacturers Association.

Nimmerjahn, A., Kirchhoff, F., & Helmchen, F. (2005). Resting microglial cells are highly dynamic surveillants of brain parenchyma in vivo. *Science, 308*(5726), 1314-1318. doi: 10.1126/science.1110647

Nuyts, J. (2002). On estimating the variance of smoothed MLEM images. [Article]. *Ieee Transactions on Nuclear Science, 49*(3), 714-721. doi: 10.1109/tns.2002.1039553

Oakes, T. R., Sossi, V., & Ruth, T. J. (1998). Normalization for 3D PET with a low-scatter planar source and measured geometric factors. [Article; Proceedings Paper]. *Physics in Medicine and Biology, 43*(4), 961-972. doi: 10.1088/0031-9155/43/4/023

Ollinger, J. M. (1996). Model-based scatter correction for fully 3D PET. *Phys Med Biol, 41*(1), 153-176.

Ouchi, Y., Yoshikawa, E., Sekine, Y., Futatsubashi, M., Kanno, T., Ogusu, T., & Torizuka, T. (2005). Microglial activation and dopamine terminal loss in early Parkinson's disease. [Article]. *Annals of Neurology, 57*(2), 168-175. doi: 10.1002/ana.20338

Owen, D. R., Gunn, R.N., Wadsworth, G., Lewis, A., Rhodes, C., Bennacef, I., Parker, C.A., Matthews, P.M., Rabiner, E.A. (2012). An 18 kDa translocator protein (TSPO) polymorphism (Ala147Thr) explains variation in PBR28 binding affinity between human subjects. *J. Cereb. Blood Flow Metab, 32*, 1-5.

Owen, D. R., Howell, O. W., Tang, S. P., Wells, L. A., Bennacef, I., Bergstrom, M., . . . Parker, C. A. (2010). Two binding sites for H-3 PBR28 in human brain: implications for TSPO PET imaging of neuroinflammation. *Journal of Cerebral Blood Flow and Metabolism, 30*(9), 1608-1618. doi: 10.1038/jcbfm.2010.63

Owen, D. R., Rabiner, E. A., Gunn, R. N., Matthews, P. M., & Parker, C. A. (2010). PBR28, PBR06 and PBR111 bind two distinct TSPO sites in human brain tissue. *Neuroimage, 52*, S30-S31. doi: 10.1016/j.neuroimage.2010.04.214

Owen, D. R. J., Gunn, R. N., Rabiner, E. A., Bennacef, I., Fujita, M., Kreisl, W. C., . . . Parker, C. A. (2011). Mixed-Affinity Binding in Humans with 18-kDa Translocator Protein Ligands. [Article]. *Journal of Nuclear Medicine, 52*(1), 24-32. doi: 10.2967/jnumed.110.079459

Panin, V. Y., Kehren, F., Michel, C., & Casey, M. (2006). Fully 3-D PET reconstruction with system matrix derived from point source measurements. *IEEE Trans Med Imaging, 25*(7), 907-921.

Papadopoulos, V., Baraldi, M., Guilarte, T. R., Knudsen, T. B., Lacapere, J. J., Lindemann, P., . . . Gavish, M. (2006). Translocator protein (18kDa): new nomenclature for the peripheral-type benzodiazepine receptor based on its structure and molecular function. [Research Support, Non-U.S. Gov't Review]. *Trends in Pharmacological Sciences, 27*(8), 402-409.

Pavese, N., Gerhard, A., Tai, Y. F., Ho, A. K., Turkheimer, F., Barker, R. A., . . . Piccini, P. (2006). Microglial activation correlates with severity in Huntington disease: a clinical and PET study. *Neurology, 66*(11), 1638-1643.

Persson, A., Ehrin, E., Eriksson, L., Farde, L., Hedstrom, C. G., Litton, J. E., . . . Sedvall, G. (1985). Imaging of [11C]-labelled Ro 15-1788 binding to benzodiazepine receptors in the human brain by positron emission tomography. [Research Support, Non-U.S. Gov't]. *Journal of Psychiatric Research, 19*(4), 609-622.

Petittaboue, M. C., Baron, J. C., Barre, L., Travere, J. M., Speckel, D., Camsonne, R., & Mackenzie, E. T. (1991). Brain Kinetics and Specific Binding of C-11 PK 11195 to Omega-3 Sites in Baboons - Positron Emission Tomography Study. [Note]. *European Journal of Pharmacology, 200*(2-3), 347-351.

Phelps, M. E. (2006). *PET: Physics, Instrumentation and Scanners*. New York: Springer Science+Business Media, LLC.

Phelps, M. E., Mazziota, J. C., & Schelbert, H. R. (1986). *Positron Emission Tomography and Autoradiography: Principles and Applications for the Brain and Heart.*: Raven Press.

PMOD Technologies Ltd. (2010). Users Guide: PMOD Kinetic Modeling (PKIN) Version 3.2 (pp. 129). Zurich: PMOD Technologies Ltd.

Podgorsak, E. B. (2006). *Radiation Physics for Medical Physicists*. Berlin: Springer-Verlag.

Politte, D. G. a. S., D.L. (1991). Corrections for accidental coincidences and attenuation in maximum-likelihood image reconstruction for positron-emission tomography. *IEEE Tranactions on Medical Imaging, 10*(1), 82-89.

Price, C. J. S., Wang, D., Menon, D. K., Guadagno, J. V., Cleij, M., Fryer, T., . . . Warburton, E. A. (2006). Intrinsic activated microglia map to the peri-

infarct zone in the subacute phase of ischemic stroke. *Stroke, 37*(7), 1749-1753.

Price, J. C. K., William E; Lopresti, Brian J; Lu, Xueling; Hoge, Jessica A ;, Ziolko, S. K. H., Daniel P; Meltzer, Carolyn C; DeKosky, Steven T and, & Mathis, C. A. (2005). Kinetic modeling of amyloid binding in humans using PET imaging and Pittsburgh Compound-B. *Journal of Cerebral Blood Flow & Metabolism, 25*, 1528–1547. doi: 10.1038/sj.jcbfm.9600146

Quillard, J. A. R., John F.; Wilde, Eric; Vernon, Mark; Mock, George. (1983). A study of corporate use of personal computers (Vol. no. 109. Working paper (Sloan School of Management), pp. 1512-1583).

Rahmim, A., Cheng, J. C., Blinder, S., Camborde, M. L., & Sossi, V. (2005). Quantitative accuracy considerations in dynamic state-of-the-art PET imaging (when average counts-per-LOR are (much) less than unity). In B. Yu (Ed.), *2005 IEEE Nuclear Science Symposium Conference Record, Vols 1-5* (pp. 2253-2255). New York: Ieee.

Rao, V. L. R., & Butterworth, R. F. (1997). Characterization of binding sites for the omega(3) receptor ligands H-3 PK11195 and H-3 RO5-4864 in human brain. [Article]. *European Journal of Pharmacology, 340*(1), 89-99. doi: 10.1016/s0014-2999(97)01395-2

Ratchford, J. N., Endres, C. J., Hammoud, D. A., Pomper, M. G., Shiee, N., McGready, J., . . . Calabresi, P. A. (2012). Decreased microglial activation in MS patients treated with glatiramer acetate. [Article]. *Journal of Neurology, 259*(6), 1199-1205. doi: 10.1007/s00415-011-6337-x

Rehfeld, N. S., Stute, S., Apostolakis, J., Soret, M., & Buvat, I. (2009). Introducing improved voxel navigation and fictitious interaction tracking in GATE for enhanced efficiency. *Physics in Medicine and Biology, 54*(7), 2163-2178. doi: 10.1088/0031-9155/54/7/021

Reilhac, A. (2013, 02/06/2013). PET-SORTEO home page 2013, from http://sorteo.cermep.fr/home.php

Reserve Bank of Australia. (2013). Reserve Bank of Australia Exchange Rate Data Retrieved 02/11/2013, 2013, from http://www.rba.gov.au/statistics/hist-exchange-rates/index.html

Ridge, D., Becker, D., Merkey, P., & Sterling, T. (1997). *Beowulf: Harnessing the power of parallelism in a Pile-of-PCs*. New York: I E E E.

Rogers, D. W. O., Bielajew, A. F., Nelson, W. R., & Hirayama, H. (1986). Coherent Scatter and Stopping Power Effects in EGS4. [Meeting Abstract]. *Medical Physics, 13*(4), 593-593.

Schiffer, W. K. (2011). Imaging in Neurology Research III: Focus on Neurotransmitter Imaging. In F. a. P. Kiessling, B.J. (Ed.), *Small Animal Imaging: Basics and Practical Guide* (pp. 515-541). Heidelberg: Springer.

Schmidtlein, C. R., Beattie, B. J., Bailey, D. L., Akhurst, T. J., Wang, W., Gonen, M., . . . Humm, J. L. (2010). Using an external gating signal to estimate noise in PET with an emphasis on tracer avid tumors. [Article]. *Physics in Medicine and Biology, 55*(20), 6299-6326. doi: 10.1088/0031-9155/55/20/016

Scott, L. R. (2005). *Scientific parallel computing / L. Ridgway Scott, Terry Clark, Babak Bagheri* (T. Clark & B. Bagheri, Trans.). Princeton, N.J. ; Oxford :: Princeton University Press.

Sekine, Y., Ouchi, Y., Sugihara, G., Takei, N., Yoshikawa, E., Nakamura, K., . . . Cadet, J. L. (2008). Methamphetamine causes microglial activation in the brains of human abusers. *Journal of Neuroscience, 28*(22), 5756-5761.

Semega, J. (2009). *Median Household Income for States: 2007 and 2008 American Community Surveys*.

Shah, F., Hume, S. P., Pike, V. W., Ashworth, S., & McDermott, J. (1994). Synthesis of the Enantiomers of N-Methyl-C-11 PK-11195 and Comparison of Their Behaviours as Radioligands for PK Binding-sites in Rats. [Article]. *Nuclear Medicine and Biology, 21*(4), 573-581.

Spinks, T. J., Jones, T., Bailey, D. L., Townsend, D. W., Grootoonk, S., Bloomfield, P. M., . . . Reed, J. (1992). Physical Performance of a Positron Tomograph for Brain Imaging With Retractable Septa. [Article]. *Physics in Medicine and Biology, 37*(8), 1637-1655.

Spinks, T. J., Jones, T., Gilardi, M. C., & Heather, J. D. (1988). Physical Performance of the Latest Generation of Commercial Positron Scanner. [Article]. *Ieee Transactions on Nuclear Science, 35*(1), 721-725.

Sterling, T., Cwik, T., Becker, D., Salmon, J., Warren, M., Nitzberg, B., & Ieee. (1998). *An assessment of Beowulf-class computing for NASA requirements: Initial findings from the first NASA workshop on Beowulf-class clustered computing.* Paper presented at the 1998 Ieee Aerospace Conference Proceedings, Vol 4, New York.

Strother, S. C., Casey, M. E., & Hoffman, E. J. (1990). Measuring PET scanner sensitivity: relating countrates to image signal-to-noise ratios using noise equivalents counts. *Nuclear Science, IEEE Transactions on, 37*(2), 783-788. doi: 10.1109/23.106715

Stroud, K. A. B., D.J. (2001). *Engineering Mathematics* (5th ed.). New York: Palgrave MacMillan.

Surti, S., & Karp, J. S. (2004). Imaging characteristics of a 3-dimensional GSO whole-body PET camera. *Journal of Nuclear Medicine, 45*(6), 1040-1049.

Surti, S., Kuhn, A., Werner, M. E., Perkins, A. E., Kolthammer, J., & Karp, J. S. (2007). Performance of Philips Gemini TF PET/CT scanner with special consideration for its time-of-flight imaging capabilities. *J Nucl Med, 48*(3), 471-480.

Tai, Y. F., Pavese, N., Gerhard, A., Tabrizi, S. J., Barker, R. A., Brooks, D. J., & Piccini, P. (2007). Imaging microglial activation in Huntington's disease. *Brain Research Bulletin, 72*(2-3), 148-151.

Takikawa, S., Dhawan, V., Robeson, W., Chaly, T., Spetsieris, P., & Eidelberg, D. (1993). Simplified Quantitative FDOPA PET Studies Using an Estimated Input Function Derived From a Population Blood Curve. [Meeting Abstract]. *Journal of Nuclear Medicine, 34*(5), P180-P181.

Takikawa, S., Dhawan, V., Robeson, W., Spetsieris, P., Chaly, T., & Eidelberg, D. (1992). Noninvasive Quantitative FDG-PET Studies with an Estimated Input Function Derived From a Population Arterial Blood Curve. [Meeting Abstract]. *Radiology, 185*, 138-138.

Teräs, M., Tolvanen, T., Johansson, J. J., Williams, J. J., & Knuuti, J. (2007). Performance of the new generation of whole-body PET/CT scanners: Discovery STE and Discovery VCT. *Eur J Nucl Med Mol Imaging, 34*(10), 1683-1692. doi: 10.1007/s00259-007-0493-3

Thiel, A., & Heiss, W.-D. (2011). Imaging of microglia activation in stroke. *Stroke, 42*(2), 507-512.

Thielemans, K., Tsoumpas, C., Mustafovic, S., Beisel, T., Aguiar, P., Dikaios, N., & Jacobson, M. W. (2012). STIR: software for tomographic image reconstruction release 2. *Phys Med Biol, 57*(4), 867-883. doi: 10.1088/0031-9155/57/4/867

Tomasi, G., Edison, P., Bertoldo, A., Roncaroli, F., Singh, P., Gerhard, A., . . . Turkheimer, F. E. (2008). Novel reference region model reveals increased microglial and reduced vascular binding of C-11(R)-PK11195 in patients

with Alzheimer's disease. *Journal of Nuclear Medicine, 49*(8), 1249-1256. doi: 10.2967/jnumed.108.050583

Tortora, G. J., & Grabowski, S. R. (1993). *Principles of Anatomy and Physiology* (7th ed.). New York: Harper Collins.

Towson, J. E. C. (2003). Radiation Dosimetry and Protection in PET. In P. E. Valk, D. L. Bailey, D. W. Townsend & M. Maisey (Eds.), *Positron Emission Tomography: Basic Science and Clinical Practice*. London: Springer-Varlag.

Turkheimer, F. E., Edison, P., Pavese, N., Roncaroli, F., Anderson, A. N., Hammers, A., . . . Brooks, D. J. (2007). Reference and target region modeling of C-11 -(R)-PK11195 brain studies. [Article]. *Journal of Nuclear Medicine, 48*(1), 158-167.

Turner, M. R., Cagnin, A., Turkheimer, F. E., Miller, C. C. J., Shaw, C. E., Brooks, D. J., . . . Banati, R. B. (2004). Evidence of widespread cerebral microglial activation in amyotrophic lateral sclerosis: an [11C](R)-PK11195 positron emission tomography study. *Neurobiology of Disease, 15*(3), 601-609.

Upton, G. C., Ian. (2011). *A Dictionary of Statistics* (2nd ed.). New York: Oxford University Press.

Venneti, S., Wiley, C. A., & Kofler, J. (2009). Imaging microglial activation during neuroinflammation and Alzheimer's disease. *Journal Of Neuroimmune Pharmacology: The Official Journal Of The Society On NeuroImmune Pharmacology, 4*(2), 227-243.

Warren, M. S., Becker, D. J., Goda, M. P., Salmon, J. K., & Sterling, T. (1997). *Parallel supercomputing with commodity components*. Athens: C S R E a Press.

Watson, C. C., Newport, D., & Casey, M. E. (1996). A Single Scatter Simulation Technique for Scatter Correction in 3D PET. In P. Grangeat & J.-L. Amans (Eds.), *Three-Dimensional Image Reconstruction in Radiology and Nuclear Medicine* (Vol. 4, pp. 255-268): Springer Netherlands.

Wiley, C. A., Lopresti, B. J., Becker, J. T., Boada, F., Lopez, O. L., Mellors, J., . . . Mathis, C. A. (2006). Positron emission tomography imaging of peripheral benzodiazepine receptor binding in human immunodeficiency virus-infected subjects with and without cognitive impairment. *Journal of Neurovirology, 12*(4), 262-271.

Yamamoto, S., Horii, H., Hurutani, M., Matsumoto, K., & Senda, M. (2005). Investigation of single, random, and true counts from natural radioactivity

in LSO-based clinical PET. [Article]. *Annals of Nuclear Medicine, 19*(2), 109-114.

Yaqub, M., Boellaard, R., Kropholler, M. A., Lubberink, M., & Lammertsma, A. A. (2004). Simulated annealing in pharmacokinetic modeling of PET neuroreceptor studies: accuracy and precision compared with other optimization algorithms. In J. A. Seibert (Ed.), *2004 IEEE Nuclear Science Symposium Conference Record, Vols 1-7* (pp. 3222-3225).

Yaqub, M., van Berckel, B. N. M., Schuitemaker, A., Hinz, R., Turkheimer, F. E., Tomasi, G., . . . Boellaard, R. (2012). Optimization of supervised cluster analysis for extracting reference tissue input curves in (R)- C-11 PK11195 brain PET studies. [Article]. *Journal of Cerebral Blood Flow and Metabolism, 32*(8), 1600-1608. doi: 10.1038/jcbfm.2012.59

Yasuno, F., Ota, M., Kosaka, J., Ito, H., Higuchi, M., Doronbekov, T. K., . . . Suhara, T. (2008). Increased Binding of Peripheral Benzodiazepine Receptor in Alzheimer's Disease Measured by Positron Emission Tomography with C-11 DAA1106. [Article]. *Biological Psychiatry, 64*(10), 835-841. doi: 10.1016/j.biopsych.2008.04.021

Yelick, K. C., Susan; Draney, Brent; Canon, Richard Shane. (2011). *The Magellan Report on Cloud Computing for Science*. U.S. Department of Energy Retrieved from http://science.energy.gov/ascr/.

Yokokura, M., Mori, N., Yagi, S., Yoshikawa, E., Kikuchi, M., Yoshihara, Y., . . . Ouchi, Y. (2011). In vivo changes in microglial activation and amyloid deposits in brain regions with hypometabolism in Alzheimer's disease. *European Journal of Nuclear Medicine & Molecular Imaging, 38*(2), 343-351.

Zaidi, H. (2006). Monte Carlo Modelling in Nuclear medicine Imaging. In H. Zaidi (Ed.), *Quantitative Analysis in Nuclear Medicine Imaging* (pp. 358-390). New York: Springer Science+Business Media Inc.

Zaidi, H., Labbe, C., & Morel, C. (1998). Implementation of an environment for Monte Carlo simulation of fully 3-D positron tomography on a high-performance parallel platform. [Article]. *Parallel Computing, 24*(9-10), 1523-1536. doi: 10.1016/s0167-8191(98)00069-6

Zaidi, H., Montandon, M. L., & Meikle, S. (2007). Strategies for attenuation compensation in neurological PET studies. *Neuroimage, 34*(2), 518-541. doi: 10.1016/j.neuroimage.2006.10.002

Zanzonico, P. (2011). Noninvasive Imaging for Supporting basic Research. In F. a. P. Kiessling, B.J. (Ed.), *Small Animal Imaging: Basics and Practical Guide* (pp. 3-16). Heidelberg: Springer.

Zhang, M. R., Maeda, J., Ogawa, M., Noguchi, J., Ito, T., Yoshida, Y., . . . Suzuki, K. (2004). Development of a new radioligand, N-(5-fluoro-2-phenoxyphenyl)-N-(2- F-18 fluoroethyl-5-methoxybenzyl)acet amide, for PET imaging of peripheral benzodiazepine receptor in primate brain. [Article]. *Journal of Medicinal Chemistry, 47*(9), 2228-2235. doi: 10.1021/jm0304919

Zhang, M. R., Ogawa, M., Maeda, J., Ito, T., Noguchi, J., Kumata, K., . . . Suzuki, K. (2006). [2-11C]isopropyl-, [1-11C]ethyl-, and [11C]methyl-labeled phenoxyphenyl acetamide derivatives as positron emission tomography ligands for the peripheral benzodiazepine receptor: radiosynthesis, uptake, and in vivo binding in brain. [Research Support, Non-U.S. Gov't]. *Journal of Medicinal Chemistry, 49*(9), 2735-2742.